UNIVERSIDADE DO PORTO

FACULDADE DE ENGENHARIA

Master's Thesis

Development of Ballistic Protection for Military Aircraft: An investigation on material models with strain rate effects

André Rocha

Supervisor: Prof. Dr. Volnei Tita

Thesis submitted to Universidade do Porto – Faculdade de Engenharia
in partial fulfillment of the requirements for the degree of
Master in Mechanical Engineering - Aeronautical and Vehicles Structures

MEM

U.PORTO

FEUP FACULDADE DE ENGENHARIA
UNIVERSIDADE DO PORTO

DEPARTAMENTO DE ENGENHARIA MECÂNICA
Faculdade de Engenharia

October, 2024

Candidate: André Rocha, No. 202202496, up202202496@up.pt

Scientific Guidance: Prof. Dr. Volnei Tita, voltita@sc.usp.br

U.PORTO

FEUP FACULDADE DE ENGENHARIA
UNIVERSIDADE DO PORTO

DEPARTAMENTO DE ENGENHARIA MECÂNICA

Faculdade de Engenharia

Rua Dr. Roberto Frias, Porto

October, 2024

“To most people, the sky is the limit. To those who love aviation, the sky is home”.

Jerry Crawford

Acknowledgements

This work was possible thanks to the guidance and support of several people whose contributions were fundamental throughout the process.

Firstly, I would like to express my sincere thanks to Professor Dr. Volnei Tita for his guidance and the knowledge he passed on throughout this journey. I would also like to thank him for his availability and for, whenever necessary, connecting me with other colleagues to ensure the best possible support for my work.

I would also like to thank all the teachers and colleagues who have crossed my academic path, both during my bachelor's and master's degrees.

Last but not least, I would like to thank my family and friends for always being by my side and supporting me on this academic journey.

In particular, I would like to thank my parents for always providing me with all the conditions and encouraging me to study. Their valuable advice since childhood has been fundamental to my education and development as a person.

Abstract

Composite materials are widely used in both civil and military aviation due to their high strength and specific stiffness, offering significant advantages such as reduced fuel consumption, increased load capacity, and improved aerodynamic performance. Its integration into military aircraft occurred earlier than in civil aviation due to more flexible certification standards, focusing on performance factors such as speed and weapon load capacity. Composites have also proven effective in ballistic protection, offering a lighter alternative to traditional metals like steel or titanium. Ongoing research, including experimental and computational studies, aims to use and optimize hybrid laminates, that combine ceramic, metallic, and composite materials to enhance the ballistic performance.

The response of a structure can vary significantly depending on whether a load is applied gradually or suddenly. However, in the study of ballistic impacts, the effect of the strain rate is sometimes neglected in the literature. The aim of this work is to develop and explore approaches/models capable of simulating hybrid structures under ballistic impact, taking into account the effects of the strain rate. The first phase of the present work focused on the study of low-velocity impacts, initially using 2D models and later 3D models. All results were compared with experimental data from the literature, revealing a strong correlation between the simulated models and the experiments. Subsequently, high-velocity impact simulations were conducted. The initial analyses focused, individually, on laminates with unidirectional composite laminates and ceramic plates, and comparisons with data from the literature confirmed the quality of the numerical results. Next, hybrid laminates consisting of a ceramic front plate followed by unidirectional composite layers were studied. It became clear that hybridizing the protective structure was beneficial, as it increased the energy absorption. Additionally, laminates with unidirectional composite layers showed inferior performance compared to laminates with woven layers. The final part of the work involved adapting the models and criteria for simulating composite laminates with woven layers. Upon completing the simulations, a comparison of the numerical results with experimental data showed a good correlation, indicating the validity of the approach taken.

It was concluded it is very important to explore different methodologies capable of simulating hybrid laminates under high-velocity impacts, while also paving the way for

future improvements in the field.

Keywords: Balistic impact, Hybrid laminate, Strain rate effect, Explicit dynamic simulation

Resumo

Materiais compósitos são amplamente utilizados, tanto na aviação civil, como na militar, devido à sua alta resistência e rigidez específica, oferecendo vantagens significativas, como redução do consumo de combustível, aumento da capacidade de carga e melhoria no desempenho aerodinâmico. A sua integração em aeronaves militares ocorreu previamente à integração na aviação civil, devido a padrões de certificação mais flexíveis, com foco em fatores de desempenho como velocidade e capacidade de carga de armas. Os compósitos mostram-se, também, eficazes na proteção balística, oferecendo uma alternativa mais leve aos metais tradicionais como aço ou titânio. Trabalhos em curso, incluindo estudos experimentais e computacionais, visam a utilização e otimização de laminados híbridos, que combinam materiais cerâmicos, metálicos e compósitos para melhorar o desempenho balístico.

A resposta de uma estrutura pode variar significativamente dependendo se a carga é aplicada gradualmente ou de forma repentina. No entanto, no estudo de impactos balísticos, o efeito da taxa de deformação é, por vezes, negligenciado na literatura. O objetivo deste trabalho é desenvolver e explorar abordagens/modelos capazes de simular estruturas híbridas sob impacto balístico, tendo em conta os efeitos da taxa de deformação. A primeira fase do trabalho concentrou-se no estudo de impactos de baixa velocidade, inicialmente utilizando modelos 2D e depois modelos 3D. Todos os resultados foram comparados com dados experimentais presentes na literatura, revelando uma forte correlação entre os modelos simulados e os dados experimentais. Em seguida, foram realizadas simulações de impactos de alta velocidade. As análises iniciais focaram-se, individualmente, em laminados compósitos unidirecionais e placas cerâmicas, e as comparações com dados da literatura confirmaram a qualidade dos resultados numéricos. Em seguida, foram estudados laminados híbridos, compostos por uma placa frontal cerâmica seguida de camadas unidirecionais de compósito. Ficou claro que a hibridização da estrutura de proteção foi benéfica, pois aumentou a absorção de energia. Além disso, os laminados com camadas de compósito unidirecionais mostraram desempenho inferior em comparação com camadas bidirecionais. A última parte do trabalho envolveu a adaptação dos modelos e critérios para simulação de laminados compósitos com camadas bidirecionais. Após a conclusão das simulações, a comparação dos resultados numéricos com os dados experimentais mostrou uma boa correlação, indicando a validade da abordagem adotada.

Concluiu-se que é de fundamental importância explorar diferentes metodologias capazes de simular laminados híbridos sob impactos de alta velocidade, abrindo assim caminho

para futuras melhorias na área.

Palavras-Chave: Impacto balístico, Laminado híbrido, Efeito da taxa de deformação, Simulação dinâmica explícita

Contents

List of Figures vii

List of Tables ix

List of Acronyms xi

List of Symbols xiii

1 Introduction 1
- 1.1 Contextualisation and Objectives . . . 1
- 1.2 Methodology . . . 2
- 1.3 Document Organization . . . 3

2 Literature Review 5
- 2.1 Composite Materials . . . 5
  - 2.1.1 Matrices . . . 6
  - 2.1.2 Reinforcements . . . 7
  - 2.1.3 Composite structures in aeronautical engineering . . . 9
  - 2.1.4 Hybrid Composite Laminates . . . 10
- 2.2 Military Aircraft Certification . . . 12
  - 2.2.1 MIL-STD-662F . . . 16
- 2.3 Ballistic Protections . . . 17
  - 2.3.1 Composite materials for ballistic protections . . . 18
    - Failure mechanisms in composite materials under impact . . . 20
    - Hybrid laminates for ballistic applications . . . 22
  - 2.3.2 Ballistic protections development and practical examples . . . 22
- 2.4 Dynamic Explicit Finite Element Modelling . . . 23

3 Models' theoretical description 27
- 3.1 Hashin Criterion . . . 28
  - 3.1.1 Hashin Criterion - Damage Evolution Law . . . 30
- 3.2 Modified Ladeveze Criterion . . . 35
  - 3.2.1 Modified Ladeveze Criterion - Damage Evolution Law . . . 36
- 3.3 Strain rate effect on polymer matrix composites . . . 39

3.4 Inter-laminar failure model 40
3.4.1 Inter-laminar failure model - Damage Evolution Law 41
3.5 Johnson–Holmquist model 42
3.6 Damage models and FEM software connection 44

4 Case studies: Low-velocity impacts 47
4.1 Low velocity Impact - 2D Approach 48
4.1.1 2D - Results 52
4.2 Low velocity impact - 3D approach 57
4.2.1 3D - Results 58
4.2.2 3D Approach - Shear loss coefficients sensitivity analysis 61
4.2.3 3D - Results with strain rate effect 63
4.3 Low velocity impact - 3D approach with cohesive elements 65
4.3.1 3D - Results with strain rate effect and cohesive elements 66

5 Case studies: High-Velocity/Ballistic Impacts 69
5.1 High velocity impact - Unidirectional composite laminate plate 70
5.1.1 Unidirectional composite laminate plate - Results 72
5.1.2 Shear loss coefficients sensitivity analysis 73
5.2 High velocity impact - Ceramic plate 75
5.2.1 High velocity impact on ceramic plate - Results 77
5.3 High velocity impact - Hybrid laminate plate 78
5.3.1 Hybrid laminate - Model-1 79
5.3.2 Hybrid laminate - Model-2 80
5.3.3 High velocity impact on hybrid laminate - Results 81
5.4 High velocity impact - Woven composite 86
5.4.1 High velocity impact on woven composite - Results 88

6 Conclusions 91
6.1 Future Work 93

Appendix A Simulating hybrid laminates in Abaqus 107
A.1 Accessing JH-2 criteria 107
A.2 Run a simulation with JH-2 criteria and a VUMAT simultaneously 110

Appendix B Abaqus tutorial: low-velocity impact on composite laminates 111

List of Figures

2.1 General structure of a composite material [14] 5
2.2 The evolution of composites use in the aeronautical industry [3] 10
2.3 Examples of laminate configurations (Adapted from [27]) 11
2.4 GLARE usage in the Airbus A380 (Extracted from [32]) 12
2.5 Nimrod MR2 Aircraft (Extracted from[37]) 14
2.6 MIL-STD-662F set up [8] 17
2.7 (a) - A-10C Thunderbolt II ("Warthog") [49], (b) - Titanium "Bathtub" [50] 18
2.8 Fibres ballistic performance comparison. Adapted from [52] 19
2.9 Back face cone formation 21
2.10 Ballistic panels [59] 23
2.11 Example function, $f(t)$ 24

3.1 d parameter evolution 31
3.2 Linear elastic and linear softening regime 32
3.3 Matrix damage surface 36
3.4 Damage evolution and thermodynamic force (Adapted from [70]) 38
3.5 Loading modes I, II and III [80] 41

4.1 Final mesh for Hashin 2D models. (a) - SC8R model, (b) - S4 model 49
4.2 Final assembly and boundary conditions for Hashin 2D models 50
4.3 Final mesh for Modified Ladeveze model 52
4.4 2D Hashin criterion results for $[0]_{10}$ laminate 54
4.5 2D Hashin criterion results for $[+45/-45/+45/0/90]_s$ laminate 54
4.6 2D Hashin criterion results for $[0/90/0/90/0]_s$ laminate 55
4.7 Comparison of 2D criteria results for $[0]_{10}$ laminate 56
4.8 Comparison of 2D criteria results for $[+45/-45/+45/0/90]_s$ laminate . 56
4.9 Comparison of 2D criteria results for $[0/90/0/90/0]_s$ laminate 57
4.10 (a) - 3D plate mesh, (b) - 3D model assembly 58
4.11 Comparison of different criteria results for $[0]_{10}$ laminate 59
4.12 Comparison of different criteria results for $[+45/-45/+45/0/90]_s$ laminate 60
4.13 Comparison of different criteria results for $[0/90/0/90/0]_s$ laminate 60

4.14 Hashin 3D criterion results for $[+45/-45/+45/0/90]_s$ laminate under 10.8 J impact 61
4.15 S_{mt} sensitivity analysis 63
4.16 S_{mc} sensitivity analysis 63
4.17 Comparison of Hashin 3D criteria results for $[+45/-45/+45/0/90]_s$ laminate 64
4.18 Comparison of Hashin 3D criteria results for $[0/90/0/90/0]_s$ laminate 65
4.19 Hashin 3D criteria results for $[+45/-45/+45/0/90]_s$ laminate under 10.8 J impact 65
4.20 Hashin 3D criteria with cohesive elements results for $[+45/-45/+45/0/90]_s$ laminate under 5.91 J impact 66
4.21 Iter-laminar damage of 5.91 J impact for $[+45/-45/+45/0/90]_s$ laminate. (a) - experimental data [86], (b) - numerical data 67

5.1 L1 laminate: (a) - final mesh; (b) - final assembly 72
5.2 Final Mesh: (a) - Projectile; (b) - Ceramic plate 76
5.3 Final assembly 76
5.4 Ceramic plate boundary conditions 77
5.5 Evolution of the projectile's kinetic energy 78
5.6 Model-1: (a) - final mesh; (b) - final assembly 79
5.7 Model-2: (a) - final mesh; (b) - final assembly 81
5.8 Model-1 results comparison 83
5.9 Model-2 results comparison 85
5.10 Model-2: Damage evolution for 600 m/s impact (sectional view) 85
5.11 Woven laminate: (a) - final mesh; (b) - final assembly 87
5.12 Woven laminate: (a) - impact evolution (side view); (b) - penetration hole (back view) 89

A.1 (a) - Creating the material; (b) - Generating input file 108
A.2 Instruction to run the Job 110
A.3 Instruction to run the Job with JH-2 and the Hashin 3D criterion. 110

List of Tables

2.1 Current *European Military Airworthiness Requirements* (EMARs) [40], [41] 15
2.2 Current *European Military Airworthiness Documents* (EMADs) [40], [41] . 15
2.3 MIL-STD-662F description [44] 17

3.1 Maximum scale factor values [78] 40
3.2 Access to material models 45

4.1 Composite material properties (*Carbon Fibre Reinforced Polymer* (CFRP)) [70], [86], [87] 48
4.2 S_{mt} and S_{mc} values 58
4.3 Cohesive elements properties 66

5.1 CFRP properties [86], [87], [96] 71
5.2 S_{mt} and S_{mc} values - High velocity impact 71
5.3 Residual velocity comparison of high-speed impact in CFRP unidirectional laminates 72
5.4 S_{mt} and S_{mc} sensitivity analysis of the L1 laminate at an impact velocity of 40 m/s 74
5.5 S_{mt} and S_{mc} sensitivity analysis of the L2 laminate at an impact velocity of 91 m/s 74
5.6 Silicon carbide properties (SiC) [97] 77
5.7 Alumina 99.5 % purity properties [82], [99] 81
5.8 Model-1 results 82
5.9 Model 2 results - 400 m/s impact 83
5.10 Model 2 results - 600 m/s impact 84
5.11 GFRP properties (E glass) [100], [101] 87
5.12 Maximum scale factor values - woven composite [78] 87
5.13 Woven composite laminate results comparison 88

List of Acronyms

2D	*Two dimensional*
3D	*Three dimensional*
AMC	*Acceptable Means of Compliance*
ARALL	*Aramid-Reinforced Aluminium Laminate*
CARALL	*Carbon Reinforced Aluminium Laminate*
CDM	*Continuum Damage Mechanics*
CFRP	*Carbon Fibre Reinforced Polymer*
DoD	*Department of Defence*
EASA	*European Union Aviation Safety Agency*
EDA	*European Defence Agency*
EMACC	*European Military Airworthiness Certification Criteria*
EMADs	*European Military Airworthiness Documents*
EMARs	*European Military Airworthiness Requirements*
EMJAAO	*European Military Joint Airworthiness Authorities Organisation*
EU	*European Union*
FAA	*Federal Aviation Administration*
FEM	*Finite Element Methods*
GLARE	*Glass Reinforced Aluminium Laminate*
GM	*Guidance Material*
GUI	*Graphical User Interface*
H3D	*Hashin 3D*
H3D+SRD	*Hashin 3D with Strain Rate Effect*

HR	*High rate*
ICAO	*International Civil Aviation Organisation*
IR	*Intermediate rate*
ISAs	*International Standardisation Agreements*
JH-2	*Johnson-Holquimist-2*
LVI	*Low-Velocity Impact*
MAA	*Military Aviation Authority*
MAWA	*Military Airworthiness Authorities*
MIL-HDBK	*Military Handbook*
MIL-STD	*Military Standard*
NGS	*Non-government Standards*
NMAAs	*National Military Airworthiness Authorities*
PBO	*Polyphenylene Benzobisoxazole*
PE	*Polyethylene*
PEEK	*Polyether ether ketone*
QS	*Quasi-static*
RAF	*Royal Air Force*
SF	*Scale Factors*
U.S.Army	*United States Army*
UD	*Unidirectional*
UHMWPE	*Ultra-High Molecular Weight Polyethylene*
UK	*United Kingdom*
USA	*Unite States of America*
USAF	*United States Air Force*
USN	*United States Navy*
VUMAT	*Vectorized User Material*

List of Symbols

Symbol	Description	Units
a	Acceleration	$\mathrm{m/s^2}$
c_d	Dilatational wave speed	$\mathrm{m/s}$
$\mathbf{C}$	Damping matrix	$\mathrm{Ns/m}$
$\mathbf{C}_d$	Damaged elasticity matrix	Pa
d	Damage variable	–
E_{tr}	Transferred energy	J
E	Modulus of elasticity	Pa
E_{DL}	Delamination energy	J
E_D	Secondary fibres deformation energy	J
E_{SP}	Shear plug energy	J
E_{sp}	Energy absorption capacity	$\mathrm{m^2/s^2}$
$E_{abs.target}$	Energy absorbed by the target	J
E_{BFC}	Back face cone deformation energy	J
E_F	Friction energy	J
E_{MC}	Matrix cracking energy	J
E_{Tf}	Primary fibres failure energy	J
F	Force	N
f	Vector of nodal forces	N
G	Fracture energy	$\mathrm{J/m^2}$
I	Internal force vector	N
$\mathbf{K}$	Stiffness matrix	$\mathrm{N/m}$
l_c	Characteristic length	m
$\mathbf{M}$	Mass matrix	kg
m	Mass	kg
P	Applied load vector	N
S	Laminate shear strength	Pa
t	Time	s
$\ddot{u}$	Acceleration vector	$\mathrm{m/s^2}$
$\dot{u}$	Velocity vector	$\mathrm{m/s}$

Symbol	Description	Units
u	Displacement vector	m
V_s	Sonic velocity / Impact velocity	$\mathrm{m/s}$
v	Velocity	$\mathrm{m/s}$
V_r	Residual velocity	$\mathrm{m/s}$
X_C	Laminate compressive strength in fibre direction	Pa
X_T	Laminate tensile strength in fibre direction	Pa
Y_C	Laminate compressive strength in matrix direction	Pa
Y_T	Laminate tensile strength in matrix direction	Pa
ρ	Density	$\mathrm{kg/m^3}$
ν	Poisson coefficient	–
$\dot{\varepsilon}$	Strain rate	$\mathrm{s^{-1}}$
σ_{rupt}	Rupture stress	Pa
ε_{rupt}	Rupture strain	–
ω	Frequency	$\mathrm{rad/s}$
σ	Acting stress	Pa
δ	Displacement	m
ε	Strain	–

Chapter 1

Introduction

1.1 Contextualisation and Objectives

Composite materials are known for their high strength and specific stiffness. In the aeronautical industry, the replacement of metals with these materials has been crucial to the development of lighter aircraft [1]. The introduction of this type of material has been slow, largely due to the certifying bodies. Since their behaviour differs from traditional materials such as aluminium or steel, the certifying agencies are concerned and are directing their efforts towards ensuring that composite structures maintain the same level of safety. Still, components such as wings, empennage, fuselage and fan blades are now often made from composites. As a result, there have been reductions in fuel consumption, increased load capacity and improvements in aerodynamic performance. Currently, widebody aircraft from the two main civil aircraft manufacturers, Boeing and Airbus, such as the B787 and A350, have approximately 50 per cent of their structural weight made up of composite materials [1]–[3].

In military aviation, the use of composite materials came about earlier as a result of more relaxed certification procedures. Although the safety demonstrated by the aircraft is important, its performance is the main objective, emphasising aspects such as weapon load capacity, maximum speed, manoeuvrability and operational flexibility [4]. Still in this field of aviation, composite materials have also emerged as a viable solution for the ballistic protection of aircraft. Using materials such as steel or titanium to ballistically protect aircraft has been used in aircraft such as the A-10C Thunderbolt II, but the high

density of these metals only allows for localised protection in order not to considerably increase the weight of the aircraft and reduce its performance [5].

With the development of composite materials and research into their performance in ballistic impacts, it has become feasible to implement ballistic protection in military aircraft with a low impact on their operation. However, it should be emphasised that the performance of these materials is not perfect. To this end, various studies have been carried out to create hybrid structures/plates, for example combining ceramic, metallic and composite materials. The objective is to overcome the individual deficiencies of each constituent [6], [7].

In addition to experimental studies and testing, the development of this type of laminate is also carried out using computational numerical methods, such as the finite element method. By employing material models that accurately describe the behavior of the different components, it becomes possible to explore various combinations of hybrid laminates without the high costs associated with physical experiments [8].

In this sense, the main motivation behind this dissertation is the investigation of material models for the development of a hybrid laminate plate for the protection of military aircraft. The design of a structure of this type can be divided into three distinct phases: conceptual design, preliminary design and detailed design. Since this dissertation is the first approach to the problem, it is inserted in the conceptual phase where requirements such as weight and thickness, may be considered secondary.

Thus, the primary objective of this work is to evaluate material models and/or approaches capable of simulating hybrid laminates subjected to ballistic or high-velocity impacts. To achieve this, dynamic explicit analyses should be employed in conjunction with *Three dimensional* (3D) models that account for the strain rate effect. Finally, cohesive elements should not be used, although their impact may still be assessed.

1.2 Methodology

To fulfill the stated objective, a progressive strategy was employed. Rather than initiating the project with high-speed impacts, it was initiated with low-speed impacts, formerly explored and experimentally characterized, providing a robust foundation for the starting point. Accordingly, the following methodology was employed:

- Studying low-velocity impacts in unidirectional composite laminates, with *Two dimensional* (2D) criteria.
- Subsequently, the same impacts were studied using 3D criteria, initially excluding the strain rate effect and later incorporating it.
- Studying high-velocity impacts on unidirectional composite laminates (using 3D criteria, both with and without the strain rate effect) and on ceramic materials.

- Exploring high-speed impacts in hybrid laminates made up of layers of unidirectional composite material and ceramic material.
- Adapting and analysing the performance of the 3D criterion used in unidirectional composite laminates for woven composite laminates subjected to high-velocity impacts.

1.3 Document Organization

The structure of the document is presented below. The chapters follow the order in which the project is developed, emphasising the progressive approach to the problem.

Chapter 1 - It introduces the work developed. It begins by contextualising the project and the objectives it should fulfil, as well as presenting the methodology employed.

Chapter 2 - This chapter presents a literature review. It is not only essential for acquiring relevant theoretical knowledge, but also for understanding the context of the problem and identifying the best way to orientate it. It begins with the study of composite materials and their constituents, focusing on laminated structures in the aeronautical industry. It also covers the certification of military aircraft and the development of ballistic protection structures. Finally, in the context of numerical modeling, explicit dynamic simulations are addressed.

Chapter 3 - It presents and describes in detail all the criteria used and the respective property degradation laws for the numerical simulations carried out. It also includes their implementation in the finite element software used.

Chapter 4 - This chapter covers simulations of low-speed impacts. All the models developed are described in detail and the results obtained are discussed and compared with experimental ones.

Chapter 5 - Following on from the previous chapter, it covers ballistic/high-velocity simulations. All the models are described in detail and, when possible, the results are compared with literature data.

Chapter 6 - It summarises the work carried out, highlighting the main conclusions, especially regarding the results obtained in chapters 4 and 5. In the final section, it presents a set of future activities to be developed as a complement to this study.

Chapter 2

Literature Review

2.1 Composite Materials

A composite material is understood to be the product resulting from the joining of two or more materials. Under some load cases such as compression and flexural loads, the final product exhibits properties and advantages superior to those presented by their constituents individually [9], [10].

In recent decades, a great deal of focus has been placed on this type of material, especially in the transport industry. However, composite materials are present in human life since its origin. One example is the very constitution of human bones. Its composition includes organic fibres, inorganic crystals, water and fats, making it a natural composite [11]. Moving on to human-made composites, the first evidences point to the use of straw and clay and the superposition of different oriented wood plies, to build means of transport (such as canoes) and houses [12]. As a general principle, the two main constituents of a composite material are the matrix and the fibre, as illustrated in the following Figure 2.1 [10], [13]. The next subchapters 2.1.1 and 2.1.2 are dedicated to explaining the constituents in a more comprehensive format.

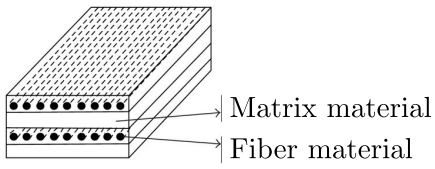


Figure 2.1: General structure of a composite material [14]

2.1.1 Matrices

The matrix is the constituent in which the fibres are dispersed and is therefore responsible for:

- Keeping the fibres correctly positioned (acting as a binder).
- Protecting the fibres during manufacture and the lifetime of the component/structure.
- Dictating the chemical and electrical properties of the resulting composite material.
- Transferring loads through the structure.
- Withstand inter laminar shear loads.

In terms of its constituent materials, polymers, ceramics, metals and carbon can be found. However, the first two are the most common as they allow to obtain the lowest manufacturing costs [13].

1. Polymeric matrices - can be further divided into thermoplastic and thermosetting. Thermosetting resins have a tridimensional interconnected/ cross-linked molecular structure that gradually consolidates during the curing process. It can take place at room temperature, but the application of heat and pressure is common in order to shorten the curing time. Once the curing process is complete, its shape can no longer be altered, which makes it difficult to recycle. These properties lead them to exhibit higher stiffness and temperature resistance. The most common thermosetting matrix is epoxy, presenting the following attributes [9], [10], [13]:

- Good adhesion to fibres.
- Good dimensional stability.
- Low susceptibility to voids during manufacture.
- Good resistance to adverse conditions.
- Fragile behaviour.
- Good corrosion resistance.

In addition to epoxy, the following thermosetting matrices can be found: polyesters, vinyl esters, bismaleimides, cyanate esters, polyimides and phenolics [15].

With regard to thermoplastic matrices, their properties are not defined by the cross-linking of the molecules in the curing process, but rather by the very characteristics of the molecules (monomers) that make it up. Therefore, by heating thermosetting matrices above their glass transition temperature, they enter a liquid/pasty state, allowing them to be moulded. Finally, it simply cools down to maintain the desired shape, thus reducing manufacturing time. Unlike thermosetting matrices, thermoplastic polymers can be repeatedly

heated/cooled, allowing manufacturing errors to be corrected and facilitating its recycling. When compared to thermosetting matrices, they also tend to have the following advantages:

- Higher strain to failure.
- Good resistance to chemicals.
- Good thermal stability.
- Low moisture absorption.

Concerning thermoplastic matrices, polyether ether ketone, polyphenylene sulfide and polyether ketone ketone, are some examples that can be found in the industry.

2. Ceramic matrices - are characterized by their very brittle behaviour, high strength and hardness and excellent resistance to very high-temperature environments [16]. The last properties are usually the principal reason why these materials are used, and is the one that decides which ceramic matrix to use. This characteristic is usually measured by the melting temperature. In almost all cases, it is higher than 1600°, except glass. For instance, the melting temperature of some ceramic matrices, such as, Aluminium Oxide/Alumina (Al_2O_3), Chromium Oxide-III (Cr_2O_3) and Niobium carbide (NbC) is 2050°, 2435° and 3499° respectively [10], [13].

Still in the context of ceramic matrices, cement can also be found. In the literature, it is often dealt separately from the materials listed above. However, cement, which originates from limestone, is widely used in construction, as it has good resistance and bonding properties [9], [17].

3. Metal matrices - are used as a means of improving the properties of common metal alloys. Metal alloys are not composed of just one pure metal, but the percentage of the other constituents compared to the main one is low, so they are not considered composites. By adding reinforcements to the metal alloys, properties such as wear and creep resistance are enhanced. Aluminium, magnesium, lead and nickel alloys are common metal matrices in the industry [9], [18], [19].

4. Carbon matrices - are mainly obtained by thermal decomposition of pitch or phenolic resin. Like ceramic matrices, they are particularly resistant to high temperatures and can reach working temperatures close to 2000°. Compared to ceramic matrices, they allow for the production of lighter components. However, the entire manufacturing process for carbon matrices is expensive, affecting the final products cost. In addition, they are very reactive with oxygen, so their advantages are more evident when used in inert environments [13], [20].

2.1.2 Reinforcements

Reinforcements are the dispersed constituent in the matrix. Their main function is to carry the loads, as well as, increase the rigidity and strength of the matrix. Different types of

reinforcements are available, each with specific characteristics and applications. In terms of type, they can be found in the form of particles, long or short fibres, plates and 2D or 3D fabrics [20], [21].

The superior mechanical properties of reinforcements compared to the matrix mean that they define the general properties of the final composite material. Therefore, the amount of reinforcement present in the material is an important and decisive measure. This parameter is evaluated by the volume fraction, which varies between 0 and 1, or 0 and 100 when expressed as a percentage [10].

With regard to the materials used in reinforcements, three major classes are found: carbon, glass and organic, mainly combined with polymeric matrices.

1. Carbon fibres - are produced from the thermal decomposition of cellulose, pitch or polyacrylonitrile. Usually, the process starts with obtaining the primary products (cellulose, pitch or polyacrylonitrile), followed by a stabilization process to enable the subsequent high temperature processes. The heat treatments can be carbonization only or carbonization followed by graphitization. The former leads to the production of carbon fibres, characterized by high strength and carbon contents ranging from $80-95\%$. The second process allows the carbon content to be increased to values above 95%, resulting in high stiffness fibres, known as graphite fibres [20].

Generally, this type of fibres is manufactured with diameters of around 8 μm and have a density between $1.6-2.0\ g/cm^3$. As far as mechanical properties are concerned, carbon fibres can have tensile strengths of more than 3000 *MPa*, while graphite fibres can have Young's Moduli of 500 *GPa* or more [13], [20].

2. Glass fibres - are obtained using silica (SiO_2) as the main precursor, along with small amounts of oxides such as calcium, boron and sodium oxides. The manufacturing process begins by melting the raw materials in a funnel that feeds a reservoir filled with circular holes. By the action of gravity, the material passes through the orifices to form filaments which are then wound. The final product has a diameter of between 8-15 μm and a density of around 2.5 g/cm^3 [13], [20].

Glass fibres can be further subdivided into three classes: E-Glass, C-Glass and S-Glass. The E stands for good electrical properties, nevertheless it also presents intermediate mechanical properties. C-Glass is employed when the need for good corrosion resistance is required, however, lower mechanical properties than E-Glass are demanded. Finally, S-Glass presents the best mechanical properties and temperature resistance, combined with a higher manufacturing price [13], [20].

3. Organic fibres - owe their name to the presence of long chains of carbon-containing molecules. Two main classes of organic fibres can be found, *Ultra-High Molecular Weight Polyethylene* (UHMWPE) and Aramid fibres. The polymeric materials that originate them have long, disorganized molecular chains. Therefore, in order to obtain the best mechanical properties, during the manufacturing process, it is important to produce fibres with properly aligned and extended molecular structures. As such, processes such as synthesis

and extrusion followed by stretching are used to manufacture this type of reinforcement. Polyethylene/high-density polyethylene is used as the percusor material for UHMWPE fibres. For aramid fibres, synthetic polyamides are used as base (for instance para-phenylene terephthalamide).

This type of fibre is characterized by high tensile stresses, high stiffness, high strain at failure, low density and good abrasion resistance. It should be noted that organic fibres are often known by their commercial names, such as Spectra or Dyneema for UHMWPE fibres and Kevlar or Nomex for aramid fibres [13], [20].

In addition to the three groups described in this section, ceramic, natural, boron or basalt reinforcements can also be found.

2.1.3 Composite structures in aeronautical engineering

The use of composite materials in the aeronautical industry is constantly growing. Fibre-reinforced polymeric matrices account for the largest share of this type of material in the industry. This can be justified by their high specific strength and stiffness and the possibility of tailoring their properties according to the specific application. Improved resistance to fatigue and corrosion are also advantages of using composite materials over conventional aeronautical metals such as steel or aluminium [10], [22].

Although extremely attractive, its introduction into the aeronautical industry, whether civilian or military, has been very controlled by the certifying authorities. Once they behave differently from ordinary metallic materials, extensive testing is required to ensure that composites maintain the high safety standards used in aeronautics. The use of the so-called "Building Block" strategy is a good methodology for investigating and demonstrating the behaviour of this type of material. The method starts by carrying out static, fatigue and damage tolerance tests on coupons, then on elements followed by sub-components and finally full-scale structures. Apart from supporting the design and certification phase, it is also vital for improving manufacturing processes [2], [10].

As mentioned above, the use of composite components in aircraft makes it possible to reduce their structural weight. However, weight reduction also entails other benefits, such as: lower fuel consumption, extra capacity to carry more cargo or capability to reduce wing area and engine power. Coupling these advantage with the tailoring capability offered by composites, structures such as wings and empennage can be designed with better aerodynamic performance, further increasing the overall efficiency of the aircraft [10], [22].

With regard to military aviation, several examples of the application of composite materials can be found. The first evidence of the use of these materials dates back to the 1950s and was restricted to a few components. Today, in modern aeroplanes, their use is indispensable, and it's present in most of the aircraft's structures. Such structures include, wings, empennage, vertical stabilizers, fuselages, doors/covers and engine components [10], [23].

Figure 2.2 shows the percentage of composite structures in relation to the total aircraft weight, from the 1970s to the end of the 2010s. Regarding military aviation (marked in

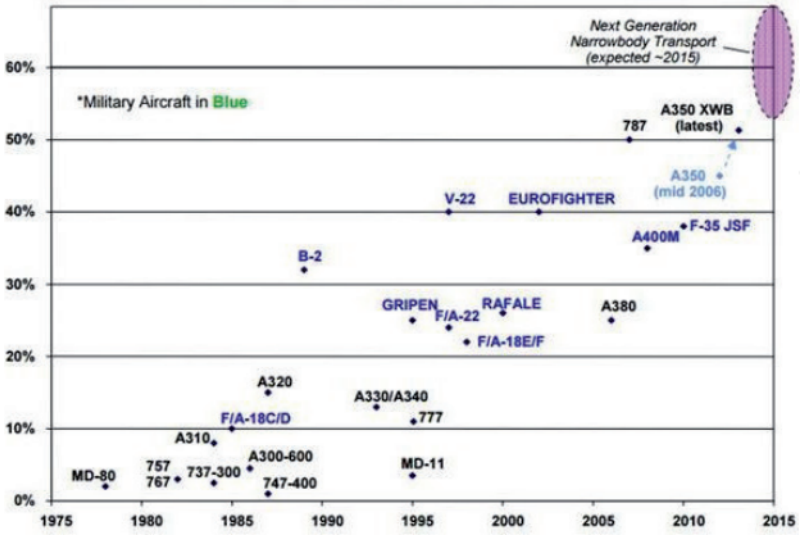


Figure 2.2: The evolution of composites use in the aeronautical industry [3]

blue) it is possible to observe the growth trend by comparing, for instance, the F/A-18C/D (1980s) where about 10% concerns composites to the most recent F-35 JSF (2010) where the percentage increases to around 40%. In fact, this trend is also present in civil aviation. For example, the MD-80 aircraft (1970) had only 10% of its structural weight in composite material, while aircraft such as the B787 or A350 have values of around 50%, which is a key factor for their successful performance [3].

As a practical example of the use of composites, the Lockheed S-3A aircraft, developed in the 1960s for submarine surveillance, initially had aluminium spoilers weighing around 5.9 kg each. The alternative developed later uses CFRP and a honeycomb core. The final weight is 3.6 kg, leading to a reduction of approximately 40% [22]. Moving forward to the 1990s, the Lockheed Martin F-22 Raptor is fitted with composite materials in various structures. The spars and skin of the wings, the empennage, and the fuselage of the F-22 are some examples of the application of CFRP, totalling around 23% of the aircraft's structural weight [22], [23]. As a more up-to-date example, the C-390 Millennium aircraft developed by Embraer for multi-mission transport. Its design uses composite materials in elements such as the flaps, ailerons, rudder and horizontal tail plane [24], [25].

2.1.4 Hybrid Composite Laminates

A common method of manufacturing polymer matrix composite components is to overlap laminae to form a laminate. A lamina, or ply, is made up of the matrix-reinforcement agglomerate, the latter of which can be in the form of continuous unidirectional, bidirectional or woven fibres. The predominant orientation of the fibres will define the direction of the greatest strength of the ply, resulting in anisotropic behaviour. The thickness of the ply is considerably inferior when compared to the length and width dimensions [20], [26].

Taking a unidirectional lamina as an example (i.e. all fibres oriented at 0°), the direction with the highest stiffness and strength is the 0° direction. At 90° is the direction with the lowest properties, since the lamina's response is characterized by the matrix. The same response would be obtained if a laminate was created by stacking successive parallel unidirectional plies. In order to make the laminate's response more isotropic, it is common to stack plies with different orientations (see Figure 2.3). In this way, the design of a component not only requires the selection of materials, but also the selection of the orientations of the layers that best satisfy the loading conditions to which it is subjected [20], [26].

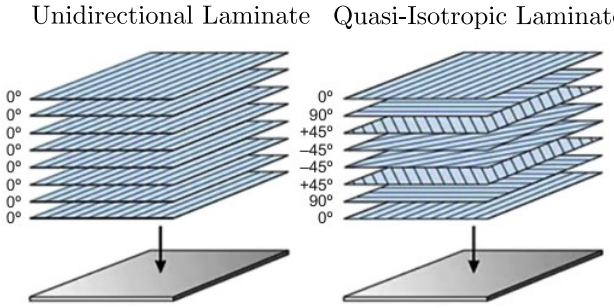


Figure 2.3: Examples of laminate configurations (Adapted from [27])

As seen in subsections 2.1.1 and 2.1.2, various matrices and reinforcements are available, each with its own advantages. In an attempt to combine the properties of these different constituents and create a material with superior characteristics, hybrid laminate composites have emerged.

In mechanical engineering, this type of laminate is mainly used in structural components and impact protection equipment. Examples include *Glass Reinforced Aluminium Laminate* (GLARE), *Aramid-Reinforced Aluminium Laminate* (ARALL) and *Carbon Reinforced Aluminium Laminate* (CARALL). They are made up of an alternating stack of composite laminates (glass, aramid or carbon) and thin metal layers, essentially aluminium.

The possibility of reducing the weight of components while maintaining excellent mechanical properties has attracted the attention of the aeronautical industry. Examples include the use of GLARE, upper fuselage and tail surfaces of the Airbus A380 (see Figure 2.4), bulk cargo floor of the Boeing 777, forward bulkhead Radome of the Learjet 45 and in the military field frames for the Airbus A400M. Its widespread use is due to its good resistance to fatigue, fire and impact. The latter characteristic has been exploited by the *Federal Aviation Administration* (FAA) in the development of blast-resistant aircraft containers [28]–[30].

ARALL was used in the manufacture of the Boeing C-17 Globemaster cargo cover as well as the Fokker F27 subshell wings. In the latter, it enabled a weight reduction of around 30%. Due to the presence of organic fibres, especially aramid, it has excellent impact and wear resistance. The use of CARALL, although more limited, is found, for example, in shock-absorbing helicopter mounts and aeroplane seats. It has excellent impact resistance



Figure 2.4: GLARE usage in the Airbus A380 (Extracted from [32])

and high energy absorption, but the complexity of production is an obstacle to its wider use [28].

In addition to combinations between fibre-reinforced polymers and metals, hybrid composites can be found with a totally polymeric matrix but with the presence of different materials in the reinforcement. Since carbon fibre composites are more expensive than glass fibres, the automotive industry saw a solution in using carbon reinforcements intercalated with glass reinforcements in a polymer matrix. In this way, superior mechanical properties were ensured (due to the presence of carbon fibres), but the price of the components was reduced.

In the field of impact protection, the use of laminated composites is also proving to be an advantage [6], [31]. This topic will be discussed in further detail in section 2.3, in the context of ballistic protection.

2.2 Military Aircraft Certification

As far as aircraft certification is concerned, there is a big difference between the civil and military branches. This divergence is due the fact that each type of aircraft is developed for completely different purposes. Civil aircraft, such as the Airbus A320 or Boeing B737 family, are designed to meet the needs of the air market (passenger and freight transport), using well-established technologies and aiming for low operating costs. On the other hand, military aircraft are developed with the purpose of ensuring a country's security, and can carry out air combat, patrol, medical evacuation or troop/armour transport missions. Therefore, this type of aircraft is equipped with state-of-the-art systems, often at the development stage, since the aim is to gain an advantage over the enemy in the event of a threat. In this way, the operational cost becomes less important and the aircraft's manoeuvrability and versatility in adverse situations stands out [4], [33], [34].

The high degree of regulation in the civil aviation industry began in 1944 at the Chicago Convention, with the creation of the *International Civil Aviation Organisation* (ICAO), whose aim is to produce policies and standards that ensure safety in the civil aviation sector for its members. Nevertheless, ICAO has no legal power, which is left to regulatory/certifying bodies. Currently, the *Federal Aviation Administration* (FAA) in the United States

and *European Union Aviation Safety Agency* (EASA) in the *European Union* (EU) are the most notable. Other bodies can be found in different regions of the globe, however, they are strongly based on the aforementioned organisations. Both the FAA and EASA present a set of documents intended to regulate and certify the design of an aircraft, as well as the organisations responsible for its design, production and operation, guaranteeing a high level of safety [34]–[36].

With regard to the military sector, there is a completely different context. In this case, there are no universal regulations, so each country has its own *Military Aviation Authority* (MAA), which develops the requirements and procedures to be followed. When compared to civil aviation, the following characteristics of military aircraft certification stand out [4], [34]:

- Limited public information.
- Distribution and standardisation of information varies from country to country, reducing the transparency and homogeneity of the certification process.
- Governments can certify their state aircraft (civilian registered aircraft used in military operations).
- Acceptance of higher risk levels.
- The degree of rigour of the various evaluation phases is not consistent. It can be affected by various factors such as the available budget or the type of aircraft.
- Use of extremely recent technologies, which may still be under development.

These differences, although seen as beneficial in terms of keeping processes confidential and thus having a strategic advantage in the event of a threat, can lead to considerable problems. One example was the crash of the *Royal Air Force* (RAF) Nimrod MR2 Aircraft (Registration XV230) in Afghanistan in 2006 (see Figure 2.5) [37]. During a reconnaissance mission, the aircraft suffered a catastrophic fire in mid-flight, which resulted in its crash and consequently the death of all the crew members. The investigations concluded that the cause of the fire was due to overflow during air-to-air refuelling or a leak in the fuel system. The ignition source was identified as hot air ducts. In addition, design flaws and organisational problems were also identified as contributing factors. In this way, the investigation report presents a series of lessons and recommendations. Among the 10 recommendations, the need for a "New Military Airworthiness Regime" is particularly noteworthy. From this new regime, the following tasks emerge [37]:

- Establish a new *Military Aviation Authority* (MAA).
- Clear identification of those responsible for airworthiness.
- Develop readable and concise regulations.



Figure 2.5: Nimrod MR2 Aircraft (Extracted from[37])

- Implement a single risk management system.

These observations led to a remodelling of the structure of the *United Kingdom* (UK) military airworthiness system. As a result, all matters relating to military aeronautics are concentrated in an independent department of the UK Ministry of Defence [34].

As far as the EU is concerned, the *European Defence Agency* (EDA) was created in 2004 with the aim of improving defence and promoting cooperation between its members. Four years later, in 2008, the *Military Airworthiness Authorities* (MAWA) Forum was held. This convention was attended by representatives from each EDA member and was designed to harmonise their airworthiness requirements [34], [38]. To this end, the following objectives were defined:

- Common regulatory framework.
- Common certification processes.
- Common certification/design codes.
- Common approach to preservation of airworthiness.
- Arrangements for mutual recognition.
- Formation of a *European Military Joint Airworthiness Authorities Organisation* (EMJAAO) [39].

This joint effort has led to the publication of a series of *European Military Airworthiness Requirements* (EMARs) and *European Military Airworthiness Documents* (EMADs), which aim to keep as close as possible to the regulations applied to civil aviation, in this case developed by EASA. This set of EMARs includes guidelines for *Acceptable Means of Compliance* (AMC) and *Guidance Material* (GM). It is important to emphasise that the use of these tools for the purposes of certifying EDA members' military aircraft is purely voluntary [34], [40]. The following Tables 2.1 and 2.2 summarise the documents and give a brief description of them.

Table 2.1: Current *European Military Airworthiness Requirements* (EMARs) [40], [41]

Continued Airworthiness
EMAR 21 - Presents all requirements for certification of a new military aircraft, or a change to an existing type, its design and related activities.
EMACC (*European Military Airworthiness Certification Criteria*) - Presents all the design criteria that are currently defined and available for developing a military certification baseline.
Continuing Airworthiness
EMAR M - Defines the procedures to be adopted to ensure the maintenance of airworthiness. The requirements imposed on the personnel and organisations that carry out continuing airworthiness are also specified.
EMAR 66 - Describes the training and education that aircraft maintenance personnel must have.
EMAR 145 - Establishes the requirements to be met by an organisation to qualify for the issue or continuation of an approval for the maintenance of aircraft and components.
EMAR 147 - Details the requirements that an organisation must meet to be able to conduct aircraft maintenance training and examination.
EMAR CAMO - Establishes the requirements to be met by an organisation to qualify for the issue or continuation of an approval certificate for the management of continuing airworthiness of an aircraft and of components for installation.

Table 2.2: Current *European Military Airworthiness Documents* (EMADs) [40], [41]

Current EMADs
EMAD 1 – Lists, defines and explains important acronyms contained in the EDA MAWA documents.
EMAD 20 – Provides the NMAAs information on how to use AMC 20 in a military environment. Note that AMC 20 was developed by EASA, thus aiming civil aviation.
EMAD MFTP - Establishes the Military Flight Test Permit Procedures
EMAD R – Defines the process of recognition. In other words, it details the procedure that EDA members must take in order to be recognised for following the guidelines of the harmonisation process.

In the same manner that the EASA is not responsible for certifying military aircraft in the *European Union* (EU), the FAA does not assume this responsibility in the *Unite States of America* (USA). The *Department of Defence* (DoD) delegates to its members, the *United States Air Force* (USAF), *United States Navy* (USN) and the *United States Army* (U.S.Army) to carry out this task. In turn, each sector has an entity responsible for defining

criteria, drawing up standards and issuing airworthiness certificates. All sectors follow a set of military criteria and standards developed under the Defence Standardisation Program [35], [42].

The Defence Standardisation Program was launched after the II World War, with the aim of reducing costs and increasing operational efficiency in military activities. The various documents can be classified as Defence Specifications; Defence Standards; Defence Handbooks; Data Item Descriptions; Federal standards, federal specifications, and commercial item descriptions; *Non-government Standards* (NGS) and *International Standardisation Agreements* (ISAs) [42].

Regarding aeronautical certification, the document MIL-HDBK-516C *Airworthiness Certification Criteria* is particularly noteworthy. It establishes a set of airworthiness certification criteria, standards and means of compliance. It should not be used as a requirement, but rather as a basis for the various organisations to support their certification basis. Instructions regarding the design of the structure, the various systems of an aircraft, its maintenance or how to obtain material properties are some topics covered [35], [43].

2.2.1 MIL-STD-662F

This subsection addresses specifically the MIL-STD-662F military standard, entitled V_{50} *Ballistic Test for Armor*, once it's used by some authors as a reference for numerical simulations [44].

MIL-STD-662F presents a set of conditions and procedures for the experimental determination of V_{50}, i.e., *"the velocity at which the probability of penetration of an armor material is 50 percent"*. Its use is directed towards, among other purposes, the development of internal/external aircraft armouring [44].

For a better understanding of the standard, a detailed description is given in Table 2.3, listing and describing the various chapters.

Furthermore, Figure 2.6 presents a simplification of the test set-up. First the plate/armour is properly fixed. A thin aluminium plate called a "witness plate" is placed behind it, which is responsible for determining whether total or partial penetration has occurred. After several firings, V_{50} is calculated as the arithmetic mean between the highest total penetration velocity and the lowest partial penetration velocity [8], [44].

Table 2.3: MIL-STD-662F description [44]

Chapter	Description
1	Defines the objective of the standard and its applicability.
2	Lists the documentation used as a reference.
3	Lists and defines all the concepts/parameters used in the standard.
4	Presents the requirements for the materials to be used (projectile, weapon, measuring material, etc.).
5	Details the requirements for test preparation and conditions, for processing the data obtained, and for preparing the report.
6	Provides additional information.
Table I	Provides test velocities and distances for different projectiles.

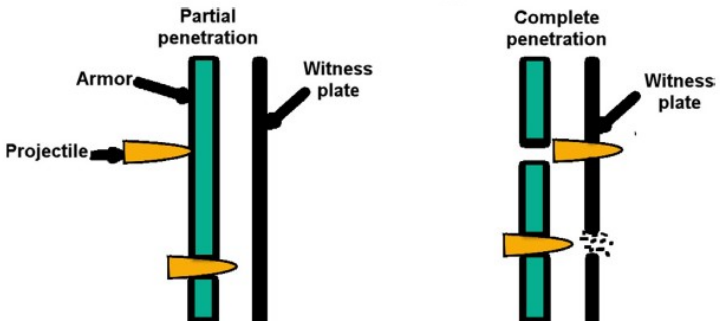


Figure 2.6: MIL-STD-662F set up [8]

2.3 Ballistic Protections

Ballistic protections are designed to prevent projectiles from injuring people or damaging material goods. Its application is not restricted to security forces or the military, but can also be used by civilians. Therefore, various types of equipment have been developed to accommodate their wide range of uses [8]. The two main categories of ballistic protection are soft and hard. Soft equipment should provide protection from projectiles with velocities up to 500 m/s, for higher velocities, the classification transitions to hard. In military applications, protections primarily align with the hard category, due the need to defend against sophisticated armaments. Protections are applied, for example, to tanks, ground combat vehicles, ships, helicopters and aeroplanes, the latter being of particular interest to this thesis [45], [46]. In addition, ballistic protections can be also classified based on their malleability, categorized into flexible or rigid equipment. Flexible protections include, for instance, bomb blankets and ballistic resistant vests. On the other hand, panels, shields and helmets are examples of rigid protections [47].

For a material to be suitable for ballistic protection, it needs to absorb the projectile's kinetic energy and dissipate it quickly [8], [47]. Traditionally, metallic and ceramic materials were used. However, once they exhibit high density values, their application on mobile equipments, such as aircraft or helicopters, becomes particularly problematic, as excessive structural weight is introduced. It can lead to loss of efficiency and range, reduction in cargo/weapons transport capacity, and it can also affect the vehicle's manoeuvrability. The A-10C Thunderbolt II ("Warthog") military aircraft is an example where metal materials are used for ballistic protection. Introduced into service in 1977 with the aim of assisting ground forces, this aircraft features a ballistic protection box, nicknamed "bathtub" due to its geometry, which is intended to shield the pilot as well as certain flight control systems. To this end, the structure was made from 3.8 cm thick titanium plates, totalling a weight of around 550 kg [5], [48].

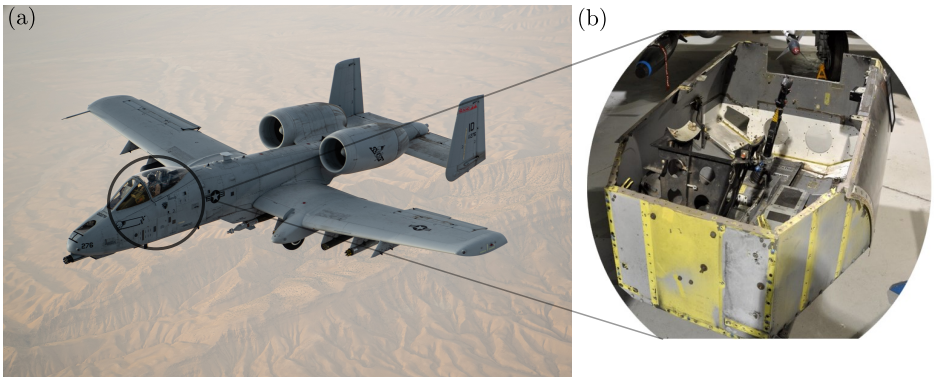


Figure 2.7: (a) - A-10C Thunderbolt II ("Warthog") [49], (b) - Titanium "Bathtub" [50]

2.3.1 Composite materials for ballistic protections

In order to reduce the weight of personal and vehicles ballistic protection equipment, the search for lightweight materials that are at the same time highly resistant to impact has gained prominence. In this sense, the constant development of composite materials has made it possible to use matrix-reinforcement combinations that are extremely efficient, from a ballistic point of view, while maintaining low weight. The focus is essentially on polymer matrix composites reinforced with organic fibres, namely aramid and UHMWPE fibres, the latter sometimes referred as high performance fibres [47], [51]. Furthermore, glass, carbon, and *Polyphenylene Benzobisoxazole* (PBO) fibers are also utilized, although on a smaller scale [51], [52].

In order to assess the ballistic performance of the different fibres available, the concepts of sonic velocity (V_s) and specific energy absorption (E_{sp}) are introduced, whose calculation is presented in Equation 2.1 and 2.2, respectively [47], [52]. Sonic speed, as the name suggests, refers to the speed at which a sound wave propagates through the fibre, and is related to the fibre's modulus of elasticity (E) and density (ρ). This term is related to the

material's ability to propagate a shock wave upon impact. Therefore, higher sonic velocity values lead to faster propagation of shock waves, resulting in quicker energy dissipation. With regard to the fibre's energy absorption capacity (E_{sp}), Equation 2.2 highlights that the key properties are tensile and strain at rupture (σ_{rupt} and ε_{rupt}, respectively) [47], [52].

$$V_s = \sqrt{\frac{E}{\rho}} \tag{2.1}$$

$$E_{sp} = 0.5\sigma_{rupt}\varepsilon_{rupt}/\rho \tag{2.2}$$

By multiplying the two previous parameters, Cunniff [53] proposed a new dimensionless metric, U^* (Equation 2.3), for comparing ballistic performance.

$$U^* = \frac{\sigma_{rupt}\varepsilon_{rupt}}{2\rho}\sqrt{\frac{E}{\rho}} \tag{2.3}$$

Figure 2.8 evaluates the ballistic performance of some fibres using the parameters mentioned previously (Equations 2.1 and 2.2). It shows the high ballistic capacity of high-performance fibres such as Dyneema and Spectra (indicated in red). These fibres present higher values of specific energy absorption and sonic velocity, indicating a great capacity to quickly dissipate and absorb energy from an impact. The good performance of PBO fibres also stands out. With regard to aramid fibres, although they are organic like high-performance fibres, they have considerably lower characteristics.

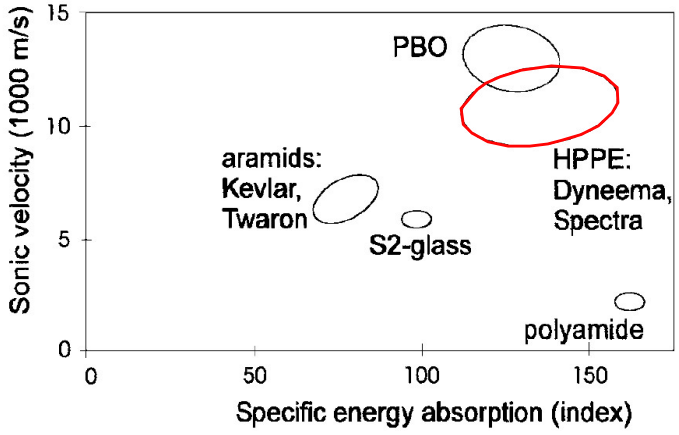


Figure 2.8: Fibres ballistic performance comparison. Adapted from [52]

In the manufacture of ballistic protection equipment, fibres can be arranged in 2D or 3D, the latter being less commonly used. Both 2D and 3D fabrics can be woven, nonwoven or knitted. In addition, the 2D configuration also offers the possibility of using *Unidirectional* (UD) fibres [8].

As far as the final structure is concerned, the fabrics can be used stand-alone ("loose") or impregnated with resin (forming a composite). "Loose" fabrics are commonly found in personal protective equipment like body armour, where flexibility and comfort are desired. These are layered until the required protection is achieved. Note that, they are typically utilized in conjunction with thin plates made of metallic or ceramic materials, which assist in dissipating the impact energy [8], [51].

When rigid protection plates are used, 2D structures are preferable. They are impregnated with resin and stacked to form a laminate. The plies can be in the form of woven or UD fibres, nevertheless, the latter has some advantages over woven fabrics. As in UD laminaes the fibres are all aligned and there is no interlacing between them, a faster response and shock wave propagation is obtained. Furthermore, reduced back face deformation is observed [51]. Regarding the resin or matrix that binds the fibres, both thermosetting and thermoplastic polymers are used. Epoxy, phenolics, and polyesters are examples of thermosetting matrices employed. Ballistic tests show that this type of resin has some inconveniences, particularly its brittle behaviour, described above in section 2.1.1, which promotes the propagation of cracks during impact. On the other hand, the more ductile response of thermoplastic matrices such as *Polyether ether ketone* (PEEK) and *Polyethylene* (PE) leads them to have a higher residual strength after impact [45], [54].

Failure mechanisms in composite materials under impact

The designing of ballistic protection equipment not only involves selecting the fibre and matrix (if applicable), but also aspects such as: choosing the type of fibre arrangement (2D, 3D, woven, UD, etc.) and the respective volume fraction; their orientation; the specific location of each orientation; the final thickness of the protection and, not least, an understanding of the structure failure mechanisms during the impact [51], [55].

Laminated composites can present two types of failure [55]:

- Intra-laminar: Fibre failure, matrix failure or failure of the interface between the matrix and the fibre
- Inter-laminar: delamination of the plies

Its occurrence during an impact event is described in more detail in the following paragraphs.

When the projectile comes into contact with the laminate, transverse (along the thickness) and longitudinal (in the plane) shock waves propagate in it. Initially, the transverse wave causes the upper layers to compress, causing some material to crush and forming a cone on the back face (see Figure 2.9). As the projectile advances, the height of the cone increases. This motion is mainly counteracted by the fibres, which gradually deform to the point where they reach the rupture strain and fail in tension. At the same time, matrix cracking and delaminations occur, caused by in-plane and out-of-plane compression. The

occurrence of delaminations is also amplified by the fact that, as the projectile penetrates, there is less thickness in the resistant material, and it is easier to separate the unperforated plies from the rest. Additionally, plug formation is present, resulting from through-thickness shear deformation [55], [56].

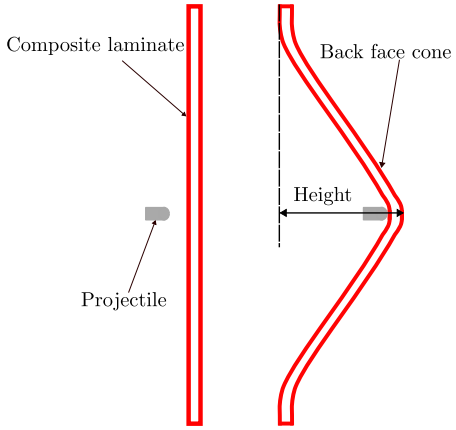


Figure 2.9: Back face cone formation

The occurrence of each of the failure mechanisms results in energy dissipation. They allow the understanding of how the laminate/target absorbs the impact energy. In this sense, reference [56], in an analytical approach, proposes an expression for calculating the energy absorbed by the composite target ($E_{abs.target}$). To this end, the fibres are separated into two classes. Primary fibres are those that come into contact with the projectile and can break, while the remaining fibres are the secondary ones. The projectile is assumed to be rigid and to move uniformly throughout the impact, fibres act independently on each ply and longitudinal and transverse waves have the same propagation speed across the laminate. Finally, in addition to the failure mechanisms described above, back face cone formation and friction between the projectile and the laminate are included. In some cases, even if total rupture of fibres occurs, the friction between the projectile and target can be sufficient to prevent it from exiting on the back face and reach total penetration. Hence, the importance given by the authors to this energy absorption mechanism. Considering the above, reference [56] proposes the following Equation 2.4:

$$E_{abs.target} = E_{Tf} + E_D + E_{DL} + E_{SP} + E_{MC} + E_F + E_{BFC} \tag{2.4}$$

Where, E_{Tf} represents the energy from primary fibres deformation and failure (if it occurs), E_D is the energy due to secondary fibres' deformation, E_{DL} is the delamination energy, E_{SP} is the shear plug energy, E_{MC} is the matrix cracking energy, E_F represents the friction energy and E_{BFC} is the back face cone formation energy.

Hybrid laminates for ballistic applications

With the aim of pushing further the energy absorbed by the target while maintaining a low weight, engineers saw an opportunity in the use of hybrid composites. Combinations of composite materials and metal or ceramic plates, as well as the use of different types and configurations of fibres were evaluated.

Reference [6] evaluated the ballistic performance of a laminate composed of carbon, Kevlar and UHMWPE. The results showed that, compared to a composite with only Kevlar reinforcements, the energy absorption capacity was increased by around 16%. In a different study [31], it was concluded that the use of laminates with identical proportions of carbon and glass fibres increased energy absorption by 17% and 30% more than using only carbon or glass fibres, respectively. Reference [57], in a phased experimental study, explored several configurations of hybrid laminates composed of Dyneema, polypropylene and aluminium. Their location and orientation was varied in order to understand the laminate back face deformation and ballistic limit. It was concluded that hybrid configurations could be beneficial, not only from the ballistic point of view, but also regarding the final cost of the product. Combining high performance materials with more affordable ones, can result in good end product with a reduced price.

Reference [7], again, by means of experimental tests, carried out a series of ballistic tests on hybrid laminates. In addition, analytical expressions have been developed to predict the material's behaviour. Ceramics, Dyneema, Kevlar and wood were the subject of research. Experimental data indicates that the presence of a layer of ceramic material on the front surface fragments the projectile, which is subsequently stopped more effectively by the organic fibres.

Within composite materials made with UHMWPE fibres, reference [58] explored the combined use of woven and UD plies to form laminates. It was previously known that woven layers perform better under shear stress and UD layers better under tension stress. Therefore, placing woven fabrics in the front layers and UD in the back ones led to better performance than using them alone. From the various experimental and numerical tests conducted, the best configuration uses 25% woven layers and 75% UD layers.

2.3.2 Ballistic protections development and practical examples

The development of the first ballistic protection structures consisted essentially in successive experimental tests until the desired characteristics were achieved. This type of equipment was therefore associated with high costs, as both the materials and the tests were expensive. In this sense, as in many areas of engineering, the emergence of numerical methods, particularly *Finite Element Methods* (FEM), proved to be an advantage. By knowing the individual properties of each material and the test conditions, it has become possible to recreate real impact scenarios in a computer environment. As a result, the development of ballistic protection now involves a balance between numerical simulations and experimental

tests. It should be noted that the latter are still essential for calibrating and validating numerical methods, but since they are carried out less frequently, the final cost of the product is reduced. Various finite element method software packages are currently in use, including Abaqus, CATIA V5 and Ansys [8].

In the field of military aviation, there are currently no aircraft completely armoured with composite materials or any other type of material. Meanwhile, several companies offer modular protective solutions for installation on aircraft. These consist of panels, essentially made of composite material and often hybrids, to be placed in areas of the aircraft such as pilot and copilot seats, cargo doors, floors, loading and unloading ramps and engine fairings (see Figure 2.10). It is important to note that these companies rely heavily on the use of advanced numerical methods, accompanied by standardised experimental tests [59]–[61].



Figure 2.10: Ballistic panels [59]

2.4 Dynamic Explicit Finite Element Modelling

The effort to reduce costs associated with experimental tests, speed up research phase, and optimize manufacturing processes are some of the factors that have contributed to the rapid growth and development of computer simulations in engineering. In this sense, various methodologies have emerged, however, *Finite Element Methods* (FEM) stand out, as already mentioned in section 2.3.2 [62].

FEM uses a set of differential equations that define the problem in question. These are then solved, returning an approximate result. To do this, the geometric domain must be divided or discretised, and shape functions must be employed. The domain is discretised by generating a mesh. Triangular or quadrilateral elements are used for 2D problems, while tetrahedral or hexahedral elements are used for 3D cases. For each node an approximate value of the unknown parameters is returned [62], [63].

When solving a dynamic problem with FEM, in particular, two different approaches come into play, namely, implicit and explicit simulation. To better understand the differences, consider the simple function $f(t)$ shown in Figure 2.11, in which $f(t_1)$ is known, and the aim is to determine $f(t_1+1)$. Equations 2.5 and 2.6 describe, respectively, the implicit and explicit method of solving the problem. Bearing in mind that, Δt refers to the difference between t_1+1 and t_1, it is possible to conclude that the only difference is on the point

used to calculate the derivative or slope of the function, $\frac{df(t)}{dt}$. The implicit method uses the derivative at the unknown point, so it is necessary to use numerical methods such as Newton iteration, to solve the equation. The explicit method, on the other hand, allows the problem to be solved directly as it uses the derivative at the known point [64], [65].

$$f(t_1+1) = f(t_1) + \Delta t \left.\frac{df(t)}{dt}\right|_{t=t_1+1} \tag{2.5}$$

$$f(t_1+1) = f(t_1) + \Delta t \left.\frac{df(t)}{dt}\right|_{t=t_1} \tag{2.6}$$

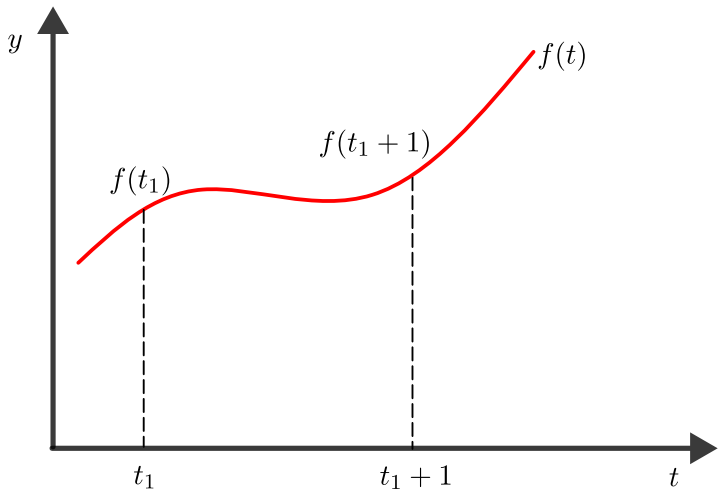


Figure 2.11: Example function, $f(t)$

The differences presented above are the key factor that defines in which situations each method should be applied for solving dynamic problems with finite element software. Although unconditionally stable, the implicit method is not suitable for solving fast events or complex three-dimensional problems. The need to apply an iterative method for each increment considerably increases computation times. This is also aggravated by the need to manipulate the tangent stiffness matrix, which can also diverge in such situations. In this way, the implicit method is more suitable for events with a longer duration, such as fatigue tests, creep, quasi-static loads or slightly non-linear processes [64], [66].

By contrast, the nature of the explicit method makes it advantageous for simulating short-term events such as drop tests and impacts, or problems involving penetration and large deformations that result in material failure. It is therefore a methodology widely used in the development of ballistic structures, as in the case of this work [64], [66]. Thus, a more detailed description of its implementation in the finite element software Abaqus is provided in the following paragraphs. Firstly, consider the Equation 2.7, designated as the Equation of Motion:

$$M\ddot{u} + C\dot{u} + Ku = f \tag{2.7}$$

Where, M, C and K are, respectively the mass, damping and stiffness matrix. f represents the vector of nodal forces, finally $\ddot{u}$, $\dot{u}$ and u represent, respectively, the acceleration, velocity and displacement vector at each node.

To solve this second order differential equation, the explicit central-difference integration rule is used, resulting in Equation 2.8 and 2.9 [67].

$$\dot{u}_{(i+\frac{1}{2})} = \dot{u}_{(i-\frac{1}{2})} + \frac{\Delta t_{(i+1)} + \Delta t_{(i)}}{2} \ddot{u}_{(i)} \tag{2.8}$$

$$u_{(i+1)} = u_{(i)} + \Delta t_{(i+1)} \dot{u}_{(i+\frac{1}{2})} \tag{2.9}$$

Where, i represents the increment number in an explicit dynamics step.

It can then be concluded that the value of the displacement, u, can be determined by knowing $\dot{u}_{(i-\frac{1}{2})}$ and $\ddot{u}_{(i)}$, which only relate to the previous increment. Finally, the value of $\ddot{u}_{(i)}$ is computed by using the diagonal element mass matrix, resulting in Equation 2.10 [67].

$$\ddot{u}_{(i)} = M^{-1}(P_{(i)} - I_{(i)}) \tag{2.10}$$

Where, P and I are, respectively, the applied load vector and the internal force vector.

It is important to emphasise that, unlike the implicit method, the explicit approach is conditionally stable. For this case, stability occurs if the time increment, Δt meets the following condition (Equation 2.11) [67]:

$$\Delta t \leq \frac{2}{\omega_{max}} \tag{2.11}$$

Where, ω_{max} is the highest frequency of the system.

Chapter 3

Models' theoretical description

The previous literature review covered the different failure mechanisms of composite materials during an impact event. To accurately simulate this type of material in such scenarios, it is necessary to use material models that not only include failure criteria indicating whether failure occurs but also describe how the damage evolves.

Regarding failure criteria, several types are found in the literature. The diversity can arise either because the authors approach the subject differently or as refinements/extensions of already established criteria. As a result, some methods do not consider the individual failure of the matrix and/or reinforcement, for instance, Tsai-Wu, Tsai-Hill, Azzi-Tsai, Hoffman and Chamis. These criteria rely on mathematical expressions calibrated from experimental procedures. On the other hand, some authors have developed methods where matrix and fibre failure are computed separately. In this context, examples of such models include, the Hashin criterion, Puck criterion, Yamada and Sun Criterion and Chang and Chang Criterion [68], [69].

The failure criteria for composite materials used in the development of this work are:

- Hashin criterion in its 2D and 3D versions.
- Criterion developed by Ferreira [70] during his master's thesis. To facilitate the comprehension of this document, this criterion will be referred to as the Modified Ladeveze criterion.

The simulation of delaminations/interlaminar failure is carried out using a model based on traction separations laws together with demage evolution based on fracture energy.

At last, as mentioned above, the final stage of the project is to use hybrid laminates, in this case, combining ceramic materials with composites. In this way, the Johnson-Holquimist criterion will be used to describe the behaviour of ceramic materials.

Therefore, this section is dedicated to the theoretical explanation of the previously listed failure criterion as well as the accompanying damage evolution laws.

3.1 Hashin Criterion

The first version of this criterion was presented in 1973 in a joint work between Z. Hashin and A. Rotem, and was named the Hashin-Rotem criterion. Its formulation can be found at [71]. Seven years later (1980), the same model was refined by Z. Hashin, resulting in the so-called Hashin criterion, both in its 2D and 3D versions [68], [72].

As mentioned previously, this criterion distinguishes between failure of the matrix or failure of the reinforcement/fibre. In addition, a distinction is made between failure of the constituent in tension and compression. To do this, a set of acting stresses and allowable stresses is employed. The formulation for the 3D version is presented below, Equation 3.1 to 3.4 [68], [72].

Fibre failure in tension

$$\left(\frac{\sigma_{11}}{X_T}\right)^2+\left(\frac{\sigma_{12}}{S_{12}}\right)^2+\left(\frac{\sigma_{13}}{S_{13}}\right)^2\geq 1 \qquad (\sigma_{11}\geq 0) \tag{3.1}$$

Fibre failure in compression

$$\left(\frac{\sigma_{11}}{X_C}\right)^2\geq 1 \qquad (\sigma_{11}<0) \tag{3.2}$$

Matrix failure in tension

$$\left(\frac{\sigma_{22}+\sigma_{33}}{Y_T}\right)^2+\frac{1}{S_{23}^2}(\sigma_{23}^2-\sigma_{22}\sigma_{23})\left(\frac{\sigma_{12}}{S_{12}}\right)^2+\left(\frac{\sigma_{13}}{S_{13}}\right)^2\geq 1 \qquad (\sigma_{22}+\sigma_{33}\geq 0) \tag{3.3}$$

Matrix failure in compression

$$\begin{aligned}&\left(\frac{\sigma_{22}+\sigma_{33}}{2S_{23}}\right)^2+\left[\left(\frac{Y_c}{2S_{23}}\right)^2-1\right]\frac{\sigma_{22}+\sigma_{33}}{Y_C}+\\&+\frac{1}{S_{23}^2}(\sigma_{23}^2+\sigma_{22}\sigma_{33})+\left(\frac{\sigma_{12}}{S_{12}}\right)^2+\left(\frac{\sigma_{13}}{S_{13}}\right)^2\geq 1 \qquad (\sigma_{22}+\sigma_{33}<0)\end{aligned} \tag{3.4}$$

Where, σ_{11}, σ_{22} and σ_{33} represent, respectively, the stress acting on the laminae in the direction of the fibres, matrix and in the thickness direction. σ_{12}, σ_{13} and σ_{23} are shear stresses acting on the laminae. X_T and X_C stand for tensile (T) and compressive (C) strength in fibre direction, whereas Y_T and Y_C reprsent the tensile and compressive strength in matrix direction. Finally, S_{12}, S_{13}, S_{23} stand for laminae shear strengths.

The adaptation of the criterion to 2D involves simplifying the previous set of equations by removing the effect of the stresses acting in the third direction, i.e., in the thickness of the lamina, σ_{13}, σ_{23} e σ_{33}. Therefore, Equation 3.5 to 3.8 presents the modifications implemented.

Fibre failure in tension

$$\left(\frac{\sigma_{11}}{X_T}\right)^2 + \left(\frac{\sigma_{12}}{S_{12}}\right)^2 \geq 1 \qquad (\sigma_{11} \geq 0) \tag{3.5}$$

Fibre failure in compression

$$\left(\frac{\sigma_{11}}{X_C}\right)^2 \geq 1 \qquad (\sigma_{11} < 0) \tag{3.6}$$

Matrix failure in tension

$$\left(\frac{\sigma_{22}}{Y_T}\right)^2 + \left(\frac{\sigma_{12}}{S_{12}}\right)^2 \geq 1 \qquad (\sigma_{22} + \sigma_{33} \geq 0) \tag{3.7}$$

Matrix failure in compression

$$\left(\frac{\sigma_{22}}{2S_{23}}\right)^2 + \left[\left(\frac{Y_c}{2S_{23}}\right)^2 - 1\right]\frac{\sigma_{22}}{Y_C} + \left(\frac{\sigma_{12}}{S_{12}}\right)^2 \geq 1 \qquad (\sigma_{22} + \sigma_{33} < 0) \tag{3.8}$$

In this way, both 2D and 3D versions, only consider intra-laminar failure, i.e. matrix and fibre failure. Inter-laminar failure, such as delaminations, are not taken into account. However, this phenomenon, as described in the literature review (section 2.3) are common in impact events. Disregarding them can lead to discrepancies when comparing the results obtained by the criterion with experimental data [68].

Additionally, when it comes to fibre failure under stress, it is common to find the presence of an α parameter. This is responsible for quantifying the weight that shear stresses (σ_{12} and σ_{13}) have in this failure mode. Therefore, rewriting Equations 3.1 and 3.5 gives Equation 3.9 and 3.10 respectively.

$$\left(\frac{\sigma_{11}}{X_T}\right)^2 + \alpha\left(\frac{\sigma_{12}}{S_{12}}\right)^2 + \alpha\left(\frac{\sigma_{13}}{S_{13}}\right)^2 \geq 1 \qquad (\sigma_{11} \geq 0) \qquad (3.9)$$

$$\left(\frac{\sigma_{11}}{X_T}\right)^2 + \alpha\left(\frac{\sigma_{12}}{S_{12}}\right)^2 \geq 1 \qquad (\sigma_{11} \geq 0) \qquad (3.10)$$

3.1.1 Hashin Criterion - Damage Evolution Law

The previous subchapter was dedicated to presenting the criteria that defines if damage occurs and under what circumstances, according to the Hashin criterion. In the presence of damage, it is necessary to define how it evolves and which characteristics of the material are affected by it.

In the context of composite materials, various methodologies based on *Continuum Damage Mechanics* (CDM) have been developed to model the evolution of damage [73]. In this work, the damage evolution law that accompanies the Hashin criterion (2D and 3D) is based on the fracture energy dissipated during damage. The level of damage is controlled by a set of variables, d, relating to the different failure modes. These are calculated with the introduction of equivalent displacements, δ_{eq}. In addition, δ_{eq} is determined taking into account equivalent stresses, σ_{eq}, and the fracture energies, G_c, of the composite material in question. Regarding the effect of damage on the material, it will be responsible for degrading its stiffness properties [74].

Next, a detailed description of the damage evolution law used in the 3D Hashin criterion is presented. As explained above, the variable d is determined using a series of equivalent displacements, δ_{eq}.

$$d_I = \frac{\delta^f_{I,eq}(\delta_{I,eq} - \delta^0_{I,eq})}{\delta_{I,eq}(\delta^f_{I,eq} - \delta^0_{I,eq})} \qquad (3.11)$$

Where, the subscript I can be substituted by ft, fc, mt and mc in the case of fibre tension, fibre compression, matrix tension and matrix compression, respectively. The superscript f identifies the final equivalent displacement and the superscript 0 concerns the equivalent displacement at the beginning of damage. The absence of any superscript ($\delta_{I,eq}$) indicates the current equivalent displacement.

Equation 3.11 also demonstrates that the parameter d always takes on a value between 0 and 1, inclusive. Figure 3.1 illustrates the evolution of d according to the equivalent displacements.

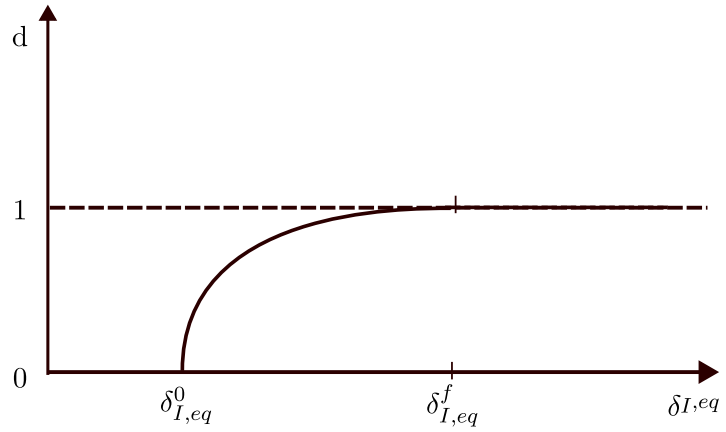


Figure 3.1: d parameter evolution

Moving on to the variables involved in d computation, the following Equations 3.12 to 3.15 introduce the calculation of the current equivalent displacements' calculations.

$$\delta_{ft,eq} = l_c \sqrt{\langle \varepsilon_{11}^2 \rangle + \varepsilon_{12}^2 + \varepsilon_{13}^2} \tag{3.12}$$

$$\delta_{fc,eq}^{fc} = l_c \langle -\varepsilon_{11} \rangle \tag{3.13}$$

$$\delta_{mt,eq} = l_c \sqrt{\langle \varepsilon_{22}^2 \rangle + \langle \varepsilon_{33}^2 \rangle + \varepsilon_{12}^2 + \varepsilon_{23}^2 + \varepsilon_{13}^2} \tag{3.14}$$

$$\delta_{mc,eq} = l_c \sqrt{\langle -\varepsilon_{22}^2 \rangle + \langle -\varepsilon_{33}^2 \rangle + \varepsilon_{12}^2 + \varepsilon_{23}^2 + \varepsilon_{13}^2} \tag{3.15}$$

Where, l_c corresponds to a characteristic length and ε_{xy} to the different strain components. $\langle\rangle$ is the Macaulay operator, defined as:

$$\langle x \rangle = \frac{x + |x|}{2}, \forall x \in \mathbb{R} \tag{3.16}$$

Once δ_{eq} has been determined, the equivalent stresses, σ_{eq}, can be calculated, by the set of Equations 3.17 to 3.20.

$$\sigma_{ft,eq} = \frac{l_c(\langle \sigma_{11} \rangle \langle \varepsilon_{11} \rangle + \sigma_{12}\varepsilon_{12} + \sigma_{13}\varepsilon_{13})}{\delta_{eq}^{ft}} \tag{3.17}$$

$$\sigma_{fc,eq} = \frac{l_c \langle -\sigma_{11} \rangle \langle -\varepsilon_{11} \rangle}{\delta_{eq}^{fc}} \tag{3.18}$$

$$\sigma_{mt,eq} = \frac{l_c(\langle \sigma_{22} \rangle \langle \varepsilon_{22} \rangle + \langle \sigma_{33} \rangle \langle \varepsilon_{33} \rangle + \sigma_{12}\varepsilon_{12} + \sigma_{23}\varepsilon_{23} + \sigma_{13}\varepsilon_{13})}{\delta_{eq}^{mt}} \tag{3.19}$$

$$\sigma_{mc,eq} = \frac{l_c(\langle -\sigma_{22}\rangle\langle -\varepsilon_{22}\rangle + \langle -\sigma_{33}\rangle\langle -\varepsilon_{33}\rangle + \sigma_{12}\varepsilon_{12} + \sigma_{23}\varepsilon_{23} + \sigma_{13}\varepsilon_{13})}{\delta_{eq}^{mc}} \tag{3.20}$$

Regarding the equivalent displacement at the beginning of damage, it is calculated according to Equation 3.21.

$$\delta_{I,eq}^{0} = \frac{\delta_{I,eq}}{\sqrt{F_I}} \tag{3.21}$$

Where F_I represents a failure parameter and is obtained by the failure criterion expressions (Equation 3.1 to 3.4).

Finally, it remains to present the calculation of $\delta_{I,eq}^{f}$. To do this, the fracture energy of the respective failure mode, $G_{I,c}$ and the equivalent stress at the onset of damage, $\sigma_{I,eq}^{0}$, are used, as presented in Equation 3.22. To better understand the relationship Figure 3.2 is presented. The fracture energy, $G_{I,c}$ (represented by the shaded area of the triangle), concerns the energy that the material will absorb during the several failure modes. Up to $\sigma_{I,eq}^{0}$ the material is under linear elastic regime. Higher stress values place the material over linear softening, once damage as occurred [74].

$$\delta_{I,eq}^{f} = \frac{2G_{I,c}}{\sigma_{I,eq}^{0}} \tag{3.22}$$

Regarding $\sigma_{I,eq}^{0}$ its calculation philosophy is similar to that of $\delta_{I,eq}^{0}$:

$$\sigma_{I,eq}^{0} = \frac{\sigma_{I,eq}}{\sqrt{F_I}} \tag{3.23}$$

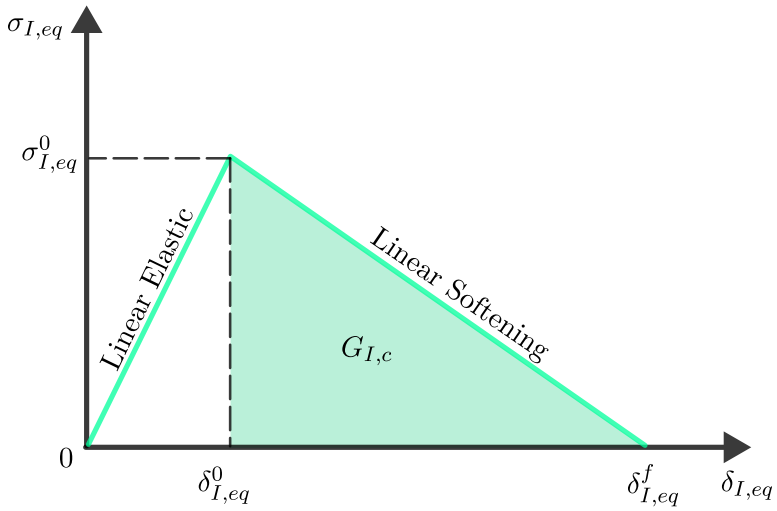


Figure 3.2: Linear elastic and linear softening regime

Having now fully explained the calculation of d, it is necessary to describe how it affects

the material response. Equation 3.24 shows the expression used to calculate the stress state, where σ represents the stress tensor, C the elasticity matrix and ε the strain tensor. Therefore, in the event of damage, the variable d_I will be non-zero, affecting the components of the elasticity matrix C. This, in turn, will be called the damaged elasticity matrix, C_d,whose calculation is shown in Equation 3.25 and 3.26.

$$\sigma = C\varepsilon \tag{3.24}$$

$$C_d = \frac{1}{D}\begin{bmatrix} C_{11} & C_{12} & C_{13} & 0 & 0 & 0 \\ C_{21} & C_{22} & C_{23} & 0 & 0 & 0 \\ C_{31} & C_{32} & C_{33} & 0 & 0 & 0 \\ 0 & 0 & 0 & C_{44} & 0 & 0 \\ 0 & 0 & 0 & 0 & C_{55} & 0 \\ 0 & 0 & 0 & 0 & 0 & C_{66} \end{bmatrix} \tag{3.25}$$

with,

$$\begin{aligned} C_{11} &= d_f E_{11}(1 - d_m \nu_{23}\nu_{32}) \\ C_{22} &= d_m E_{22}(1 - d_f \nu_{13}\nu_{31}) \\ C_{33} &= E_{33}(1 - d_f d_m \nu_{12}\nu_{21}) \\ C_{12} = C_{21} &= d_f d_m E_{11}(\nu_{21} + \nu_{23}\nu 31) \\ C_{13} = C_{31} &= d_f E_{11}(\nu_{31} + d_m \nu_{21}\nu_{32}) \\ C_{23} = C_{32} &= d_m E_{22}(\nu_{32} + d_f \nu_{12}\nu_{31}) \\ C_{44} &= D d_f d_m G_{12} \\ C_{55} &= D d_f d_m G_{23} \\ C_{66} &= D d_f d_m G_{13} \\ d_f &= (1 - d_{ft})(1 - d_{fc}) \\ d_m &= (1 - S_{mt} d_{mt})(1 - S_{mc} d_{mc}) \\ D &= 1 - d_f d_m \nu_{12}\nu_{21} - d_m \nu_{23}\nu_{32} - d_f \nu_{13}\nu_{31} - 2 d_f d_m \nu_{21}\nu_{32}\nu_{13} \end{aligned} \tag{3.26}$$

Where, E_{ii} ($i = 1,2$ or 3) represents the modulus of elasticity, G_{ij} ($i, j = 1,2,3$ with $i \neq j$) is the shear modulus and ν_{ij} ($i, j = 1,2,3$ with $i \neq j$) is the Poisson coefficient. S_{mt} and S_{mc} are coefficients for control of shear stiffness loss, under matrix tension and compression.

Next, a description of the simplifications is introduced, to apply the damage degradation law to the 2D case. Essentially, the changes focus on the calculation of $\delta_{I,eq}$ (Equation 3.27 to 3.30), $\sigma_{I,eq}$ (Equation 3.31 to 3.34) and C_d (Equation 3.35 and 3.36).

$$\delta_{ft,eq} = l_c \sqrt{\langle \varepsilon_{11}^2 \rangle + \varepsilon_{12}^2} \tag{3.27}$$

$$\delta_{fc,eq}^{fc} = l_c\langle -\varepsilon_{11}\rangle \tag{3.28}$$

$$\delta_{mt,eq} = l_c\sqrt{\langle\varepsilon_{22}^2\rangle + \varepsilon_{12}^2} \tag{3.29}$$

$$\delta_{mc,eq} = l_c\sqrt{\langle -\varepsilon_{22}^2\rangle + \varepsilon_{12}^2} \tag{3.30}$$

$$\sigma_{ft,eq} = \frac{l_c(\langle\sigma_{11}\rangle\langle\varepsilon_{11}\rangle + \sigma_{12}\varepsilon_{12})}{\delta_{eq}^{ft}} \tag{3.31}$$

$$\sigma_{fc,eq} = \frac{l_c\langle -\sigma_{11}\rangle\langle -\varepsilon_{11}\rangle}{\delta_{eq}^{fc}} \tag{3.32}$$

$$\sigma_{mt,eq} = \frac{l_c(\langle\sigma_{22}\rangle\langle\varepsilon_{22}\rangle + \sigma_{12}\varepsilon_{12})}{\delta_{eq}^{mt}} \tag{3.33}$$

$$\sigma_{mc,eq} = \frac{l_c(\langle -\sigma_{22}\rangle\langle -\varepsilon_{22}\rangle + \sigma_{12}\varepsilon_{12})}{\delta_{eq}^{mc}} \tag{3.34}$$

$$C_d = \frac{1}{D}\begin{bmatrix} C_{11} & C_{12} & 0 \\ C_{21} & C_{22} & 0 \\ 0 & 0 & C_{66} \end{bmatrix} \tag{3.35}$$

with,

$$\begin{aligned} C_{11} &= d_f E_{11} \\ C_{22} &= d_m E_{22} \\ C_{66} &= d_s G_{12} D \\ C_{12} &= C_{21} = d_f d_m E_{11} \nu_{21} \\ d_f &= (1-d_{ft})(1-d_{fc}) \\ d_m &= (1-d_{mt})(1-d_{mc}) \\ d_s &= 1 - d_f d_m \\ D &= 1 - d_f d_m \nu_{12}\nu_{21} \end{aligned} \tag{3.36}$$

Note that, in this case, a new variable is introduced, d_s, responsible for quantifying shear damage.

3.2 Modified Ladeveze Criterion

The following criteria, was developed by Ferreira [70] as part of his master's thesis, resulting in the following publication *"Computational analyses of composite plates under low-velocity impact loading"* [75]. It is also important to note that the aforementioned material model combines the work developed by Ribeiro et al. [76] and Ladeveze et al. [77], hence the nomination attributed to it. Therefore, for a more detailed explanation, it is advisable to read the references listed above.

As with the previous criterion, fibre and matrix failure are considered and inter-laminar failure (delaminations) is also disregarded. Furthermore, it does not take into account the stresses in the third direction, i.e. along the thickness, and is therefore similar to the 2D version of Hashin criterion.

With regard to fibre failure, two different expressions are used, differentiating tensile failure, Equation 3.37, from compressive failure, Equation 3.38.

Fibre failure in tension

$$\frac{\sigma_{11}}{X_T} \geqslant 1 \tag{3.37}$$

Fibre failure in compression

$$\frac{-\sigma_{11}}{X_{C0}} \geqslant 1 \tag{3.38}$$

Where, X_T represents the tensile strength in fibre direction and X_{C0} is the linear elastic limit strength under compression in fibre direction.

Regarding matrix failure, only one expression is used for tensile, compressive and shear failure. Equation 3.39 defines mathematically the damage surface, also illustrated in Figure 3.3.

Matrix failure

$$f = 1 - \left(\frac{\sigma_{12}^2}{S_{12_0}^2} + \frac{\sigma_{22}^2}{Y_{C0}^2} \right) \geqslant 0 \tag{3.39}$$

Where, S_{12_0} is linear elastic shear strength limit and Y_{C0} the linear elastic limit strength under compression transverse to the fibre direction.

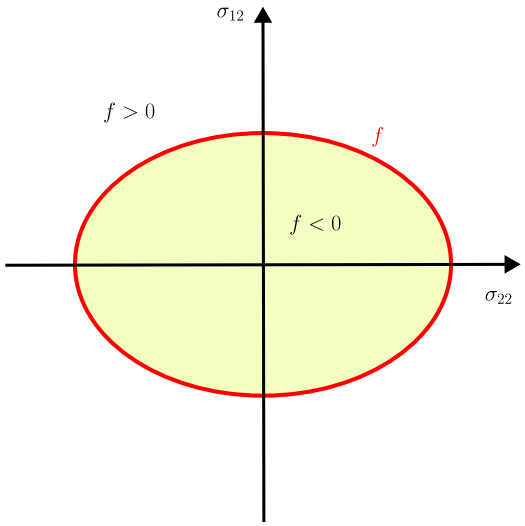


Figure 3.3: Matrix damage surface

3.2.1 Modified Ladeveze Criterion - Damage Evolution Law

A different approach to the one detailed above is used in this damage degradation law. In this case, the non-linear behaviour of the fibres and matrix in compression is taken into account, and thermodynamic forces are used to describe the degradation of the matrix in traction and shear. Nevertheless, material stiffness is also the property affected [75]. In this way, the explanation of the degradation law will follow a slightly different format, while maintaining the same nomenclature.

With regard to the failure of the fibre in tension, it is assumed that, if it happens, total degradation of the fibre occurs. Thus, $d_{ft} = 1$ is assumed, reducing E_{11} to zero, i.e. the stiffness in the direction of the fibre (Equation 3.40). In addition, the Poisson's ratio, ν_{12}, is degraded (Equation 3.41).

Fibre failure in tension - Degradation Law

$$E_{11} = E_{110}(1 - d_{ft}) \tag{3.40}$$

$$\nu_{12} = \nu_{120}(1 - d_{ft}) \tag{3.41}$$

Where, E_{110} and ν_{120} is equal to the initial modulus of elasticity in the fibre direction and the initial Poisson coefficient, respectively.

In compressive fibre degradation, a damage variable is not used, for instance d_{fc}, but with an expression that describes the non-linear behaviour of the fibre in compression (Equation 3.42), the secant modulus.

Fibre failure in compression - Degradation Law

$$E_{11} = \frac{X_{C0}}{|\varepsilon_{11}|}(1 - f(\varepsilon_{11})) + f(\varepsilon_{11})E_{110} \tag{3.42}$$

Where ε_{11} represents the strain in the fibre direction and $f(\varepsilon_{11})$ is a parameter determined experimentally.

Matrix damage occurs due to the presence of microcracks and voids, that when subjected to stress transverse to the fibres and shear stresses (respectively σ_{22} and σ_{12}) result in a non-linear response. Another important aspect is the occurrence of self-healing in the matrix. It happens because compressive transverse stresses ($\sigma_{22} < 0$) introduce deformations that close microcracks and voids. Therefore, in this situation, as with fibre compression, the d_{mc} parameter will not control degradation. As for the d_s parameter, it controls the degradation of the matrix due to either positive or negative shear stresses.

From the previous statements and before proceeding with the mathematical description, two different scenarios can be found:

- **Condition 1** - Matrix under tensile damage and tensile or compressive shear stress. Matrix tensile and shear damage controlled by thermodynamic forces.
- **Condition 2** - Matrix under compressive damage and tensile or compressive shear stress. Matrix compressive damage controlled by an experimentally calibrated expression and shear damage controlled by thermodynamic forces.

The concept of damaged-material strain energy, E_D, is now introduced, crucial for obtaining the thermodynamic forces. Its calculation can be found in Equation 3.43.

$$E_D = \frac{1}{2}\left[\frac{\langle\sigma_{22}\rangle_+^2}{E_{220}(1-d_{mt})} + \frac{\langle\sigma_{22}\rangle_-^2}{E_{220}} + \frac{|\sigma_{12}|^2}{G_{120}(1-d_s)}\right] \tag{3.43}$$

Where, E_{220} is the initial modulus of elasticity transverse to fibre direction and G_{120} is the initial shear modulus. Note that, although similar to the Macaulay operator, $\langle x\rangle_{+/-}$ has a different mathematical meaning, shown in Equation 3.44.

$$\begin{aligned} \langle x\rangle_+ &= x, \;\; if \;\; x \geq 0, \;\; else \;\; \langle x\rangle_+ = 0 \\ \langle x\rangle_- &= x, \;\; if \;\; x \leq 0, \;\; else \;\; \langle x\rangle_- = 0 \end{aligned} \tag{3.44}$$

Deriving E_D in order of the damage variables d_{mt} and d_s, results in the two components of the thermodynamic forces Y_2 and Y_6, Equation 3.45 and 3.46, respectively. When linearly combined, trough Equation 3.47 result in the combined thermodynamic force, $\hat{Y}$. According to reference [77] thermodynamic forces can be compared to energy release rates. Thermodynamic forces control damage propagation in the same way as the energy release rate rules crack propagation.

$$Y_2 = \frac{\partial E_D}{\partial d_{mt}} = \frac{\langle\sigma_{22}\rangle_+^2}{2E_{220}(1-d_{mt})^2} \tag{3.45}$$

$$Y_6 = \frac{\partial E_D}{\partial d_s} = \frac{{\sigma_{12}}^2}{2G_{120}(1-d_s)^2} \tag{3.46}$$

$$\hat{Y} = Y_6 + bY_2 \tag{3.47}$$

Where, Y_2 is the transverse component of the thermodynamic force and Y_6 the shear component. Coefficient b quantifies the amount of coupling between the two components and is determined trough experimental tests.

Based on the concepts presented above and by carrying out experimental tests, it is possible to explicitly calculate the damage variables d_{mt} and d_s trough Equation 3.48 and 3.49.

$$d_s = \frac{\sqrt{\hat{Y}} - \sqrt{Y_0}}{\sqrt{Y_C}} \tag{3.48}$$

$$d_{mt} = \frac{\sqrt{\hat{Y}} - \sqrt{Y_0{}'}}{\sqrt{Y_C{}'}} \tag{3.49}$$

Where, the values of $Y_0{}'$, Y_0, $Y_C{}'$ and Y_C are determined experimentally by means of quasi-static cyclic tests.

Reference [70] provides a detailed description of all the experimental tests carried out and the post-processing of the results in order to obtain the parameters mentioned above. Figure 3.4 shows the evolution of the damage parameter d_{mt} in relation to the thermodynamic forces. Note that for the shear case, the evolution follows the same pattern.

Once obtained the expressions that determine the damage variables for matrix tension and shear have, it is possible to present the final equations that define the degradation of the composite's properties.

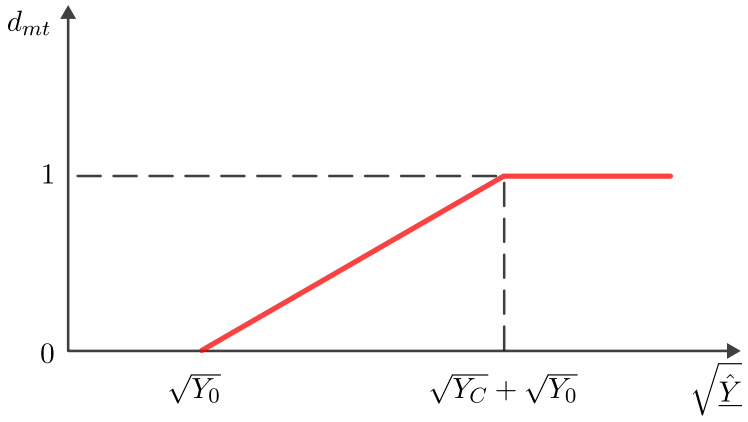


Figure 3.4: Damage evolution and thermodynamic force (Adapted from [70])

Equation 3.50 presents matrix damage in tension. As with fibre in tension, the Poisson coefficient is also affected, in this case ν_{21} (Equation 3.51).

Matrix failure in tension - Degradation Law

$$E_{22} = E_{220}(1 - d_{mt}) \tag{3.50}$$

$$\nu_{21} = \nu_{210}(1 - d_{mt}) \tag{3.51}$$

Where, E_{220} and ν_{210} are, respectively, the initial modulus of elasticity transverse to the fibre direction and the initial Poisson coefficient.

Regarding matrix failure in compression, the damage evolves according to an expression similar to fibre in compression.

Matrix failure in compression - Degradation Law

$$E_{22} = \frac{Y_{C0}}{\varepsilon_{22}}(1 - g(\varepsilon_{22})) + g(\varepsilon_{22})E_{220} \tag{3.52}$$

Where ε_{22} is the strain transverse to the fibre direction and $g(\varepsilon_{22})$ is a parameter determined experimentally, such as stated for $f(\varepsilon_{11})$.

Finally, it remains to define the shear damage evolution. Using the damage parameter d_s trough Equation 3.53 the shear modulus, G_{12} is degraded.

Matrix failure in shear - Degradation Law

$$G_{12} = G_{120}(1 - d_s) \tag{3.53}$$

Where, G_{120} is the initial shear modulus.

Once the entire degradation process has been explained, all that remains is to assemble the damaged stiffness matrix, C_d. Since this is a criterion focused on 2D problems, C_d has the same structure as Equation 3.35 and 3.36 (Hashin 2D). Nevertheless, there is a particular distinction, in this case d_s is not calculated by a combination of matrix and fibre damage but is determined independently, as explained above.

3.3 Strain rate effect on polymer matrix composites

Before going on to describe the introduction of the strain rate effect, it is important to mention that, in this work, the effect of the strain rate is only incorporated into the 3D Hashin criterion.

With regard to composite materials, the effect of strain rate, $\dot{\varepsilon}$, mainly affects stiffness, fracture toughness and strength properties. *Scale Factors* (SF) are used to adjust them, but

their weight depends on the strain rate regime applied. Therefore, three different regimes are applied [78]:

- Quasi-static (QS), if $\dot{\varepsilon} \leq 0.1\ s^{-1}$.
- Intermediate rate (IR), if $0.1 < \dot{\varepsilon} < 100\ (s^{-1})$.
- High rate (HR), if $\dot{\varepsilon} \geq 100\ s^{-1}$.

For the *Quasi-static* (QS) regime, no influence is considered. For the *Intermediate rate* (IR), a linear adjustment of the scale factor is made. Finally, in the *High rate* (HR) case, the maximum value of the scale factor is used. The different conditions described are mathematically represented in Equation 3.54 [78].

$$SF = \begin{cases} 1.0,\ for\ QS \\ \frac{(\dot{\varepsilon}-0.1)(SF_{max}-1)}{100-0.1}+1,\ for\ IR \\ SF_{max},\ for\ HR \end{cases} \tag{3.54}$$

Once the regimes and conditions have been presented, it remains to present the maximum values of the scaling factors for the different properties affected. Note that only the in-plane and out-of-plane transverse stiffness is affected, E_{22} and E_{33} respectively. This is because for unidirectional composites, it is assumed that the stiffness in the fibre direction, E_{11}, is defined entirely by the properties of the fibre and is insensitive to the strain rate. The same philosophy of thought applies to fracture energies, so only those relating to the matrix are affected [78]. Table 3.1 presents the maximum values of the scaling factors.

Table 3.1: Maximum scale factor values [78]

Property	$E_{22} = E_{33}$	X_C	X_T	Y_C	Y_T	$G_{mc,c}$	$G_{mt,c}$
SF_{max}	1.29	1.39	1.38	1.37	1.38	1.63	1.23

3.4 Inter-laminar failure model

Inter-laminar failure or delamination is, as explained in section 2.3.1, one of the failure mechanisms associated with composite laminates. In this work, this phenomenon will be introduced by means of cohesive elements, which describe both the initiation and propagation phases of inter-laminar failure.

To describe the behaviour of this type of failure, the work developed by Camanho and Dávila [79] was used. According to the authors, the occurrence of delaminations under mix mode loading is fairly common, i.e., a combination of Mode I, II and III, illustrated in Figure 3.5. Thus, the initiation of this type of damage is given by the following Equation 3.55.

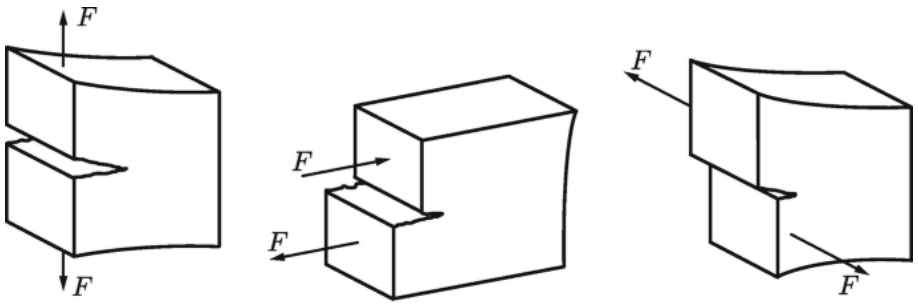
$$\left(\frac{\langle t_n \rangle}{t_n{}^{max}}\right)^2 + \left(\frac{t_s}{t_s{}^{max}}\right)^2 + \left(\frac{t_t}{t_t{}^{max}}\right)^2 = 1 \tag{3.55}$$

Where, t_n, t_s and t_t represent, respectively the normal and shear acting traction forces. The same parameters with the upperscript *max* indicate the maximum admissible values for each of them.

The following Equation 3.56 is used to determine the acting stresses.

$$\begin{bmatrix} t_n \\ t_s \\ t_t \end{bmatrix} = \begin{bmatrix} K_n & 0 & 0 \\ 0 & K_s & 0 \\ 0 & 0 & K_t \end{bmatrix} \begin{bmatrix} \delta_n \\ \delta_s \\ \delta_t \end{bmatrix} \tag{3.56}$$

Where, K_n, K_s and K_t are, respectively, the normal and shear initial penalty stiffness. δ_n, δ_s and δ_t concern the separation displacements.



(a) Mode I (b) Mode II (c) Mode III

Figure 3.5: Loading modes I, II and III [80]

3.4.1 Inter-laminar failure model - Damage Evolution Law

Once damage has been initiated, the damage evolution must be introduced. In this case it is based on fracture energy and has a linear evolution. The damage parameter, d, quantifies the amount of damage, and is determined through effective displacements, by the following Equation 3.57 [67], [79].

$$d = \frac{\delta_{eff}{}^{f}(\delta_{eff}{}^{max} - \delta_{eff}{}^{0})}{\delta_{eff}{}^{max}(\delta_{eff}{}^{f} - \delta_{eff}{}^{0})} \tag{3.57}$$

Where, $\delta_{eff}{}^{0}$ is the effective displacement at the beggining of damage, $\delta_{eff}{}^{max}$ is the maximum value of the effective displacement attained during the loading history and $\delta_{eff}{}^{f}$ is the effective displacement at complete failure. The last two components are determined, respectively, by calculated by Equation 3.58 and 3.59.

$$\delta_{eff}{}^{max} = max\left\{\sqrt{\langle\delta_n\rangle^2 + \delta_s{}^2 + \delta_t{}^2}\right\} \tag{3.58}$$

$$\delta_{eff}{}^{f} = \frac{2G^{C}}{T_{eff}{}^{0}} \tag{3.59}$$

Where, G^C is the fracture energy and $T_{eff}{}^0$ is the effective traction at damage initiation, computed by Equation 3.60.

$$T_{eff}{}^{0} = K\delta_{eff}{}^{0} \tag{3.60}$$

Finally, the influence of loading mode in the fracture toughness is included by the Benzeggagh-Kenane mixed-mode criterion, commonly referred to as B-K criterion, expressed in Equation 3.61.

$$G_n{}^{C} + (G_s^C - G_n{}^{C}) \left(\frac{G_S}{G_T}\right)^{\eta} = G^C \tag{3.61}$$

With: $G_S = G_s + G_t$ and $G_T = G_n + G_s$.
Where, $G_n{}^C$, G_s^C and G_t^C are the critical fracure energies needed to cause failure in normal and shear directions. G_n, G_s and G_t concern the work done by the normal and shear acting forces. Finally, η is a material parameter, determined experimentally.

3.5 Johnson–Holmquist model

In order to model the behaviour of brittle material, such as ceramics, under impacts, the Johnson–Holmquist model is widly used approach. In the present work, the second version of that model, commonly referred to as JH-2, is implemented in Abaqus explicit [81], [82]. In order to successively degrades the material, the JH-2 model also uses a damage variable, d ($0 \leqslant d \leqslant 1$), which increases as plastic deformation increases. Dimensionless strenths and pressures are also a characteristic of this model.

To start the model description, the normalized equivalent stress, σ^* is presented in Equation 3.62.

$$\sigma^* = \sigma_i{}^* - d(\sigma_i{}^* - \sigma_f{}^*) \tag{3.62}$$

Where, $\sigma_i{}^*$ is the normalized intact equivalent stress and $\sigma_f{}^*$ is the normalized fracture equivalent stress. Note that the privous mentioned stresses are normalized in the following form (Equation 3.63):

$$\sigma^* = \frac{\sigma}{\sigma_{HEL}} \tag{3.63}$$

Where, σ is the equivalent Von Mises stress and σ_{HEL} is the equivalent stress at the Hugoniot elastic limit (HEL). The HEL is a parameter that represents the maximum stress that the ceramic material can be submitted to, under fast compression without internal rearrangement of the material at the shock front [83].

Back to the Equation 3.62, $\sigma_i{}^*$ and $\sigma_f{}^*$ can be computed from, respectively, Equation 3.64 and 3.65.

$$\sigma_i{}^* = A(P^* + T^*)^N + (1 + C ln\dot{\varepsilon}^*) \leqslant \sigma_{imax} \tag{3.64}$$

$$\sigma_f{}^* = B(P^*)^M + (1 + C ln\dot{\varepsilon}^*) \leqslant \sigma_{fmax} \tag{3.65}$$

Where, A, B, C, M, N, σ_{imax} and σ_{fmax} are material parameters. P^* and T^* are the normalized pressure and maximum tensile hydrostatic pressure, computed by dividing, respectively, the actual pressure, P, and the maximum tensile hydrostatic pressure, T, by the pressure at HEL, P_{HEL}. Finally, $\dot{\varepsilon}^*$ concerns the dimensionless strain rate, obtained by the ratio of the actual strain rate, $\dot{\varepsilon}$, to the reference strain rate, $\dot{\varepsilon}_0$, which normally takes the value of 1.0 s^{-1}

Moving forward to the damage parameter, d, as previously mentioned, it is related to the plastic deformation in the following manner (Equation 3.66):

$$d = \sum \frac{\Delta\varepsilon^p}{\varepsilon_f{}^p} \tag{3.66}$$

Where, $\Delta\varepsilon^p$ is the increment in equivalent plastic strain during a cycle of integration and $\varepsilon_f{}^p$ is the equivalent plastic strain required to cause fracture at a constant pressure. Equation 3.67 is also used to obtain the last parameter.

$$\varepsilon_f{}^p = D_1(P^* + T^*)^{D_2} \tag{3.67}$$

D_1 and D_2 are damage constants. It is also possible to find, in some applications of this model, the presence of limiting values of $\varepsilon_f{}^p$, namely $\varepsilon_{fmin}{}^p$ and $\varepsilon_{fmax}{}^p$.

Finally, some considerations need to be made regarding the hydrostatic pressure, P. Its calculation is subdivided into two scenarios: the first refers to the absence of damage ($d = 0$), while the second is used when damage occurs ($d > 0$). For the first case, the following Equation 3.68 is applied.

$$P = K_1\mu + K_2\mu^2 + K_3\mu^3 \tag{3.68}$$

Where, K_1 (bulk modulus), K_2 and K_3 are constants, and μ is the volumetric strain.

Note that Equation 3.68 is only valid if the material is under compression ($\mu < 0$). If tension is the condition ($\mu > 0$), P is determined by Equation 3.69.

$$P = K_1\mu \tag{3.69}$$

Moving on to the second case, Equation 3.70 is used.

$$P = K_1\mu + K_2\mu^2 + K_3\mu^3 + \Delta P \tag{3.70}$$

It is possible to observe that a prssure increment, ΔP, was included to account the presence of bulking or dilatation. Its calculation is presented in Equation 3.70.

$$\Delta P_{t+\Delta t} = -K_1 \mu_{t+\Delta t} + \sqrt{K_1 \mu_{t+\Delta t} + \Delta P_t} + 2\beta K_1 \Delta U \tag{3.71}$$

Where, ΔU is the incremental energy loss and β accounts for the fraction of elastic energy loss converted to potential hydrostatic energy.

3.6 Damage models and FEM software connection

The purpose of this subsection is to explain the implementation of the models described above in the finite element solver. Abaqus [84] was the software used in this work. Through Table 3.2 it is possible to identify how each model was accessed.

With regard to the 2D Hashin and inter-laminar failure criterion and the corresponding degradation laws, both are contained in the base version of Abaqus. As such, no extra activities were required beyond fully understanding the formulation by consulting Abaqus' online manual [67], and using the *Graphical User Interface* (GUI) developed by Abaqus.

On the other hand, the 3D version of the Hashin criterion as well as the Modified Ladeveze criterion are not present in the Abaqus library. However, Abaqus offers the user the possibility of creating their own material models by means of "User Subroutines". Note that each subroutine must be elaborated according to specific templates provided by Abaqus and using the Fortran programming language. Since explicit simulations were used, the models were introduced by means of *Vectorized User Material* (VUMAT). These criteria and the accompanying degradation laws have therefore been applied in this thesis, using the previous work of Miranda [85] and Ferreira [70] for, respectively, the 3D Hashin criterion plus the influence of strain rate and the Modified Ladeveze criterion. As well as Ferreira's model, the model presented by Miranda was developed during his master's thesis, with the aim of simulating composite structures for crashworthiness, tanking into account the progressive failure of the structure and the effects of the strain rate. Yet, in the present work, some changes were made to adapt the codes to the cases under study, which involves the introduction of element elimination in both subroutines. In the final stage of the work, the 3D Hashin criterion, along with the strain rate effect, were modified to allow the simulation of woven composite laminates. The modifications will be addressed, when appropriate, in the following chapters.

Finally, the only thing left to mention is the *Johnson-Holquimist-2* (JH-2) criterion. It is contained in the Abaqus model library, but cannot be accessed via the graphical interface. To use it, you need to create a material with a specific name and make changes to the input file (.INP) so that it is correctly interpreted by Abaqus during the simulation. A description of the whole process can be found in Appendix A, as well as the coupling of it with Hashin 3D's VUMAT, an essential process for hybrid laminates simulation.

Table 3.2: Access to material models

Model/Criteria	**Available in Abaqus?**	**Access/Implementation**
Hashin 2D	Yes	GUI
Hashin 3D	No	VUMAT [85]
Modified Ladeveze	No	VUMAT[70]
Inter-laminar damage	Yes	GUI
JH-2	Yes	.INP file

Chapter 4

Case studies: Low-velocity impacts

This chapter details the application of the composite material models, described above, to a *Low-Velocity Impact* (LVI). The impact chosen for replication was previously studied by Tita [86]. Thus, the presence of experimental data is an asset for validating the results obtained in this work.

It was decided to initially use an LVI, so impact events were studied gradually. This way, after gaining experience in modelling and manipulating subroutines, it is possible to move on to ballistic impacts with more developed knowledge, decision-making accuracy and critical thinking.

Still within the low-speed impact, a progressive approach was adopted, introducing complexity gradually, according to the following chronology of tasks:

- **Case study 1 -** Create a 2D model of the impact for the Hashin 2D criterion. Thus, only Abaqus resources are used.
- **Case study 2 -** Use the same 2D model, however, run the VUMAT regarding the Modified Ladeveze criterion.
- **Case study 3 -** Create a 3D model of the impact. Run the simulations with the 3D Hashin criterion version. Lastly, incorporate the influence of strain rate and account for the presence of delaminations.

The development of case studies 1 and 2 led to the writing of a Tutorial. This briefly describes the criteria used and shows how to create the models in Abaqus step by step. It is available in the Appendix B.

After running all the simulations, the results obtained were always checked against experimental and numerical data, whenever possible.

The LVI studied by Tita *et al.* [86] consists of a composite CFRP laminate with three different configurations, $[0]_{10}$, $[+45/-45/+45/0/90]_s$ and $[0/90/0/90/0]_s$. Each one of the ten plies is 0.18 mm thickness resulting in a 1.8 mm thickness laminate. To simplify the simulation, the modelling of the plate clamping mechanism has been removed. Therefore, only a circular shaped plate was assumed with a radius of 40 mm. The impactor/projectile has the shape of a sphere with a radius of 8 mm and 1.205 kg of mass. It hits the plate with 5.91 J meaning it has an initial velocity of 3.13 m/s. In addition, a 10.8 J impact was studied for the $[+45/-45/+45/0/90]_s$ configuration, increasing the mass of the impactor to 2.205 kg. This will only be studied for the 3D Hashin criterion.

Given that the composite material used was common to all the simulations, Table 4.1 lists all the necessary properties.

The following subsections 4.1 and 4.2 divide the study into 2D and 3D, respectively, detailing the development of the models and the results obtained.

As far as the results are concerned, the evolution of the impact reaction forces and the energy transferred to the plate were always compared.

Table 4.1: Composite material properties (CFRP) [70], [86], [87]

General properties			**Damage initiation properties**			**Damage evolution properties**		
Property	Unit	Value	Property	Unit	Value	Property	Unit	Value
E_{11}	GPa	127	X_T	MPa	1400	G^c_{ft}	N/mm	48.40
E_{22}= E_{33}	GPa	10	X_C	MPa	930	G^c_{fc}	N/mm	60.30
G_{12}=G_{13}	GPa	5.40	X_{C0}	MPa	253	G^c_{mt}	N/mm	4.50
G_{23}	GPa	3.05	Y_T	MPa	47	G^c_{mc}	N/mm	8.50
ν_{12}=ν_{13}	-	0.34	Y_C	MPa	130	$\sqrt{Y_0}$	MPa	0.066270
ν_{23}	-	0.31	Y_{C0}	MPa	60.30	$\sqrt{Y_C}$	MPa	1.186159
ρ	ton/m^3	1.58	S_{12}=S_{13}	MPa	53	$\sqrt{Y_0{}'}$	MPa	0.013425
			S_{120}	MPa	47	$\sqrt{Y_C{}'}$	MPa	6.125483
			S_{23}	MPa	89	b	-	0.929007

4.1 Low velocity Impact - 2D Approach

Hashin 2D models

For the Hashin 2D criterion, two different models were developed, one using conventional shell elements (S4) and the other with continuum shell elements (SC8R). Conventional shell elements have rotational and displacement degrees of freedom and are suitable for problems where thickness is reduced when compared to the other dimensions. On the other hand, continuum shell elements only have displacement degrees of freedom like solid

elements, nevertheless, their constitutive behaviour is similar to conventional shell elements [67].

Modelling the plate with conventional shell elements means initially disregarding the thickness. Only in the definition of the section the thickness of each ply is assigned, and consequently the total thickness of the plate. To use continuum shell elements, once they discretize the component three-dimensionally, it is necessary model the plate as a solid body, considering its thickness. These two approaches were executed bearing in mind the plate/ply dimensions and the material properties, previously described.

To increase the accuracy of the results, a square section was created in the centre of the plate, allowing for a refinement of the mesh. As such, for both cases, elements with approximately 1.5 mm size were used in the impact region and 2.5 mm for the outer edges of the plate (note that, some simulations were carried out with different mesh sizes until the mentioned values were chosen). Regarding the continuum shell model, four elements were used across the thickness. These configurations meant that the model with conventional shell elements had a total of 1364 S4 elements and the model with continuum shell elements 6032 SC8R elements. Furthermore, reduced integration plus hourglass control "enhanced" were employed in the continuum shell model and element deletion was disabled in both cases. In section 4.1.1 a more detailed discussion about what led to the introduction of hourglass control is made. Figure 4.1 illustrates the final meshes.

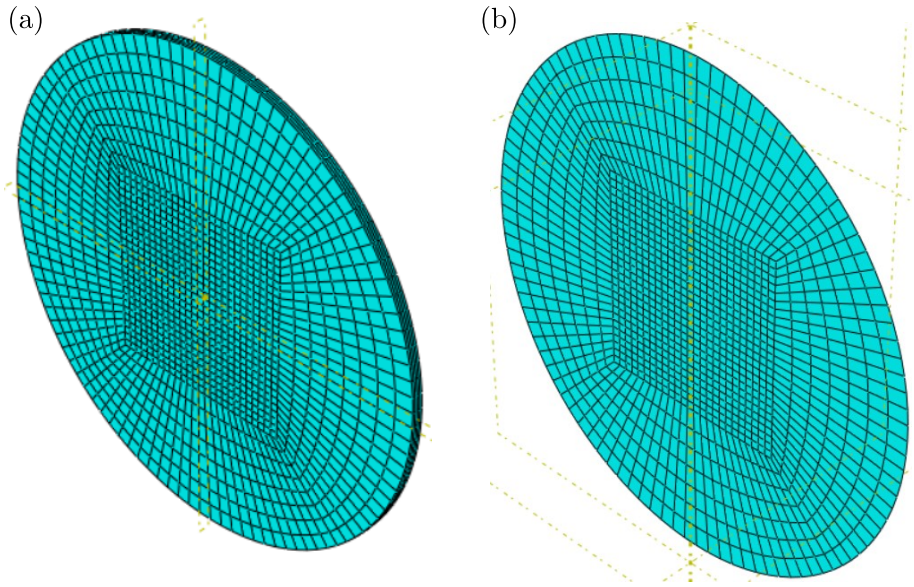


Figure 4.1: Final mesh for Hashin 2D models. (a) - SC8R model, (b) - S4 model

For the projectile, a rigid analytical surface was used, assuming it to behave as rigid body, thus absent of deformations. The interaction between the projectile and the plate was defined using general contact with hard contact for normal behaviour and friction was disregarded ("frictionless").

Regarding boundary conditions, all the outer edges off the composite plate were fixed (constrained in all degrees of freedom). For the projectile, the same was imposed, except its movement along "z" axis. It was also along this axis that the initial velocity of the projectile (3.13 m/s) was assigned. The final assembly as well as the boundary conditions are illustrated in Figure 4.2. Note that, as both models use the same settings only the conventional shell one is presented.

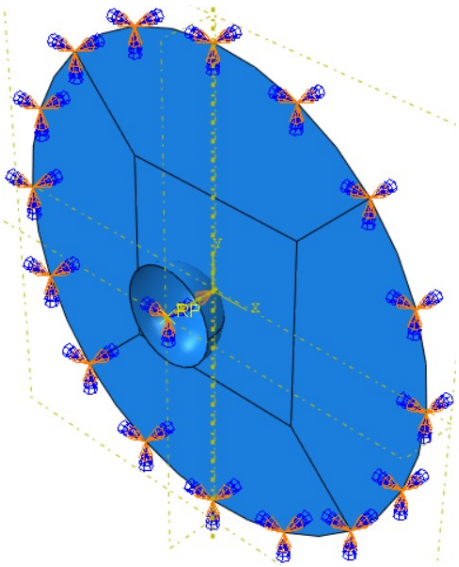


Figure 4.2: Final assembly and boundary conditions for Hashin 2D models

Modified Ladeveze model

Next, the model developed for the Modified Ladeveze criterion is described. The VUMAT subroutine was designed with the intention of using conventional shell elements (S4), so essentially the same steps described above for the S4 case were applied to the plate modelling. However, some modifications were necessary, including the introduction of additional material properties, mesh element size and contact definition. As far as the last two are concerned, their adjustment was iterative, i.e., they were calibrated after running successive simulations and analysing the results.

The use of a VUMAT and shell elements required the manual introduction of the transverse shear stiffness components, K_{11}, K_{12} and K_{22} according to Equations 4.1 to 4.3.

$$K_{11} = \frac{5}{6} G_{12} t_{laminate} \tag{4.1}$$

$$K_{12} = 0 \tag{4.2}$$

$$K_{22} = \frac{5}{6} G_{23} t_{laminate} \tag{4.3}$$

Where, $t_{laminate}$ represents the laminate thickness.

To better explain the adjustment of the element size, it is necessary to give a brief introduction to dilatational wave speed, c_d, which refers to the velocity at which waves propagate through a medium and is determined according to Equation 4.4 [67].

$$c_d = \sqrt{\frac{\hat{\lambda} + 2\hat{\mu}}{\rho}} \tag{4.4}$$

Where, $\hat{\lambda}$ and $\hat{\mu}$ are Lamé's parameters, computed with Equations 4.5 and 4.6 [67].

$$\hat{\lambda} = \frac{E\nu}{(1+\nu)(1-2\nu)} \tag{4.5}$$

$$\hat{\mu} = \frac{E}{2(1+\nu)} \tag{4.6}$$

When fibres or matrix fail, material properties are degraded. Thus, degraded elements present lower Lamé's parameters, resulting in lower dilatational wave speeds, once the density is constant. In turn, this situation, decreases the maximum deformation speed at which the element can be subjected. To prevent the elements from deforming or collapsing unrealistically, Abaqus constantly computes the ratio of "deformation speed to wave speed". Warnings are given when the ratio is equal or higher than 0.3 and the simulation is interrupted if it is equal to 1. To overcome this problem, it is necessary to explore how Abaqus calculates the deformation speed. Consulting the FEM software documentation, it is concluded that the deformation speed is equal to "largest absolute value of all the deformation rate components of an element times the element characteristic length l_c" [67]. The deformation rate components are controlled by the impact properties, so the only parameter to be adjusted is the characteristic length, by changing the element size.

The first measure was to reduce the element size, which consequently reduces the characteristic length, the deformation speed and finally the ratio. However, after successive reductions in mesh size, the errors/warnings remained. Although it may seem contradictory, given the expressions presented above, the solution relies on increasing the elements size. Even if this method implies an increase in L_e, it is compensated by an increase in the stiffness of the plate, which leads to a reduction in the speed of deformation and therefore in the ratio. Note that both the deformation speed and the dilatational wave speed vary during the simulation, as a result of the different phases of the impact and the degradation of the properties, which is why the calibration was not so linear.

The final configuration has elements with a size of 4 mm, both on the outer edge of the plate and in the central region, totalling only 512 elements. In terms of the type, conventional shell elements with reduced integration (S4R), plus "enhanced" hourglass control were employed. Figure 4.3 presents the final mesh.

In addition, element elimination was introduced in the VUMAT code. If any of the damage variables d_f, d_m or d_s reach 0.99, elimination occurs. It was found that the absence

of elements deletion, in this criterion, was leading to very high reaction forces and to the introduction of energy in the system.

The finest adjustment involves redefining the contact between the projectile and the plate. In this case, surface-to-surface contact is used and friction is introduced, through a friction coefficient of 0.16 for tangential behaviour. Hard Contact for normal behaviour is maintained.

Finally, both the modelling of the projectile and the application of the various boundary conditions were unchanged.

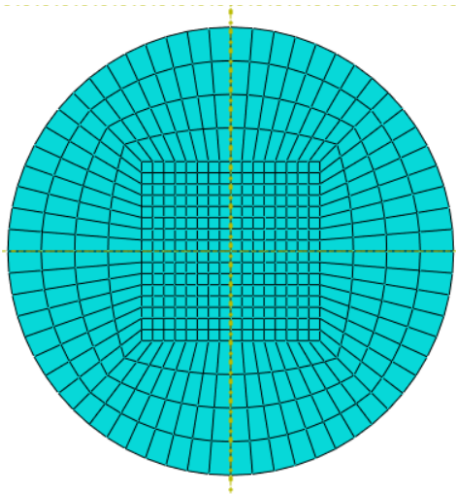


Figure 4.3: Final mesh for Modified Ladeveze model

4.1.1 2D - Results

After running the several analyses, the results were post-processed in order to obtain information about the energy transferred to the plate and the reaction forces over the impact period.

With regard to the transferred energy, $E_{tr}(t)$, the evolution of the projectile's velocity was extracted and applied to Equation 4.7.

$$E_{tr}(t) = \frac{1}{2} m_p (v_0^2 - v(t)^2) \tag{4.7}$$

Where, m_p is the projectile mass, v_0 is the initial velocity of the projectile and $v(t)$ the projectile velocity at instant t.

The reaction forces, F, are obtained by extracting the acceleration in the "z" or 3 direction of the projectile, a_3, which is then multiplied by its mass, as shown in Equation 4.8. For comparison purposes, the reaction force in the "z" direction of the fixed plate nodes was extracted. They were then summed, and the results equalled those obtained by the acceleration of the projectile. Since the first method involved fewer data manipulation, it was the method chosen.

$$F = m_p a_3 \tag{4.8}$$

Figures 4.4 to 4.6 compare the results obtained with the 2D Hashin criteria with experimental results of [86], for the three different laminate configuration.

The experimental data shows that in the first phase of the impact, energy is transferred to the plate, with a maximum value of around 5.91J. Subsequently, the energy value decreases due to some elastic recovery of the plate. In the final phase, it gradually stabilizes at a plateau, which is the value related to the energy absorbed by the laminate's failure mechanisms.

As far as the numerical results are concerned, it is clear that both with Continuum Shell elements (SC8R) and conventional Shell elements (S4), the maximum peak energy results are very close to the experimental ones. However, there are some differences in the values for absorbed energy and impact time. In all the cases, the absorbed energy was found to be lower than the experimental. This is essentially due to the limitations of the 2D Hashin criterion. As mentioned earlier, it does not take into account the occurrence of delaminations. However, for the simulations with conventional shell elements, higher values of absorbed energy were obtained than those with the continuum shell, although both far from the real value.

It should be also noted that, the experimental data indicates a higher absorbed energy value for the $[0]_{10}$ laminate and similar values for the $[+45/-45/+45/0/90]_s$ and $[0/90/0/90/0]_s$ laminates. The numerical data, mainly with SC8R elements, also captures this trend.

In terms of impact time, the $[0]_{10}$ and $[0/90/0/90/0]_s$ laminates show a much longer time than that obtained experimentally for S4 elements, since the energy curve is more elongated. For SC8R elements, the curve is clearly closer to the experimental one, but the energy peak occurs earlier in all laminates. This last observation is also present in reference [75] results, mainly for $[+45/-45/+45/0/90]_s$ laminate.

Moving on to the reaction force data, experimental results show that the maximum force values are associated with the $[+45/-45/+45/0/90]_s$ laminate, then $[0/90/0/90/0]_s$ and finally $[0]_{10}$. With regard to impact times, a value close to 5.5 ms was obtained experimentally for the $[0]_{10}$ laminate, 4 ms for the $[0/90/0/90/0]_s$ and 3.8 ms for the $[+45/-45/+45/0/90]_s$.

The numerical data shows that S4 elements have difficulty to correctly describe the evolution of the reaction forces. For the $[0]_{10}$ and $[0/90/0/90/0]_s$ laminates, the curve obtained is completely incorrect as it shows much lower force values and longer impact times. For the $[+45/-45/+45/0/90]_s$ laminate, the S4 elements capture the evolution trend of the experimental curve well, but the maximum values are considerably lower.

Moving on to the SC8R elements, it can be seen that satisfactory results are obtained for the three laminates analysed. For the $[0]_{10}$ and $[0/90/0/90/0]_s$ layups, the curves show force values and impact times similar to the experimental ones. For the $[+45/-45/+$

$45/0/90]_s$ laminate, the impact time remained similar to those obtained with S4 elements, but the reaction force curve has become closer to the experimental one.

Finally, a few comments should be made regarding the fact that in all laminate configurations, when compared to the experimental data, the simulations always return higher values of transferred energy and reaction forces in the first phase of the impact. This is due to differences in the boundary conditions applied to the plate. In the simulations, it was assumed that the edge of the plate was fixed, preventing rotation and translation movements in all directions. However, this is not entirely true: during the experimental tests, there may be slippage between the plate and the clamps that hold it in place, as well as some rotation, leading to these differences. This topic was explored in greater detail in reference [70].

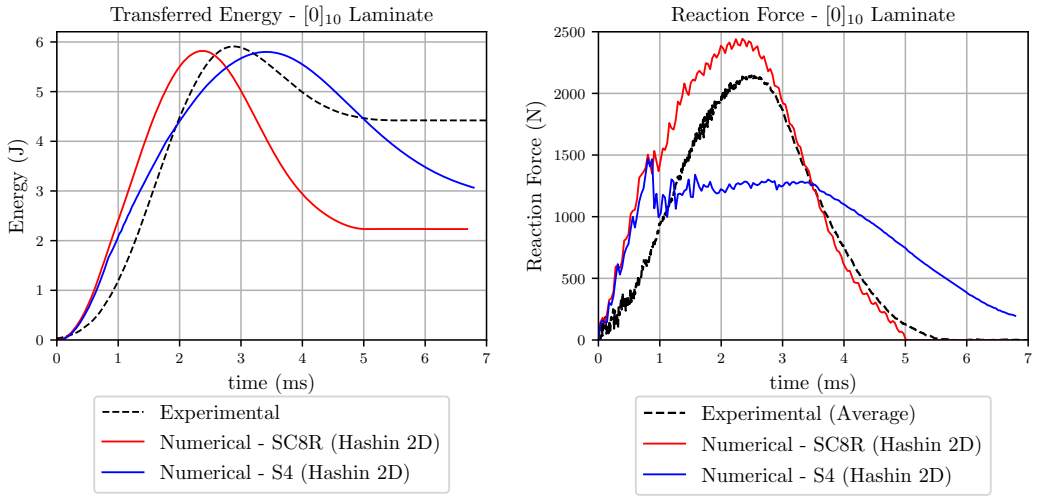


Figure 4.4: 2D Hashin criterion results for $[0]_{10}$ laminate

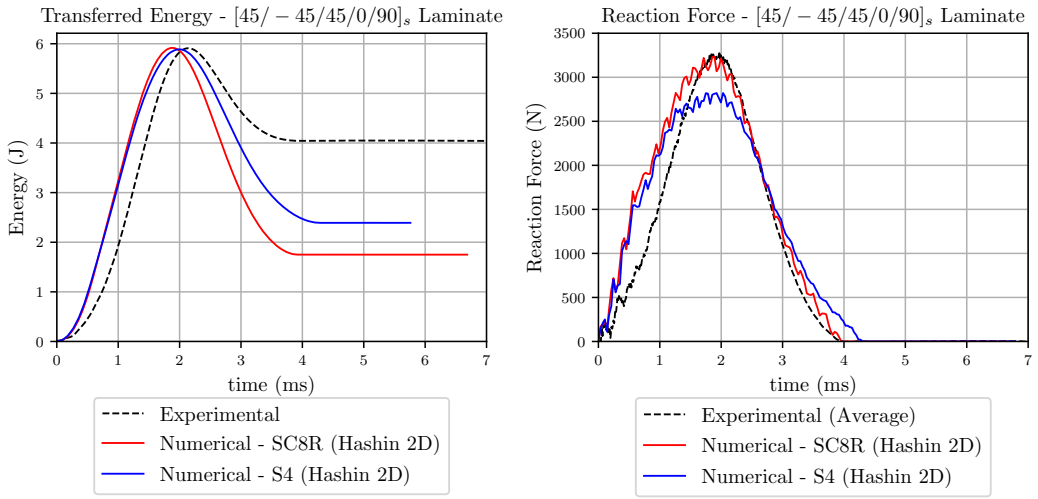


Figure 4.5: 2D Hashin criterion results for $[+45/-45/+45/0/90]_s$ laminate

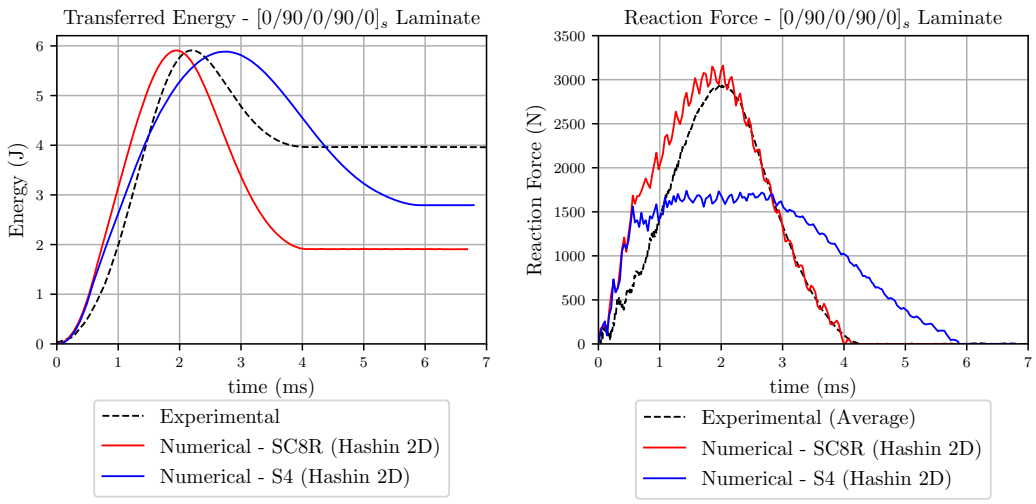


Figure 4.6: 2D Hashin criterion results for $[0/90/0/90/0]_s$ laminate

Since the model with SC8R elements returned the best results for the 2D Hashin criterion, it will be compared with the values obtained from the Modified Ladeveze criterion (Mod. Ladeveze).

With regard to the energy transferred to the plate, it can be seen that in the initial phase of the impact, i.e. up to the maximum value, the response is similar for both the Hashin criterion and the subroutine (Mod. Ladeveze). However, there is a slight trend for the subroutine curve to be closer to the experimental data. This can be observed for the $[0]_{10}$ laminate at the maximum value obtained, and for the $[+45/-45/+45/0/90]_s$ laminate by the gap reduction.

Concerning the final phase of the curve, it is clear that the values obtained by the subroutine are considerably lower than the experimental ones, and close to those of the Hashin criterion. This is due the fact that both models do not take into account the phenomenon of delamination. However, the experimental data points to higher absorbed energy values in the $[0]_{10}$ laminate and similar values in the $[+45/-45/+45/0/90]_s$ and $[0/90/0/90/0]_s$ configurations. The numerical data obtained by the Hashin criterion tends to capture this trend better. The subroutine, on the other hand, although it returns the highest value for the $[0]_{10}$ laminate, shows a considerable difference between the other two configurations.

Regarding the maximum values, for the $[0]_{10}$ laminate the subroutine delivers results identical to the experimental ones, opposing the higher values of the Hashin criterion. For the other configurations, both models are close to the experimental.

In the final phase of the impact, i.e. the projectile's return, the Hashin criterion better captures the evolution of the reaction forces. The Mod. Ladeveze results show slightly higher values, resulting in longer impact times than the Hashin criterion. This behaviour is beneficial in the case of the $[0]_{10}$ composite as it brings the impact time closer to the experimental one, but for the other composites it leads to an impact time around 0.5 ms longer than the real.

Finally, it can also be concluded that the effect of the plate boundary condition is also present for the Mod. Ladeveze criterion, in the sense that it shows higher values of transferred energy and reaction forces in the first phase of the impact, in the $[0]_{10}$ and $[0/90/0/90/0]_s$ laminates. For the $[+45/-45/+45/0/90]_s$ configuration, results at this impact phase are considerably closer to the experimental ones.

In summary, it can be concluded that the Mod. Ladeveze criterion shows the best results in the initial phase of the impact, up to the maximum force value. In the return phase, the Hashin criterion tends to capture better the evolution of forces.

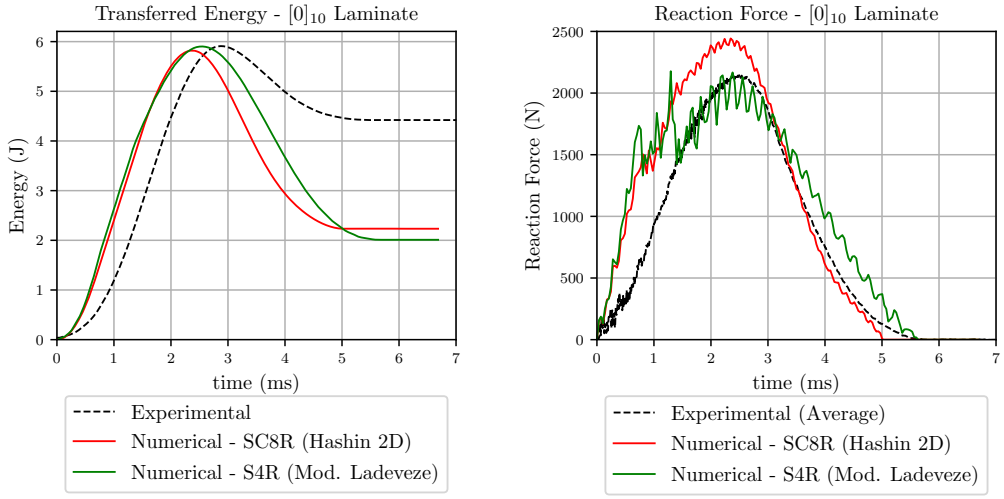


Figure 4.7: Comparison of 2D criteria results for $[0]_{10}$ laminate

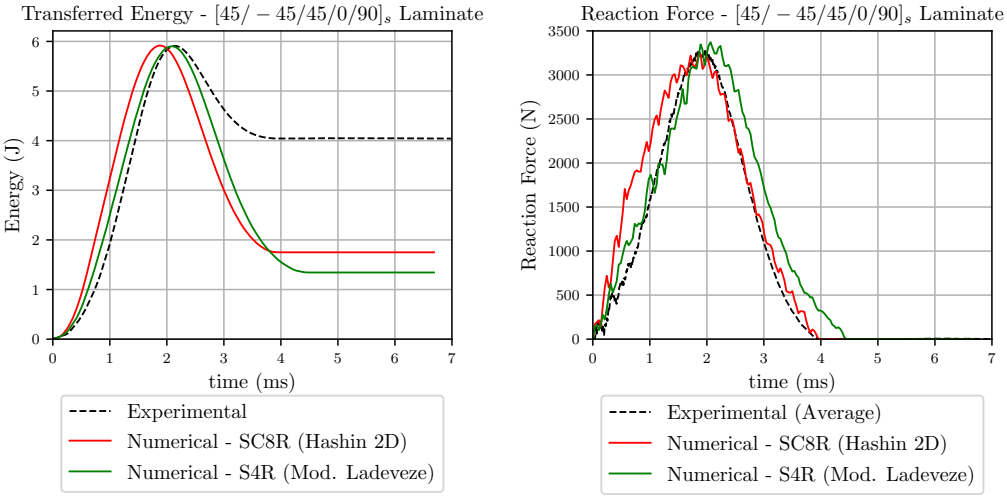


Figure 4.8: Comparison of 2D criteria results for $[+45/-45/+45/0/90]_s$ laminate

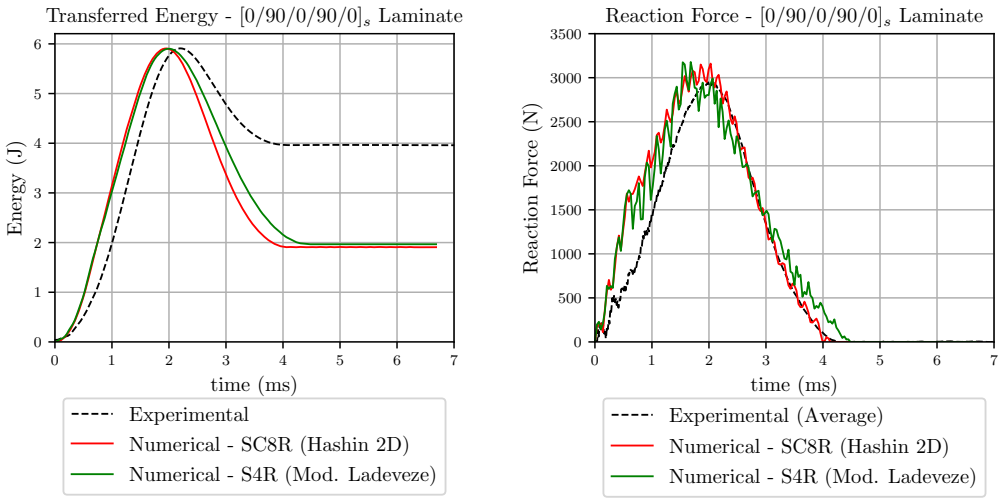


Figure 4.9: Comparison of 2D criteria results for $[0/90/0/90/0]_s$ laminate

4.2 Low velocity impact - 3D approach

The development of the 3D model is very similar to that developed previously using continuous shell elements (SC8R). However, instead of discretizing the thickness into just four elements, ten were used, i.e. one element for each layer of the laminate. In addition, a more refined mesh was also implemented, using 0.8 mm elements in the centre region and keeping 3 mm elements in the remaining regions. In order to reduce computing times, solid elements with reduced integration were implemented, resulting in a total of 35200 C3D8R elements, illustrated in Figure 4.10 (a). Finally, to avoid the hourglass effect resulting from the use of elements with reduced integration, stiffness-type hourglass control was used, along with distortion control.

As far as the projectile is concerned, it follows the same process as described above. The interaction between the projectile and the plate uses the general contact algorithm, with hard contact for normal behaviour and tangential friction with a coefficient of 0.15. The boundary conditions remain the same for both the projectile and the plate. The final assembly is presented in Figure 4.10 (b).

The first part of the analysis only considers the 3D Hashin criterion, while the next stage adds the effect of the strain rate. With regard to the subroutine used, which contains the 3D Hashin criterion described in subsection 3.1, different S_{mt} and S_{mc} parameters were used for the different laminate configurations. It should be remembered that these parameters control the shear stiffness loss. Note that with this criterion the impact of 10.8 J will also be studied, which required a new tuning of S_{mt} and S_{mc}. Table 4.2 lists the values used for the different cases studied. These parameters will be studied in greater detail as part of a sensitivity analysis introduced in section 4.2.2. The following sections 4.2.1 and 4.2.3 present and discuss the results obtained.

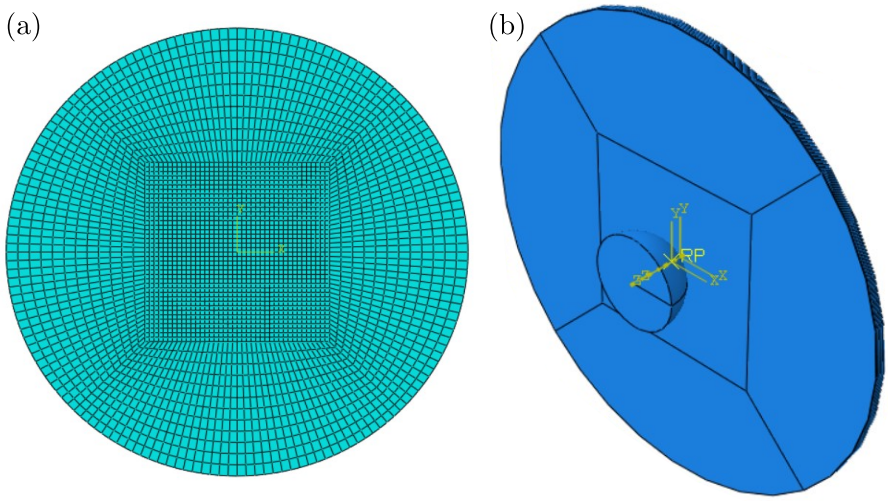


Figure 4.10: (a) - 3D plate mesh, (b) - 3D model assembly

Table 4.2: S_{mt} and S_{mc} values

		5.91 J Impact		**10.8 J Impact**
Laminate Configuration	$[0]_{10}$	$[+45/-45/+45/0/90]_s$	$[0/90/0/90/0]_s$	$[+45/-45/+45/0/90]_s$
S_{mt}	0.70	0.50	0.50	0.40
S_{mc}	0.70	0.30	0.30	0.31

4.2.1 3D - Results

After finalizing all the numerical simulations, the results were gathered and post-processed as explained above (section 4.1.1). In order to better understand the performance of the 3D criteria, it was decided to compare them with the numerical results of the 2D cases for the 5.91 J impact. Therefore, transferred energy and reaction force plots are illustrated in Figures 4.11, 4.12, 4.13 for the 5.91 J impact, and Figure 4.14 for the 10.8 J impact.

Starting by analysing the impact of 5.91 J (Figure 4.11 - 4.13), it is possible to see a great similarity in the energy transferred between the results of the 3D and 2D Hashin criteria, for all laminate configurations. However, the final value of the energy absorbed by the plate, signalled by the plateau, is higher for all cases than both the 2D Hashin criterion and the Mod. Ladeveze. Even so, it is far from the experimental values, as once again the occurrence of delamination was disregarded.

As far as reaction forces are concerned, the similarity of results between the 2D and 3D versions of the Hashin criterion is once again verified. Nonetheless, for laminate $[0]_{10}$, in the peak force region, the 3D criterion is closer to the experimental data, returning lower force values than the 2D version.

Moving on to the impact of 10.8 J (Figure 4.14), the trend of the results, both for the energy transferred and for the reaction forces, is maintained. The maximum energy value is similar to the experimental one, but it occurs earlier. As far as absorbed energy is concerned,

the plateau also shows a lower value than the experimental one, due to delamination not being taken into account.

With regard to the reaction forces, the values are higher than the experimental ones in the first impact phase. The peak region is well captured by the criterion. In the final phase, there is a slight departure from the experimental data, resulting in a slightly longer impact time.

Since the boundary conditions were not altered, the values of transferred energy and reaction forces remain slightly higher than the experimental, ones in the initial phase of the impact, for all the simulated cases.

In addition, it can be concluded that for all the models implemented (2D and 3D), the results that differ most from the experimental ones are for the $[0]_{10}$ laminate. Of all the laminates, this is the configuration with the most anisotropic behaviour, since all the unidirectional layers have the fibres aligned in the same direction, 0°. Experimental analyses of [86], conclude that this kind of laminate exhibit a greater tendency for matrix failure. Nevertheless, fibre failure is also important in the rear layers (opposite to the impacted face) due to tensile stresses. As fibre rupture release more energy than matrix failure, higher absorbed energy is obtained with $[0]_{10}$ laminate. As a result, the models have greater difficulty in characterising the behaviour of this laminate.

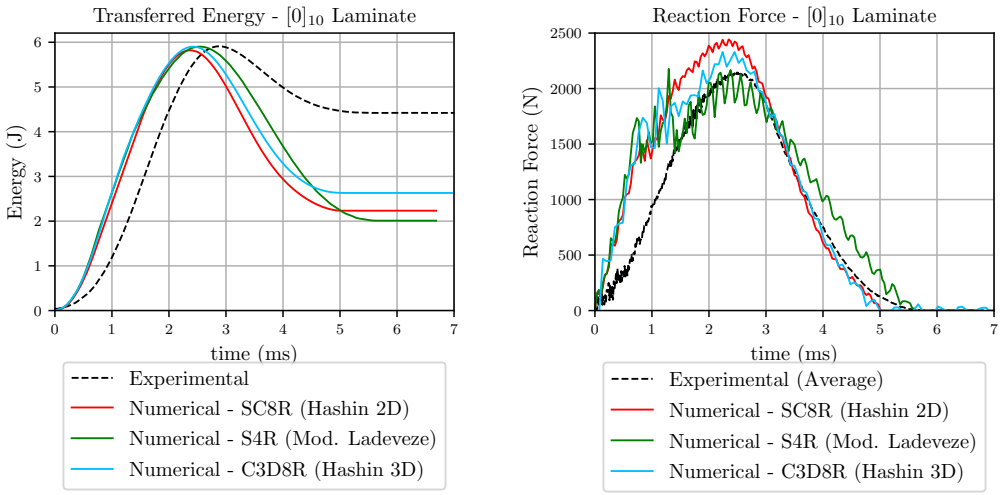


Figure 4.11: Comparison of different criteria results for $[0]_{10}$ laminate

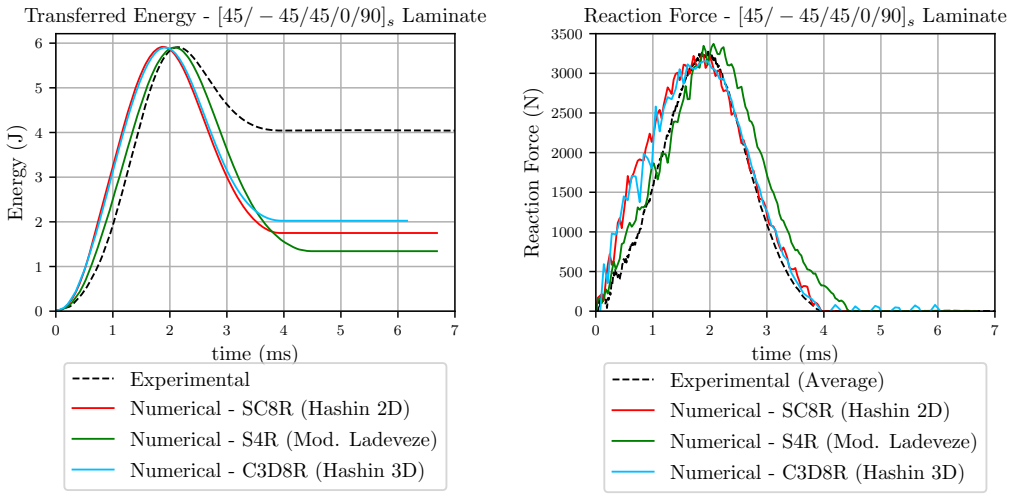


Figure 4.12: Comparison of different criteria results for $[+45/-45/+45/0/90]_s$ laminate

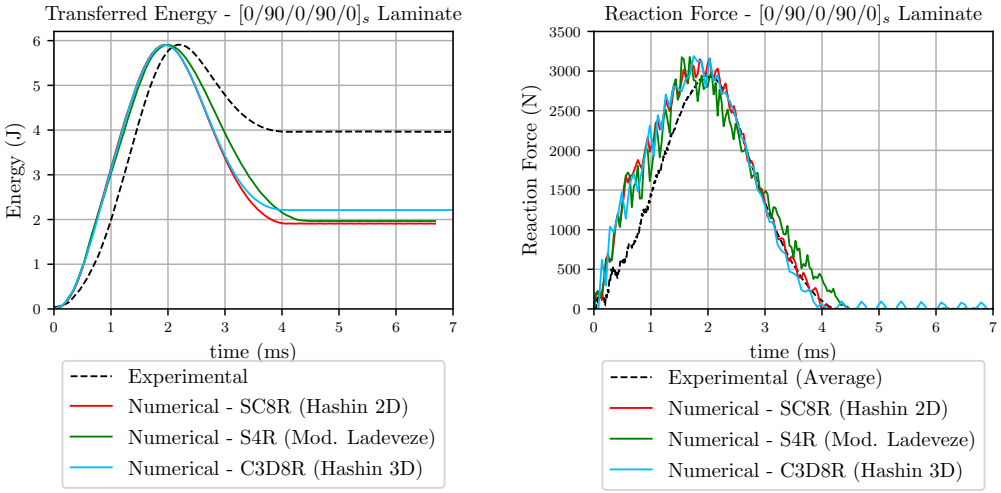


Figure 4.13: Comparison of different criteria results for $[0/90/0/90/0]_s$ laminate

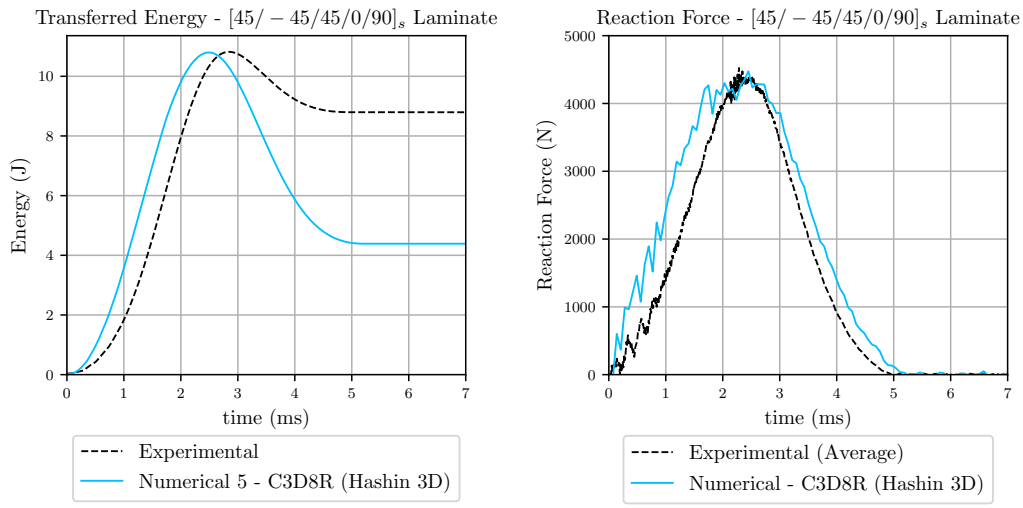


Figure 4.14: Hashin 3D criterion results for $[+45/-45/+45/0/90]_s$ laminate under 10.8 J impact

4.2.2 3D Approach - Shear loss coefficients sensitivity analysis

This subsection presents a sensitivity analysis of the shear loss coefficients, namely S_{mt} and S_{mc}, contained in the 3D Hashin criterion. This study emerges after the first simulations did not return satisfactory results, revealing much lower impact forces and high impact times. These simulations used S_{mt} equal to 0.90 and S_{mc} equal to 0.50, since these were the values recommended by various references, namely [88]–[90], for simulating low-velocity impacts on composite structures. It should be emphasised that these references did not state why these figures were used.

On the other hand, the reference [91], using the same values, also obtains results far removed from the experimental ones. However, the opposite effect is observed: higher reaction forces and lower impact times. By varying S_{mt} and S_{mc}, the researchers claim that to simulate low-velocity impacts on composite materials using this criterion, these parameters should be between 0.96 and 0.99. Such a statement does not hold true in this study, as the best results were obtained using lower values of S_{mt} and S_{mc}, as shown above in Table 4.2. As well as varying with the laminate stacking sequence, it varies with the impact energy.

Note that the shear loss coefficients directly affect the damage parameter of the matrix, d_m (recall Equation 3.26). In turn, the relationship between them is inverse, with higher S_{mt} and S_{mc} values leading to the matrix damage parameter to approach zero (i.e. total damage).

Figures 4.15 and 4.16 present the sensitivity analysis performed for the $[+45/-45/+45/0/90]_s$ laminate under a 10.8 J impact. In fact, all the cases presented in Table 4.2 underwent a sensitivity study, in the following order:

1. $[+45/-45/+45/0/90]_s$ laminate under a 5.91 J impact.
2. $[0/90/0/90/0]_s$ laminate under a 5.91 J impact.

3. $[0]_{10}$ laminate under a 5.91 J impact.

4. $[+45/-45/+45/0/90]_s$ laminate under a 10.8 J impact.

In order not to make the document difficult to read, it was decided to present only one of the cases, as they all followed the same methodology: varying only one of the parameters individually, starting with S_{mt} and then S_{mc}. Although the most important criterion for comparison is the evolution of the reaction force, the evolution of the transferred energy is also presented. To perform the sensitivity analysis, the parameters were varied manually, then the simulations were run and the data extracted.

Since for the laminate $[+45/-45/+45/0/90]_s$ subjected to an impact of 5.91 J, the best results use S_{mt} equal to 0.50 and S_{mc} equal to 0.30, that was the starting point for 10.8 J impact study, on that same laminate. From Figure 4.15, it can be concluded that this set of values present the lowest reaction force and the highest impact time. Regarding the energy evolution, the highest absorbed energy is achieved. On the other hand, reducing S_{mt} to 0.40 the highest reaction forces are obtained, and the impact reduces to a value very close to the experimental one. In this case, the lowest absorbed energy value is obtained. The intermediate values, namely, 0.42 and 0.45 return reactions forces close to the experimental data, however with higher impact times. On the other hand, the absorbed energies are similar, but intermediate to the two cases previously mentioned. Therefore, the case with S_{mt} equal to 0.40 was selected for further tuning of S_{mc}, in order to slightly reduce the maximum value of the reaction force and maintain the impact time.

In Figure 4.16 the S_{mc} sensitivity analysis is presented. Varying this parameter has the same effects as described above, both for the evolution of reaction forces and energy. Therefore, the numerical simulation was adjusted by slightly increasing S_{mc} to 0.31. Note that the maximum value of the reaction force decreases, yet an increase in the impact time is inevitable.

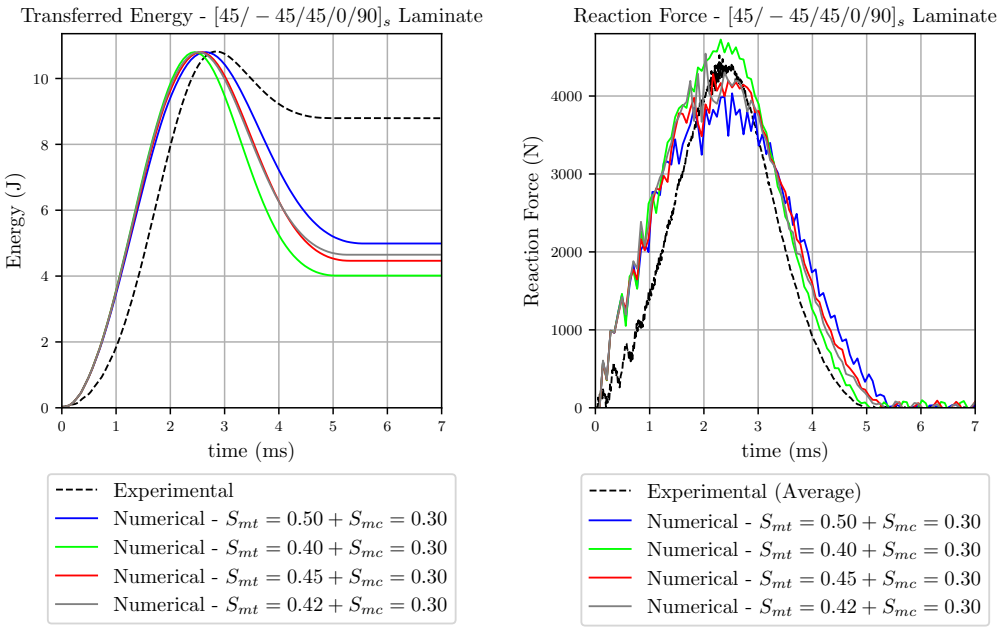


Figure 4.15: S_{mt} sensitivity analysis

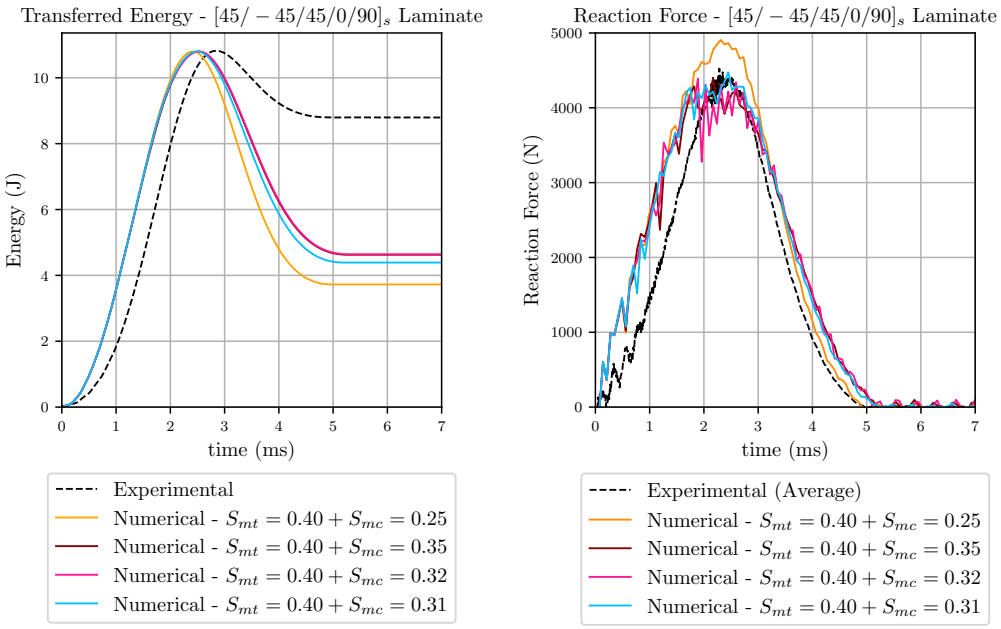


Figure 4.16: S_{mc} sensitivity analysis

4.2.3 3D - Results with strain rate effect

Once the simulations had been carried out using the base version of 3D Hashin criterion and the impact of S_{mt} and S_{mc} parameters had been understood, the effect of the strain rate was introduced.

As explained above, in the section 4.2.1, the $[0]_{10}$ laminate is a particular case of greater calibration difficulty, so it was decided to exclude it from this analysis. The Abaqus models were therefore unmodified, with only the VUMAT subroutine being changed. As for S_{mt} and S_{mc}, they were kept the same as for the base Hashin 3d criterion (please refer to Table 4.2). The results of the 5.91 J impact are presented in Figures 4.17 and 4.18, as for the impact of 10.8 J is the Figure 4.19.

For all impacts, it can be seen that all the transferred energy results, with and without the effect of the strain rate, are extremely close. However, it is clear that the energy absorbed is higher after the introduction of the strain rate effect, being less evident in composite $[+45/-45/+45/0/90]_s$ on an impact of 5.91 J (Figure 4.17). As far as reaction forces are concerned, they are all very similar, with maximum values that are barely altered and similar impact times.

Therefore, it can also be concluded that the S_{mt} and S_{mc} parameters do not require any adjustment after introducing the effect of the strain rate.

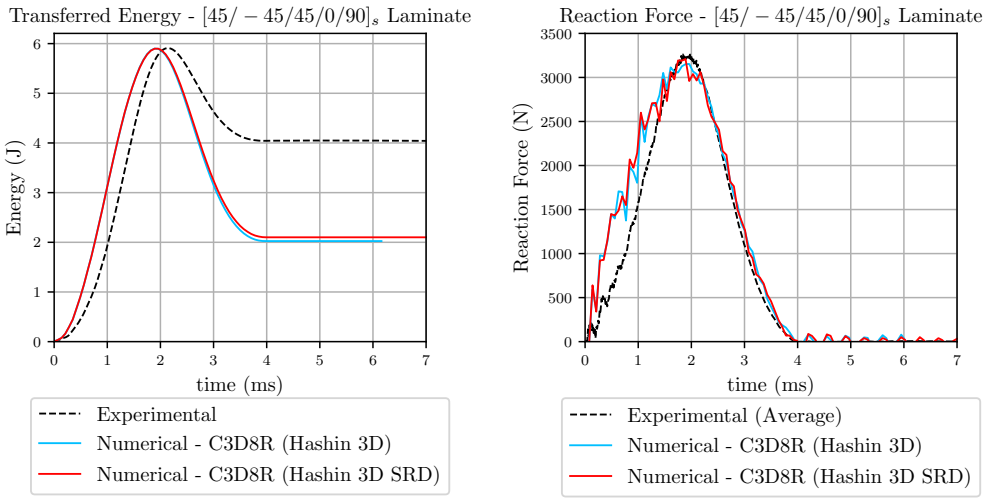


Figure 4.17: Comparison of Hashin 3D criteria results for $[+45/-45/+45/0/90]_s$ laminate

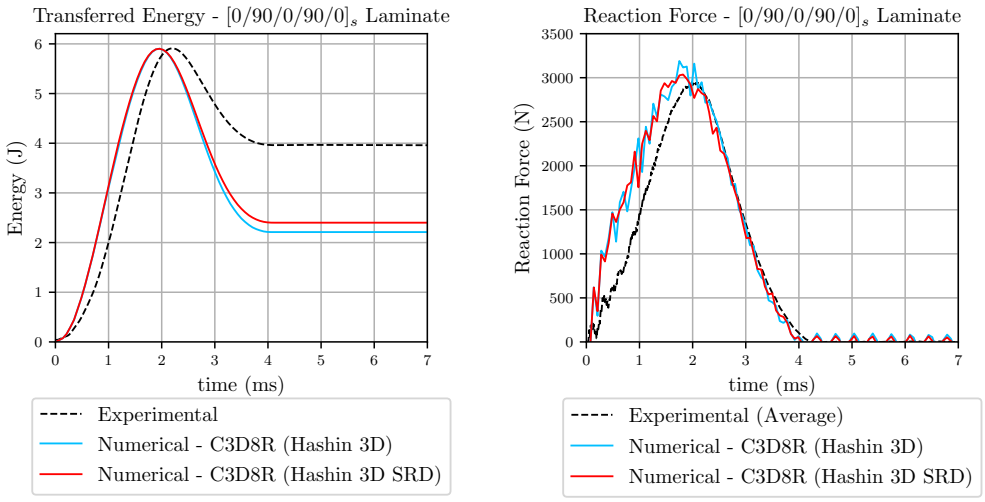


Figure 4.18: Comparison of Hashin 3D criteria results for $[0/90/0/90/0]_s$ laminate

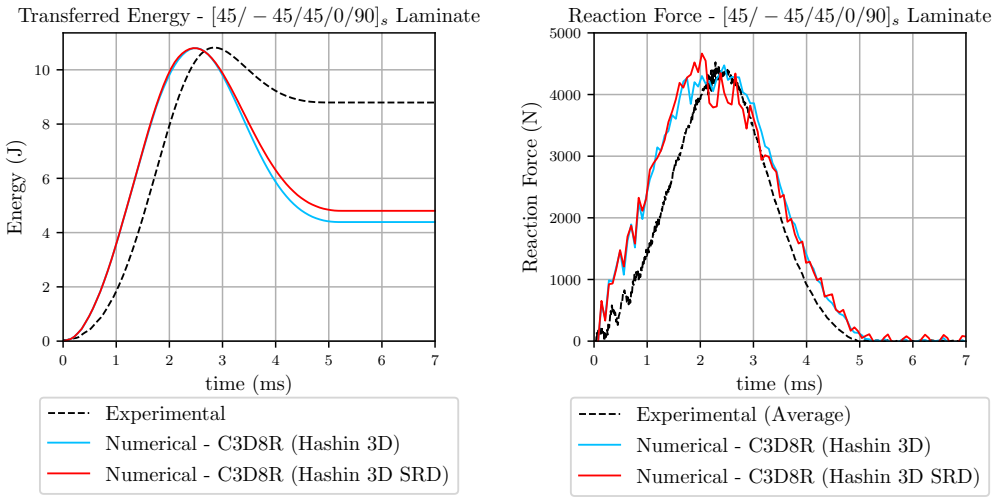


Figure 4.19: Hashin 3D criteria results for $[+45/-45/+45/0/90]_s$ laminate under 10.8 J impact

4.3 Low velocity impact - 3D approach with cohesive elements

Also in the study of low-velocity impact, it was decided to try to implement a model that introduces the effect of inter-laminar failure. The main aim of this model was to obtain transferred energy curves that were closer to the experimental ones.

To this end, a layer of cohesive elements (COH3D8) was introduced between two consecutive layers of the laminate. However, the success of this model was severely limited as the inter-laminar properties of the material used in the experimental tests were unknown. Even resorting to the literature, it proved difficult to identify which set of properties was most appropriate. Nevertheless, the properties in Table 4.3 were used.

A thickness of $5.4\mu m$ was used for the layer of cohesive elements. All other settings have been maintained, resulting in a mesh with 35200 C3D8R elements and 31680 COH3D8 elements. The following section 4.3.1 presents and discusses the results.

Table 4.3: Cohesive elements properties

Property	Unit	Value	Property	Unit	Value
ρ	ton/m^3	1.6	${G_n}^C$	N/mm	0.6
$K_{n/s/t}$	GPa	5.0	${G_{s/t}}^C$	N/mm	2.1
${t_{n/s/t}}^{max}$	MPa	30.0	η	-	1.45

4.3.1 3D - Results with strain rate effect and cohesive elements

The intention was to use the same simulation sequence, i.e. starting with a 5.91 J impact on the $[+45/-45/+45/0/90]_s$ and $[0/90/0/90/0]_s$ laminates and finally the $[+45/-45/+45/0/90]_s$ laminate on a 10.8 J impact. However, the first results proved to be quite divergent from the projected ones, so it was decided to analyse them in detail and only then, if feasible, proceed with the remaining simulations.

Figure 4.20 shows that both the transferred energy and the reaction force do not have satisfactory results. With regard to the transferred energy, the opposite result is obtained, as lower values of absorbed energy are returned by the model. As for the reaction forces, the evolution of the curve is similar, but it shows much higher peaks than the other models and the experimental values.

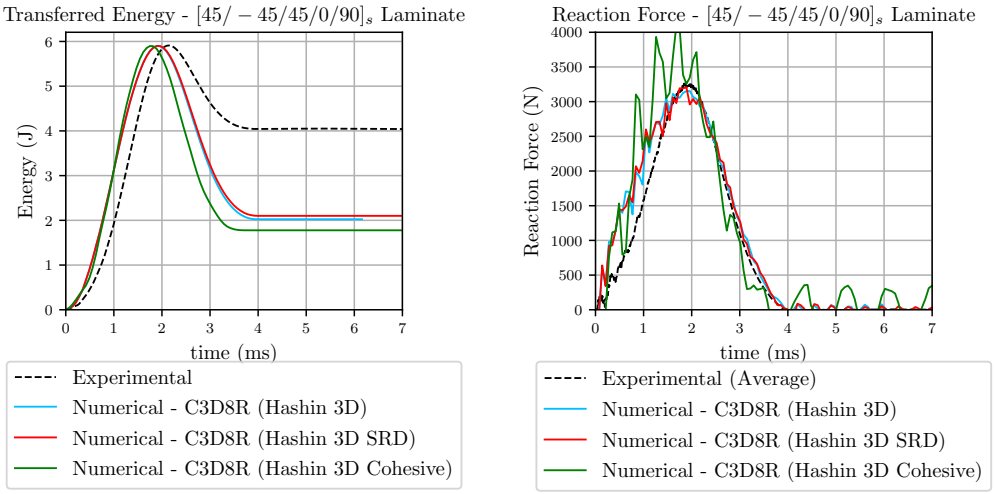


Figure 4.20: Hashin 3D criteria with cohesive elements results for $[+45/-45/+45/0/90]_s$ laminate under 5.91 J impact

In a final analysis, the zone affected by inter laminar damage was compared between the C-scan ultrasound analysis and the numerical simulation, respectively Figure 4.21(a)

and Figure 4.21(b). Although this comparative analysis is not quantitative, it allows to understand whether the shape of the simulated delaminations is similar to the experimental ones.

From Figure 4.21, it can be concluded that the numerical simulation presents data close to the experimental ones, showing the occurrence of delaminations in the form of "peanut shape". In addition, their orientation, $0°, +/-45°$ and $90°$ is consistent with the experimental analysis.

From the above, everything points to the cause of incorrect results being explained exclusively by the use of incorrect properties in the cohesive layer. In order to improve them, it would be necessary to carry out new simulations until a set of properties was found that correctly described the material in question. This could be a time-consuming process, so it was decided to leave the introduction of cohesive elements to the next stage, i.e. the ballistic simulation.

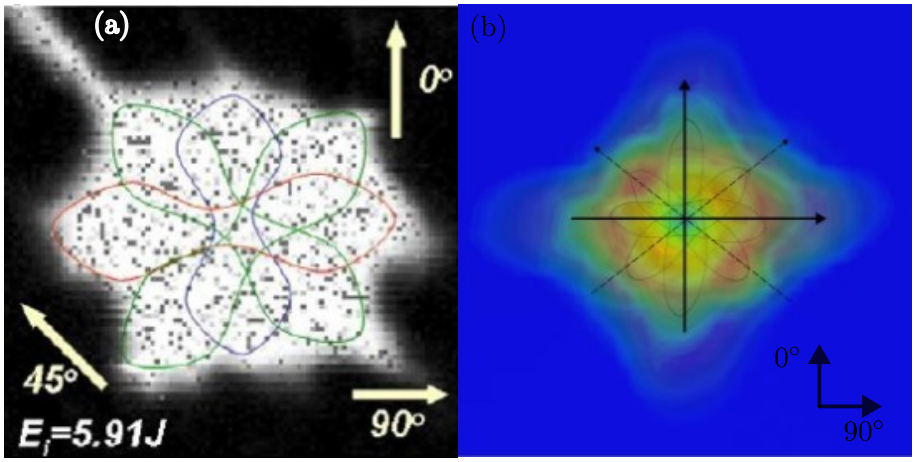


Figure 4.21: Iter-laminar damage of 5.91 J impact for $[+45/-45/+45/0/90]_s$ laminate. (a) - experimental data [86], (b) - numerical data

Chapter 5

Case studies: High-Velocity/Ballistic Impacts

This section is dedicated to the study of high-velocity impacts, often also labelled as ballistic impacts. The ultimate goal is to develop a model/approach capable of correctly describe the behaviour of a hybrid laminate subjected to a high-velocity impact, considering the effects of the strain rate.

In the literature, much of the work carried out in the field of hybrid armours uses essentially combinations of composite, ceramic and metallic materials. Within the composite material, the greater use of laminates with woven layers to the detriment of unidirectional ones is notorious. Even though it was developed for unidirectional composites, the 3D Hashin criterion is often used by authors to determine the failure onset of laminates with woven layers [92]–[94]. There are, however, authors who prefer to adapt or fully develop models to better describe the behaviour of this type of structure [95].

In the present work, the focus is on the study of unidirectional composites and the effect of their hybridisation with the addition of ceramic material. As the aim is to develop three-dimensional models, the behaviour of the composite materials is only described by the 3D Hashin criterion. Note that at this stage, the deletion of elements was introduced in VUMAT. This occurs when one of the damage parameters, d, is greater than or equal to 0.99. This section also introduces the Jonhson-Holquimist model, specifically to describe the behaviour of ceramic materials.

As in the previous section, the study of high-speed impacts is carried out gradually.

Firstly, the 3D Hashin criterion and its degradation law are validated. Next, the Jonhson-Holquimist model is validated for the ceramic material. Then, once the two models have been validated individually, the study of plate hybridisation is carried out. No cohesive elements were introduced in any of the phases in which composite laminates were used, therefore, delaminations were disregarded. Finally, in the last part of this section, a study is made of the use of the 3D Hashin model and its property degradation law for woven composite laminates.

Before proceeding with the description of the various case studies, it is important to note that, in the literature, it is not common to find the evolution of reaction force and transferred energy during the several impact stages, regarding high-velocity impacts. However, the main parameters for comparison are often the final residual velocity of the projectile and/or the total energy absorbed by the plate. As a result, it becomes more complicated to understand whether the model correctly describes all phases of the high-speed impact event.

5.1 High velocity impact - Unidirectional composite laminate plate

This first stage is based on the experimental work carried out by Lee and Sun [96]. In the experimental work all CFRP plates present a squared shape 100 mm wide and are fixed to a support with a circular hole measuring 43.5 mm in diameter. As in the low-velocity impact simulations, the clamping grips are not modelled. Therefore, only the circular region of the plates is modelled, applying the boundary conditions to its outer edges.

Two different laminates were studied, the first present the following stacking sequance, $([0/90/+45/-45]_s)_2$ leading to a 2 mm thickness, thus 0.125 mm per ply. Regarding the studied impact velocities in this laminate, V_s, two were studied: 40 and 79 m/s. The second laminate is the result of duplicating the previous one, i.e, $([0/90/+45/-45]_s)_4$, thus, a total thickness of 4 mm. For this case, an impact velocity of 91 m/s is simulated. In order to make this document easier to read, the first laminate will be called L1 and the second L2. Finally regarding the projectile, it is a cilinder with a diameter of 14.5 mm and 24 mm length. Table 5.1 lists the properties of the CFRP used.

Once the geometry of the different components had been defined, models of them and the final assembly were created in Abaqus, as in the previous tests.

Regarding the composite plate a 28 mm squared central partition was introduced to allow mesh refinement in the impact zone. In that region elements with an approximate size of 0.6 mm were used, whereas in the outer regions elements with 3 mm were implemented (the values were adjusted after successive simulations). In the thickness direction, one element per layer was used. As in the 3D model of the low-velocity impact, hexahedral elements with reduced integration were used, along with second-order accuracy, distortion control, and stiffness-type hourglass control. These configurations result in a mesh with a

total of 17860 C3D8R elements for the L1 laminate and 35720 C3D8R elements for the L2 laminate (double of L1 model). In both models element deletion was activated.

Table 5.1: CFRP properties [86], [87], [96]

General properties			**Damage initiation properties**			**Damage evolution properties**		
Property	Unit	Value	Property	Unit	Value	Property	Unit	Value
E_{11}	GPa	138	X_T	MPa	1400	G^c_{ft}	N/mm	48.40
E_{22}= E_{33}	GPa	9.65	X_C	MPa	930	G^c_{fc}	N/mm	60.30
G_{12}=G_{13}	GPa	5.24	Y_T	MPa	47	G^c_{mt}	N/mm	4.50
G_{23}	GPa	3.24	Y_C	MPa	130	G^c_{mc}	N/mm	8.50
ν_{12}=ν_{13}	-	0.3	S_{12}=S_{13}	MPa	53			
ν_{23}	-	0.49	S_{23}	MPa	89			
ρ	ton/m^3	1.55						

The modelling of the projectile uses analytical surfaces, as its deformations are not taken into account. It has been assigned a mass of 30 g as well as the 3 distincted impact velocities.

To model the interaction between the target and projectile, 'hard contact' was chosen for the normal contact, while frictionless condition was applied for the tangential contact, as no experimental parameters were available.

Regarding boundary conditions, the degrees of freedoom of the outer edges of the pate were completly restrained, and the projectile was only allowd to move in the "z" or impact direction. Figure 5.1 presents both the mesh and final assembly for L1 laminate.

Finally, it remains to address the values of the shear loss stiffness coefficients. As with the low-velocity impact test, they influence the laminate's response, and it was also necessary to adjust them to obtain the best results. In order to understand the trend of the results when varying these parameters, a sensitivity analysis was once again carried out (see 5.1.2). The final results for the different simulations are shown in Table 5.2.

Table 5.2: S_{mt} and S_{mc} values - High velocity impact

	L1 laminate		**L2 laminate**
V_s **(m/s)**	40	79	91
S_{mt}	0.55	0.55	0.30
S_{mc}	0.35	0.35	0.30

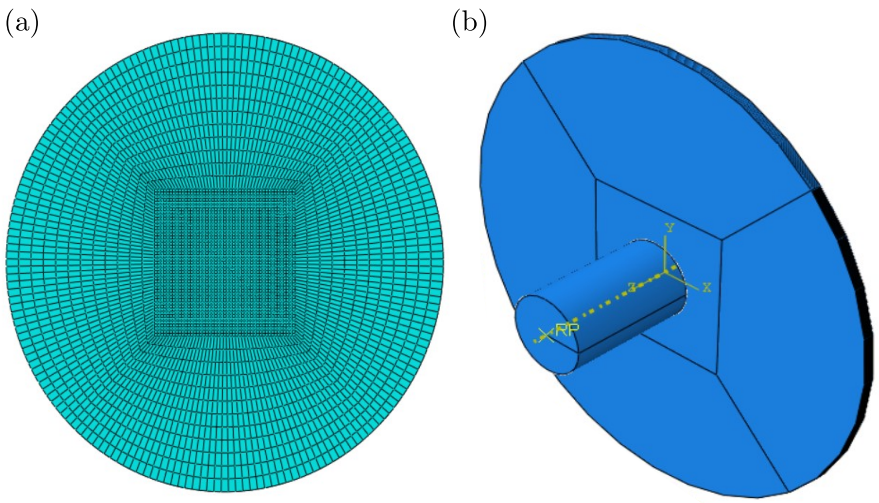


Figure 5.1: L1 laminate: (a) - final mesh; (b) - final assembly

5.1.1 Unidirectional composite laminate plate - Results

Once all the models had been created, the simulations were carried out. Initially with only the *Hashin 3D* (H3D) criterion, the effect of the strain rate was later added (H3D+SRD).

In order to understand the performance of the numerical data, it was only possible to compare the residual velocity obtained with Abaqus and that of the literature, as this was the only data provided. Table 5.3 concentrates this comparison and provides the associated relative error.

Table 5.3: Residual velocity comparison of high-speed impact in CFRP unidirectional laminates

Laminate	V_s (m/s)	V_r (m/s) experimental [96]	V_r (m/s)		V_r (m/s)	
			H3D	Error (%)	H3D+SRD	Error (%)
L1	40	16	16.4	2.5	15.5	3.1
	79	65	64.6	0.6	62.8	3.4
L2	91	59	60.7	2.9	57.7	2.2

From the aforementioned results, it is possible to see a fairly good correlation between the experimental and numerical data. In all the cases evaluated, the experimental results, with and without the effect of the strain rate, always show a relative error of less than 3.5 %. Moreover, it is concluded that the exclusion of interlaminar failure in the finite element models did not result in significant discrepancies between the numerical and experimental residual velocities. The experimental work indicated that, in all three cases analyzed, full penetration of the projectile into the plate occurred, which was also confirmed in the numerical data analysis. Thus, the complete rupture of the matrix and fibers, which are responsible for the majority of the energy absorption, diminishes the significance of the

energy dissipated through delaminations. Consequently, the disregard for delaminations in high-velocity impacts has a lesser impact compared to low-velocity impacts.

Finally, there is a slight tendency for models that account for the strain rate effect to exhibit lower residual velocities. This can be explained by the manner in which this effect is introduced. It should be noted that certain properties of the composite material are scaled to increase both tensile and compressive strength (as detailed in Section 3.3). In this context, the material properties are "enhanced," thereby improving its mechanical performance and allowing for greater energy absorption.

In addition, the shear loss coefficients values were calibrated considering only the 3D Hashin criterion. If a new adjustment of the parameters was made taking into account the effect of the strain rate, the errors obtained in H3D+SRD from Table 5.3 could be reduced.

5.1.2 Shear loss coefficients sensitivity analysis

As with the low-velocity impact, the calibration of the S_{mt} and S_{mc} parameters proved to be extremely important for obtaining satisfactory numerical results for high-velocity impacts on unidirectional composite laminates. As well as achieving the good results, this sensitivity analysis is important for checking whether the variation in the coefficients follows the same pattern as the one presented above, for low-speed impacts (recall Section 4.2.2). For this purpose, all the simulations used the 3D Hashin criterion, without the effect of the strain rate. The results were considered satisfactory when the error was less than 5 %. Once again, the values were varied manually, the simulations were carried out and finally the results were extracted.

Table 5.4 shows the results obtained for the L1 composite subjected to an impact of 40 m/s, i.e. 24 J. To start the simulations it was intended to use the optimum S_{mt} and S_{mc} values of the 10.8 J impact of Section 4.2.2. Nevertheless, a input error occurred and S_{mt} and S_{mc} were equaled to 0.6 and 0.4, respectively. As it wasn't expected to obtain satisfactory results, using the low velocity impact parameters, it was decided to proceed with the analysis. The results for case 1 indicate a high residual velocity and therefore a lower absorbed energy. Reducing the value of S_{mc} by 0.05 shows a slight approximation to the experimental data by around 3.3 percentage points. In case 3, S_{mt} was reduced by 0.05. A greater influence of this coefficient can then be seen, since the reduction is 10 percentage points compared to case 2 and differs only 2.5 % from the experimental data.

Note that in this analysis, to reduce the residual velocity and consequently increase the absorbed energy, it was necessary to reduce the values of the coefficients. This tendency is contrary to that seen in the low-velocity impacts.

The values from Case 3 were subsequently used to initiate the analysis of the impact at 79 m/s, corresponding to 93.6 J on the same laminate. However, unlike what was observed in the low-velocity impact, the increase in impact energy by approximately four times did not necessitate a further update of the parameters. Therefore, it was not relevant to carry out a new sensitivity analysis.

Finally, the impact of 91 m/s, or 124 J, on laminate L2 was explored. It is worth remembering that this is a duplicate of L1, so the optimum values for this laminate were used as a starting point. However, analysing Case 1 in Table 5.5, it can be seen that the residual velocity is high. Following the trend seen for the previous case, the value of S_{mt} and S_{mc} was successively lowered, until in Case 5, with both parameters equalised at 0.30, a residual velocity only 2.9% different from the experimental one was obtained.

Once the analysis is finalised, an inverse trend can be observed. While in the sensitivity analysis of the low-velocity impact, lower values of S_{mt} and S_{mc} indicated lower absorbed energies, the opposite is true for the high-velocity impact. However, the dynamics of the simulated impacts are different: in the low velocity impact, the projectile has a higher mass and lower velocity, with no penetration. In the case of a high-velocity impact, projectiles with a considerably lower mass fully penetrate the plate, making rupture of the matrix and fibre much more pronounced.

It can also be seen that for the L1 laminate, the simulations with different impact speeds/energies did not require adjustments to the coefficients. This was not the case for the low speed impact, meaning that saturation of these parameters is possible at a certain level of impact energy.

Table 5.4: S_{mt} and S_{mc} sensitivity analysis of the L1 laminate at an impact velocity of 40 m/s

Case	S_{mt}	S_{mc}	V_r **(m/s) Experimental [96]**	V_r **(m/s) H3D**	**Error (%)**
1	0.6	0.4		19	15.8
2	0.6	0.35	16	18	12.5
3	0.55	0.35		16.4	2.5

Table 5.5: S_{mt} and S_{mc} sensitivity analysis of the L2 laminate at an impact velocity of 91 m/s

Case	S_{mt}	S_{mc}	V_r **(m/s) Experimental [96]**	V_r **(m/s) H3D**	**Error (%)**
1	0.55	0.35		66.7	13.1
2	0.50	0.35		65.3	10.7
3	0.50	0.30	59	65.3	10.7
4	0.40	0.35		64.3	9.0
5	0.30	0.30		60.7	2.9

5.2 High velocity impact - Ceramic plate

The *Johnson-Holquimist-2* (JH-2) model is widely used to simulate ceramic materials under impact. As such, it has been extensively explored and validated in various works found in the literature. The aim of this section is not to validate it, but to gain practice with it, so that when building a hybrid laminate, the results obtained are reliable. To this end, numerical simulations carried out by Sharma *et al.* [97] were used as a reference.

The model consists of a square plate with a side length of 200 mm and 10 mm thick. It is impacted by a cylindrical projectile with a radius of 5 mm, a mass of 28 g and an initial velocity of 250 m/s. The ceramic material that makes up the plate is silicon carbide (SiC) and has the properties shown in the following Table 5.6. As for the projectile, as in all previous simulations, it remains rigid, discarding its deformations.

In the modelling, as in the reference article, only a quarter of the problem was modelled, given its symmetry. The aim is to reduce computing time. On the ceramic plate, a square partition 20 mm wide was also created in the impact region to refine the mesh. In this same region, an element with a size equal to 1 mm was defined, while in the more distant regions, a size of 3 mm was defined. Note that the creation of this partition only makes it possible to generate a structured mesh in the region of greatest refinement. In the remaining regions, the mesh is of the sweep type. In the thickness direction, 15 elements were used. Regarding the type of element, the use of hexahedral elements with reduced integration along with second-order precision, distortion control and sitffness-type hourglass control was maintained. All these parameters result in a mesh with 95550 C3D8R elements.

Moving on to the projectile, this time it was not modelled with an analytical surface but using the rigid body type. The major difference is that it is necessary to generate a mesh even if the deformations do not exist. 1272 elements, with a size of approximately 0.5 mm and of the R3D4 type, were used to discretise the projectile. Figure 5.2 and 5.3 shows, respectively, the different meshes and the final assembly.

With regard to the interaction between the plate and the projectile, no information was mentioned in the article. It was therefore assumed that normal contact was of the "hard contact" type and that there would be no tangential friction.

For the boundary conditions, faces A and B of the plate were completely fixed, while faces C and D have symmetry in x and y respectively, as shown in Figure 5.4. For the projectile, the same conditions were applied as in the previous cases, allowing only translational movement in the direction of impact.

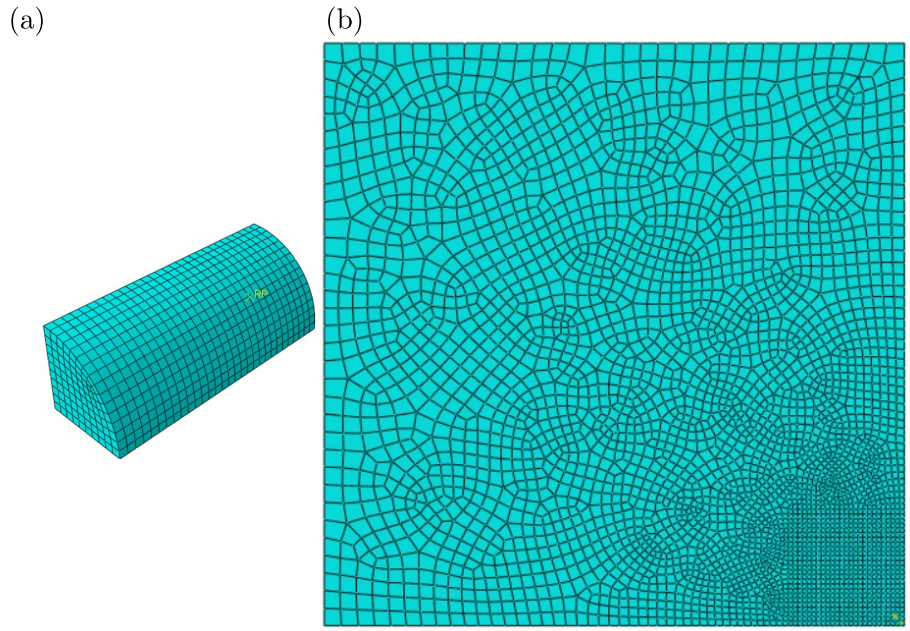


Figure 5.2: Final Mesh: (a) - Projectile; (b) - Ceramic plate

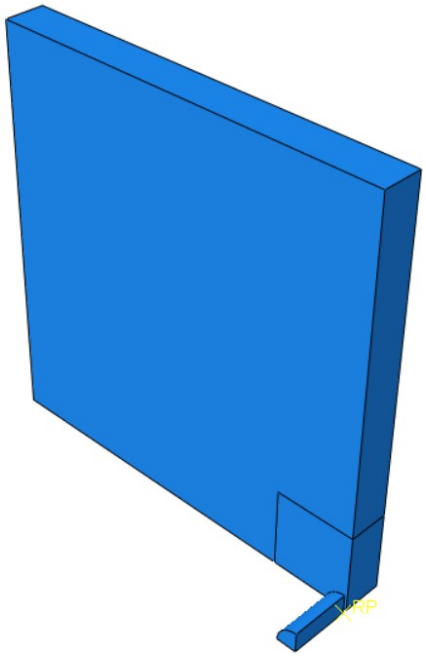


Figure 5.3: Final assembly

Table 5.6: Silicon carbide properties (SiC) [97]

Property	Unit	Value	Property	Unit	Value
ρ	ton/m^3	3.22	HEL	GPa	11.70
G	GPa	193	P_{Hel}	GPa	5.13
A	-	0.96	β	-	1
B	-	0.43	D_1	-	0.48
C	-	0.009	D_2	-	0.48
n	-	0.65	ε_{fmax}	-	1.20
m	-	1	ε_{fmin}	-	0
$\dot{\varepsilon}_0$	-	1	K_1	GPa	220
T	MPa	750	K_2	GPa	361
σ_{Imax}	GPa	12.20	K_3	GPa	0
σ_{fmax}	GPa	1.30	F_s	-	0.60

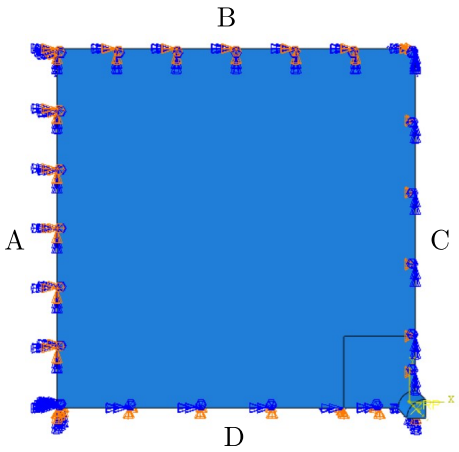


Figure 5.4: Ceramic plate boundary conditions

5.2.1 High velocity impact on ceramic plate - Results

After carrying out the simulation, a comparison was made between the evolution of the kinetic energy obtained and that of the reference [97]. Analysing Figure 5.5 it is clear that in the initial phase there is a certain distance between the two curves. The curve presented by Sharma *et al.* [97] has a very steep slope in the initial moments, showing a very rapid reduction in the projectile's velocity. On the other hand, the curve obtained in this study, although also steep, shows a smaller drop. These differences in the initial phase of the impact last until the projectile penetrates completely, characterised by the end of the reduction in its kinetic energy. Since the reference curve is initially steeper, it has a shorter impact time and a more severe transition.

However, in the phase after total penetration, both curves stabilise a plateau of similar kinetic energy. Sharma *et al.* [97] show a final kinetic energy percentage of around 32 %, while the one obtained is 33.5 %, a difference of 1.5 percentage points. In other words, this

results in a deviation of around 4.7 % of the values obtained in this work in relation to the work by Sharma *et al.*

With regard to the difference in results, it is important to reiterate that the authors of [97] do not present the interaction conditions/properties between the plate and the projectile. This is an important point that could lead to the initial differences between the curves presented above. However, with regard to the final value of the percentage of the projectile's kinetic energy, a difference of less than 5 % is obtained.

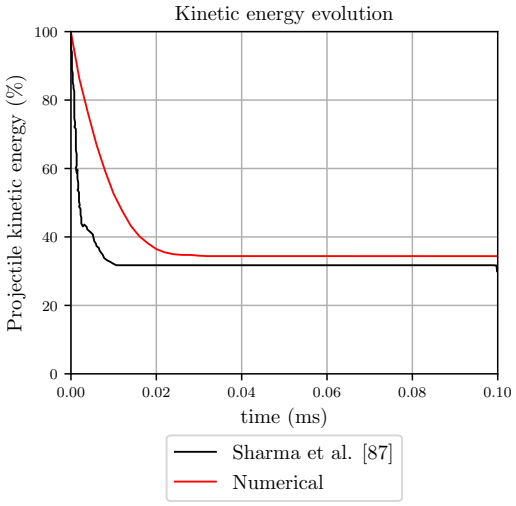


Figure 5.5: Evolution of the projectile's kinetic energy

5.3 High velocity impact - Hybrid laminate plate

Once the modelling strategy and the *Hashin 3D* criterion with the influence of strain rate for unidirectional composites and the JH-2 criterion for ceramic materials have been validated, it is possible to safely move on to the creation of models with hybrid laminates.

In this context, two different models have been created. The first (Model 1) aims to use the previous L1 composite laminate together with an additional layer of silicon carbide of the same thickness. In this way, a laminate with the same thickness as L2 was obtained, but with a hybrid composition. Remember that L2 resulted from the duplication of L1. By simulating this new hybrid laminate at the same impact velocity/energy as L2, it is possible to determine the impact of the ceramic layer. The second model (Model 2) aims to compare the performance of a unidirectional composite laminate versus a woven composite laminate. To this end, the work carried out by Goda *et al.* [82] was used as basis. The authors study the performance of a hybrid laminate composed of a front layer of alumina followed by layers of woven composite. This work intends to replace the woven plies by unidirectional ones and investigate the impact, specially on the residual velocity/absorbed energy.

5.3.1 Hybrid laminate - Model-1

With regard to the first study, the modelling is very similar to that described for the L1 composite, with the addition of a 2 mm front layer of ceramic material. The properties of the composite and ceramic materials are shown in Tables 5.1 and 5.6, respectively. As far as the mesh is concerned, some changes were made, essentially associated with the generation of a more refined mesh throughout the plate.

In the centre of the plate, the refinement made it possible to eliminate the presence of distorted elements and reduce the artificial energies. Note that the presence of different materials in the plate makes it even more heterogeneous. This makes the shock wave dispersion phenomenon even more complex, and in this case led to the occurrence of distorted elements. A better understanding of this phenomenon can be found in the work carried out by Žmindák *et al.* [98]. Regarding artificial energies, they are purely numerical and are used by the finite element software to prevent the hourglass effect. In the more distant region, the refinement made it possible to reduce the effects of the boundary conditions. Translating this into figures, the central region has square elements measuring 0.3 mm, while the outermost edges have been given a size of 3 mm. As far as thickness is concerned, no changes were made in the composite laminate region, so one element per layer was used. For the ceramic region, 10 elements were used, i.e. with a size of 0.2 mm.

With regard to the type of element and its configurations, the same settings described for the previous models have been maintained. The final mesh has 515034 elements of type C3D8R.

The projectile is not subject to any modifications. Its interaction with the plate remains the same, as it was used in both the 5.1 and 5.2 sections. The same applies to the boundary conditions: the plate is completely fixed at the edges and the projectile is only allowed to move in the direction of impact. Figure 5.6 shows the final mesh and assembly.

For S_{mt} and S_{mc}, the optimum values of the L1 laminate were maintained, i.e. 0.55 and 0.35 respectively.

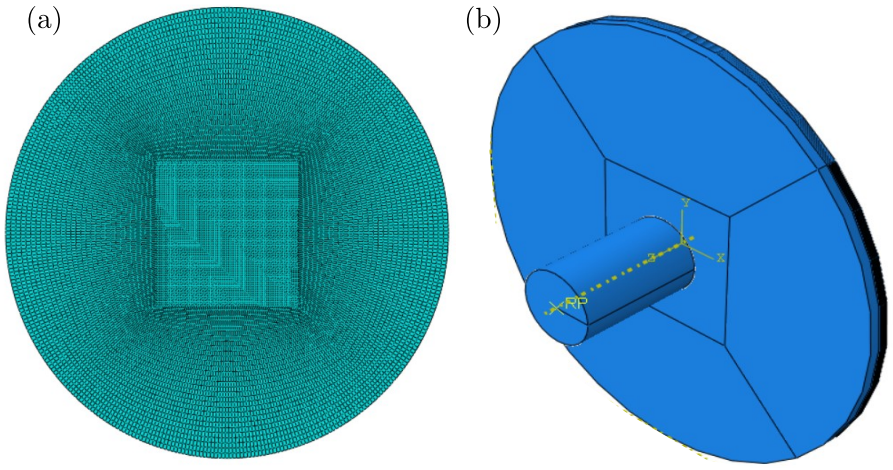


Figure 5.6: Model-1: (a) - final mesh; (b) - final assembly

5.3.2 Hybrid laminate - Model-2

The second model is composed of a rectangular plate with 100 mm per 150 mm and 14.8 mm thickness. The ceramic layer, in this case alumina with 99.5 % purity, is 10 mm thick. The remaining 4.8 mm is made up of 16 layers of CFRP (0.3 mm per ply). In reference [82], the woven layers have the following configuration $[+45/-45/0/90/+45/-45/0/90]_s$. In this work, this stacking sequence is maintained, but with unidirectional layers. The properties of the CFRP and alumina are listed in Table 5.1 and 5.7, respectively.

This plate is impacted by a cylindrical projectile with a diameter of 16.5 mm, a height of 32 mm and a mass of 11 g. It is assigned two different initial velocities, 400 m/s and 600 m/s, which translate into an impact energy of 880 J and 1980 J, respectively.

With regard to the plate mesh, as with the previous models, the impact zone has a more refined discretisation. For this purpose, two square partitions were created, one 20 mm wide and the other 60 mm. The second region is used to create a smooth transition between the smaller elements and the further region of the impact. Elements measuring 1.25 mm were used in the impact region, as the elements move away from this location they increase to a maximum size of 4 mm. In the thickness direction, one element is used for each layer of CFRP (0.3 mm). In the ceramic region the elements have a size of 1.25 mm, however, as one gets closer to the CFRP the size is reduced to 0.3 mm in order to smooth the transition between materials. Reduced integration hexahedral elements were also used, with second order accuracy, distortion control and hourglass control of the stiffness type. The final mesh has 282505 C3D8R elements.

As in all previous cases, the projectile is assumed to be rigid. Its modelling involves the use of an analytical surface and therefore does not require the generation of a mesh.

The interaction between the plate and the projectile uses "hard contact" for normal contact. For tangential contact, the "penalty" type is used, with a friction coefficient of 0.28, presented by Goda *et al.* [82].

Finally, it remains to present the boundary conditions. The plate has its outer edges completely fixed and the projectile only has translational movement in the direction of impact. Figure 5.7 shows the mesh generated and the final set.

As the composite region of Model-2 presents a thickness close to L2 laminate and its stacking sequance is simmilar, S_{mt} and S_{mc} were equaled to 0.30 and 0.30 respectively (optimum L2 values).

Table 5.7: Alumina 99.5 % purity properties [82], [99]

Property	Unit	Value	Property	Unit	Value
ρ	ton/m^3	3.80	HEL	Gpa	5.90
G	GPa	135	P_{Hel}	GPa	2.20
A	-	0.99	β	-	1
B	-	0.77	D_1	-	0.01
C	-	0	D_2	-	1.00
n	-	0.38	ε_{fmax}	-	2.00
m	-	1	ε_{fmin}	-	0
$\dot{\varepsilon}_0$	-	1	K_1	GPa	200
T	MPa	275	K_2	GPa	0
σ_{Imax}	GPa	∞	K_3	GPa	0
σ_{fmax}	GPa	0.50	F_s	-	0.20

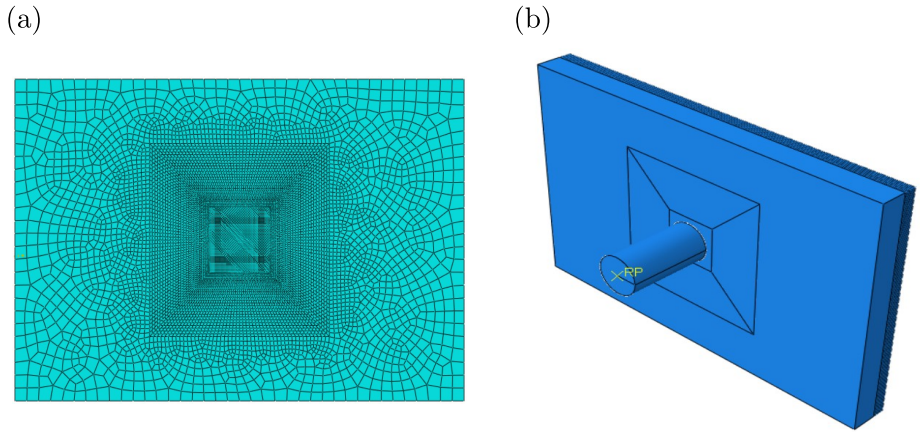


Figure 5.7: Model-2: (a) - final mesh; (b) - final assembly

5.3.3 High velocity impact on hybrid laminate - Results

After creating the various models, simulations were carried out. The 3D Hashin criterion with strain rate effect (H3D+SRD) was used for composite materials and the Jonhson-Holquimist criterion for ceramic materials.

Table 5.8 lists the results obtained for Model-1 and compares them with the results obtained in section 5.3 for L2. It is therefore noticeable that using 2 mm of carbon silicon instead of repeating the composite sequence reduces the residual velocity by around 38 %, from 57.7 m/s to 38.6 m/s. These values can also be evaluated from the point of view of absorbed energy. Of the 124.2 J initially supplied to the projectile, around 74.8 J is absorbed by the laminate made entirely of unidirectional CFRP. The hybridisation of the laminate shows an absorbed energy of 101.9 J, thus showing an increase of around 22 percentage points (the result of lower residual velocity).

Figure 5.8 shows the evolution of the velocity and energy absorbed, in addition to the data mentioned and analysed above. Note that in the initial phase of the impact, the hybrid laminate shows a much greater reduction in projectile velocity and, consequently, greater energy absorption, due to the characteristics of the ceramic material. For instance, at a time equal to 0.05 m/s the hybrid laminate has absorbed around 80 J, whereas the L2 laminate only absorbed around 45 J. After the failure, about 0.05 ms after the start of the impact, there is a smoother evolution of both parameters, since it is the composite material that predominantly sustains the impact loads.

It is also possible to observe a longer impact time for the hybrid laminate. In this case, both the projectile velocity and the energy absorbed by the plate stabilise at around 0.15 m/s. The laminate composed entirely of CFRP, on the other hand, stabilises at 0.11 m/s.

From the previously mentioned analysis, it is clear that hybridising the structure by adding a ceramic layer is advantageous from the point of view of energy absorption performance. However, it must be borne in mind that the density of this material is higher than that of composite materials. In this particular case, the density of silicon carbide is about 2.1 times greater than the CFRP used, a crucial aspect when it comes to developing aircraft structures. However, when compared to metallic materials, it presents attractive characteristics. Recall the practical case presented in section 2.3 where the aircraft used a ballistic protection structure made of titanium, that presents a density about 1.4 times greater than silicon carbide.

Table 5.8: Model-1 results

Laminate	L2	SiC + L1
V_S **(m/s)**	91	
Impact energy (J)	124.2	
V_r **(m/s)**	57.7	38.6
Absorbed energy (J)	74.8 [60.2 %]	101.9 [82 %]

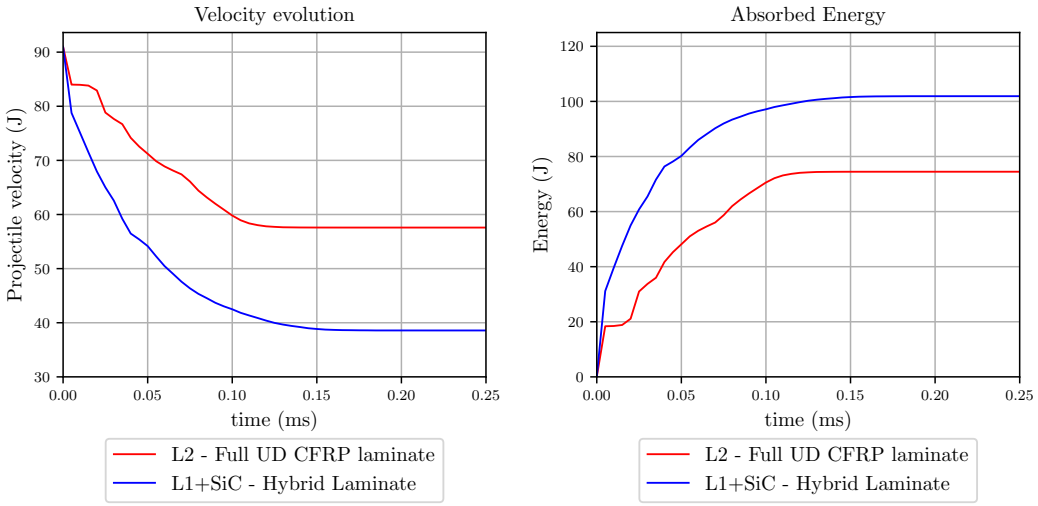


Figure 5.8: Model-1 results comparison

Moving on to Model-2, a comparison of the results can be found in Tables 5.9 and 5.10, for the 400 and 600 m/s impacts, respectively.

For an impact of 400 m/s, the plate simulated by Goda *et al.* [82] is able to absorb all the energy of the impact, since the projectile reduces its speed to 0 m/s, and even rebounds with a velocity of 2.3 m/s. On the other hand, the plate developed in this work, which has unidirectional CFRP layers, is unable to absorb all the impact energy. A residual velocity of 94.6 m/s is obtained, which means that 94.4 % of the energy is absorbed.

With regard to the 600 m/s impact, the laminate provided by reference [82] is no longer able to prevent total penetration of the projectile, so it exits with a residual velocity of 104.5 m/s. Even so, it is able to absorb almost all of the impact energy, around 97 %. As in the previous case, the laminate studied in this paper has a higher residual velocity, around 225.9 m/s, and as such a lower absorbed energy, only 86 %.

Table 5.9: Model 2 results - 400 m/s impact

Laminate	Alumina (10mm) + CFRP Woven (4.8 mm) [82]	Alumina (10mm) + CFRP UD (4.8 mm)
V_s **(m/s)**	400	
Impact energy (J)	880	
V_r **(m/s)**	0 [−2.3]	94.6
Absorbed energy (J)	880 [100 %]	830.8 [94.4 %]

Table 5.10: Model 2 results - 600 m/s impact

Laminate	Alumina (10mm) + CFRP Woven (4.8 mm) [82]	Alumina (10mm) + CFRP UD (4.8 mm)
V_s **(m/s)**	600	
Impact energy (J)	1980	
V_r **(m/s)**	104.5	225.9
Absorbed energy (J)	1919.9 [97 %]	1699.3 [86 %]

Figure 5.9 shows the evolution of velocity and absorbed energy over the course of the impact for the different impact velocities, regarding the laminate developed in this work. It would be useful to make a comparison between that data that obtained by Goda *et al.* [82], but this reference does not include such information.

As in Model-1, a very abrupt drop in velocity is visible for the two simulated impact velocities. This is due to the presence of the 10 mm alumina front layer. In order to better understand this evolution, a qualitative comparison is made between the data from this study and the analyses carried out in the reference used.

According to Goda *et al.* [82], as soon as the projectile hits the plate, the ceramic material opposes its movement. The initial damage to the alumina is conical, but the projectile does not penetrate it. At the front of the alumina, the damage occurs due to high compressive stresses, while at the alumina-CFRP interface, the damage to the ceramic material occurs due to tensile stresses. These two types of damage propagate leading to total failure of the ceramic material, allowing the projectile to advance along the thickness of the laminate. The remaining kinetic energy is then absorbed by the composite material. This begins to deflect until its constituents, the matrix and fibres, fracture. For the 400 m/s impact, these mechanisms were sufficient to dissipate the impact energy, but for 600 m/s this was not the case and the projectile exited with a residual velocity. It should be noted that for both impact speeds the damage to the composite material began without the projectile penetrating it.

The previous description is verified in this work, even though unidirectional, non-woven CFRP layers were used. Figure 5.10 (a) shows the initial moment when the projectile hits the ceramic plate, essentially placing it under compression. Moving on to Figure 5.10 (b), the conical damage propagation in the alumina is evident (yellow lines). In addition, tensile stresses at the interface begin to cause damage, until in Figure 5.10 (c) there is complete damage to the ceramic material and deflection of the CFRP layers begins. In Figure 5.10 (d), damage to the composite material is also evident. The failure of the matrix and fibre leads to the release of small fragments, also reported by Goda *et al.* [82]. Furthermore, it is noticeable between Figure 5.10 (b) and (d) that in addition to the damage propagating in the direction of the thickness of the laminate, it also propagates in its length and width, as the damage cone becomes successively more open.

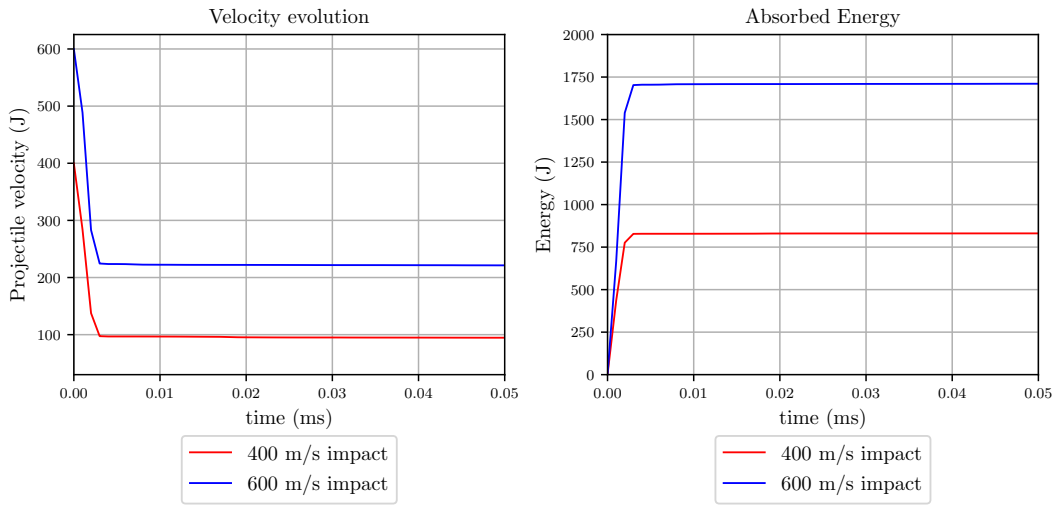


Figure 5.9: Model-2 results comparison

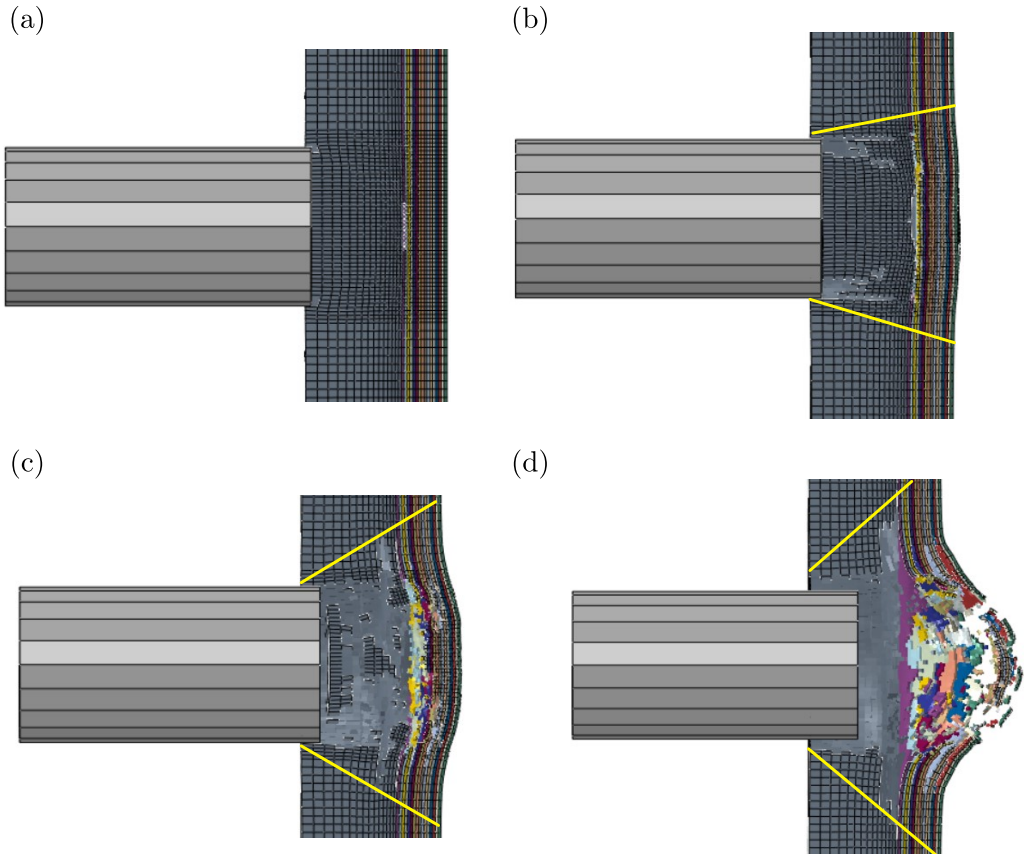


Figure 5.10: Model-2: Damage evolution for 600 m/s impact (sectional view)

5.4 High velocity impact - Woven composite

In this last section, the performance of the 3D Hashin criterion with and without the influence of the strain rate will be evaluated for ballistic impacts on woven composite plates. To this end, the experimental work of Muhi *et al.* [100] was used.

The simulated experiment consists of a square plate with 80 mm sides and 1.8 mm thickness, made up of 4 layers of GFRP whose properties are shown in the following Table 5.11. Note that the plate is fixed by a set of circular supports with a diameter of 50 mm, so only this circular region was modelled. The projectile has a cylindrical shape with a diameter of 7.85 mm, a height of 25 mm and a mass of 7.45 g. It is assigned an initial/impact velocity of 176 m/s, resulting in an initial kinetic energy of 115.4 J.

As with the models built previously, a central region was created for mesh refinement, in this case a 16 mm square partition. Elements with a size of 0.2 mm were used in this area, while elements with an overall size of 2 mm were used in the more distant regions. With regard to thickness, one element per layer was used, i.e., 0.45 mm. The element type chosen remained the same, C3D8R, along with second-order accuracy, distortion control and hourglass control of the stiffness type. These configurations resulted in a final mesh with 43520 elements (see Figure 5.11 (a)).

As for the projectile, its deformations were discarded so it was modelled with an analytical surface.

Some changes were necessary for the interaction between the projectile and the plate. The first approach used "hard contact" for normal contact and disregarded friction for tangential interaction. However, as soon as the projectile hit the plate, the simulation aborted due to the presence of distorted elements, that were simultaneously, in the frontal layer of the plate and in contact with the projectile. In this particular case, it was due to the low stiffness of the woven composite. The solution found was to soften the initial impact by using exponential contact in the normal direction and limiting the contact stiffness. The parameter calibration process was trial and error, resulting in a clearance of $1E-5$ mm, a pressure of $1E-6$ MPa and a maximum contact stiffness of $10E3$ MPa. The final assembly is illustrated in Figure 5.11 (b).

Finally, some changes were made to the 3D Hashin criterion and the effect of the strain rate. With regard to the 3D Hashin criterion, it was necessary to define the values for S_{mt} and S_{mc}. These were studied in greater detail for unidirectional composites, but for woven structures there was no reference value. The first option was to use the optimum values of the L1 laminate (section 5.1), given the proximity of both in terms of thickness. However, this set of values did not allow the simulation to run to its end. It was terminated due to the presence of distorted elements in the damaged region and where elements had to be eliminated. After successive variations of these parameters, it was realised that using S_{mt} and S_{mc} equal to 1, the simulation ran without errors.

Table 5.11: GFRP properties (E glass) [100], [101]

General properties			**Damage initiation properties**			**Damage evolution properties**		
Property	Unit	Value	Property	Unit	Value	Property	Unit	Value
$E_{11} = E_{22}$	GPa	23.10	X_T	MPa	442	G^c_{ft}	N/mm	65
E_{33}	GPa	6.87	X_C	MPa	337	G^c_{fc}	N/mm	65
G_{12}	GPa	4.0	Y_T	MPa	442	G^c_{mt}	N/mm	65
$G_{23} = G_{13}$	GPa	1.80	Y_C	MPa	337	G^c_{mc}	N/mm	65
ν_{12}	-	0.15	S_{12}=S_{13}	MPa	75			
$\nu_{23} = \nu_{31}$	-	0.25	S_{23}	MPa	58			
ρ	ton/m^3	2.10						

With regard to the effect of the strain rate, note that in unidirectional composites, E_1 was not affected by the strain rate, as it was assumed that this was essentially characterised by the fibre. Continuing with this line of thinking, and taking into account that in woven laminates there are also fibres in the transverse direction, hence E_1 is equal to E_2, it was decided that the latter would not be affected by the strain rate either. With regard to tensile and compressive strength, different scaling factors were used in both the 1 direction (X_T and X_C) and the 2 direction (Y_T and Y_C), since in unidirectional composites, a response dominated by the fibre in the 1 direction and by the matrix in the 2 direction was considered. In light of the above, it was decided to equalise the scaling factors in tensile in the 1 and 2 directions, and to do the same in compression. Table 5.12 summarises the changes made in the transition from unidirectional to woven composite.

Table 5.12: Maximum scale factor values - woven composite [78]

Property	E_{33}	X_C	X_T	Y_C	Y_T	$G_{mc,c}$	$G_{mt,c}$
SF_{max}	1.29	1.39	1.38	1.39	1.38	1.63	1.23

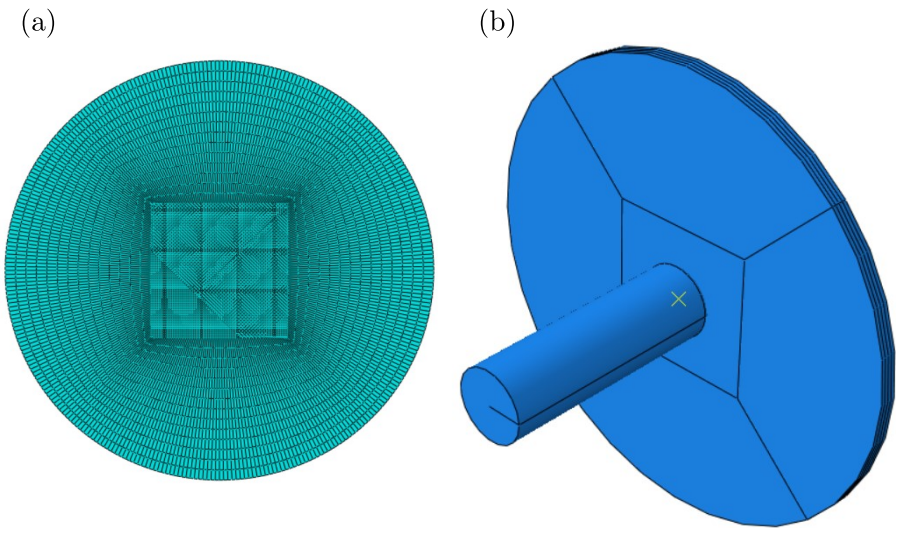


Figure 5.11: Woven laminate: (a) - final mesh; (b) - final assembly

5.4.1 High velocity impact on woven composite - Results

After performing the simulations, the data obtained was compared with the experimental results of [100]. As in most of the works available in the literature, only the residual velocities are used for analysis purposes. Table 5.13 shows the results and the comparative analysis.

Since the plate is relatively thin, it was expected that its performance would be low in a high-speed impact. This is verified by both the experimental data from Muhi *et al.* and the numerical data from the present work. The latter, with and without the effect of the strain rate, returns higher residual velocity values than the experimental ones. As seen for the unidirectional laminate in section 5.1.1, the effect of the strain rate, scaling the material properties, tends to reduce the residual velocity values. In this case, this effect is closer, albeit slightly, by about 0.6 percentage points.

The simulations, with and without the strain rate effect, yielded residual velocity values differing by less than 5 % from the experimental results. This indicates that the outcomes are satisfactory, suggesting that the decisions made in adapting the criteria for woven composites are valid. It should also be noted that no layers of cohesive elements were inserted to introduce the effect of delamination/inter-laminar damage.

Finally, a "visual" comparison is made between the experimental and numerical impact dynamics. Muhi *et al.* [100] state that the projectile penetration caused a hole in the plate with the same diameter as the projectile itself. As a result a circular plug (also with the same diameter as the projectile) was pulled out of the plate. This description is also verified by experimental data and is illustrated in the following Figure 5.12. This indicates that in addition to the final result of the projectile's velocity being acceptable, the models are able to describe the dynamics of the impact to some extent.

Table 5.13: Woven composite laminate results comparison

	Experimental results [100]	**Numerical results**	
		H3D	**H3D+SRD**
V_s (m/s)		176	
Impact energy (J)		115.4	
V_r (m/s)	161	167 [3.7 %]	166 [3.1 %]

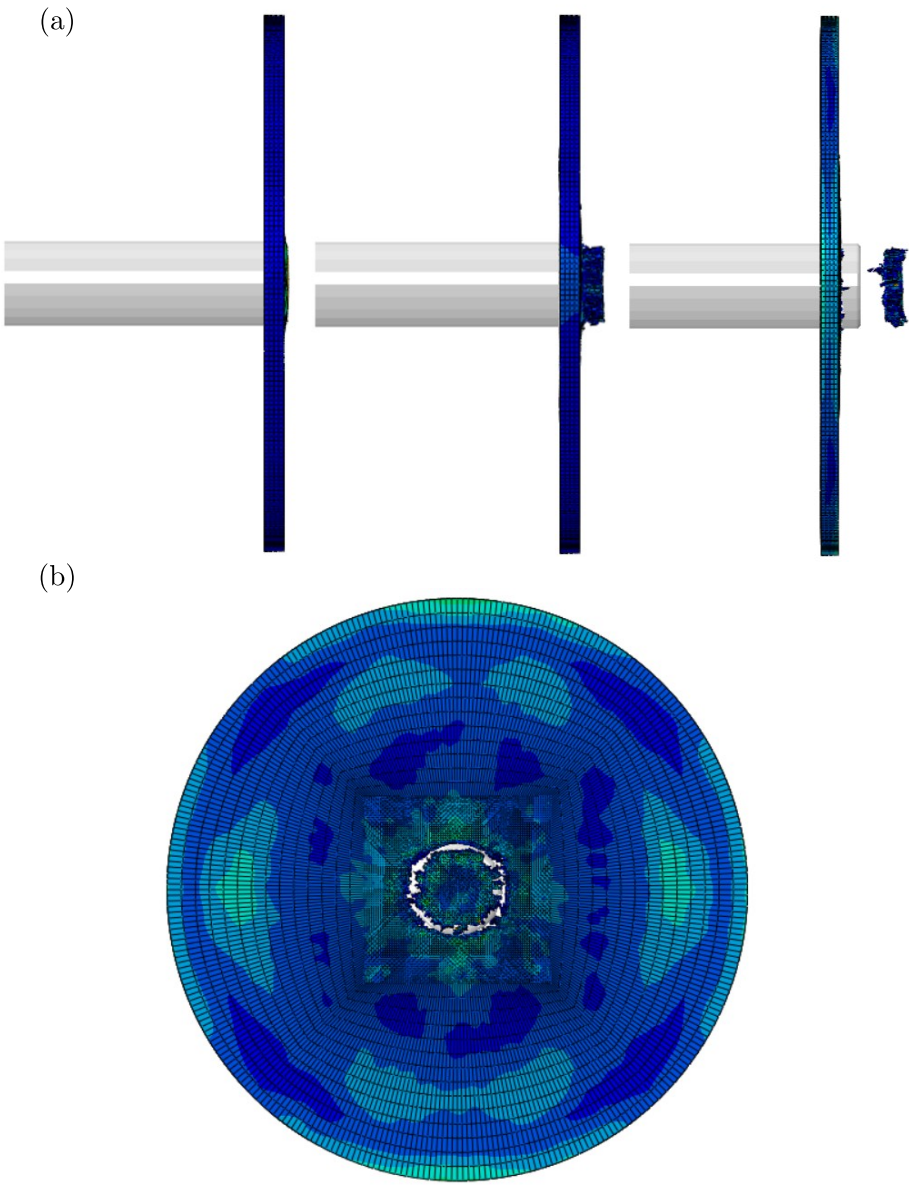


Figure 5.12: Woven laminate: (a) - impact evolution (side view); (b) - penetration hole (back view)

Chapter 6

Conclusions

Considering the investigation of material models for low-velocity impact, the analysis was further divided into 2D and 3D approaches. For the 2D approaches, the 2D Hashin criterion and the Modified Ladeveze criterion were used. The results obtained indicate a similarity between the 2D Hashin criterion with continuous shell elements (SC8R) and the Modified Ladeveze criterion with shell elements with reduced integration (S4R). Both adequately describe the evolution of the reaction force curves throughout the impact, when compared with experimental data. On the other hand, the transferred energy curve obtained with these models deviates slightly from the experimental one. This is because the actual plate mounting conditions are not replicated in this work, and delaminations are not taken into account. Since fibre and matrix breakage in a low-velocity impact is not very common, the energy dissipated by delaminations is important in the final value of the energy absorbed by the plate. Finally, in the 2D models, the results obtained with the model using the 2D Hashin criterion and shell elements (S4) proved to be far from experimental. It tended to have higher impact times and lower reaction forces than the experimental data for all the simulated laminates.

Moving on to the 3D approach, the influence of the shear loss coefficients on the performance of the 3D Hashin criterion is particularly noteworthy. The sensitivity analysis carried out indicates that, in low velocity impacts, changing the laminate stacking sequence or increasing the impact energy implies adjusting these parameters. They were calibrated essentially by comparing the evolution of the reaction forces obtained with the experimental ones. From this study it was concluded that higher values of S_{mt} and S_{mc} imply lower reaction forces, longer impact times and greater energy absorbed by the plate, while lower

values of S_{mt} and S_{mc} produce the opposite effect. The introduction of the strain rate effect did not require a further adjustment of the shear loss coefficients.

Comparing the best results of the 2D models and the results of the 3D models (with and without the effect of the strain rate), a similar response is observed between them. However, it is clear that the 3D models tend to exhibit higher absorbed energy values than the 2D models, albeit far from the experimental ones. The final analysis of the 3D model aimed to resolve this issue by introducing cohesive elements to simulate inter-laminar damage. Nonetheless, the fact that the correct properties of the elements were unknown meant that this attempt did not return correct results. Still, it was possible to obtain delaminated areas similar to those observed experimentally. On the other hand, the reduced size of the cohesive elements, particularly in the thickness direction, led to a significant increase in simulation times.

In summary, both the 2D and 3D approaches produced results that correctly describe the low-velocity impact in terms of the evolution of the reaction forces. The evolution of the transferred energy shows a good correlation rergarding the maximum value, but in the final phase there is a deviation of the numerical results from the experimental ones.

Once the analyses of low-velocity impacts were complete, the next step was ballistic impacts. The first simulations were essential to understand whether the performance of the three-dimensional models with the 3D Hashin criterion and the method that incorporates the influence of the strain rate were suitable for this type of impact.

The results obtained for high-velocity impacts on unidirectional composite laminates are in agreement with experimental data from the literature, presenting errors always lower 3.5 %, even without taking into account the effect of delaminations. Once again, it was realised that the quality of the results is affected by the shear loss coefficients, so a new sensitivity analysis was carried out. However, the basis for comparison, in this case, was only the value of the projectile's residual velocity. The study shows that higher values of S_{mt} and S_{mc} return higher residual velocities and therefore lower absorbed energies. The opposite is true if the value of the coefficients decreases. This trend is the opposite of what was seen previously (low-velocity impact). As far as impact energy/velocity is concerned, increasing it did not imply adjusting the parameters again, which was not the case when varying the thickness of the laminate.

The second phase in the study of ballistic impacts involves simulating ceramic materials. The criterion/model implemented has already been extensively studied and validated in the literature, but carrying it out proved essential in order to gain practice with it. The results obtained, when compared to the literature, show some deviation in the initial phase due to some assumptions made, as some parameters were unknown. However, when analysing the final kinetic energy of the projectile, a difference of less than 5 % was obtained between the results of this work and those of the literature.

Thus, the conditions were met for simulating high-velocity impacts on hybrid laminates

containing a ceramic front layer followed by unidirectional composite ones. The first analyses concluded that the hybridisation of the plates is beneficial. Replacing half the thickness of a composite plate with ceramic material revealed an increase of 22 percentage points in absorbed energy. On the other hand, the second analysis aimed to study the impact of replacing the layers of woven laminate with unidirectional laminate. The results indicate that unidirectional laminates perform worse. While for an impact of 400 m/s the hybrid laminate with woven composite is able to absorb all the impact energy, the version with unidirectional composite absorbs around 94.4 %. This trend is maintained if the impact energy is increased, since for a speed of 600 m/s the hybrid laminate with woven composite absorbs around 97 % of the energy, while the plate simulated in this work only absorbs 86 %.

Finally, impact simulations were carried out on woven composite laminates. To do this, modifications had to be made to both the 3D Hashin criterion and to the approach that takes into account the effect of the strain rate. The influence of shear loss coefficients was also recognised in laminates made of woven layers, however, a sensitivity analysis was not carried out. In this case, unitary values were assumed for these coefficients. With regard to the effect of the strain rate, the changes implemented were to ensure a similar response in both the 1 and 2 directions. The results obtained, with and without the effect of the strain rate, reflect a difference of less than 4 % compared to the experimental data in the literature. A visual analysis of the plate during impact also reveals a good correlation with the experimental data.

Based on the conclusions outlined above, it can be determined that this work effectively addresses the problem at hand. It provides a methodology capable of simulating hybrid laminates under high-velocity impacts. In addition, it also offers the potential for further improvements and paves the way for future work in the field, as listed next.

6.1 Future Work

The following points suggest activities to enhance or complement this dissertation:

- Conduct high-velocity impact experiments to obtain projectile velocity and reaction forces evolution, aiming to more accurately calibrate shear loss coefficients for both unidirectional and woven composites.
- Perform experimental tests on hybrid laminates following the outlined approach, with the goal of comparing the developed models to the experimental results.
- Develop and simulate models that incorporate hybrid laminates with woven composite layers, as a continuation of the final part of this work.
- Develop models that use the impact conditions described in standards, such as MIL-STD-662F.

- Incorporate an optimisation model to accelerate shear loss coefficients calibration.

Bibliography

[1] A. T. Institute, "Composite material applications in aerospace," *Composite Materials*, pp. 1–12, 2018.

[2] C. Harris, M. Shuart, and J. Starnes, "Design and manufacturing of aerospace composite structures, state-of-the-art assessment," *Journal of Aircraft - J AIRCRAFT*, vol. 39, pp. 545–560, Jul. 2002. DOI: 10.2514/2.2992.

[3] M. B. Afzal, "Modeling of damage evolution of fiber-reinforced composite structure," in Dec. 2020, ISBN: 978-1-78984-792-5. DOI: 10.5772/intechopen.93323.

[4] K. Biswas, "Military airworthiness and certification procedures: Global scenario," in *Proceedings of the International Conference on Modern Research in Aerospace Engineering*, S. Singh, P. Raj, and S. Tambe, Eds., Singapore: Springer Singapore, 2018, pp. 315–331.

[5] U. S. A. Force. "A-10c thunderbolt ii." (2024), [Online]. Available: https://www.af.mil/About-Us/Fact-Sheets/Display/Article/104490/a-10c-thunderbolt-ii/ (visited on 06/13/2024).

[6] Z. Li, Y. Xue, B. Sun, and B. Gu, "Ballistic penetration damage for hybrid carbon/kevlar/uhmwpe fiber laminated composites: Experimental and numerical techniques," *Composite Structures*, vol. 316, p. 117 037, 2023, ISSN: 0263-8223. DOI: https://doi.org/10.1016/j.compstruct.2023.117037. [Online]. Available: https://www.sciencedirect.com/science/article/pii/S0263822323003811.

[7] L. Peng, M. Tan, X. Zhang, *et al.*, "Investigations of the ballistic response of hybrid composite laminated structures," *Composite Structures*, vol. 282, p. 115 019, 2022, ISSN: 0263-8223. DOI: https://doi.org/10.1016/j.compstruct.2021.115019. [Online]. Available: https://www.sciencedirect.com/science/article/pii/S0263822321014410.

[8] K. Bilisik, M. Syduzzaman, G. Erdogan, and M. Korkmaz, "3 - advances in ballistic protection," in *Functional and Technical Textiles*, ser. The Textile Institute Book Series, S. Maity, K. Singha, and P. Pandit, Eds., Woodhead Publishing, 2023, pp. 71–139, ISBN: 978-0-323-91593-9. DOI: https://doi.org/10.1016/B978-0-323-91593-9.00023-7. [Online]. Available: https://www.sciencedirect.com/science/article/pii/B9780323915939000237.

[9] D. D. Chung, *Composite materials: functional materials for modern technologies*. Springer Science & Business Media, 2003.

[10] T. J. Reinhart, "Overview of composite materials," in *Handbook of Composites*, S. T. Peters, Ed. Boston, MA: Springer US, 1998, pp. 21–33, ISBN: 978-1-4615-6389-1. DOI: 10.1007/978-1-4615-6389-1_2. [Online]. Available: https://doi.org/10.1007/978-1-4615-6389-1_2.

[11] K. K. Chawla and K. K. Chawla, "Strength, fracture, fatigue, and design," *Composite Materials: Science and Engineering*, pp. 229–258, 1987.

[12] V. Šerifi, M. Tarić, D. Jevtić, A. Ristovski, and M. Isović, "Historical development of composite materials," *The Annals of the University of Oradea. Econ. Sci*, pp. 1–8, 2018.

[13] D. Hull and T. W. Clyne, "Preface to second edition," in *An Introduction to Composite Materials* (Cambridge Solid State Science Series), Cambridge Solid State Science Series. Cambridge University Press, 1996, pp. xiv–xvi.

[14] S. Bavan and G. Mohan Kumar, "Finite element analysis of a natural fiber (maize) composite beam," *Journal of Engineering*, vol. 2013, Jan. 2013. DOI: 10.1155/2013/450381.

[15] F. Campbell, "Chapter 3 - thermoset resins: The glue that holds the strings together," in *Manufacturing Processes for Advanced Composites*, F. Campbell, Ed., Amsterdam: Elsevier Science, 2004, pp. 63–101, ISBN: 978-1-85617-415-2. DOI: https://doi.org/10.1016/B978-185617415-2/50004-6. [Online]. Available: https://www.sciencedirect.com/science/article/pii/B9781856174152500046.

[16] F. de Oliveira Braga, F. S. da Luz, S. N. Monteiro, and É. P. Lima Jr., "Effect of the impact geometry in the ballistic trauma absorption of a ceramic multilayered armor system," *Journal of Materials Research and Technology*, vol. 7, no. 4, pp. 554–560, 2018, ISSN: 2238-7854. DOI: https://doi.org/10.1016/j.jmrt.2018.06.019. [Online]. Available: https://www.sciencedirect.com/science/article/pii/S2238785418302060.

[17] M. I. of Technology. "Explained: Cement vs. concrete — their differences, and opportunities for sustainability." (2020), [Online]. Available: https://news.mit.edu/2020/explained-cement-vs-concrete-understanding-differences-and-sustainability-opportunities-0403 (visited on 04/01/2024).

[18] S. Kabir, C. A. Shahed, M. S. H. Ador, I. A. Choudhury, and F. Ahmad, "Review of the developments in composite materials over the last 15 years," in *Reference Module in Materials Science and Materials Engineering*, Elsevier, 2023, ISBN: 978-0-12-803581-8. DOI: https://doi.org/10.1016/B978-0-323-96020-

5.00044-3. [Online]. Available: https://www.sciencedirect.com/science/article/pii/B9780323960205000443.

[19] M. Toozandehjani, N. Kamarudin, Z. Dashtizadeh, E. Y. Lim, A. Gomes, and C. Gomes, "Conventional and advanced composites in aerospace industry: Technologies revisited," *Am. J. Aerosp. Eng*, vol. 5, no. 9, pp. 9–15, 2018.

[20] K. K. Chawla, "Carbon fiber/carbon matrix composites," in *Composite Materials: Science and Engineering*. Cham: Springer International Publishing, 2019, pp. 297–311, ISBN: 978-3-030-28983-6. DOI: 10.1007/978-3-030-28983-6_8. [Online]. Available: https://doi.org/10.1007/978-3-030-28983-6_8.

[21] P. D. Pastuszak and A. Muc, "Application of composite materials in modern constructions," *Key Engineering Materials*, vol. 542, pp. 119–129, Feb. 2013. DOI: 10.4028/www.scientific.net/KEM.542.119.

[22] R. M. Jones, *Mechanics Of Composite Materials*. Taylor & Francis, Inc., 1999.

[23] L. F. Vosteen and R. N. Hadcock, "Composite chronicles: A study of the lessons learned in the development, production, and service of composite structures," NASA, Tech. Rep., 1994.

[24] Embraer. "Defesa & segurança - c-390 millennium." (2024), [Online]. Available: https://defense.embraer.com/pt/air/c-390/ (visited on 06/21/2024).

[25] Aernnova. "Embraer programs." (2024), [Online]. Available: https://www.aernnova.com/en/programs-and-products/embraer-programs/ (visited on 06/21/2024).

[26] Z. Hasan, *Tooling for composite aerospace structures: Manufacturing and applications*. Butterworth-Heinemann, 2020.

[27] S. Rana and R. Fangueiro, "1 - advanced composites in aerospace engineering," in *Advanced Composite Materials for Aerospace Engineering*, S. Rana and R. Fangueiro, Eds., Woodhead Publishing, 2016, pp. 1–15, ISBN: 978-0-08-100939-0. DOI: https://doi.org/10.1016/B978-0-08-100037-3.00001-8. [Online]. Available: https://www.sciencedirect.com/science/article/pii/B9780081000373000018.

[28] H. E. Etri, M. E. Korkmaz, M. K. Gupta, M. Gunay, and J. Xu, "A state-of-the-art review on mechanical characteristics of different fiber metal laminates for aerospace and structural applications," *The International Journal of Advanced Manufacturing Technology*, vol. 123, no. 9, pp. 2965–2991, 2022.

[29] P. Jakubczak, J. Bieniaś, K. Majerski, M. Ostapiuk, and B. Surowska, "The impact behavior of aluminum hybrid laminates," *Aircraft Engineering and Aerospace Technology: An International Journal*, vol. 86, no. 4, pp. 287–294, 2014.

[30] D. Shim, R. Alderliesten, S. Spearing, and D. Burianek, "Fatigue crack growth prediction in glare hybrid laminates," *Composites Science and Technology*, vol. 63, no. 12, pp. 1759–1767, 2003, ISSN: 0266-3538. DOI: https://doi.org/10.1016/S0266-3538(03)00082-4. [Online]. Available: https://www.sciencedirect.com/science/article/pii/S0266353803000824.

[31] P. R. S. Reddy, T. S. Reddy, K. Mogulanna, I. Srikanth, V. Madhu, and K. V. Rao, "Ballistic impact studies on carbon and e-glass fibre based hybrid composite laminates," *Procedia Engineering*, vol. 173, pp. 293–298, 2017, Plasticity and Impact Mechanics, ISSN: 1877-7058. DOI: https://doi.org/10.1016/j.proeng.2016.12.017. [Online]. Available: https://www.sciencedirect.com/science/article/pii/S1877705816344083.

[32] L. Zijian, Z. Meng, and L. Xiaoxing, "Investigation into innovative fabrication of fiber metal laminated pipe and application," *IOP Conference Series: Materials Science and Engineering*, vol. 784, p. 012 002, Apr. 2020. DOI: 10.1088/1757-899X/784/1/012002.

[33] G. Gratton, *Initial airworthiness: Determining the acceptability of new airborne systems*. Springer, 2018.

[34] L. Purton and K. Kourousis, "Military airworthiness management frameworks: A critical review," *Procedia Engineering*, vol. 80, pp. 545–564, 2014, 3rd International Symposium on Aircraft Airworthiness (ISAA 2013), ISSN: 1877-7058. DOI: https://doi.org/10.1016/j.proeng.2014.09.111. [Online]. Available: https://www.sciencedirect.com/science/article/pii/S1877705814012041.

[35] G. Jilian, B. Kangming, and J. Lintong, "Research on airworthiness management system about military aircraft development," *Procedia Engineering*, vol. 17, pp. 375–381, 2011, The 2nd International Symposium on Aircraft Airworthiness, ISSN: 1877-7058. DOI: https://doi.org/10.1016/j.proeng.2011.10.043. [Online]. Available: https://www.sciencedirect.com/science/article/pii/S1877705811027226.

[36] I. C. A. Organization. "About icao." (2024), [Online]. Available: https://www.icao.int/about-icao/Pages/default.aspx (visited on 05/15/2024).

[37] C. H.-C. QC, "The nimrod review," *An Independent Review into the Broader Issues Surrounding the Loss of the RAF Nimrod MR2 Aircraft XV230 in Afghanistan in 2006*, 2009.

[38] E. D. Agency. "What we do and what it means for you." (2024), [Online]. Available: https://eda.europa.eu/what-we-do/eda-in-short (visited on 05/17/2024).

[39] E. D. Agency. "Military airworthiness authorities (mawa) forum." (2024), [Online]. Available: https://eda.europa.eu/experts/airworthiness/mawa-forum (visited on 05/17/2024).

[40] E. D. Agency. "Approved mawa documents." (2024), [Online]. Available: https://eda.europa.eu/experts/airworthiness/mawa-documents (visited on 05/17/2024).

[41] M. A. A. (FORUM, "Frequently asked questions (faqs)," in European Defence Agency, 2015.

[42] D. of Defense. "Defense standardization - program specifications and standards." (2024), [Online]. Available: https://www.dsp.dla.mil/Specs-Standards/ (visited on 05/17/2024).

[43] *Airworthiness certification criteria*, Accessed: 2024-05-17, Department of Defense, 2008. [Online]. Available: https://quicksearch.dla.mil/qsDocDetails.aspx?ident_number=212162.

[44] *V50 ballistic test for armor*, Accessed: 2024-05-17, Department of Defense, 1997. [Online]. Available: https://quicksearch.dla.mil/qsSearch.aspx.

[45] H. Barhoumi, N. Bhouri, I. Feki, A. Baffoun, M. Hamdaoui, and S. B. Abdessalem, "Review of ballistic protection materials: Properties and performances," *Journal of Reinforced Plastics and Composites*, vol. 42, no. 13-14, pp. 685–699, 2023. DOI: 10.1177/07316844221137920. [Online]. Available: https://doi.org/10.1177/07316844221137920.

[46] Dyneema. "Soft body armor vs. hard body armor." (2024), [Online]. Available: https://www.dyneema.com/sectors/law-enforcement-and-military/soft-body-armor-vs-hard-body-armor (visited on 06/11/2024).

[47] T. Peijs, "1.5 high performance polyethylene fibers," in *Comprehensive Composite Materials II*, P. W. Beaumont and C. H. Zweben, Eds., Oxford: Elsevier, 2018, pp. 86–126, ISBN: 978-0-08-100534-7. DOI: https://doi.org/10.1016/B978-0-12-803581-8.09876-3. [Online]. Available: https://www.sciencedirect.com/science/article/pii/B9780128035818098763.

[48] N. Grumman. "A-10 thunderbolt ii." (2024), [Online]. Available: https://www.northropgrumman.com/what-we-do/air/a10-thunderbolt (visited on 06/14/2024).

[49] U. S. A. Force. "Photos a-10 thunderbolt ii." (2024), [Online]. Available: https://www.af.mil/News/Photos/igphoto/2002863777/ (visited on 06/14/2024).

[50] G. Dynamics. "The a-10 "warthog" and the future of cas." (2024), [Online]. Available: https://greydynamics.com/when-pigs-fly-the-a-10-warthog-and-the-future-of-cas/ (visited on 06/14/2024).

[51] X. Chen, "1 - introduction," in *Advanced Fibrous Composite Materials for Ballistic Protection*, X. Chen, Ed., Woodhead Publishing, 2016, pp. 1–10, ISBN: 978-1-78242-461-1. DOI: https://doi.org/10.1016/B978-1-78242-461-1.00001-7. [Online]. Available: https://www.sciencedirect.com/science/article/pii/B9781782424611000017.

[52] M. Jacobs and J. Van Dingenen, "Ballistic protection mechanisms in personal armour," *Journal of materials science*, vol. 36, no. 13, pp. 3137–3142, 2001. DOI: https://doi.org/10.1023/A:1017922000090.

[53] P. M. Cunniff, "Dimensionless parameters for optimization of textile-based body armor systems," in *Proceedings of the 18th international symposium on ballistics*, Technomic Publishing Co. Inc., vol. 2, 1999, pp. 1303–1310.

[54] D. Dimeski and V. Srebrenkoska, "Advanced prepreg ballistic composites for military helmets," 2014.

[55] Y. Sudhir Sastry, P. R. Budarapu, Y. Krishna, and S. Devaraj, "Studies on ballistic impact of the composite panels," *Theoretical and Applied Fracture Mechanics*, vol. 72, pp. 2–12, 2014, Multiscale Modeling of Material Failure, ISSN: 0167-8442. DOI: https://doi.org/10.1016/j.tafmec.2014.07.010. [Online]. Available: https://www.sciencedirect.com/science/article/pii/S0167844214001141.

[56] N. Naik, P. Shrirao, and B. Reddy, "Ballistic impact behaviour of woven fabric composites: Formulation," *International Journal of Impact Engineering*, vol. 32, no. 9, pp. 1521–1552, 2006, ISSN: 0734-743X. DOI: https://doi.org/10.1016/j.ijimpeng.2005.01.004. [Online]. Available: https://www.sciencedirect.com/science/article/pii/S0734743X05000266.

[57] T. Cwik, L. Iannucci, P. Curtis, and D. Pope, "Design and ballistic performance of hybrid composite laminates," *Applied Composite Materials*, vol. 24, Jun. 2017. DOI: 10.1007/s10443-016-9536-x.

[58] X. Chen, Y. Zhou, and G. Wells, "Numerical and experimental investigations into ballistic performance of hybrid fabric panels," *Composites Part B: Engineering*, vol. 58, pp. 35–42, Mar. 2014. DOI: 10.1016/j.compositesb.2013.10.019.

[59] Martec. "Ballistic protection for aircraft and helicopters." (2024), [Online]. Available: https://www.martec.it/?page_id=618 (visited on 07/04/2024).

[60] Integris. "Aircraft system survivability." (2024), [Online]. Available: https://www.integriscomposites.com/aerospace (visited on 07/04/2024).

[61] A. SAS. "Armor solutions." (2024), [Online]. Available: https://amefo.fr/en/defense-en/aircrafts-en/# (visited on 07/04/2024).

[62] S. Wu and L. Gu, "Introduction to the explicit finite element method for nonlinear transient dynamics," *Introduction to the Explicit Finite Element Method for Nonlinear Transient Dynamics*, Jul. 2012. DOI: 10.1002/9781118382011.

[63] "5 - solving dynamic equations in dye transport," in *Modelling, Simulation and Control of the Dyeing Process*, ser. Woodhead Publishing Series in Textiles, R. Shamey and X. Zhao, Eds., Woodhead Publishing, 2014, pp. 100–113, ISBN: 978-0-85709-133-8. DOI: https://doi.org/10.1533/9780857097583.100. [Online]. Available: https://www.sciencedirect.com/science/article/pii/B9780857091338500050.

[64] V. Tita, *Tutorial abaqus*, Universidade de São Paulo - Escola de Engenharia de São Carlos, São Paulo, 2012.

[65] Ansys. "Implicit and explicit time integration methods — lesson 2." (2024), [Online]. Available: https://innovationspace.ansys.com/courses/courses/time_integration/lessons/implicit-and-explicit-time-integration-methods-lesson-2/ (visited on 07/23/2024).

[66] Ansys. "Discussion of time-step size — lesson 3." (2024), [Online]. Available: https://innovationspace.ansys.com/courses/courses/time_integration/lessons/discussion-of-time-step-size-lesson-3/ (visited on 07/23/2024).

[67] D. Systèmes. "Abaqus version 6.6 documentation." (2024), [Online]. Available: https://classes.engineering.wustl.edu/2009/spring/mase5513/abaqus/docs/v6.6/index.html (visited on 07/01/2024).

[68] F. Paris and K. E. Jackson, "A study of failure criteria of fibrous composite materials," NASA Langley Research Center, Tech. Rep., 2001.

[69] P. P. Camanho, "Failure criteria for fibre-reinforced polymer composites," *Secção de Mecânica Aplicada, Departamento de Engenharia Mecânica e Gestão Industrial, Faculdade de Engenharia da Universidade do Porto*, 2002.

[70] G. F. O. Ferreira, "Estruturas de material compósito sob carregamento de tração e impacto: Avaliação de um modelo de material," M.S. thesis, Universidade de São Paulo Escola de Engenharia de São Carlos, São Carlos, Brasil, Sep. 2014.

[71] Z. Hashin and A. Rotem, "A fatigue failure criterion for fiber reinforced materials," *Journal of composite materials*, vol. 7, no. 4, pp. 448–464, 1973.

[72] Z. Hashin, "Fatigue failure criteria for unidirectional fiber composites," *J. appl. Mech*, vol. 47, no. 4, pp. 329–334, 1980.

[73] A. Forghani, M. Shahbazi, N. Zobeiry, A. Poursartip, and R. Vaziri, "6 - an overview of continuum damage models used to simulate intralaminar failure mechanisms in advanced composite materials," in *Numerical Modelling of Failure in Advanced Composite Materials*, ser. Woodhead Publishing Series in Composites Science and

Engineering, P. P. Camanho and S. R. Hallett, Eds., Woodhead Publishing, 2015, pp. 151–173, ISBN: 978-0-08-100332-9. DOI: https://doi.org/10.1016/B978-0-08-100332-9.00006-2. [Online]. Available: https://www.sciencedirect.com/science/article/pii/B9780081003329000062.

[74] I. Lapczyk and J. A. Hurtado, "Progressive damage modeling in fiber-reinforced materials," *Composites Part A: Applied Science and Manufacturing*, vol. 38, no. 11, pp. 2333–2341, 2007, CompTest 2006, ISSN: 1359-835X. DOI: https://doi.org/10.1016/j.compositesa.2007.01.017. [Online]. Available: https://www.sciencedirect.com/science/article/pii/S1359835X07000218.

[75] G. F. O. Ferreira, M. L. Ribeiro, A. J. Mendes Ferreira, and V. Tita, "Computational analyses of composite plates under low-velocity impact loading," *Materials Today: Proceedings*, vol. 8, pp. 778–788, 2019, 4th Brazilian Conference on Composite Materials (BCCM 4), July 22-25th 2018, ISSN: 2214-7853. DOI: https://doi.org/10.1016/j.matpr.2019.02.020. [Online]. Available: https://www.sciencedirect.com/science/article/pii/S2214785319300550.

[76] M. L. Ribeiro, D. Vandepitte, and V. Tita, "Damage model and progressive failure analyses for filament wound composite laminates," *Applied Composite Materials*, vol. 20, pp. 975–992, 2013.

[77] P. Ladeveze and E. LeDantec, "Damage modelling of the elementary ply for laminated composites," *Composites science and technology*, vol. 43, no. 3, pp. 257–267, 1992.

[78] S. Millen, A. Murphy, G. Catalanotti, and G. Abdelal, "Correction to: Coupled thermal mechanical progressive damage model with strain and heating rate effects for lightning strike damage assessment," *Applied Composite Materials*, vol. 27, pp. 1–1, Dec. 2020. DOI: 10.1007/s10443-020-09841-3.

[79] P. P. Camanho and C. G. Dávila, "Mixed-mode decohesion finite elements for the simulation of delamination in composite materials," Tech. Rep., 2002.

[80] M. Bäker, S. Reese, and V. V. Silberschmidt, "Simulation of crack propagation under mixed-mode loading," in *Handbook of Mechanics of Materials*, S. Schmauder, C.-S. Chen, K. K. Chawla, N. Chawla, W. Chen, and Y. Kagawa, Eds. Singapore: Springer Singapore, 2019, pp. 1465–1502, ISBN: 978-981-10-6884-3. DOI: 10.1007/978-981-10-6884-3_29. [Online]. Available: https://doi.org/10.1007/978-981-10-6884-3_29.

[81] G. R. Johnson and T. J. Holmquist, "An improved computational constitutive model for brittle materials," in *AIP conference proceedings*, American Institute of Physics, vol. 309, 1994, pp. 981–984.

[82] I. Goda and J. Girardot, "Numerical modeling and analysis of the ballistic impact response of ceramic/composite targets and the influence of cohesive material parameters," *International Journal of Damage Mechanics*, vol. 30, no. 7, pp. 1079–1122, 2021. DOI: 10.1177/1056789521992107. eprint: https://doi.org/10.1177/1056789521992107. [Online]. Available: https://doi.org/10.1177/1056789521992107.

[83] Y. Cheng, C. Song, Y. Tan, *et al.*, "Theoretical calculation method for the hugoniot elastic limit of hard rock based on ideal elastoplastic model," *Shock and Vibration*, vol. 2021, no. 1, p. 6 677 077, 2021.

[84] D. Systèmes. "Abaqus." (2024), [Online]. Available: https://www.3ds.com/products/simulia/abaqus (visited on 07/01/2024).

[85] M. R. D. Miranda, "Assessment of composite fuselage crashworthiness: A virtual testing methodology," M.S. thesis, Developed in the framework of a research stay at the Aeronautical, Structural Design Lab (ASD Lab) of the UC3M aerospace engineering department, and submitted to Universidade do Porto, Faculdade de Engenharia, Porto, Portugal, Jun. 2023.

[86] V. Tita, J. de Carvalho, and D. Vandepitte, "Failure analysis of low velocity impact on thin composite laminates: Experimental and numerical approaches," *Composite Structures*, vol. 83, no. 4, pp. 413–428, 2008, ISSN: 0263-8223. DOI: https://doi.org/10.1016/j.compstruct.2007.06.003. [Online]. Available: https://www.sciencedirect.com/science/article/pii/S0263822307001717.

[87] W. L. dos Santos Pinto, "Simulação de ensaio de compressão radial em compósito fabricado via filament widing: Avaliação do efeito de concentradores de tensão," pp. 1–23, 2023.

[88] J. R. Shao, N. Liu, and Z. J. Zheng, "A modified progressive damage model for simulating low-velocity impact of composite laminates," *Advances in Mechanical Engineering*, vol. 14, no. 5, p. 16 878 132 221 095 948, 2022. DOI: 10.1177/16878132221095948. eprint: https://doi.org/10.1177/16878132221095948. [Online]. Available: https://doi.org/10.1177/16878132221095948.

[89] P. Liu, B. Liao, L. Jia, and X. Peng, "Finite element analysis of dynamic progressive failure of carbon fiber composite laminates under low velocity impact," *Composite Structures*, vol. 149, pp. 408–422, 2016, ISSN: 0263-8223. DOI: https://doi.org/10.1016/j.compstruct.2016.04.012. [Online]. Available: https://www.sciencedirect.com/science/article/pii/S0263822316302513.

[90] J. Pederson, "Finite element analysis of carbon fiber composite ripping using abaqus," M.S. thesis, Clemson University, 2008.

[91] J. Zhou, P. Wen, and S. Wang, "Finite element analysis of a modified progressive damage model for composite laminates under low-velocity impact," *Composite Structures*, vol. 225, p. 111 113, 2019, ISSN: 0263-8223. DOI: https://doi.org/10.1016/j.compstruct.2019.111113. [Online]. Available: https://www.sciencedirect.com/science/article/pii/S0263822319303976.

[92] G. Guo, S. Alam, and L. D. Peel, "Numerical analysis of ballistic impact performance of two ceramic-based armor structures," *Composites Part C: Open Access*, vol. 3, p. 100 061, 2020, ISSN: 2666-6820. DOI: https://doi.org/10.1016/j.jcomc.2020.100061. [Online]. Available: https://www.sciencedirect.com/science/article/pii/S266668202030061X.

[93] A. Ramadhan, A. Abu Talib, A. Mohd Rafie, and R. Zahari, "High velocity impact response of kevlar-29/epoxy and 6061-t6 aluminum laminated panels," *Materials & Design*, vol. 43, pp. 307–321, 2013, ISSN: 0261-3069. DOI: https://doi.org/10.1016/j.matdes.2012.06.034. [Online]. Available: https://www.sciencedirect.com/science/article/pii/S0261306912004074.

[94] L. Peng, J. Zhou, Q. Wang, X. Zhang, and Z. Guan, "Numerical modelling of the ballistic impact response of hybrid composite structures," *Composites Part C: Open Access*, vol. 14, p. 100 474, 2024, ISSN: 2666-6820. DOI: https://doi.org/10.1016/j.jcomc.2024.100474. [Online]. Available: https://www.sciencedirect.com/science/article/pii/S2666682024000446.

[95] S. Xin and H. Wen, "A progressive damage model for fiber reinforced plastic composites subjected to impact loading," *International Journal of Impact Engineering*, vol. 75, pp. 40–52, 2015, ISSN: 0734-743X. DOI: https://doi.org/10.1016/j.ijimpeng.2014.07.014. [Online]. Available: https://www.sciencedirect.com/science/article/pii/S0734743X14001742.

[96] S.-W. Lee and C. Sun, "Dynamic penetration of graphite/epoxy laminates impacted by a blunt-ended projectile," *Composites Science and Technology*, vol. 49, no. 4, pp. 369–380, 1993, ISSN: 0266-3538. DOI: https://doi.org/10.1016/0266-3538(93)90069-S. [Online]. Available: https://www.sciencedirect.com/science/article/pii/026635389390069S.

[97] A. Sharma, R. Mishra, S. Jain, S. S. Padhee, and P. K. Agnihotri, "Deformation behavior of single and multi-layered materials under impact loading," *Thin-Walled Structures*, vol. 126, pp. 193–204, 2018, Special Issue on Plasticity and Impact Mechanics (IMPLAST 2016), ISSN: 0263-8231. DOI: https://doi.org/10.1016/j.tws.2017.08.021. [Online]. Available: https://www.sciencedirect.com/science/article/pii/S0263823116310606.

[98] M. Žmindák and Z. Pelagič, "Fem simulation of high velocity shock waves in fiber reinforced composites," *Engineering Mechanics*, p. 319, 2012.

[99] A. G. Edupack, "Alumina (99.5%)," Ansys, Tech. Rep., 2024, Accessed: 2024-08-30.

[100] R. Muhi, F. Najim, and M. de Moura, "The effect of hybridization on the gfrp behavior under high velocity impact," *Composites Part B: Engineering*, vol. 40, no. 8, pp. 798–803, 2009, ISSN: 1359-8368. DOI: https://doi.org/10.1016/j.compositesb.2009.08.002. [Online]. Available: https://www.sciencedirect.com/science/article/pii/S1359836809001784.

[101] G. Yang, X. Wan, and C. Hou, "Numerical investigation into ballistic impact response of hybrid woven fabric laminates," in *2017 8th International Conference on Mechanical and Aerospace Engineering (ICMAE)*, 2017, pp. 56–61. DOI: 10.1109/ICMAE.2017.8038617.

[102] D. Systèmes. "2.1.18 high-velocity impact of a ceramic target." (2024), [Online]. Available: http://130.149.89.49:2080/v2016/books/exa/default.htm?startat=ch02s01aex79.html (visited on 09/03/2024).

Appendix A

Simulating hybrid laminates in Abaqus

A.1 Accessing JH-2 criteria

As mentioned above, accessing the Johnson-Holquimist (JH-2) criterion in the finite element software Abaqus is not a straightforward procedure. This is because this material model is not included in the programme's graphical interface. However, in order to access it, it is necessary to manipulate the input file (.inp) generated by Abaqus, but first, a few procedures are required. The complete process is described below.

Initially, still in the Abaqus graphical interface, it is necessary to create a material to which the JH-2 model will be assigned. Note that this material will not be attributed any properties, it just needs to be named according to the following pattern: "ABQ_JH2_user material", for example, "ABQ_JHB_siliconCarbide" (see Figure A.1 (a)). The first part, "ABQ_JH2_" is mandatory as it serves as an identifier for the JH-2 model. The same material must then be assigned to a particular section of the component to be simulated, following the normal procedure.

Once the user has finalised the model to be simulated, they need to create a "Job" as normal and, instead of starting the simulation by selecting "submit", press "Write Input". In this way, only the input file will be generated in the selected working directory (see Figure A.1 (b)).

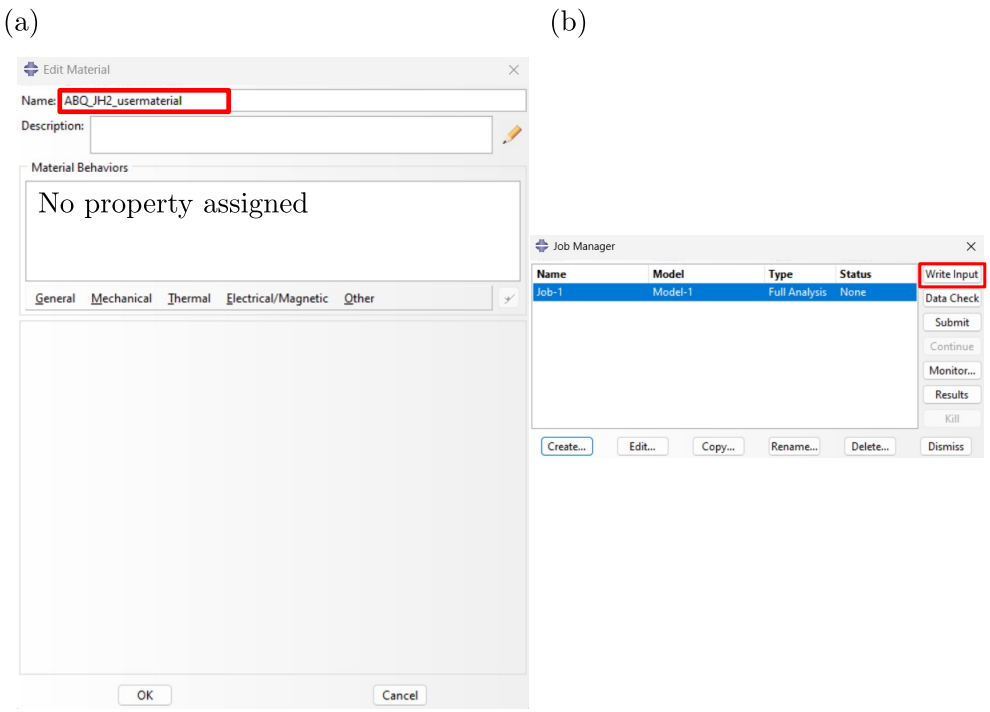


Figure A.1: (a) - Creating the material; (b) - Generating input file

Once the input file has been generated, it is necessary to open it and find the "MATERIALS" section. In this section it is required to add a section of code specific to the JH-2 model. These lines of code are available in the Abaqus documentation, in the sector "2.1.18 High-velocity impact of a ceramic target" [102]. The code to be used for silicon carbide is shown below. To change the ceramic material, it is only a question of modifying the parameter values.

```
1
2  ** MATERIALS
3  **
4  **************************************************************

5  *parameter
6  rho0 = 3.215e-9
7  G = 193000.
8  A = 0.96
9  N = 0.65
10 B = 0.35
11 M = 1.0
12 C = 0.009
13 edot0 = 1.0
14 T = 750
15 sigIMax = 1.04274
```

```
sigFMax = 0.1111111
**sigHEL=1.5*(HEL-PHEL)
**sigIMax=sigIMax/sigHEL=12200/9855=1.23795
**sigFMax=sigFMax/sigHEL=1300/9855=0.1319127
HEL = 11700
PHEL = 5130
beta = 1.0
D1 = 0.48
D2 = 0.48
efMax = 1.2
efMin = 0.0
K1 = 220000
K2 = 361000
K3 = 0.0
FS = 0.2
lDamage = 0
*Material, name=abq_jh2_siliconcarbide
*density
<rho0>
*user material, constants=32
<rho0>, <G>, <A>, <N>, <B>, <M>, <C>, <edot0>
<T>, <sigIMax>, <sigFMax>, <HEL>, <PHEL>, <beta>
<D1>, <D2>, <efMax>, <efMin>, <FS>, <lDamage>
<K1>, <K2>, <K3>
*DEPVAR, DELETE=8
8
1, PEEQ , "Equivalent plastic strain"
2, PEEQ_RATE, "Equivalent plastic strain rate"
3, DUCTCRT , "Ductile damage initiation criterion"
4, DAMAGE , "Damage variable"
5, DELTAP , "Pressure increment due to bulking"
6, YIELD , "Yield strength"
7, EVOL    , "Volumetric Strain, Mu"
8, MPSTATUS , "Material point status"
**********************************************************
```

Finally, the file must be saved and the simulation can be initiated. Nevertheless, the Abaqus graphical interface cannot be used to run the simulation, as submitting the Job would generate a new input file that would erase the previous changes. To avoid this situation, the Job should be executed using the command window, entering the instruction shown in Figure A.2. To perform parallelisation, the number of cpus allocated to the simulation must be added, using the command "cpus= ".

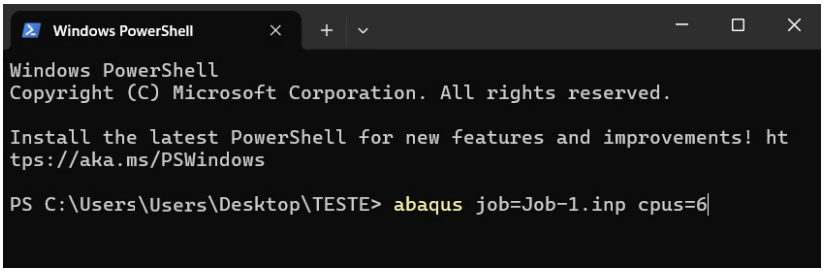


Figure A.2: Instruction to run the Job

A.2 Run a simulation with JH-2 criteria and a VUMAT simultaneously

In this study, it was necessary to carry out simulations using both the JH-2 criterion and the 3D Hashin criterion. Remember that the latter was introduced into Abaqus via a VUMAT subroutine. The normal process of connecting a VUMAT to Abaqus is done when the Job is created, via the graphical interface. However, for the reasons explained above, when the JH-2 criterion is used, the simulation must be started from the command window. Therefore, so for both models to be used at the same time, the command window is also used, slightly modifying the instruction shown in Figure A.2. It's only essential to add the command "user= name_of_subroutine.for" (see Figure A.3). Note that the subroutine must be saved in the same directory as the input file and where the simulation results will be generated.

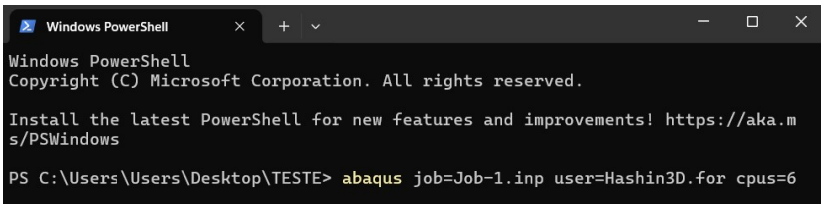


Figure A.3: Instruction to run the Job with JH-2 and the Hashin 3D criterion.

Appendix B

Abaqus tutorial: low-velocity impact on composite laminates

It is presented below a step-by-step tutorial describing the creation of models in Abaqus, as well as the extraction of results and their manipulation for low-velocity impacts. It includes the 2D Hashin and Modified Ladeveze criteria.

U.PORTO
FEUP FACULDADE DE ENGENHARIA
UNIVERSIDADE DO PORTO

Mechanical Engineering Department

Low velocity impact on a laminate composite plate Numerical analysis using Abaqus

Master in Mechanical Engineering

André Rocha - up202202496@up.pt

Guidance: Volnei Tita - voltita@sc.usp.br

Academic year 2023–2024

May 6, 2024

Contents

List of Figures **iii**

List of Tables **iv**

1 Introduction **1**
1.1 Document organisation 1

2 Theoretical Background **3**
2.1 Hashin Criterion Evolution 3
2.1.1 Damage Evolution Law - Hashin Criterion 5
2.2 Subroutine Failure Criterion 6
2.2.1 Damage Evolution Law - Subroutine 8

3 Numerical Procedure - Abaqus **11**
3.1 Continuum Shell Model 11
3.1.1 Part, Material and Assembly Definition 11
3.1.2 Step, Interaction and Loads Definition 15
3.1.3 Mesh Definition 19
3.2 Convetional Shell Model 21
3.3 Results and discussion 22
3.3.1 Energy comparisson 22
3.3.2 Reaction Force comparisson 24

4 Numerical Procedure - Abaqus and VUMAT **27**
4.1 Abaqus Modelling 27
4.2 Subroutine Overview 32
4.3 Results and Discussion 39
4.3.1 Energy comparisson 39
4.3.2 Reaction Force comparisson 41

5 Results Post-Processing **44**
5.1 Reaction Force Vs Time 44
5.2 Energy Evolution 49
5.3 Accessing Subroutine Variables 50

References **52**

Annexes **54**

List of Figures

1 Evolution of damage variable . . . 6
2 Matrix damage surface . . . 7
3 Part - Projectil . . . 11
4 Part - Plate . . . 12
5 CFRP elastic properties . . . 13
6 CFRP damage properties . . . 14
7 Composite layup procedure . . . 15
8 Assembly . . . 15
9 Field Output configuration . . . 17
10 Contact Definition . . . 18
11 Projectil constraint and inertia definition . . . 18
12 Boundary Conditions . . . 19
13 Mesh Controls . . . 20
14 Element Type . . . 21
15 Final Mesh - Continuum Shell Elements . . . 21
16 Final Mesh - Shell elements . . . 22
17 Energy - $[0]_{10}$ - Layup . . . 23
18 Energy - $[+45/-45/+45/0/90]_s$ - Layup . . . 24
19 Energy - $[0/90/0/90/0]_s$ - Layup . . . 24
20 Reaction Force - $[0]_{10}$ - Layup . . . 25
21 Reaction Force - $[+45/-45/+45/0/90]_s$ - Layup . . . 26
22 Reaction Force - $[0/90/0/90/0]_s$ - Layup . . . 26
23 User Material Definition . . . 27
24 Transverse Shear Stiffness - Composite Layup . . . 28
25 Contact "Surface-to-Surface" . . . 29
26 Contact Interaction . . . 29
27 Final Mesh - Shell elements (VUMAT Model) . . . 31
28 Job - Subroutine and Abaqus link . . . 31
29 Energy - $[0]_{10}$ - Layup . . . 40
30 Energy - $[+45/-45/+45/0/90]_s$ - Layup . . . 40
31 Energy - $[0/90/0/90/0]_s$ - Layup . . . 41
32 Reaction Force - $[0]_{10}$ - Layup . . . 42
33 Reaction Force - $[+45/-45/+45/0/90]_s$ - Layup . . . 42
34 Reaction Force - $[0/90/0/90/0]_s$ - Layup . . . 43
35 XY Data and variables selection . . . 45
36 Elements/Nodes selection . . . 45
37 Acceleration Plot . . . 46
38 Exporting Results . . . 46
39 Results - Excel . . . 47
40 Contact Force Variable Selection . . . 48
41 Node Region Selection . . . 48
42 Contact Force at Each Node - Plot . . . 49

43 Contact Force Sum 49
44 Velocity "Magnitude" - Plot 50
45 Accessing SDV - Vizualization 51
46 Accessing SDV - XY Data 51

List of Tables

1 CFRP - Properties [1, 2] 13
2 Material Model Constants 33

1 Introduction

The use of composite materials in engineering has become an increasingly common practice due to their excellent specific properties, as well as their excellent resistance to fatigue and corrosion. In this context, the aeronautical industry has also seen composites as an opportunity to make aircraft lighter and, in turn, more efficient [3].

Composite materials result from the association of at least two constituents: the matrix and the reinforcement (or fibres). Resulting in a product which presents superior properties to the independent base constituents. The matrix surrounds the reinforcements and helps transmit force throughout the component. The reinforcements are responsible for supporting the loads to which the component is subjected [4, 5].

During the service life of a composite component, it is expected to suffer impact loads. It is therefore essential to have a correct understanding of its behaviour under such situations. Generally, impacts are divided into Low or High Velocity [6]. Some authors include additional classifications, for instance: Ballistic and Hypervelocity [3].

In the event of an impact, the material absorbs part of the energy through elastic deformation and damage mechanisms. Regarding low velocity impacts, the most common damage mechanisms are: delamination, matrix failure and fibre/reinforcement failure. The activation of these mechanisms is not only the result of the material's properties. Factors such as: impactor mass, layup orientation, thickness and curvature can influence the response [3, 6].

The purpose of this document is to describe step by step the numerical modelling of a low-velocity impact on a flat laminate composite (CFRP) plate. The finite element software used is Abaqus. Two different approaches are used, the first uses only the resources (material models) available in Abaqus. The second method is based on developing a user subroutine in Fortran, which is then connected to Abaqus.

The work carried out by Tita [1] on the study of *"Failure analysis of low velocity impact on thin composite laminates: Experimental and numerical approaches"* was used as a starting point/reference. The results obtained from the simulations were compared with the experimental data of reference [1]. In addition, the numerical data obtained in reference [7] was also used to better understand the results.

1.1 Document organisation

The organisation of the document is described below:

- **Theoretical Background** - The Hashin failure criterion is introduced. Covering its theoretical formulation, variations, the available version in Abaqus and its damage evolution law. In addition, the foundation of the failure criterion used in the subroutine is explained, as well as the damage evolution law that is associated with it.

- **Numerical Procedure - Abaqus** - All the steps for numerical modelling are presented. From the generation of the parts, composite layup construction to the mesh generation. In the last subtopic, a comparison is made between the results

obtained and experimental/numerical values from the literature for three different layups.

- **Numerical Procedure - Abaqus and VUMAT** - The development of the model is presented, as is the interaction between the subroutine and Abaqus. Some particular details of how the subroutine is used are also presented. Finally, as with the model that uses Abaqus exclusively, the results obtained are presented.
- **Results Post-Processing** - Detailed information on the extraction and manipulation of results is provided. Access to variables created in subroutines is also covered.

2 Theoretical Background

In the context of composite materials, various failure criteria are found in the literature. The diversity of methods can arise either because the authors approach the subject differently or as refinements/extensions of already established criteria [8, 9].

As a result, some methods do not consider the individual failure of the matrix and/or reinforcement, for instance, Tsai-Wu,Tsai-Hill, Azzi-Tsai, Hoffman and Chamis. This criteria relies on mathematical expressions calibrated from experimental procedures [9]. On the other hand, some authors have developed methods where matrix and fibre failure are computed seperatly, in which the Hashin criterion is included. In addition, the following criteria can be found: Maximum Strain criterion, Maximum Stress criterion, Puck criterion, Yamada and Sun Criterion and Chang and Chang Criterion [8, 9].

2.1 Hashin Criterion Evolution

As mentioned previously, the Hashin criteria assumes matrix and fibre failure. It also differentiates between failure of elements under compression or tension. In 1973, Z. Hashin and A. Rotem worked together to publish the Hashin-Rotem criterion, whose equations are presented bellow [8, 10]:

- Fibre failure in tension

$$\sigma_{11} = X_T \qquad (\sigma_{11}, X_T > 0) \tag{1}$$

- Fibre failure in compression

$$-\sigma_{11} = X_C \qquad (\sigma_{11} < 0, X_C > 0) \tag{2}$$

- Matrix failure in tension

$$\left(\frac{\sigma_{22}}{Y_T}\right)^2 + \left(\frac{\sigma_{12}}{S}\right)^2 = 1 \tag{3}$$

- Matrix failure in compression

$$\left(\frac{\sigma_{22}}{Y_C}\right)^2 + \left(\frac{\sigma_{12}}{S}\right)^2 = 1 \tag{4}$$

Where:

- σ_{11} - Stress acting on fibre direction
- σ_{12} - Stress acting at the ply plane (Shear)
- σ_{22} - Stress acting normal to fibre direction
- X_T - Tensile strength in fibre direction
- X_C - Compressive strength in fibre direction
- Y_T - Tensile strength transverse to the fibre direction

- Y_C - Compressive strength transverse to the fibre direction
- S - Shear strength

Seven years later, in 1980, Hashin introduced some modifications to the model previously described, resulting in a version suitable for three dimensional problems - 3D Hashin criteria. From this, came a simplification for situations in two dimensions - 2D Hashin criteria, which is available in the finite element software Abaqus [8, 11]. Its mathematical description is presented below.

- Fibre failure in tension

$$\left(\frac{\sigma_{11}}{X_T}\right)^2 + \left(\frac{\sigma_{12}}{S}\right)^2 = 1 \qquad (\sigma_{11} > 0) \tag{5}$$

- Fibre failure in compression

$$|\sigma_{11}| = X_C \qquad (\sigma_{11} < 0) \tag{6}$$

- Matrix failure in tension

$$\left(\frac{\sigma_{22}}{Y_T}\right)^2 + \left(\frac{\sigma_{12}}{S}\right)^2 = 1 \qquad (\sigma_{22} > 0) \tag{7}$$

- Matrix failure in compression

$$\left(\frac{\sigma_{22}}{2S_T}\right)^2 + \left[\left(\frac{Y_c}{2S_T}\right)^2 - 1\right]\frac{\sigma_{22}}{Y_C} + \left(\frac{\sigma_{12}}{S}\right)^2 = 1 \qquad (\sigma_{22} < 0) \tag{8}$$

In the previous expressions a new variable was introduced, S_T that refers to the transverse shear stress, concerning the allowable value of σ_{23}.

When comparing the Hashin-Rotem criterion with the 2D-Hashin criteria, it is observed that the two main differences rely on the definition of fibre failure in tension and matrix failure in compression. Regarding fibre failure in tenstion the 2D version introduces de effect of in plane stress. The Abaqus version also introduces a parameter α ($0 \leq \alpha \leq 1$) to determine the contribution of σ_{12} to fibre failure in tension (see Equation 9) [12].

$$\left(\frac{\sigma_{11}}{X_T}\right)^2 + \alpha\left(\frac{\sigma_{12}}{S}\right)^2 = 1 \tag{9}$$

Note that all versions assume the same four different types of failure: Fibre failure in tension/compression and Matrix failure in tension/compression. However, it was described before that delaminations are also a failure mechanism present during impacts in composite structures. This is one limitation of the model that can deviate the numerical results [8, 9].

2.1.1 Damage Evolution Law - Hashin Criterion

The previous subchapter was dedicated to presenting the criteria that defines whether or not damage occurs and under what circumstances. In the presence of damage, it is necessary to define how it evolves and which characteristics/properties of the material are affected by it. It is therefore necessary to correctly formulate a damage evolution law. There are several methodologies in the literature, however, this section will only, briefly introduce the one available in Abaqus [13].

In the presence of damage, the stresses are determined by the following Equation 10:

$$\sigma = C_d \varepsilon \tag{10}$$

Where, σ represents the nominal stresses, ε the strains and C_d represents the damaged easticity matrix. The computation of C_d is as follows [13]:

$$C_d = \begin{bmatrix} (1-d_f)E_1 & (1-d_f)(1-d_m)\nu_{21}E_1 & 0 \\ (1-d_f)(1-d_m)\nu_{21}E_2 & (1-d_m)E_2 & 0 \\ 0 & 0 & (1-d_s)GD \end{bmatrix} \tag{11}$$

Where:

- E_1 - Young's Modulus in fibre direction
- E_2 - Young's Modulus transverse to fibre direction
- G - Shear modulus
- ν_{ij} - Poisson coefficient
- $D = 1 - (1-d_f)(1-d_m)\nu_{12}\nu_{21}$
- d_f - Fibre damage variable
- d_m - Matrix damage variable
- d_s - Shear damage variable

From the previous Equation 11 it is possible to identify that the factors which degrade the material properties are d_f, d_m and d_s. These parameters always take on values between 0 (no damage) and 1 (total damage). With regard to d_f and d_m, it is necessary to understand whether the damage occurs in tension or compression. To do this, the process used by Abaqus introduces a set of characteristic lengths (δ_{eq}), specific to the fibre/matrix under traction/compression. This results in the following Equation 12:

$$d_{f/m} = \frac{\delta_{eq}^f - \delta_{eq}^0}{\delta_{eq}(\delta_{eq}^f - \delta_{eq}^0)} \tag{12}$$

Where:

- δ_{eq}^0 - Initial equivalent displacement
- δ_{eq}^f - Final equivalent displacement
- δ_{eq} - Current equivalent displacement - consult the Abaqus documentation ([13]) to access a detailed demonstration of its calculation

The evolution of the parameter d is ilustrated in Figure 1.

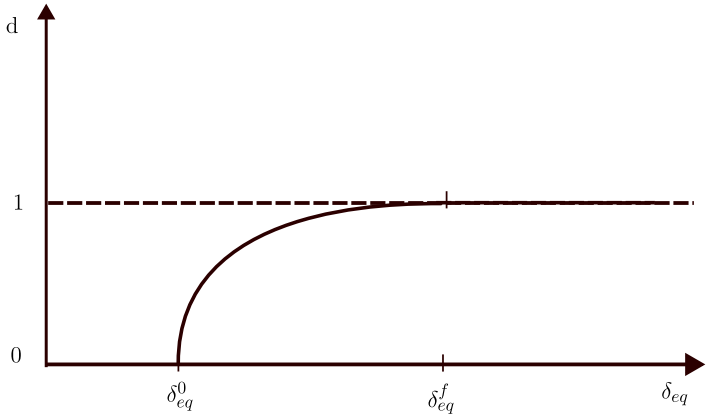


Figure 1: Evolution of damage variable

Finally, it remains to be analysed how the parameters δ^0_{eq} and δ^f_{eq} are obtained. The former is a function of the elastic stiffness and strength values, whereas the latter is function of the failure dissipated energy, G^c [13]. Therefore, it is necessary to know the different fracture energies of the material used:

- G^c_{ft} - Fiber tension fracture energy
- G^c_{fc} - Fiber compression fracture energy
- G^c_{mt} - Matrix tension fracture energy
- G^c_{mc} - Matrix compression fracture energy

Finally, the calculation of d_s is presented in Equation 13 (which depends on the damage parameters described above).

$$d_s = 1 - (1 - d^t_f)(1 - d^c_f)(1 - d^t_m)(1 - d^c_m) \tag{13}$$

2.2 Subroutine Failure Criterion

The model used in the subroutine was developed by Gregório as part of his master's thesis, resulting in the following publication *"Computational analyses of composite plates under low-velocity impact loading"* [7]. It is also important to note that the aforementioned material model was based on the following references [14] e [15].

As with the criterion described above, delaminations are also not considered. The model includes the following failure modes: fibre in tension/compression and matrix in tension/compression and shear. Each of these failure modes is independent, so failure of the fibre does not interfere with the behaviour of the matrix and vice versa. Since the mathematical formulation is more complex than that of the Hashin criterion, a staged presentation of the equations will be made to allow a better understanding of them.

- Fibre failure in tension

$$\frac{\sigma_{11}}{X_T} \geqslant 1 \tag{14}$$

- Fibre failure in compression

$$\frac{-\sigma_{11}}{X_{C0}} \geqslant 1 \tag{15}$$

Where:

- X_T - Tensile strength in fibre direction
- X_{C0} - Linear elastic limit strength under compression in fibre direction

Regarding matrix failure, only one expression was used for tensile, compressive and shear failure. Equation 16 represents a damage surface (see Figure 2), expressed as a function of the acting stresses σ_{22} and σ_{12} and the limit stresses S_{12_0} and Y_{C0}. The last two variables are, respectively, the linear elastic limit stress on shear and the linear elastic limit strength under compression transverse to the fibre direction. Therefore, if f takes on a value greater than or equal to 0, damage occurs (Equation 17).

- Matrix failure surface

$$f = 1 - \left(\frac{\sigma_{12}^2}{S_{12_0}^2} + \frac{\sigma_{22}^2}{Y_{C0}^2} \right) \tag{16}$$

- Matrix failure conditions

$$f \geqslant 0 \tag{17}$$

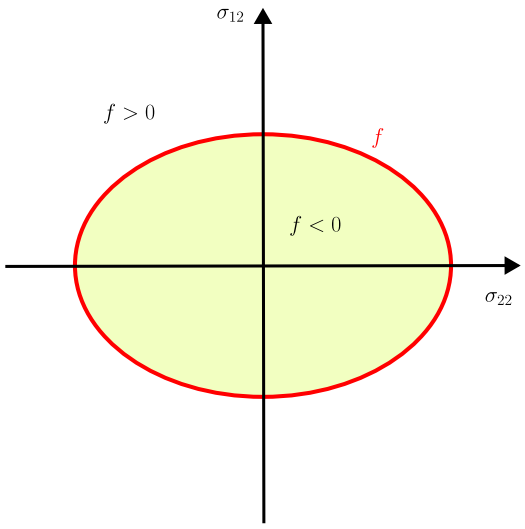


Figure 2: Matrix damage surface

2.2.1 Damage Evolution Law - Subroutine

Once the conditions that indicate whether or not damage has occurred have been established, the way in which it evolves is defined. In order to maintain the same nomenclature, the damage variables d_f, d_m and d_s will be used, the meanings of which have been explained previously.

Regarding the fibre, the properties affected by its failure are E_{11} and ν_{12}, evolving according to the following methodology:

- Fibre failure in tension - If the condition imposed by Equation 14 is met, d_f equals 1, thus indicating complete fibre degradation (Equation 18 and 19).

$$E_{11} = E_{110}(1 - d_f) \tag{18}$$

$$\nu_{12} = \nu_{120}(1 - d_f) \tag{19}$$

  Where E_{110} and ν_{120} are, respectively, the initial modulus of elasticity in the fibre direction and the inicial Poisson coefficient.

- Fibre failure in compression - Once the condition imposed by Equation 15 has been verified, the response is no longer linear. In this case, E_{11} is not updated with d_f but with an expression that describes the non-linear behaviour of the fibre in compression (Equation 20), the secant modulus.

$$E_{11} = \frac{X_{C0}}{|\varepsilon_{11}|}(1 - f(\varepsilon_{11})) + f(\varepsilon_{11})E_{110} \tag{20}$$

  Where ε_{11} representes the strain in the fibre direction and $f(\varepsilon_{11})$ is a parameter determined experimentally.

Damage to the matrix occurs due to the presence of microcracks and voids, which when subjected to stresses transverse to the fibres and shear stresses (respectively σ_{22} and σ_{12}) cause a non-linear response. Another important aspect is the occurrence of self-healing in the matrix. This happens because compressive transverse stresses ($\sigma_{22} < 0$) introduce deformations that close microcracks and voids. Therefore, in this situation, as with fibre compression, the d_m parameter will not control degradation. As for the d_s parameter, it controls the degradation of the matrix due to either positive or negative shear stresses. From the previous statements, two different situations can be found:

- **Condition 1 -** $(f \geqslant 0)$ and $(\sigma_{22} > 0)$ and $(\sigma_{12} \geqslant 0$ or $\sigma_{12} \leqslant 0)$ - In this case d_m controls the degradation of E_{22} and ν_{21}. d_s controls the degradation of G.

- **Condition 2 -** $(f \geqslant 0)$ and $(\sigma_{22} < 0)$ and $(\sigma_{12} \geqslant 0$ or $\sigma_{12} \leqslant 0)$ - In this case, the degradation of E_{22} is carried out by an experimentally calibrated equation (as in fibre compression) and d_s controls the degradation of G.

Finally, all that remains is to introduce the concept of deformation energy, E_D, crucial to the evolution of the damage parameters d_m and d_s. The calculation is shown in Equation 21. As soon as the value of E_D exceeds a critical value, total damage is assumed, equalling the parameters d_m and d_s to 1.

$$E_D = \frac{1}{2}\left[\frac{\langle\sigma_{22}\rangle_+^2}{E_{220}(1-d_m)} + \frac{\langle\sigma_{22}\rangle_-^2}{E_{220}} + \frac{|\sigma_{12}|^2}{G_{120}(1-d_s)}\right] \tag{21}$$

From the above expression it is also possible to extract the concept of thermodynamic forces (Y_2 and Y_6), which are the partial derivatives of the deformation energy in order of the damage variables (Equation 22 and 23). Subsequently, with the thermodynamic forces, it will be possible to explicitly determine d_m and d_s.

$$Y_2 = \frac{\partial E_D}{\partial d_m} = \frac{\langle\sigma_{22}\rangle_+^2}{2E_{220}(1-d_m)^2} \tag{22}$$

$$Y_6 = \frac{\partial E_D}{\partial d_s} = \frac{{\sigma_{12}}^2}{2G_{120}(1-d_s)^2} \tag{23}$$

The concept of thermodynamic force also allows the effect of transverse and shear forces overlapping to be explored. Combining them, results in $\hat{Y}$ - combined thermodynamic force (Equation 24).

$$\hat{Y} = Y_6 + bY_2 \tag{24}$$

Where b quantifies the amount of coupling. It is a characteristic of each material, determined experimentally.

Knowing the value of $\hat{Y}$ it is possible to calculate the values of d_m and d_s, according to Equations 25 and 26.

$$d_m = \frac{\sqrt{\hat{Y}} - \sqrt{{Y_0}'}}{\sqrt{{Y_C}'}} \tag{25}$$

$$d_s = \frac{\sqrt{\hat{Y}} - \sqrt{Y_0}}{\sqrt{Y_C}} \tag{26}$$

Where the values of ${Y_0}'$, Y_0, ${Y_C}'$ and Y_C are determined experimentally by means of quasi-static cyclic tests.

Now that the numerical value of d_m and d_s is known, it is possible to degrade the properties of the matrix under tensile and shear stresses. All that remains is to introduce the degradation of the matrix under compressive stress. As described for fibre compression, the matrix behaves non-linearly when the linear compressive stress limit is exceeded. Thus, the expression obtained for the evolution of E_{22} in compression (29) is similar to Equation 20.

- Matrix failure in tension

$$E_{22} = E_{220}(1-d_m) \tag{27}$$

$$\nu_{21} = \nu_{210}(1 - d_m) \tag{28}$$

Where E_{220} and ν_{210} are, respectively, the initial modulus of elasticity transverse to the fibre direction and the inicial Poisson coefficient.

- Matrix failure in compression

$$E_{22} = \frac{Y_{C0}}{\varepsilon_{22}}(1 - g(\varepsilon_{22})) + g(\varepsilon_{22})E_{220} \tag{29}$$

Where ε_{22} is the strain transverse to the fibre direction and $g(\varepsilon_{22})$ is a parameter determined experimentally.

- Matrix failure in shear

$$G_{12} = G_{120}(1 - d_s) \tag{30}$$

Where G_{120} is the initial in-plane shear modulus.

Once the damaged properties of both the fibre and the matrix have been applied using the methodology described above, a damaged elasticity matrix, C_d, identical to the one presented for the Hashin criterion (Equation 11), is obtained.

3 Numerical Procedure - Abaqus

This chapter is dedicated to describing all the steps taken to carry out the numerical simulation in Abaqus. The process was iterative, as several times after running the simulation and analysing the results, some parameters were adjusted (essentially in the mesh) to obtain the best results.

Note that the Hashin criteria available does not support the use of solid elements. However shell and continuum shell elements can be used. In an attempt to undertstand the limitations of the criteria both shell and continuum shell elements were used. As they require diferent modelling procedures, it was decided to divide this section in two subsections: Continuum Shell Model and Conventional Shell Model.

3.1 Continuum Shell Model

3.1.1 Part, Material and Assembly Definition

Two parts will be constructued: the projectil and the composite plate. Regarding the projectil it will be modelled as a semi-sphere analytical rigid surface as no deformations will be considered for it. First create a new part, select the type "Analytical rigid" and "Revolved shell", then draw a quarter circle with a radius of 8 mm. After slecting "done", the sketch line will be autimatically revolved 360°, as shown in Figure 3. As it will be demonstrated in further subsections there is the need for a reference point in the projectil. It was created in the "Part" module using the upper tool bar - "Tools" - "Reference Point". A good location is the one presented in Figure 3 (another option would be the contact point of the projectile with the plate).

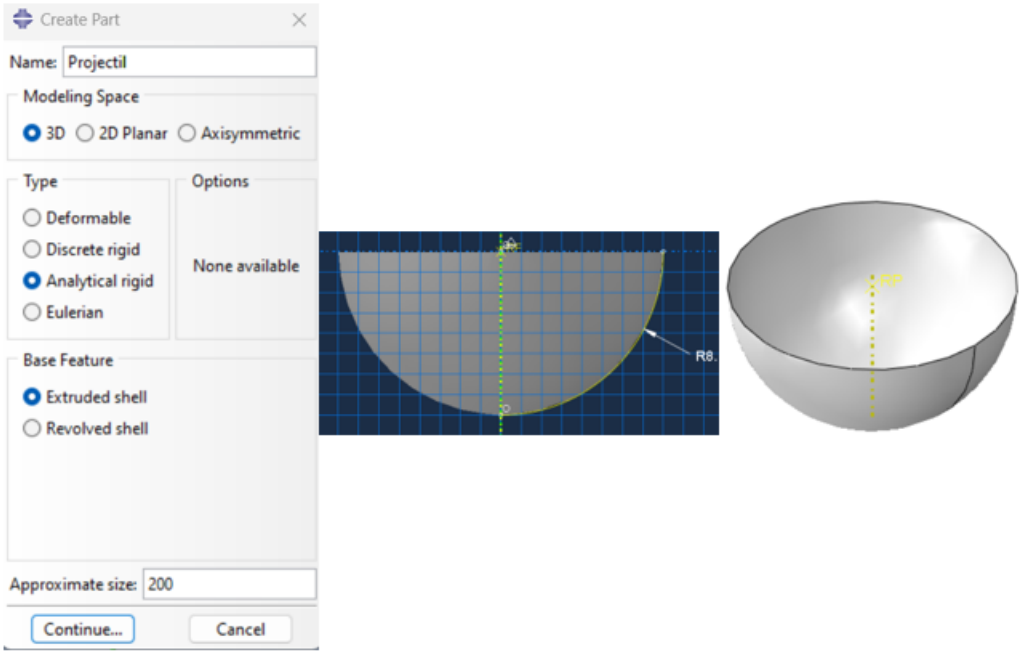


Figure 3: Part - Projectil

Regarding the composite plate, a new part needs to be created, in this case "Deformable", "Solid" (required for Continuum Shell elements) and of the type "Extrusion". Then, draw a circle with 40 mm of radius, select "done" and extrude the part with a "depth" (thinckness of 1.8 mm). Still in the part menu, some partitions will be made in the plate, so that, in the future, it will be possible to obtain an organised mesh as well as refine it in the impact region (32 mm square partition). The partitions made, as well as the entire process described above, is shown in Figure 4.

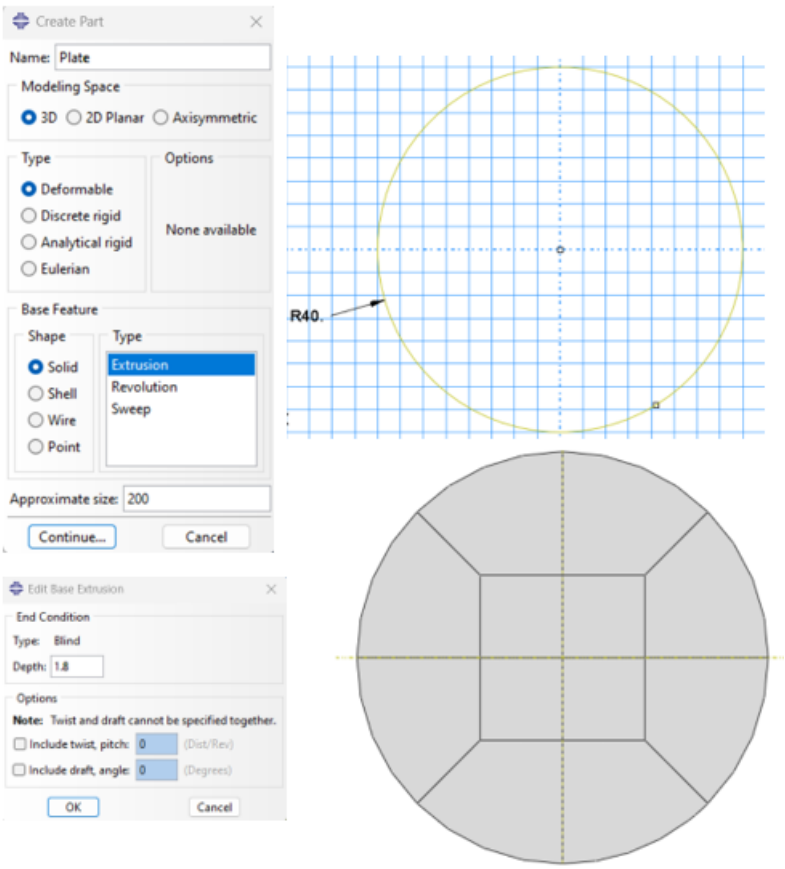


Figure 4: Part - Plate

The next step is to create the materials by introducing their mechanical properties, damage initiation model and damage evolution law. As the projectile has been assumed to be rigid, it doesn't need to be assigned a material. It is only necessary to create the composite material of the plate, in this case, a Carbon Fibre Reinforced Polymer (CFRP), whose properties can be found in Table 1.

In the module "Property" select the "Material Manager" icon and then "New Material". To introduce the density select "General" - "Density" (see Figure 5). Then select "Mechanical" - "Elasticity" - "Elastic" to introduce the elastic properties. As the CFRP isn't isotropic, select the type - "Engineering Constants" as shown in Figure 5.

Next, the properties relating to the Hashin criterion and the evolution of damage are introduced. Select "Mechanical" - "Damage for Fibre-Reinforced-Polymers" - "Hashin

Damage" and insert the values. The "Alpha" parameter will be considered 0. Finally, still in the "Hashin Damage" box, select suboptions "Damage Evolution" and insert the fracure energy values (see Figure 6).

It is important to maintain consistency in the unit system adopted. In this case: mm, MPa, N/mm, ton/mm^3 and mm/s.

Table 1: CFRP - Properties [1, 2]

Property	Unit	Value	Property	Unit	Value	Property	Unit	Value
E_{11}	GPa	127	X_T	MPa	1400	G^c_{ft}	N/mm	48.4
E_{22}= E_{33}	GPa	10	X_C	MPa	930	G^c_{fc}	N/mm	60.3
G_{12}=G_{13}	GPa	5.4	Y_T	MPa	47	G^c_{mt}	N/mm	4.5
G_{23}	GPa	3.05	Y_C	MPa	130	G^c_{mc}	N/mm	8.5
ν_{12}=ν_{13}	-	0.34	Z_T	MPa	62.3	Density	ton/m^3	1.58
ν_{23}	-	0.306	S_{12}=S_{13}	MPa	53			
			S_{23}	MPa	89			

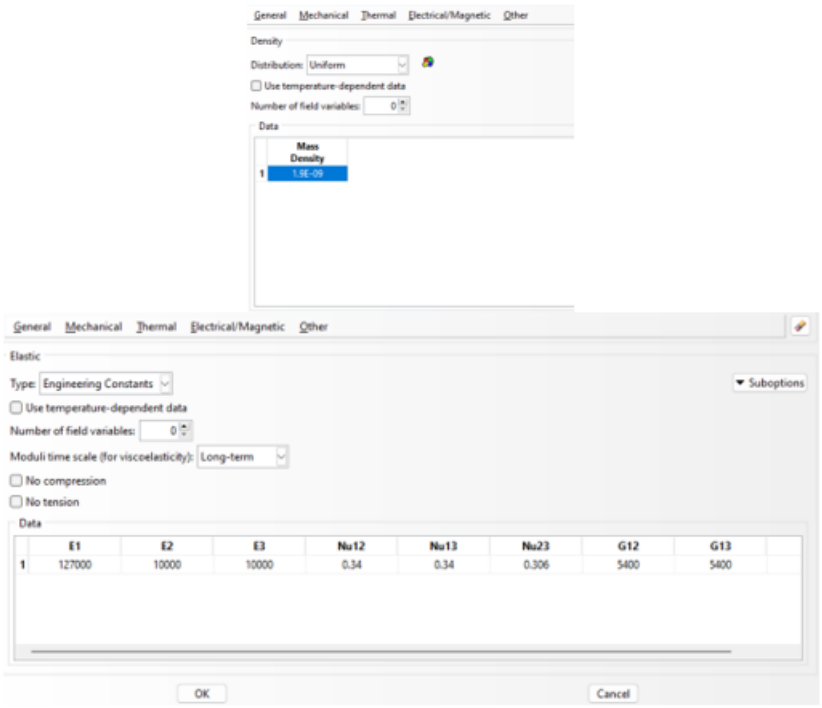


Figure 5: CFRP elastic properties

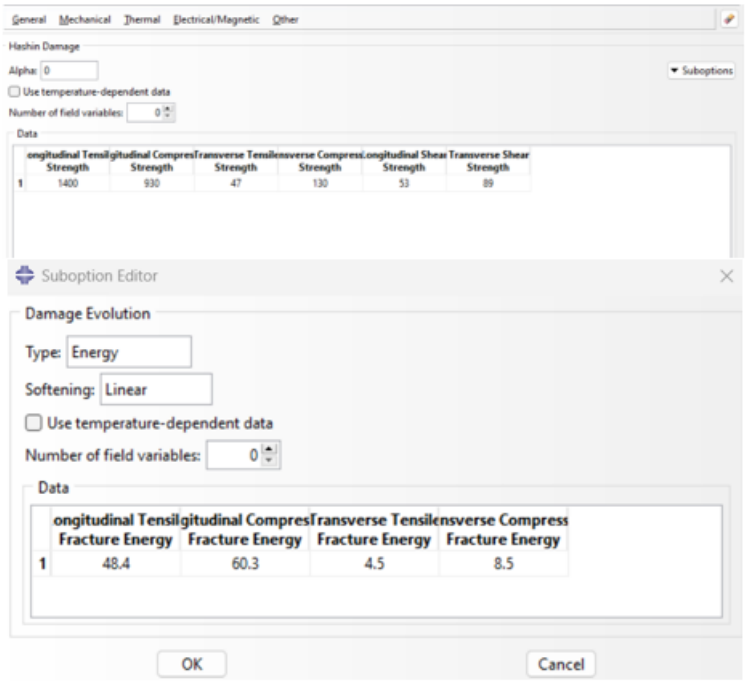


Figure 6: CFRP damage properties

Now that the material is created it is possible to construct the composite layup. In this case three diferent ones are studied $[0]_{10}$, $[+45/-45/+45/0/90]_s$ and $[0/90/0/90/0]_s$, all of them with 10 plies.

In the "Property" module select "Composite Layup Manager" and create a new one. Introduce the numer of plies required and the element type - "Continuum Shell". Then, it is necessary to select the plate part as the "Region" and the previous created material as the "Material". As the plate as a total thickness of 1.8 mm and it is composed of 10 plies, each one as a relative thickness of 0.18 mm. In the "Rotation Angle" the orientation of each ply is introduced. In the end, the part should be colored green (see Figure 7).

Moving to the next module, an "Assembly" is created by positioning the two parts. In this case the projectile was placed in the middle of the plate spaced by 1 mm, as it possible to see in Figure 8.

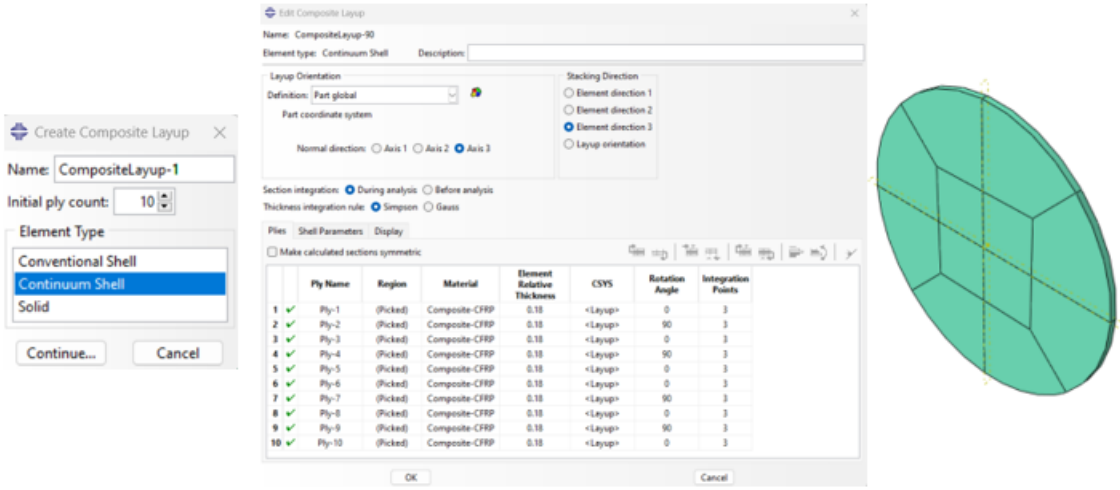


Figure 7: Composite layup procedure

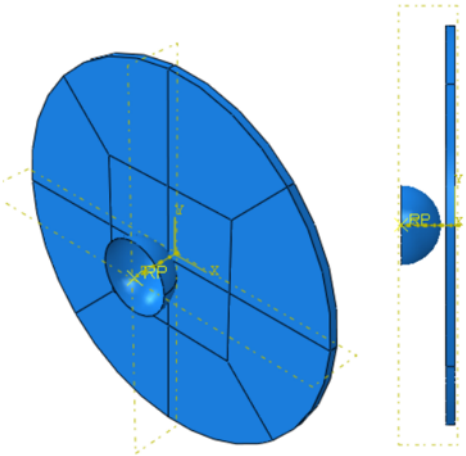


Figure 8: Assembly

3.1.2 Step, Interaction and Loads Definition

The nature of the problem to be recreated implies the use of an explicit simulation, so the step to be created must also be explicit. In the "Step" module, select the "Create Step" icon, chose the type "Dynamic Explicit" and define a time period of 0.007s. Other options could be adjusted to improve convergence of the simulation, however it was not required.

The "Field Output" is also configured in the "Step" menu. This step is important because it defines how often the data is extracted and stored. In the side toolbar, after

selecting "Field Output Manager", a window opens with the created "Field Output". In this case, simply edit the default one by selecting "Edit". In the new window, it is possible to find the different configuration options:

- Domain - specifies in which region of the model Abaqus will extract the data. In this case, the plate and reference point of the projectile must be taken into account. Different field outputs could be configured for each, but the "Whole model" domain covers both regions, so this was the preferred choice.

- Frequency - this field defines how regularly the data is extracted. In this case, in order to accurately capture the dynamics of the impact, this extraction must be relatively frequent. Therefore, it was defined that data would be extracted 200 times during the 7 ms of simulation.

- Timing - allows the user to select whether or not the previously defined intervals can be approximated. If the results are to be obtained at specific times, "Output at exact times" should be selected. In this project, this was not important, so the "Output at approximate times" option was retained.

- Output Variables - allows the user to choose which variables will be stored. As it will be described in subsection 3.3, it's necessary to obtain information on the reaction forces and transferred energy. So, it is essential to obtain data on the evolution of the projectile's velocity and acceleration. However, the reaction and contact forces present in the plate, as well as the displacements, deformations and energies of the plate, are crucial for validating the model. Finally, as damage is considered, "Damage Iniciation criteria" variable must be selected, so the damaged area is flagged.

Figure 9 illustrates the settings and variables required to define the field output described above.

The "Interaction" module is fundamental for introducing the contact between the projectile and the plate. In the present work, after some attempts, it was decided to define an interiaction property "Frictionless" for the "Tangencial Behavior" and "Hard contact" for the "Normal Behavior" (using the Interaction Property Manager). Then in the "Interaction Manager" a "General Contact (Explicit)" was defined as shown in Figure 10.

In the "Interaction" menu, it is still crucial to constraint and define the inertia of the rigid body. First, select the "Constraint Manager" icon then "create" - and the type "Rigid Body". The "Region Type" is an "Analytical Surface" and the "Reference Ponit" is the one created previously in the "Part" Module. Regarding the inertia/mass of the projectile, it is necessary to use the upper tool bar, select "Special" - "Inertia" - "Create" - "Point/Mass Inertia", select the reference point of the projectile and introduce the mass, in this case 1.205kg as isotropic. Figure 11 ilustrates the described steps.

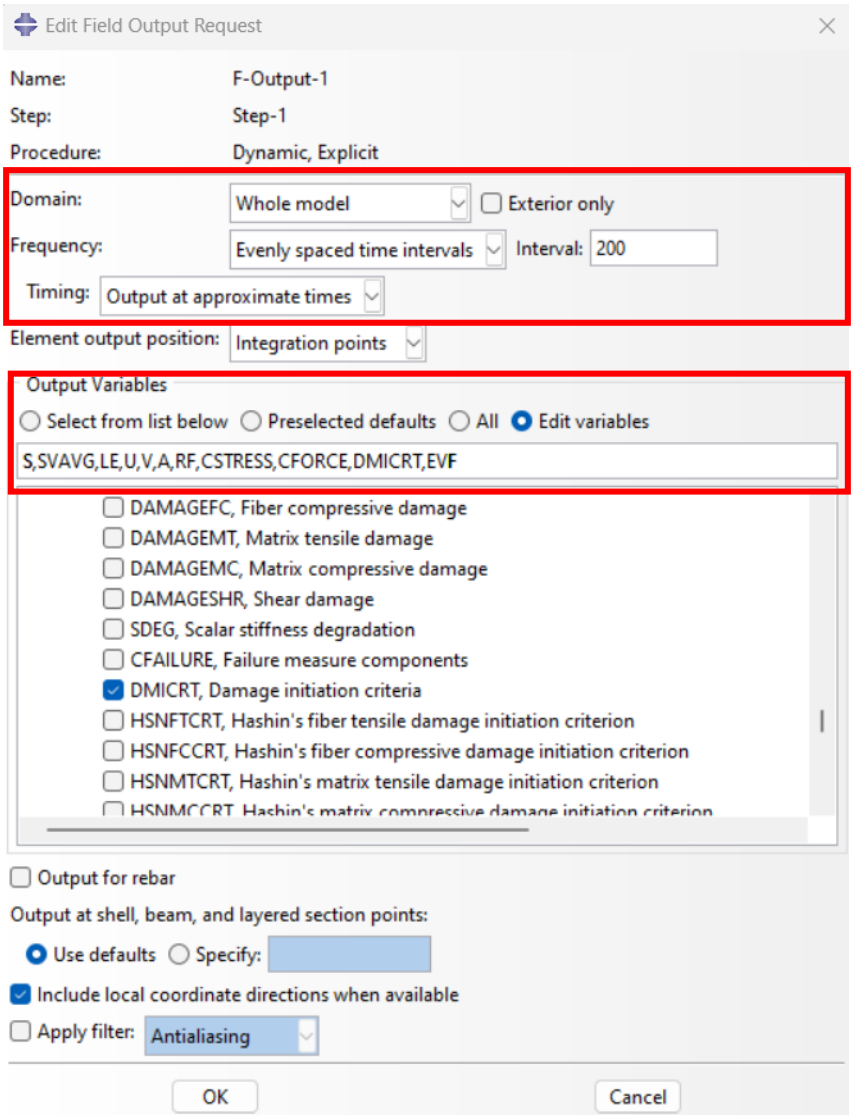


Figure 9: Field Output configuration

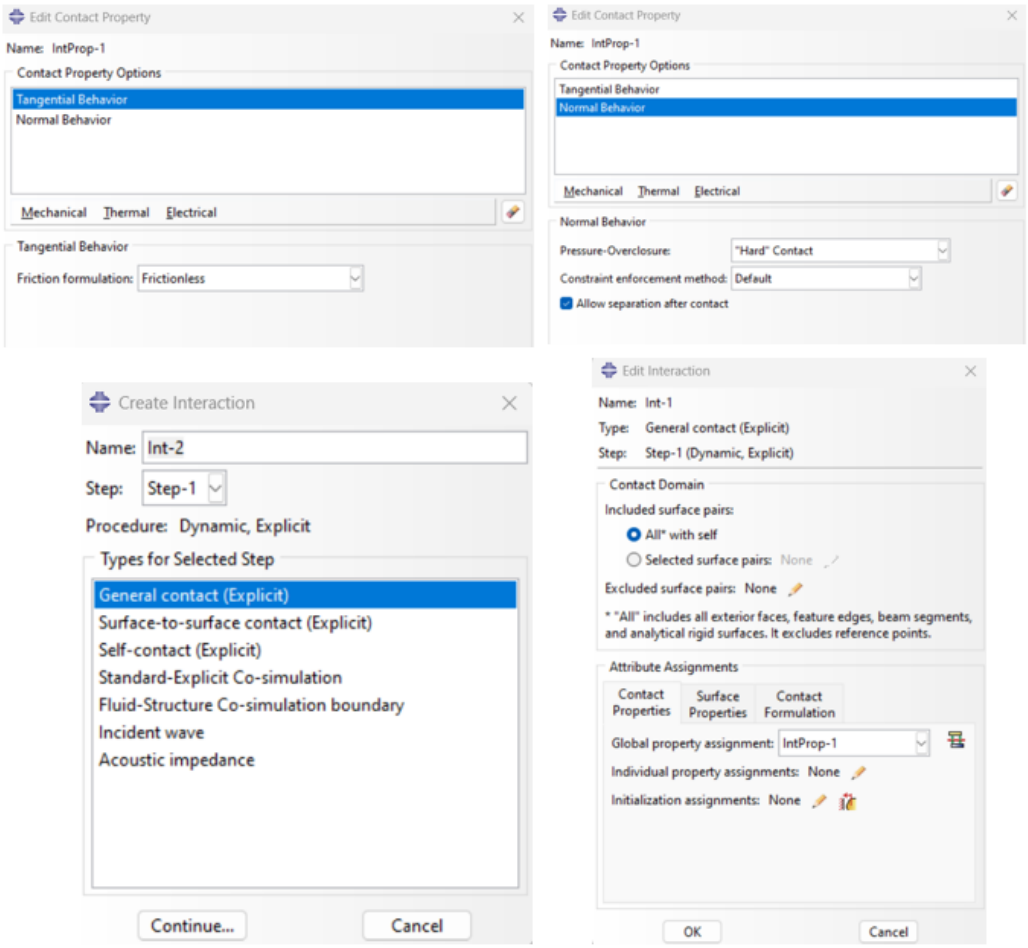


Figure 10: Contact Definition

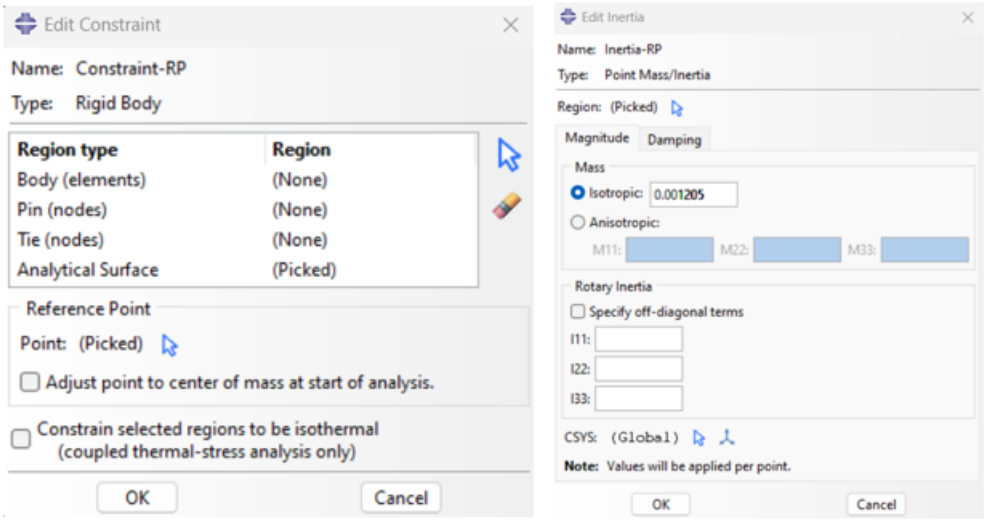


Figure 11: Projectil constraint and inertia definition

Moving on to the "Loads" module, the boundary conditions are established and the initial velocity of the projectile is assigned. Regarding boudary conditions the plate circular edges are "Encastred", so they aren't allowed to have translational or rotational movement. To assign a initial velocity to the projectil, select "Create Predifined Field" - chose the projectile reference point - select "Initial step", "Mechanical Category", and "Velocity". As the impact energy is 5.91 J, using the kinetic energy equation, it is obtained a velocicty equal to 3.13 m/s in the z direction. To ensure that the projectile only moves in the z direction, its translational movement in x and y and rotation around the x, y and z axis is also restricted (using boudary conditions manager and applying the restrictions to the reference point). The following Figure 12 ilustrates the boundary conditions.

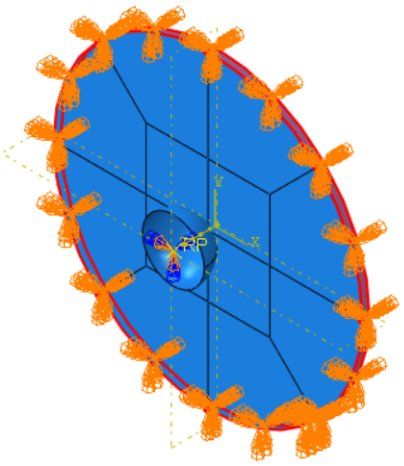


Figure 12: Boundary Conditions

3.1.3 Mesh Definition

The present subsection concerns the mesh definition. Note that, since the projectil was modelled as a analytical surface it does not require a mesh.

To generate an organised mesh, select the "Assing Mesh Controls" and select the outer partitions of the plate. The best "Technique" for those partitions is "Sweep". Ensure that the options "Medial Axis" and "Minimize mesh transition" are selected, as they are vital for a good mesh. The squared partition is assigned the "Strucured" technique. The plate should present the color scheme of Figure 13.

Now it is possible to define the elements size, for the squared partition a seed size of 1.5 mm and for the other edges a seed size of 2.5 mm. In this way, only a refined mesh was used in the contact region. In terms of thickness, 4 elements were used.

The final step concerns the definition of the element type. Using the "Assing element type" icon, select the plate, then "Continuum Shell". Ensure that the options "Explicit" and "Linear" are active. Regarding the "Element controls" some important actions should

be done. First ensure that Hexahedral elements are used, then Hourglass control is "Enhanced" and "Element Deletion" is set to "No" (see Figure 14). The impact introduces large deformations/distortions in some elements. This phenomenon leads to the introduction of artificial energies (purely numerical). Activating Hourglass control reduces these energies, improving the simulation results. As for the elimination of elements, it proved to be critical in terms of the reaction forces on the plate, so the ideal solution was to deactivate it. The final mesh is presented in Figure 15.

At this point every step has been completed, all that remains is to create the job and submit it. When creating the job, it is advisable to have parallelisation active in order to reduce simulation time.

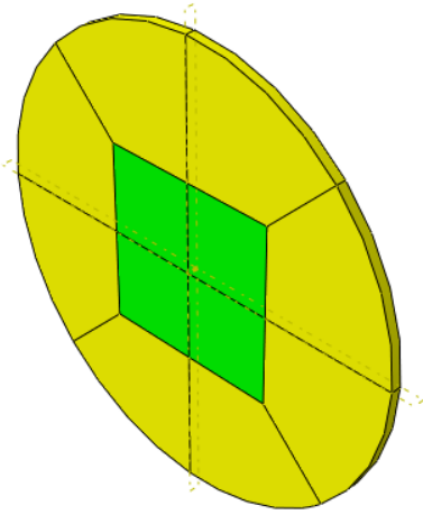


Figure 13: Mesh Controls

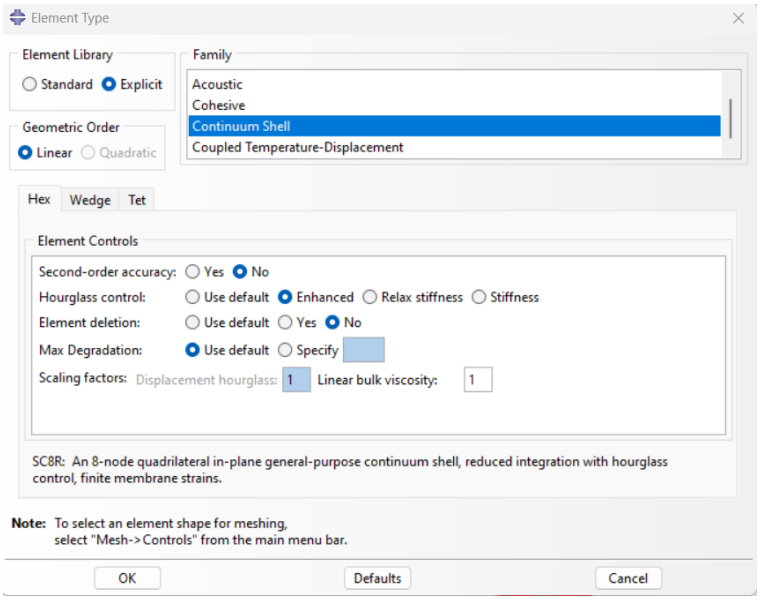


Figure 14: Element Type

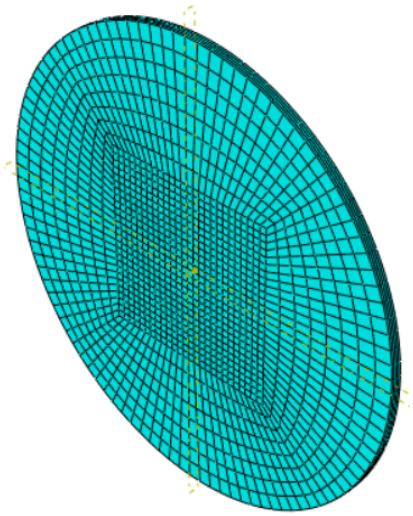


Figure 15: Final Mesh - Continuum Shell Elements

3.2 Convetional Shell Model

Creating a model using conventional shell elements is very simmilar to the process described before. The main differences are in the "Part", "Property" and "Mesh" modules. The projectile modelling is equal to the one presented previously.

To create the plate, go to the "Part" module, select "Create Part" choose "Deformable", "Shell" and of the type "Planar". Then, draw a circle with a radius of 40 mm. Partitions are also a good tool to help in the mesh generation.

Regaring the "Property" module, the material is created as explained before. The only difference is in the composite layup definition. Instead of selecting the continuum shell type, the conventional shell should be choosen.

Moving to the "Mesh" module, there is no need to assign mesh controls. Regarding the "Assign Element Type", shell elements of the type "Quad" must be selected. The option Hourglass control is only available for reduced integration, which after some simulations proved not to improve results. In this way, full integration was maintained. "Element Deletion" was also set to "No", nevertheless it also proved not to be an advantage. Figure 16 presents the obtained mesh.

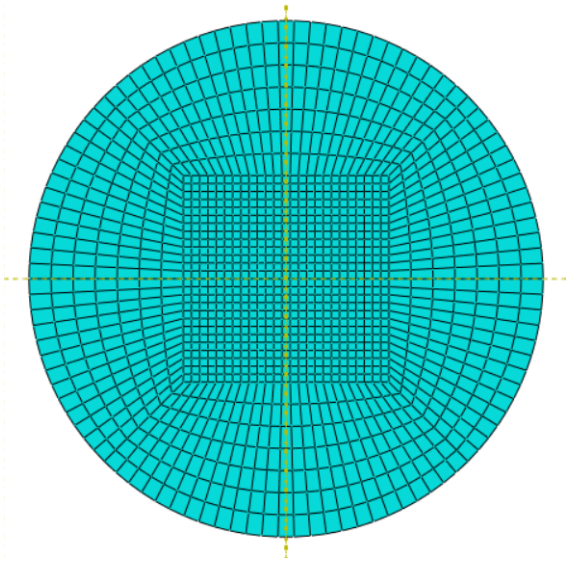


Figure 16: Final Mesh - Shell elements

3.3 Results and discussion

This section evaluates the results of the simulations described above. Essentially, the parameters to be analysed are the energy absorbed by the plate and the reaction forces. Regarding the reaction forces, to calculate them, it was extracted from the "Field Output" the evolution of the projectile acceleration. Then, by multiplying it by the projectile mass (1.205kg) the value of the force was obtained. The energy and force value was postprocessed in Matlab to elaborate comparisson plots. In Section 5 please find detailed information on how to obtain the results step-by-step.

3.3.1 Energy comparisson

Regarding energy (Figures 17-19), the experimental data shows that in the first phase of the impact, energy is transferred to the plate, with a maximum value of around 5.91J. Subsequently, the energy value decreases due to some elastic recovery of the plate. In the final phase, it gradually stabilises at a plateau, which is the value related to the energy absorbed by the laminate's failure mechanisms.

As far as the numerical results are concerned, it is clear from the same Figures that both with Continuum Shel elements (SC8R) and conventional Shell elements (S4), the maximum peak energy results are very close to the experimental ones. However, there are some differences in the values for absorbed energy and impact time.

For all the cases studied, the absorbed energy was found to be lower than the experimental test. This is essentially due to the limitations of the Hashin criterion. As mentioned earlier, this criterion does not take into account the occurrence of delaminations, a phenomenon that happens in low-velocity impacts. However, for the simulations with conventional shell elements, higher values of absorbed energy were obtained than those with the continuum shell, although both were far from the optimum value.

It should be also noted that, the experimental data indicates a higher absorbed energy value for the $[0]_{10}$ laminate and similar values for the $[+45/-45/+45/0/90]_s$ and $[0/90/0/90/0]_s$ laminates. The numerical data, mainly with SC8R elements, also captures this trend.

In terms of impact time (a phenomenon also analysed in the next subsection), the $[0]_{10}$ and $[0/90/0/90/0]_s$ laminates show a much longer time than that obtained experimentally for S4 elements, since the energy curve is more elongated. For SC8R elements, the curve is clearly closer to the experimental one, but the energy peak occurs earlier in all laminates than in the experimental curve. This last observation is also present in reference [7] results, mainly for $[+45/-45/+45/0/90]_s$ laminate.

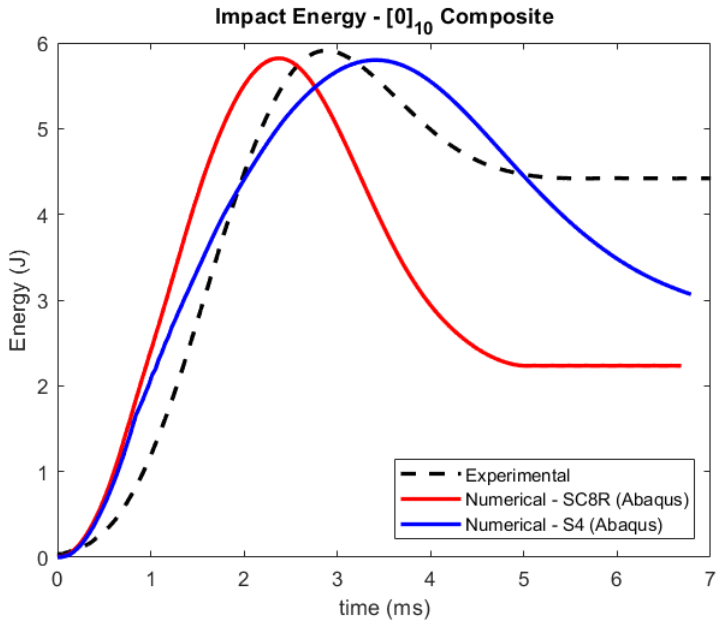


Figure 17: Energy - $[0]_{10}$ - Layup

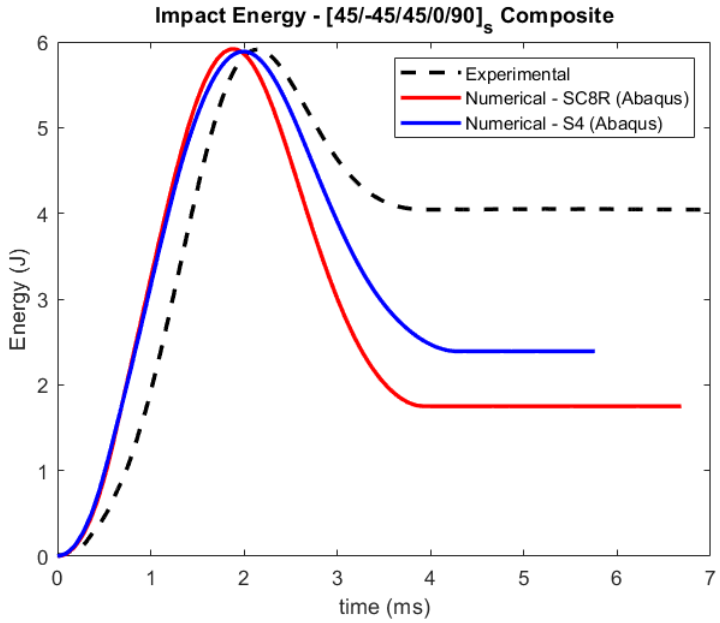


Figure 18: Energy - $[+45/-45/+45/0/90]_s$ - Layup

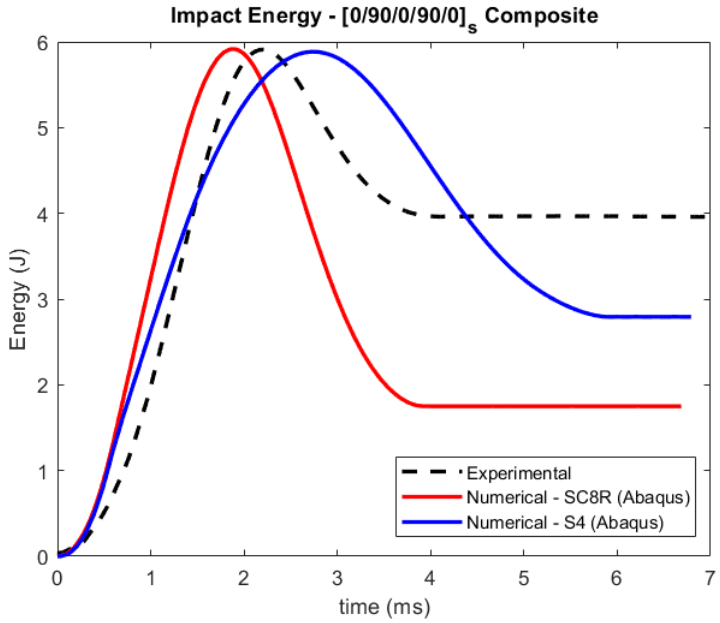


Figure 19: Energy - $[0/90/0/90/0]_s$ - Layup

3.3.2 Reaction Force comparisson

We will now analyse the reaction force data. The experimental data in Figures 20-22 shows that the maximum force values are associated with the $[+45/-45/+45/0/90]_s$ laminate, then $[0/90/0/90/0]_s$ and finally $[0]_{10}$. With regard to impact times, a value close

to 5.5 ms was obtained experimentally for the $[0]_{10}$ laminate, 4 ms for the $[0/90/0/90/0]_s$ and 3.8 ms for the $[+45/-45/+45/0/90]_s$.

The numerical data shows that S4 elements have difficulty to correctly describe the evolution of the reaction forces. For the $[0]_{10}$ and $[0/90/0/90/0]_s$ laminates, the curve obtained is completely wrong as it shows much lower force values and longer impact times. For the $[+45/-45/+45/0/90]_s$ laminate, the S4 elements capture the evolution trend of the experimental curve well, but the maximum values are considerably lower.

Moving on to the SC8R elements, it can be seen that satisfactory results are obtained for the three laminates analysed. Nevertheless, a slight deviation in the first impact instants is observed, as higher results are obtained. It is also in the first instants (0-0.8ms) that a similar response is observed between the SC8R and S4 elements, for the three composite configurations. For the $[0]_{10}$ and $[0/90/0/90/0]_s$ layups, the curves show force values and impact times similar to the experimental ones. For the $[+45/-45/+45/0/90]_s$ laminate, the impact time remained similar to those obtained with S4 elements but the reaction force curve has come closer to the experimental one.

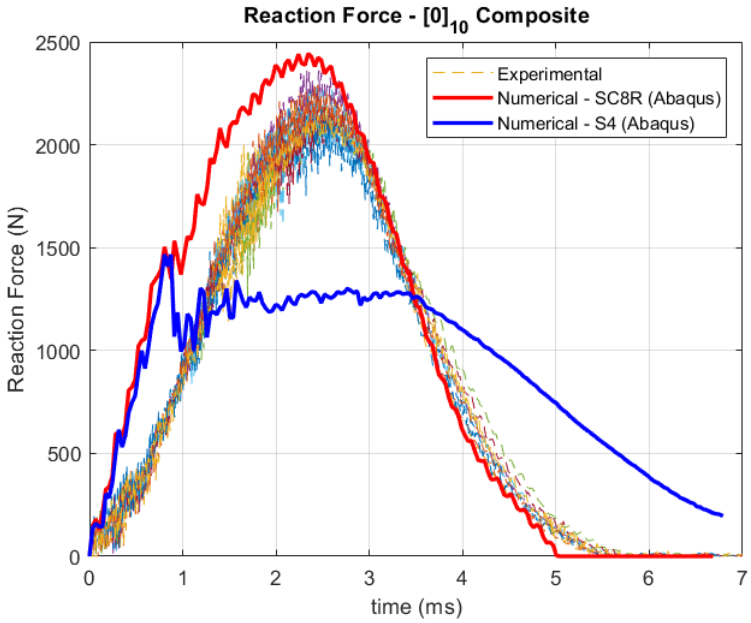


Figure 20: Reaction Force - $[0]_{10}$ - Layup

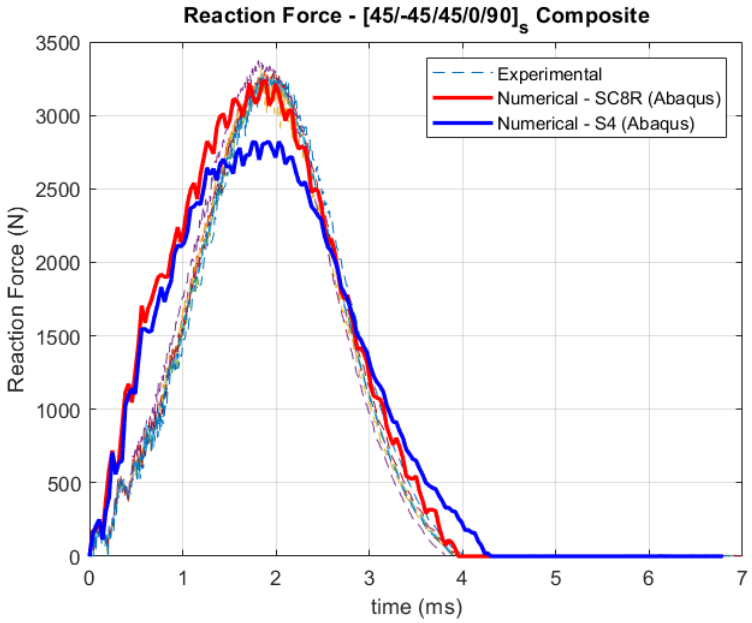


Figure 21: Reaction Force - $[+45/-45/+45/0/90]_s$ - Layup

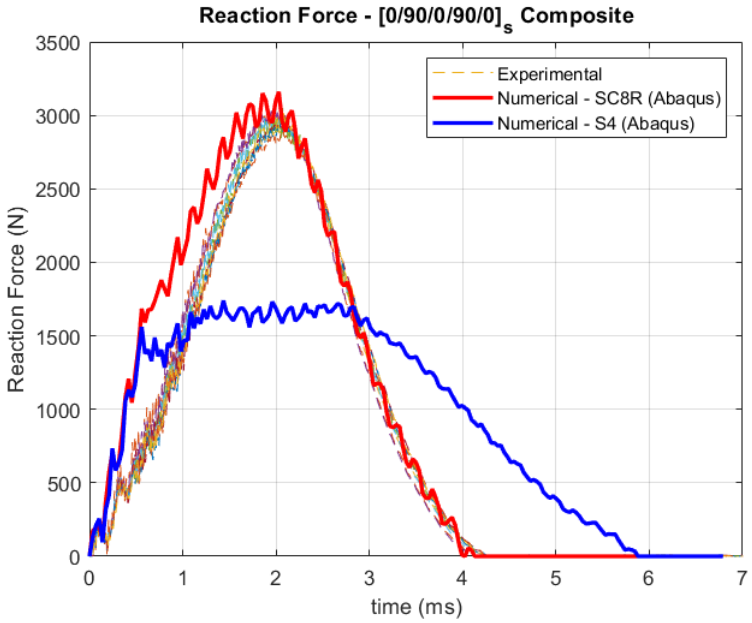


Figure 22: Reaction Force - $[0/90/0/90/0]_s$ - Layup

4 Numerical Procedure - Abaqus and VUMAT

4.1 Abaqus Modelling

The process of creating the model to run in conjunction with the subroutine is similar to the one described in chapters 3.1 and 3.2. Since conventional shell (S4) elements have been used, one possibility is to copy the previous model and apply some changes. In order not to make the document repetitive, only the different steps are described, going through all the Abaqus modules.

- **Part Module -** Both the projectile and the plate maintain the same configurations.
- **Property Module -** There are some changes in this module, mainly in the creation of the material. Abaqus has a specific section for defining the material's properties, which will then be read by the subroutine. When creating a new material, select the "General" field, then "User Material" and finally enter the mechanical constants, in this case: E_{11}, E_{22}, ν_{12} and G_{12} (see Table 1). The density is entered in the "General" - "Density" field (as in previous models). All that remains is to define the number of solution dependent variables (Depvar), i.e. the number of variables that must be stored and passed on from one iteration to the next. The "Variable Number controlling element deletion" field makes it possible to identify which of the Depvar variables is responsible for deleting elements. In this case, 19 solution dependent variables are required, with variable 17 being responsible for deleting elements. The process described above is illustrated in Figure 23.

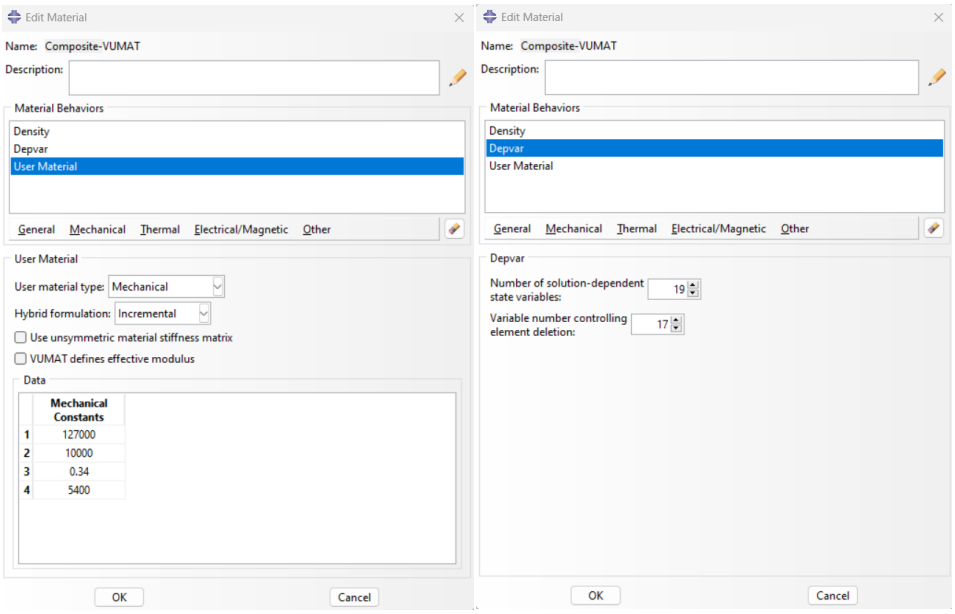


Figure 23: User Material Definition

The construction of the composite layup remains the same, except that it is necessary to change the material assigned to it and specify the transverse shear stiffness

(K_{11}, K_{12} and K_{22}). Regarding the latter, Equation 31 and 32 present its calculation. Note that K_{12} is equal to 0.

$$K_{11} = \frac{5}{6} G_{12} t \tag{31}$$

$$K_{22} = \frac{5}{6} G_{23} t \tag{32}$$

The parameters are entered in the "Shell Parameters" menu, as shown in Figure 24.

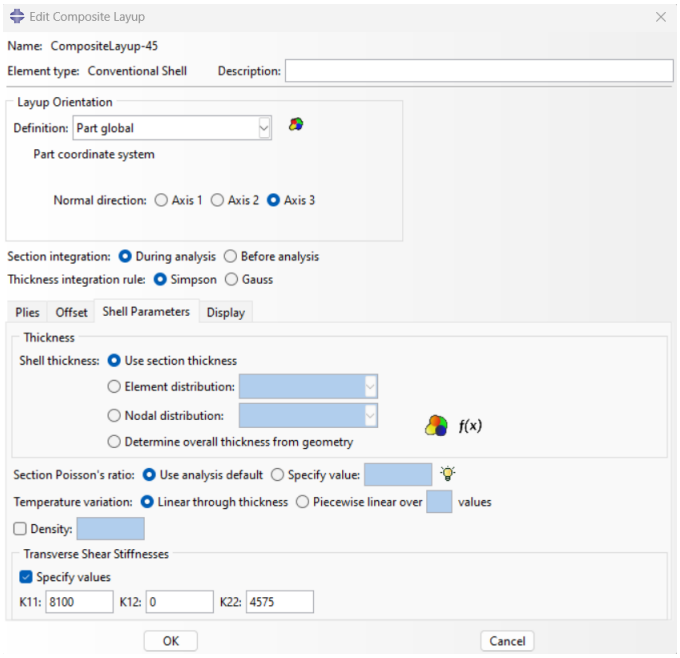


Figure 24: Transverse Shear Stiffness - Composite Layup

- **Assembly and Step Modules -** The assembly keeps the same settings as explained previously. Regarding the step it is also configured as explained before, however, the field output requires some changes, concerning the "Output Variables". In this case, the SDV - "Solution Dependent Variables" and STATUS boxes must be also ticked. The former allows the access to the subroutine variable's evolution, whose explanation and importance is detailed in the subsection 4.2. The latter allows the user to visualise the status of an element (active or deleted).

- **Interaction Module -** The use of the VUMAT subroutine revealed greater sensitivity to the way in which the contact between the projectile and the plate is defined. The final configuration uses "Surface-to-Surface" contact (see Figure 25). The adjacent interaction property uses "Hard Contact" for Normal Behaviour and a friction coefficient of 0.16 for Tangential Behaviour, as shown in Figure 26. The settings for constraint and Inertia associated with the projectile do not change.

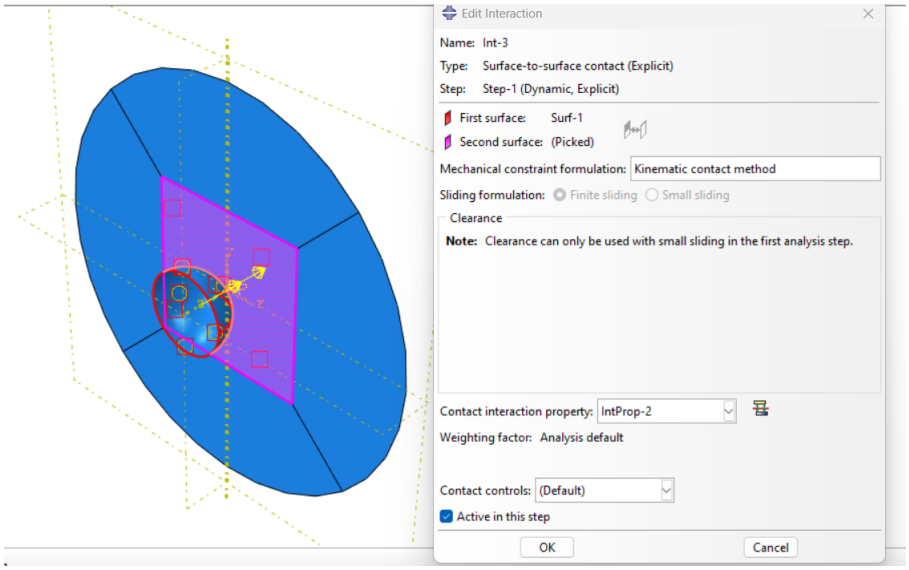


Figure 25: Contact "Surface-to-Surface"

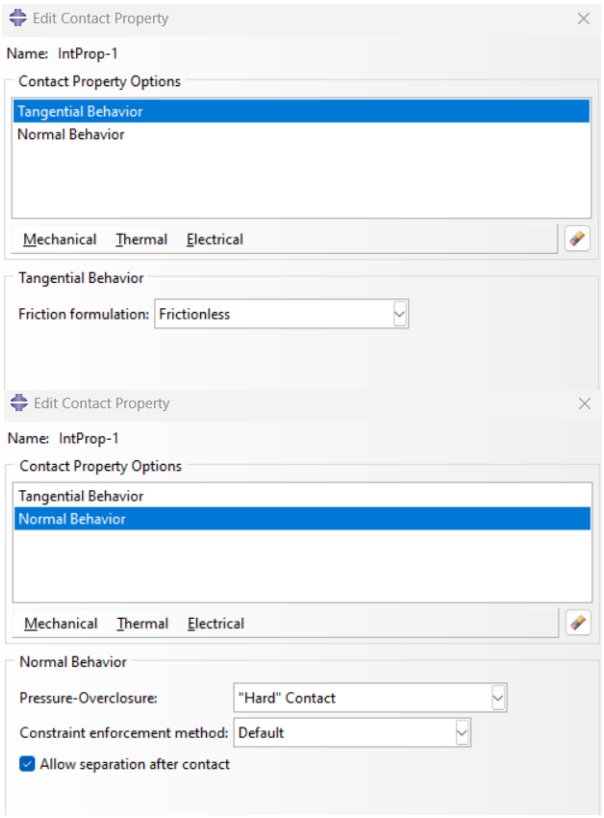


Figure 26: Contact Interaction

- **Load -** Both the projectile and the plate maintain the same configurations.

- **Mesh -** Several changes were made to this module, particularly to the size and type of element. The final parameters were obtained iteratively, guided by the errors and warnings obtained during the various simulations. As with the previous models, only the plate was assigned a mesh.

  To better explain the adjustment of the element size, it is necessary to give a brief introduction to dilatational wave speed, C_d, which refers to the velocity at which waves propagate through a medium and is determined according to Equation 33 [16].

$$C_d = \sqrt{\frac{\hat{\lambda} + 2\hat{\mu}}{\rho}} \tag{33}$$

  Where, $\hat{\lambda}$ and $\hat{\mu}$ are Lamé's parameters, computed with Equation 34 and 35 [16].

$$\hat{\lambda} = \frac{E\nu}{(1+\nu)(1-2\nu)} \tag{34}$$

$$\hat{\mu} = \frac{E}{2(1+\nu)} \tag{35}$$

  In the theoretical introduction, it was explained that when fibres or matrix fail, its properties are degraded. Thus, degraded elements present lower Lamé's parameters, resulting in lower dilatational wave speeds, once the density is constant. In turn, this situation, decreases the maximum deformation speed at wich the element can be subjected. To prevent the elements to deform or collapse unrealistically Abaqus, constantly computes the ratio of "deformation speed to wave speed". Warnings are given when the ratio is equal or higher than 0.3 and the simulation is interrupted if it is equal to 1. To overcome this problem, it is necessary to explore how Abaqus calculates the deformation speed. Consulting the FE software documentation, it is concluded that the deformation speed is equal to "largest absolute value of all the deformation rate components of an element times the element characteristic length L_e". The deformation rate components are controled by the impact properties, so the only parameter to be adusted is the characteristic length, by changing the element size.

  The first idea was to reduce the size of the element, which consequently reduces the characteristic length, the deformation speed and finally the ratio. However, after successive reductions in mesh size, the errors/warnings remained. Although it may seem contradictory, given the expressions presented above, the solution relies on increasing the elements size. Even if this method implies an increase in L_e, it is compensated by an increase in the rigidity of the plate, which leads to a reduction in the speed of deformation and therefore in the ratio. Note that both the deformation speed and the dilatational wave speed vary during the simulation, as a result of the different phases of the impact and the degradation of the properties, which is why the calibration was not so linear.

The final configuration has elements with a size of 4 mm. In terms of the type of elements, conventional shell elements with reduced integration, S4R, were used. In addition, element elimination and Hourglass control were activated. The final mesh is ilustrated in Figure 27.

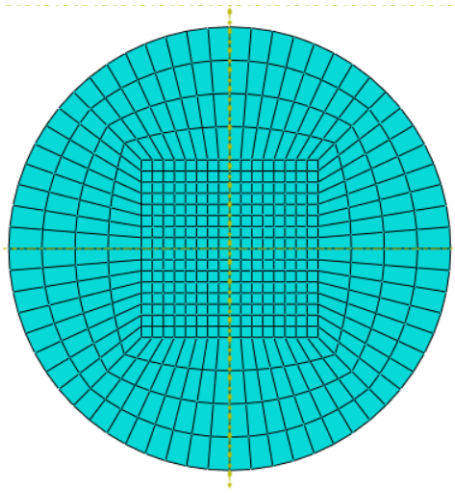


Figure 27: Final Mesh - Shell elements (VUMAT Model)

- **Job -** This module is important as it connects the subroutine with Abaqus. Initially, a new Job is created, then in the "General" option, the location of the subroutine must be entered in the "User subroutine file" field, as shown in the Figure 28.

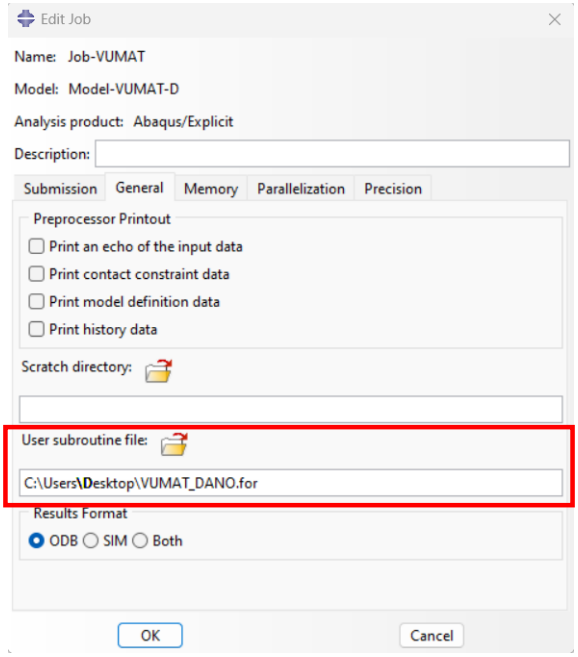


Figure 28: Job - Subroutine and Abaqus link

4.2 Subroutine Overview

The main objective of this subchapter is not to explain the process of developing a subroutine step by step, but rather to explain the structure of the code as well as making a connection with theoretical concepts. Since the impact simulation needs to be explicit, the material model has to be programmed according to VUMAT standards. The entire code can be found in the annexes (VUMAT Code).

- **VUMAT Header**

  This block of code is common to all VUMAT subroutines and shows the variables to be defined, to be updated and those that pass information from iteration to iteration. Note that these variables communicate between Abaqus and the subroutine [17].

```
      subroutine vumat(
c Read only -
     1  nblock, ndir, nshr, nstatev, nfieldv, nprops, lanneal,
     2  stepTime, totalTime, dt, cmname, coordMp, charLength,
     3  props, density, strainInc, relSpinInc,
     4  tempOld, stretchOld, defgradOld, fieldOld,
     5  stressOld, stateOld, enerInternOld, enerInelasOld,
     6  tempNew, stretchNew, defgradNew, fieldNew,
c Write only -
     7  stressNew, stateNew, enerInternNew, enerInelasNew )
c
      include 'vaba_param.inc'
C
      dimension props(nprops), density(nblock),
     1  coordMp(nblock,*),
     2  charLength(*), strainInc(nblock,ndir+nshr),
     3  relSpinInc(nblock,nshr), tempOld(nblock),
     4  stretchOld(nblock,ndir+nshr), defgradOld(nblock,ndir+nshr+nshr),
     5  fieldOld(nblock,nfieldv), stressOld(nblock,ndir+nshr),
     6  stateOld(nblock,nstatev), enerInternOld(nblock),
     7  enerInelasOld(nblock), tempNew(*),
     8  stretchNew(nblock,ndir+nshr), defgradNew(nblock,ndir+nshr+nshr),
     9  fieldNew(nblock,nfieldv), stressNew(nblock,ndir+nshr),
     1  stateNew(nblock,nstatev),
     2  enerInternNew(nblock), enerInelasNew(nblock)
C
     character*80 cmname
```

- **User Variables**

  This section defines the subroutine's internal variables, created by the user. Material properties entered in abaqus are also read. The props() variable must be used for this end.

As it is possible to see, this section is also used to declare all the constants discussed in the model's theoretical foundation. The following Table 2 lists the nomenclatures and their values.

Table 2: Material Model Constants

Property/Constant	Code Nomenclature	Unit	Value
X_T	X_T	MPa	1940*
X_{C0}	X_CO	MPa	253
X_C	X_C	MPa	930
Y_{C0}	YCO	MPa	60.3
S_{120}	S12_Y	MPa	47
$\sqrt{Y_0}$	RZYO	MPa	0.06627
$\sqrt{Y_C}$	RZYC	MPa	1.186159
$\sqrt{Y_0{}'}$	RZY0L	MPa	0.013425
$\sqrt{Y_C{}'}$	RZYCL	MPa	6.125483
b	b	-	0.929007
h	h	-	0.05164907

*1940 MPa was used to define the tensile strength in fibre direction, whereas in the Hashin criterion 1400 MPa was the limit value.

```
C --- START OF USER CODE ---
C
C - DECLARING USER VARIABLES
C
      double precision E11, E22, NU12, G12, NU21, XT, XC, d1, TF2,
     & TF6, d6, RZY0, RZYC, RZY0L, RZYCL, b, Y, XCO, YCO, FM, FF,
     &  S12, num1, h, num2, d2, YT, TF1, S12_Y

C - ASSIGNING VALUES
      parameter (XT=1940, XCO=253, XC=930, RZY0=0.06627,
     & RZYC=1.861591, YCO=60.3, RZYCL=6.125483, YT=47, S12=53,
     & h=0.05161907, RZY0L=0.013425, b=0.929007, np=10, S12_Y=47)
C
C - ADDITIONAL VARIABLES
      integer km
      dimension STRAIN(3), DDSDDE(3,3)
C
C - READING MATERIAL PROPERTIES FROM ABAQUS CAE
      E11 = props(1)
      E22 = props(2)
      NU12 = props(3)
      G12 = props(4)
      NU21 = (props(2)/props(1))*props(3)
```

- **Loop Inicialization**

  In this section, the cycle that runs every material points (nblock) is inicialised as well as the damage variables. Note that $d1 = d_f$, $d2 = d_m$ and $d3 = d_s$.

```
C - START ITERATION
     DO 100 km = 1, nblock
C
C - DAMAGE VARIABLES INITIALIZATION
      d1 = 0.0
      d2 = 0.0
      d6 = 0.0
C
C - CHECKING THE PRESENCE OF DAMAGE
      IF (stateOld(km,1) .eq. 1.0) then
         E11 = stateOld(km,5)
         d1 = stateOld(km,12)
         NU12 = stateold(km,7)
      END IF
C
      IF (stateOld(km,2) .eq. 1.0) then
         E22 = stateOld(km,6)
         d2 = stateOld(km,13)
         NU21 = stateOld(km,15)
      END IF
C
      IF (stateOld(km,3) .eq. 1.0) then
         G12 = stateOld(km,8)
         d6 = stateOld(km,14)
      END IF
C
```

- **Stress Tensor Calculation and Energy Update**

  The constitutive tensor (DDSDE) is first assembled and then used to calculate the stress tensor. The variable stressNew corresponds to the current state of stress, while stressOld retains the value of the stress in the previous iteration. It is mandatory to use stressNew and stressOld once they communicate between the subroutine and Abaqus. Next, the deformations are updated with the STRAIN variable (internal to the subroutine). Finally, the internal energy is updated. The variable enerInternNew must be used, as it also communicates between the subroutine and Abaqus. This process is not necessary, but it allows the user to monitor the evolution of energies over the course of the simulation, especially Total Energy, which should not vary by more than 5%.

```
C - FILL JACOBIAN MATRIX (DDSDDE) WITH ZEROS
     DO 20 K1 = 1, 3
```

```
          DO 10 K2 = 1, 3
              DDSDDE(K2,K1) = 0.0
10        CONTINUE
20    CONTINUE
C
C - ASSEMBLE THE CONSTITUTIVE TENSOR
       DDSDDE(1,1) = (E11)/(1.0-(NU12*NU21))
       DDSDDE(1,2) = (NU21*E11)/(1.0-(NU12*NU21))
       DDSDDE(2,2) = (E22)/(1.0-(NU12*NU21))
       DDSDDE(2,1) = (NU21*E11)/(1.0-(NU12*NU21))
       DDSDDE(3,3) = G12
C
C - STRESS PREDICTION
       stressNew(km,1) = stressOld(km,1)
      &                  +DDSDDE(1,1)*(strainInc(km,1))
      &                  +DDSDDE(1,2)*(strainInc(km,2))
      &                  +DDSDDE(1,3)*(strainInc(km,4))
       stressNew(km,2) = stressOld(km,2)
      &                  +DDSDDE(2,1)*(strainInc(km,1))
      &                  +DDSDDE(2,2)*(strainInc(km,2))
      &                  +DDSDDE(2,3)*(strainInc(km,4))
       stressNew(km,3) = stressOld(km,3) + 0.0
       stressNew(km,4) = stressOld(km,4)
      &                  +DDSDDE(3,1)*(strainInc(km,1))
      &                  +DDSDDE(3,2)*(strainInc(km,2))
      &                  +DDSDDE(3,3)*(strainInc(km,4))
C
C - STRAIN CALCULATION
       STRAIN(1) = stateOld(km,9) + strainInc(km,1)
       STRAIN(2) = stateOld(km,10) + strainInc(km,2)
       STRAIN(3) = stateOld(km,11) + strainInc(km,4)
C
C Energy calculation - (!BASE CODE MODIFICATION!)
C  (DOES NOT INTERFERE WITH RESULTS)
       stressPower = 0.5*((stressOld(km,1)+stressNew(km,1) )
      &     *(strainInc(km,1))
      &    +     ( stressOld(km,2)+stressNew(km,2) )*strainInc(km,2)
      &    +     ( stressOld(km,3)+stressNew(km,3) )*strainInc(km,3)
      &    + 2.0*( stressOld(km,4)+stressNew(km,4) )*strainInc(km,4))

       enerInternNew(km) = enerInternOld(km)
      &                    +stressPower/(1.59e-9)
C
```

- **Fibre and Matrix Failure**

  This section implements the mathematical formulation explained in subchapter 2.2, determining the failure indices. It begins the calculations on the fibre and then on

the matrix. Finally, it determines the thermodynamic forces as described in chapter 2.2.1.

```
C - EVALUATION OF THE FAILURE MODE INDICES
C -    1. - FIBRE
       IF (stressNew(km,1) .gt. 0.0) THEN
              FF = (stressNew(km,1)/XT)**2.0
       ELSE
              FF = (stressNew(km,1)/XCO)**2.0
       END IF
C
C -    2. - MATRIX
       num1 = (stressNew(km,4)**2.0)/(S12_Y**2)
       num2 = ((stressNew(km,2)-h)**2.0)/(YCO**2)
       FM = sqrt(num1+num2)
C
C - THERMODYNAMIC FORCES
       IF (stressNew(km,2) .ge. 0.0) then
          TF2 = (stressNew(km,2)**2.0)/(2.0*props(2)*((1-d2)**2))
       ELSE IF (stressNew(km,2) .lt. 0.0) then
          TF2 = 0.0
       END IF
C
       TF6 = (stressNew(km,4)**2.0)/(2.0*props(4)*((1-d6)**2))
       Y = TF6+b*TF2
```

- **Properties Degradation**

  Once the failure index has been determined, it is compared with its limit value to determine whether or not failure has occurred. If it does, the properties will be degraded. The code shown below executes this process. It starts with the fibre and then moves on to the matrix, according to subchapter 2.2.1.

```
C - CHECK FAILURE OCURRENCE + PROPERTIES DETERIORATION
C - 1. - DETERIORATE FIBRE PROPERTIES
       IF (FF .ge. 1.0) then
         IF (stressnew(km,1) .gt. 0.0) then
             d1 = 0.99
             E11 = props(1)*(1.0-d1)
             NU12 = props(3)*(1.0-d1)
             stateOld(km,1) = 1.0
         ELSE IF (stressNew(km,1) .lt. 0.0) then
             E11 = ((XCO)/abs(STRAIN(1)))*(1.0-(78.873*STRAIN(1)+1.087))
     &           + (78.873*STRAIN(1)+1.087)*props(1)
             stateOld(km,1) = 1.0
C
         END IF
```

```
      END IF
      IF (E11 .lt. 0.01*props(1)) then
        E11 = abs(0.01*props(1))
      END IF
      stateNew(km,5) = E11
      stateNew(km,7) = NU12
      stateNew(km,12) = d1
      stateNew(km,1) = 1.0
C
C - 2. - DETERIORATE MATRIX PROPERTIES
C - Condition 1
      IF ((FM .gt. 1.0)) then
        IF ((d6 .lt. 1.0) .and. (sqrt(Y) .ge. (RZY0))
     &       .and.  (sqrt(Y) .lt. (RZY0+RZYC))) then
            d6 = (sqrt(Y)-RZY0)/(RZYC)
            G12 = props(4)*(1-d6)
            stateOld(km,3) = 1.0
        END IF
        IF (d6 .ge. 1.0) then
            d6 = 0.99
        END IF
        IF (d6 .lt. stateOld(km,14)) then
            d6 = stateOld(km,14)
        END IF
        IF ((stressNew(km,2) .gt. 0.0) .and. (d2 .lt. 1.0)
     & .and. (sqrt(Y) .ge. (RZY0L))
     & .and. (sqrt(Y) .lt. (RZY0L+RZYCL))) then
            d2 = (sqrt(Y)-RZY0L)/(RZYCL)
            E22 = props(2)*(1-d2)
            NU21 = ((props(2)/props(1))*props(3))*(1-d2)
            stateOld(km,2) = 1.0
        END IF
        IF (d2 .gt. 1.0) then
            d2 = 0.99
        END IF
        IF (d2 .lt. stateOld(km,13)) then
            d2 = stateOld(km,13)
        END IF
      END IF
    C
    C - Condition 2
      IF (FM .gt. 1.0) then
        IF (stressNew(km,2) .lt. 0.0) then
            IF ((d6 .lt. 1.0) .and. (sqrt(Y) .ge. RZY0)
     &        .and. (sqrt(Y) .lt. (RZY0+RZYC))) then
              d6 = (sqrt(Y)-RZY0)/(RZYC)
              G12 = props(4)*(1-d6)
```

```
                stateOld(km,3) = 1.0
              END IF
              IF (d6 .gt. 1.0) then
                d6 = 0.99
              END IF
              IF (d6 .lt. stateOld(km,14)) then
                d6 = stateOld(km,14)
              END IF
              stateOld(km,8) = G12
              stateOld(km,14) = d6
              IF (abs(stressNew(km,2)) .gt. YC0) then
                E22 = ((YC0)/abs(STRAIN(2)))*(1.0-(4.1763*((STRAIN(2)))
     &               +0.03182))+(4.1763*((STRAIN(2)))+0.03182)*props(2)
                stateOld(km,2) = 1.0
              END IF
              stateOld(km,6) = E22
            END IF
          END IF
C
          IF (E22 .lt. 0.001*props(2)) then
            E22 = 0.001*props(2)
          END IF
```

- **Variables Update, Element Deletion and VUMAT End**

  Once the properties have been degraded, the variables need to be updated so they can be passed on to the next iteration. Before concluding the cycle, the state of the element is also assessed, in order to proceed with its elimination or not. It has been defined that if a particular element has any of the 3 damage variables greater or equal to 0.99, it will be eliminated. Finally, the subroutine is finalised with the "RETURN" and "END" commands.

```
C - STATE VARIABLES UPDATE
          stateNew(km,6) = E22
          stateNew(km,15) = NU21
          stateNew(km,13) = d2
          stateNew(km,8) = G12
          stateNew(km,14) = d6
          stateNew(km,3) = 1.0
          stateNew(km,2) = 1.0
          stateNew(km,9) = STRAIN(1)
          stateNew(km,10) = STRAIN(2)
          stateNew(km,11) = STRAIN(3)
C
          IF (stateNew(km,2) .lt. 10.0**(-6.0)) then
             stateNew(km,2) = 0.0
          ELSE IF (stateNew(km,3) .lt. 10.0**(-6.0)) then
```

```
          stateNew(km,3) = 0.0
        END IF
C
C - CONDITION FOR DELETING ELEMENTS - ((d1 or d2 or d6) >=0.99)
        IF((stateOld(km,12) .ge. 0.99) .or. (stateOld(km,13) .ge. 0.99)
       & .or. (stateOld(km,14) .ge. 0.99)) then
          stateNew(km,17) = 0.0
        END IF

100     CONTINUE
C - CODE END
        RETURN
        END
```

4.3 Results and Discussion

Once the Abaqus model and subroutine had been created, simulations were carried out for the same three laminate configurations: $[0]_{10}$, $[+45/-45/+45/0/90]_s$ and $[0/90/0/90/0]_s$. As before, the reaction forces and transferred energy are evaluated. For comparison purposes, they will be examined against the experimental results and those obtained using the Hashin criterion (in particular, the model with SC8R elements, as it returned better results).

4.3.1 Energy comparisson

With regard to the energy transferred to the plate, it can be seen that in the initial phase of the impact, i.e. up to the maximum value, the response is similar for both the Hashin criterion and the subroutine. However, there is a slight trend for the subroutine curve to be closer to the experimental data. This can be observed for the $[0]_{10}$ composite at the maximum value obtained, and for the $[+45/-45/+45/0/90]_s$ composite by the gap reduction.

With regard to the final phase of the curve, it is clear that the values obtained by the subroutine are considerably lower than the experimental ones, and close to those of the Hashin criterion. This is due the fact that both models do not take into account the phenomenon of delamination. However, the experimental data points to higher absorbed energy values in the $[0]_{10}$ composite and similar values in the $[+45/-45/+45/0/90]_s$ and $[0/90/0/90/0]_s$ configurations. The numerical data obtained by the Hashin criterion tends to capture this trend better. The subroutine, on the other hand, although it returns the highest value for the $[0]_{10}$ composite, shows a considerable difference between the other two configurations.

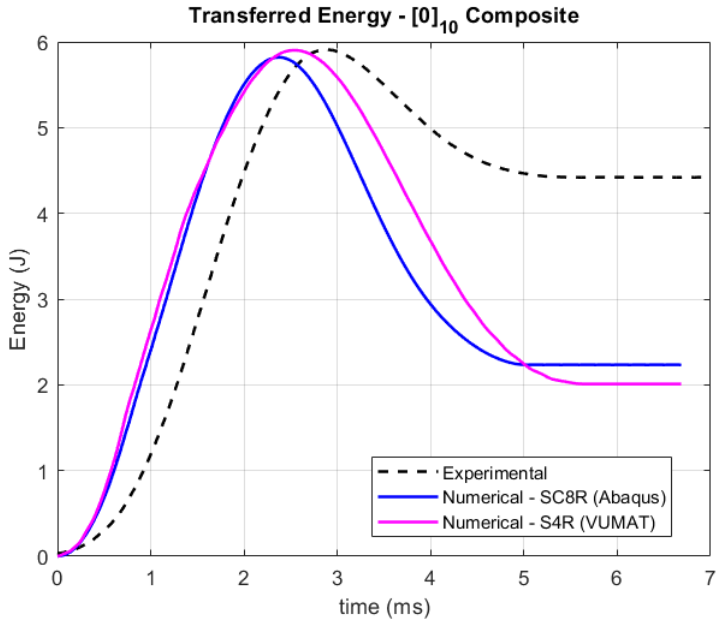


Figure 29: Energy - $[0]_{10}$ - Layup

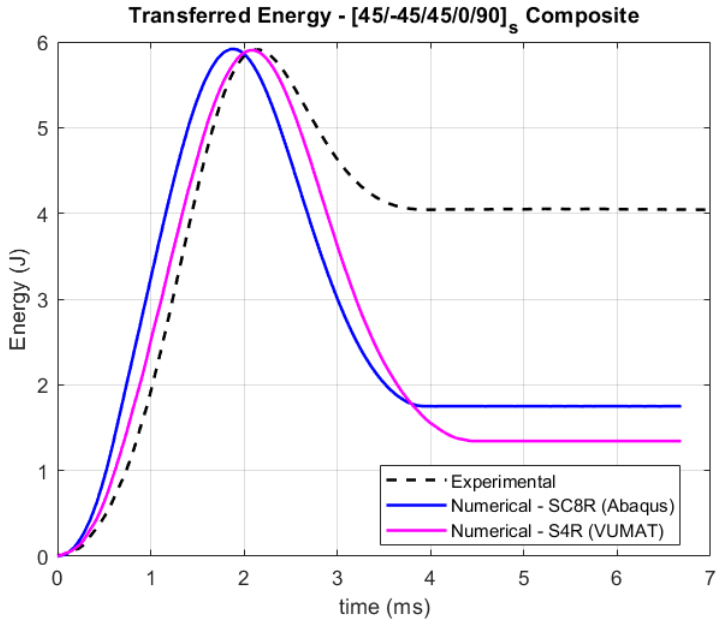


Figure 30: Energy - $[+45/-45/+45/0/90]_s$ - Layup

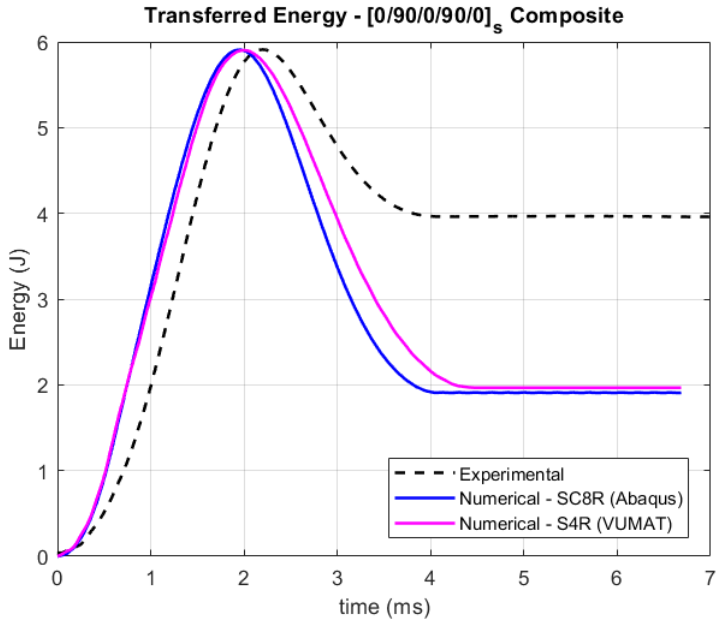


Figure 31: Energy - $[0/90/0/90/0]_s$ - Layup

4.3.2 Reaction Force comparisson

Evaluating the reaction forces for the different models, it is possible to conclude that in the initial instants (up to ≈ 1.2 ms) there is a deviation from the numerical data, in the composites $[0]_{10}$ and $[+45/-45/+45/0/90]_s$, in the sense of presenting higher force values than the experimental ones. At these same instants, for the $[0/90/0/90/0]_s$ composite, the Hashin criterion shows slightly higher results than the experimental ones, while the subroutine returns similar force values.

Regarding the maximum values, for the $[0]_{10}$ composite the subroutine delivers results identical to the experimental ones, opposing the higher values of the Hashin criterion. For the other configurations, both models are close to the experimental values.

In the final phase of the impact, i.e. the projectile's return, the Hashin criterion better captures the evolution of the reaction forces. The VUMAT results show slightly higher values, resulting in longer impact times than the Hashin criterion. This behaviour is beneficial in the case of the $[0]_{10}$ composite as it brings the impact time closer to the experimental one, but for the other composites it leads to an impact time around 0.5 ms longer than the experimental one.

To summarise, it can be concluded that the subroutine shows the best results in the initial phase of the impact, up to the maximum force value. In the return phase, the Hashin criterion best captures the evolution of forces.

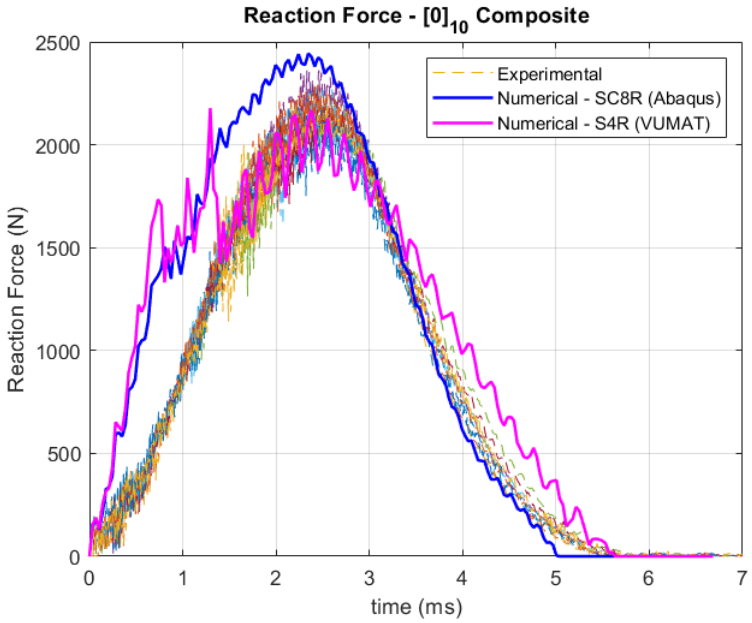


Figure 32: Reaction Force - $[0]_{10}$ - Layup

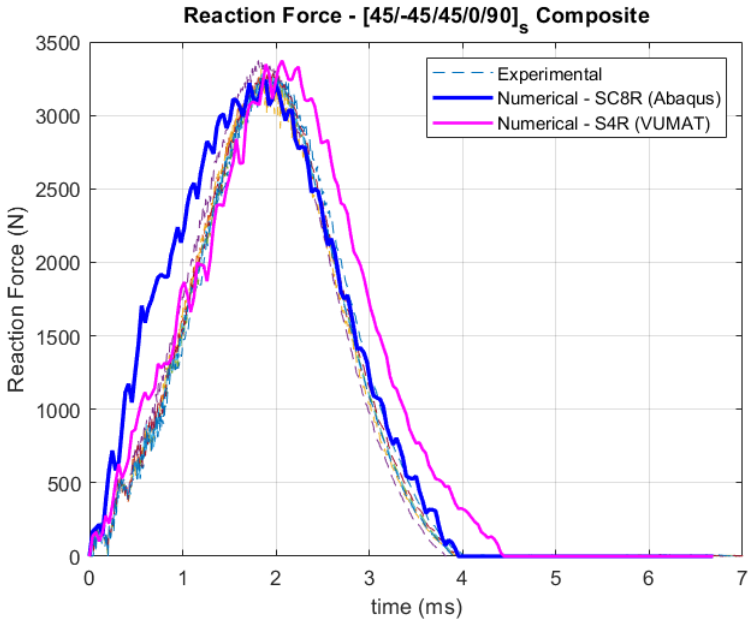


Figure 33: Reaction Force - $[+45/-45/+45/0/90]_s$ - Layup

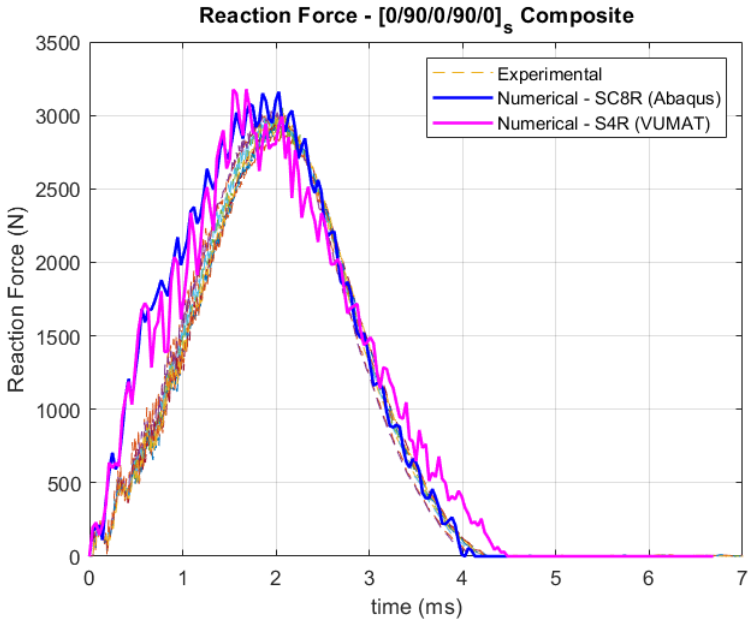


Figure 34: Reaction Force - $[0/90/0/90/0]_s$ - Layup

5 Results Post-Processing

The aim of this section is to familiarise the reader with the process of manipulating the results, in particular to obtain graphs of reaction force and energy evolution over time. In addition to Abaqus, an Excel spreadsheet will be required. Software such as MatLab may also be used, but is not obligatory.

5.1 Reaction Force Vs Time

To extract the force data, two alternatives will be presented:

- Use the acceleration of the projectile as a basis
- Use the contact forces on the plate as a basis

For the first option, select "Create XY Data" (side toolbar) and then "OBD Field Output". OBD is the type of file created by Abaqus to store all the results relating to the variables selected in the Field Output. Next, a window will open in which the variables to be accessed and the interest region will be defined. In the "Variable" tab, select the "Position" "Unique Nodal" , then select the variable to access, in this case acceleration. The three components are available, as well as their magnitude. Since the projectile only moves in z, only the third component (A3) will be evaluated. Finally, by going to the "Elements/Nodes" tab, the user selects the region from which the data will be extracted. It's good practice to create sets for regions of interest so that using "Node sets" makes it easy to select those regions. In this case, a set was created with the reference point of the projectile. Another option is to select it manually. To do this, instead of the "Node sets" option, use the "Pick from ViewPort" feature and select the reference point. It is useful to have the "Highlight items in viewport" checkbox to see if the correct regions are being selected. To finalise the process, select "Plot". The steps described above, as well as the result obtained, can be found in Figures 35 to 37.

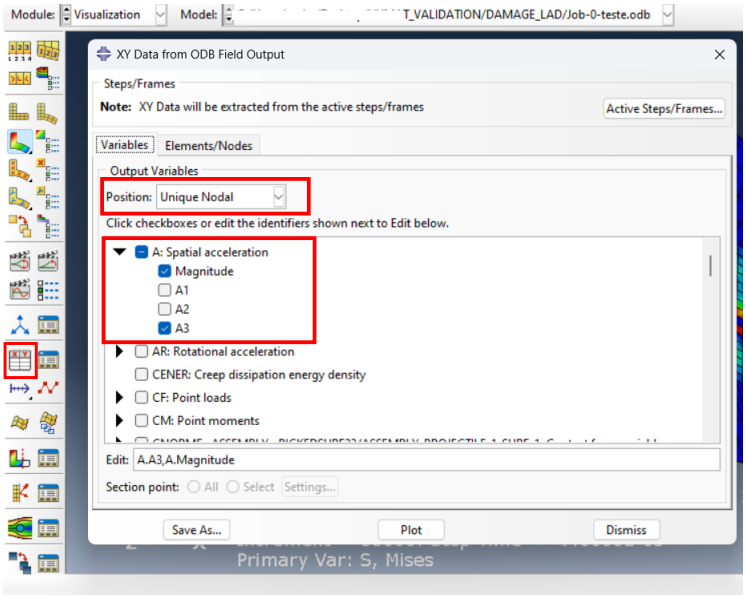


Figure 35: XY Data and variables selection

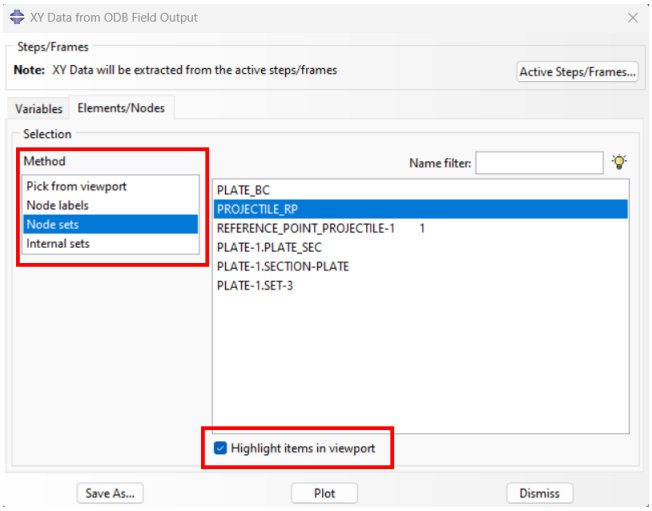


Figure 36: Elements/Nodes selection

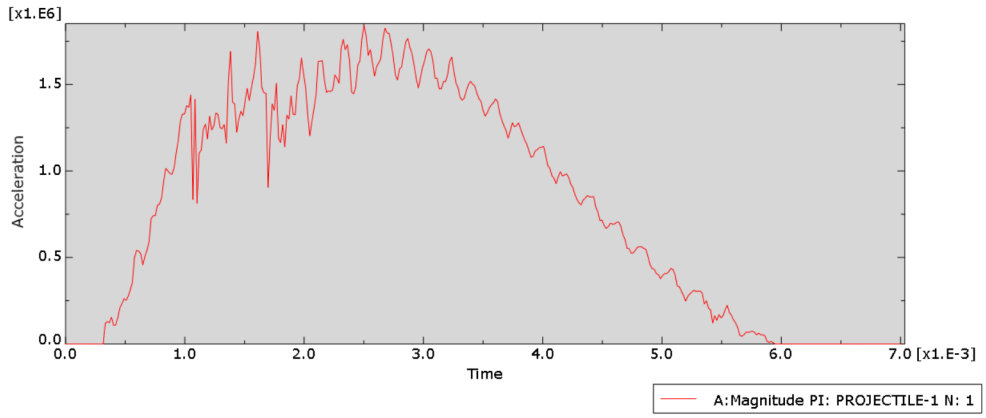


Figure 37: Acceleration Plot

Once the acceleration data has been collected, it must be multiplied by the mass of the projectile to obtain the force value. Furthermore, it is necessary to discount the initial instants, where there was no contact between the projectile and the plate. Note that this occurs because 1 mm of spacing has been left between the two.

Abaqus has data manipulation tools, but they are not very intuitive. The best option is to export the data to a spreadsheet, and then manipulate the results. For this, after creating the graph, in the top toolbar, press "Plug-ins" and then "Tools"-"Excel Utilies". To finalise the process, choose which data to export to Excel, in this case "From Current XY Plot". Figure 38 illustrates the process described.

Figure 39 shows the Excel file resulting from this process. Column A contains the time data, while column B lists the values for the projectile's acceleration. Using the functions/tools available in Excel makes it easier to manipulate the data, in order to ultimately determine the evolution of the force over time.

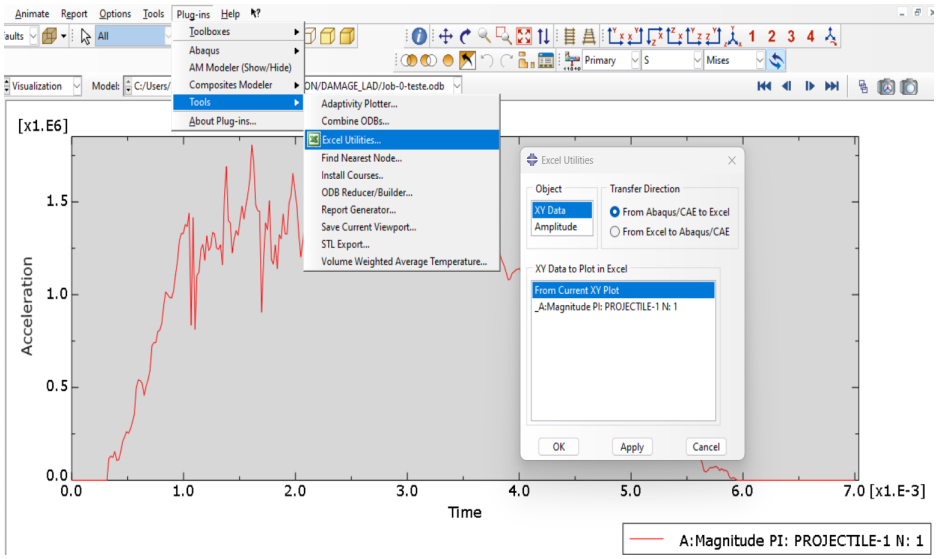


Figure 38: Exporting Results

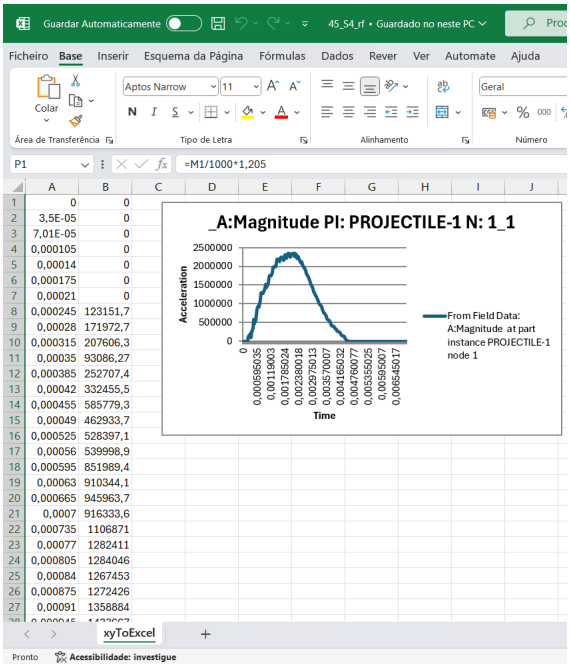


Figure 39: Results - Excel

Next, the second method for determining reaction force-time graphs is explained. The process begins, as explained above, by using "Create XY Data". Then it is necessary to change the variable and the region of interest. In this case, the variable to be used refers to the contact forces - CNORMF. The "Magnitude" component will be used because it includes the components in the 3 different directions. Although the projectile's displacement is only in the z direction (or 3), the deformation in the plate results in non-zero force values for the other directions (x and y or 1 and 2, respectively). As far as the region of interest is concerned, it is the plate and not the projectile. As the contact is very localised, only the nodes close to this region will be considered, once the rest have contact forces equal to zero. Like mentioned above, creating a set in this region is advantageous. The following Figures 40 and 41 show both the variable and the selected nodes.

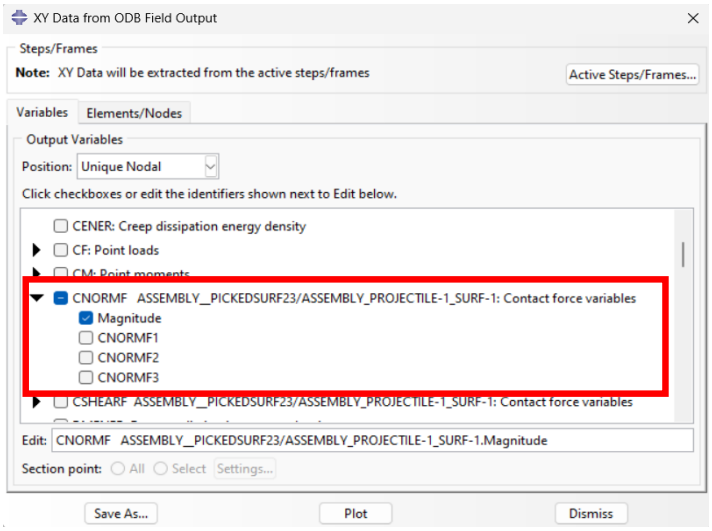


Figure 40: Contact Force Variable Selection

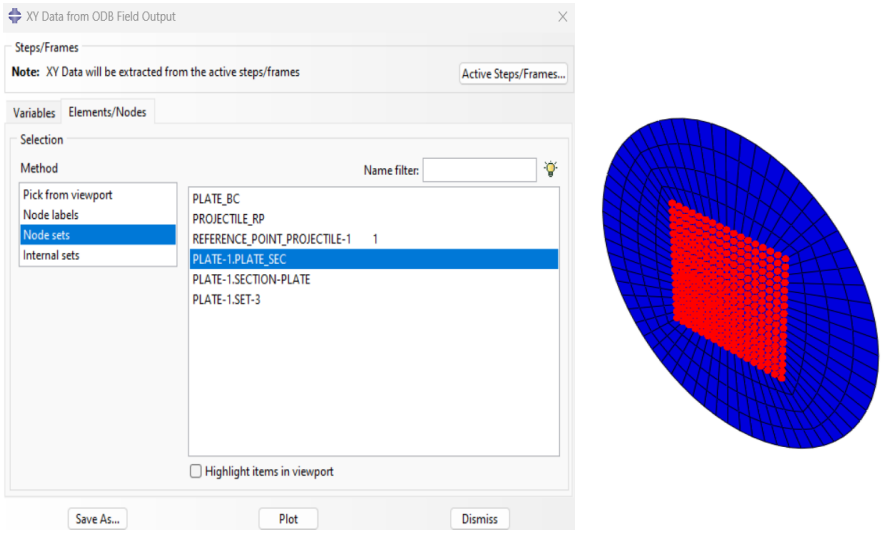


Figure 41: Node Region Selection

After pressing "Plot", a graph similar to Figure 42 will be displayed. Each curve represents the evolution of the contact force for each node, so the total force is determined by the sum of all the curves. This operation can still be carried out in Abaqus, before exporting the data. Once again, use the "XY Data" tool and select "Operate on XY Data". A window will open, allowing users to select the data and define the operations ("XY Data" and "Operator" sector). To perform the sum, select the "sum()" function in the "Operator" sector. Then, select all the curves and press "Add to Expression", followed by "Plot Expression" (see Figure 43).

Finally, a graph identical to Figure 37 will be obtained, which can be exported to Excel. In this case, as the force value is already displayed, it is only necessary to remove the initial instants before the impact initiates.

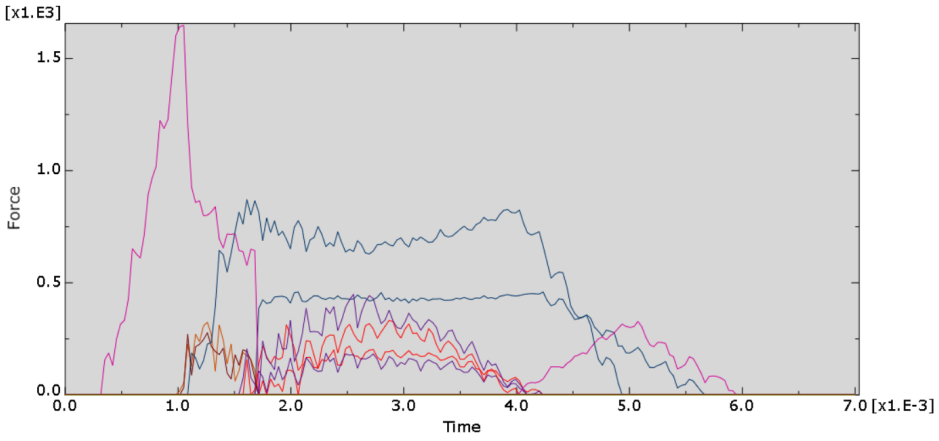


Figure 42: Contact Force at Each Node - Plot

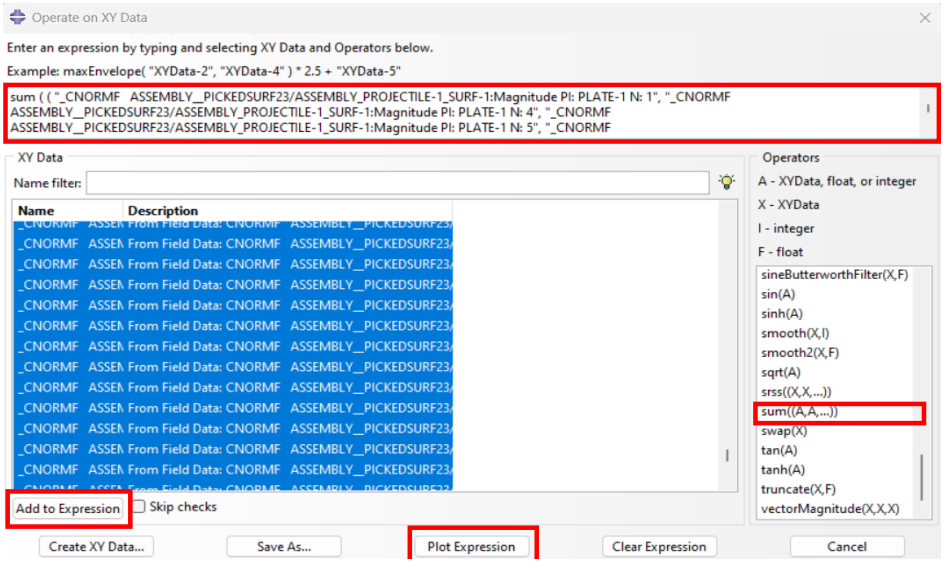


Figure 43: Contact Force Sum

5.2 Energy Evolution

To determine the evolution of the energy transferred, a methodology similar to the one explained above was applied. In this case, the variable to be taken into account is the velocity of the projectile, specifically the reference point. For the same reasons as for acceleration, only component 3 of the velocity (V3) will be non-zero. To extract always positive velocity values, the "Magnitude" component will be used instead of V3 (see Figure 44). As the projectile moves in both directions of the 3, or z, direction, the velocity has opposite signs in the forward and backward phases. Once the velocity had been extracted and the data exported to an Excel file, the following equation 36 was used to calculate the energy transferred (E_t).

$$E_t = \frac{1}{2} m_p {v_0}^2 - \frac{1}{2} m_p v(t)^2 = \frac{1}{2} m_p ({v_0}^2 - v(t)^2) \tag{36}$$

Where: m_p represents the mass of the projectile, v_0 the initial velocity of the projectile and $v(t)$ its velocity at the instant t.

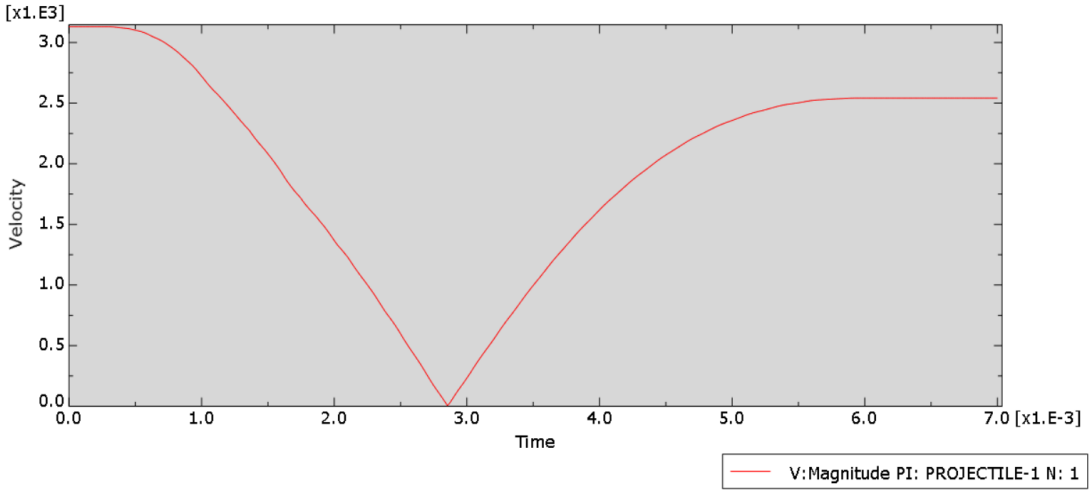


Figure 44: Velocity "Magnitude" - Plot

5.3 Accessing Subroutine Variables

As mentioned above, internal variables were created in the subroutine to store and pass information from interaction to iteration. TO understand if it operates correctly, it is vital to analyse the evolution of the variables. They are accessed in the same way as regular variables. Extra care must be taken by the user to cross-check the position assigned to the property in the subroutine. For example, SDV1 represents the property stored in the stateNew(km,1) variable. The following Figures 45 and 46 illustrate how to access them.

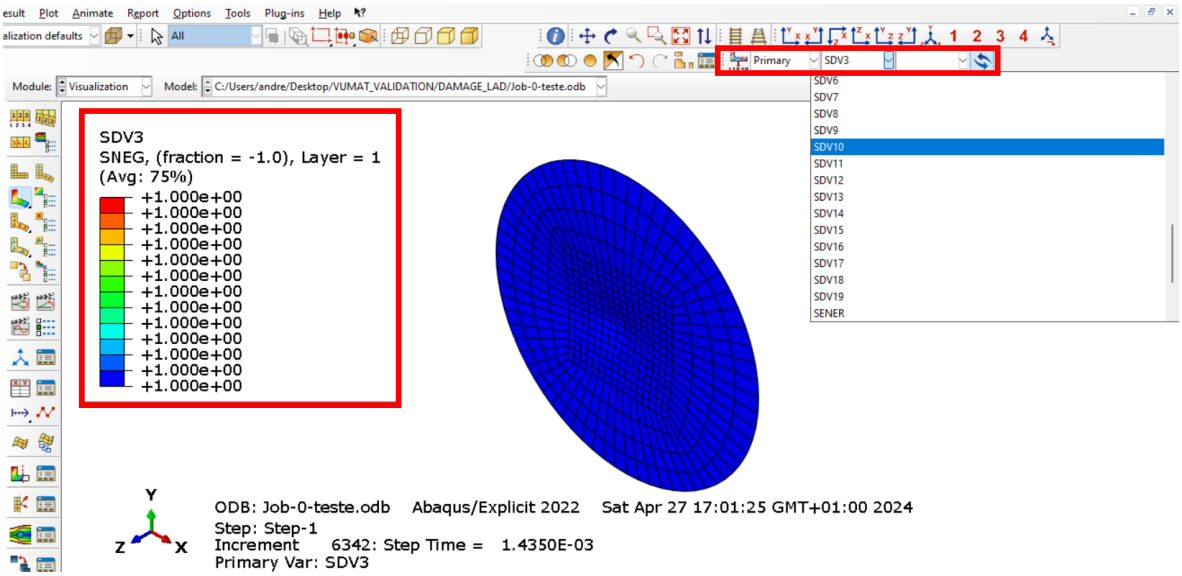


Figure 45: Accessing SDV - Vizualization

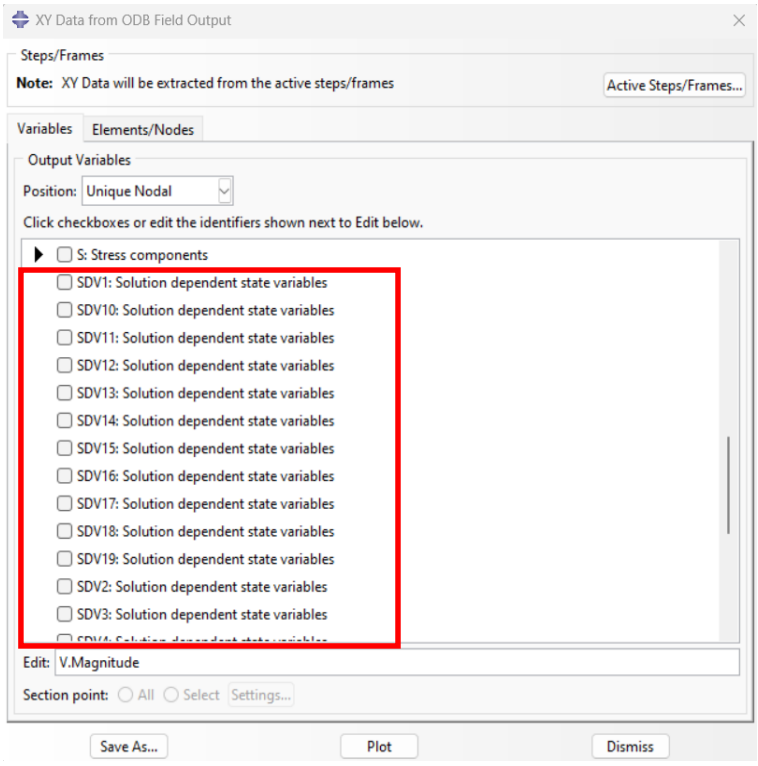


Figure 46: Accessing SDV - XY Data

References

[1] Volnei Tita, Jonas de Carvalho, and Dirk Vandepitte. Failure analysis of low velocity impact on thin composite laminates: Experimental and numerical approaches. *Composite Structures*, 83(4):413–428, 2008.

[2] Willian Leandro dos Santos Pinto. Simulação de ensaio de compressão radial em compósito fabricado via filament widing: Avaliação do efeito de concentradores de tensão. pages 1–23, 2023.

[3] Samira Gholizadeh. A review of impact behaviour in composite materials. *International Journal of Mechanical and Production Engineering*, 7(3):2320–2092, 2019.

[4] Owonubi J Shesan, Agwuncha C Stephen, Anusionwu G Chioma, Revaprasadu Neerish, and Sadiku E Rotimi. Fiber-matrix relationship for composites preparation. *Renewable and sustainable composites*, pages 1–30, 2019.

[5] Krishan Kumar Chawla and Krishan Kumar Chawla. Strength, fracture, fatigue, and design. *Composite Materials: Science and Engineering*, pages 229–258, 1987.

[6] G Minak, Mohammad Fotouhi, and M Ahmadi. Low-velocity impact on laminates. *Dynamic Deformation, Damage and Fracture in Composite Materials and Structures*, pages 147–165, 2016.

[7] Gregório Felipe Oliveira Ferreira, Marcelo Leite Ribeiro, António Joaquim Mendes Ferreira, and Volnei Tita. Computational analyses of composite plates under low-velocity impact loading. *Materials Today: Proceedings*, 8:778–788, 2019. 4th Brazilian Conference on Composite Materials (BCCM 4), July 22-25th 2018.

[8] Federico Paris and Karen E Jackson. A study of failure criteria of fibrous composite materials. Technical report, NASA Langley Research Center, 2001.

[9] Pedro Ponces Camanho. Failure criteria for fibre-reinforced polymer composites. *Secçăo de Mecânica Aplicada, Departamento de Engenharia Mecânica e Gestăo Industrial, Faculdade de Engenharia da Universidade do Porto*, 2002.

[10] Zvi Hashin and Assa Rotem. A fatigue failure criterion for fiber reinforced materials. *Journal of composite materials*, 7(4):448–464, 1973.

[11] Zvi Hashin. Fatigue failure criteria for unidirectional fiber composites. *J. appl. Mech*, 47(4):329–334, 1980.

[12] ABAQUS DS SIMULIA. 19.3.2 damage initiation for fiber-reinforced composites, 2009.

[13] ABAQUS DS SIMULIA. 19.3.3 damage evolution and element removal for fiber-reinforced composites, 2009.

[14] Marcelo Leite Ribeiro, Dirk Vandepitte, and Volnei Tita. Damage model and progressive failure analyses for filament wound composite laminates. *Applied Composite Materials*, 20:975–992, 2013.

[15] Pierre Ladeveze and E LeDantec. Damage modelling of the elementary ply for laminated composites. *Composites science and technology*, 43(3):257–267, 1992.

[16] ABAQUS DS SIMULIA. 6.3.3 explicit dynamic analysis, 2009.

[17] ABAQUS DS SIMULIA. 1.2.4 vumat user subroutine to define material behavior., 2009.

Annexes

VUMAT Code

```
subroutine vumat(
c Read only -
     1  nblock, ndir, nshr, nstatev, nfieldv, nprops, lanneal,
     2  stepTime, totalTime, dt, cmname, coordMp, charLength,
     3  props, density, strainInc, relSpinInc,
     4  tempOld, stretchOld, defgradOld, fieldOld,
     5  stressOld, stateOld, enerInternOld, enerInelasOld,
     6  tempNew, stretchNew, defgradNew, fieldNew,
c Write only -
     7  stressNew, stateNew, enerInternNew, enerInelasNew )
c
      include 'vaba_param.inc'
C
      dimension props(nprops), density(nblock),
     1  coordMp(nblock,*),
     2  charLength(*), strainInc(nblock,ndir+nshr),
     3  relSpinInc(nblock,nshr), tempOld(nblock),
     4  stretchOld(nblock,ndir+nshr), defgradOld(nblock,ndir+nshr+nshr),
     5  fieldOld(nblock,nfieldv), stressOld(nblock,ndir+nshr),
     6  stateOld(nblock,nstatev), enerInternOld(nblock),
     7  enerInelasOld(nblock), tempNew(*),
     8  stretchNew(nblock,ndir+nshr), defgradNew(nblock,ndir+nshr+nshr),
     9  fieldNew(nblock,nfieldv), stressNew(nblock,ndir+nshr),
     1  stateNew(nblock,nstatev),
     2  enerInternNew(nblock), enerInelasNew(nblock)
C
      character*80 cmname
C
C --- START OF USER CODE ---
C
C - DECLARING USER VARIABLES
C
      double precision E11, E22, NU12, G12, NU21, XT, XC, d1, TF2,
     & TF6, d6, RZY0, RZYC, RZY0L, RZYCL, b, Y, XC0, YC0, FM, FF,
     &  S12, num1, h, num2, d2, YT, TF1, S12_Y
C
C - ASSIGNING VALUES
      parameter (XT=1940, XC0=253, XC=930, RZY0=0.06627,
     & RZYC=1.861591, YC0=60.3, RZYCL=6.125483,
     & h=0.05161907, RZY0L=0.013425, b=0.929007,S12_Y=47)
C
C - ADDITIONAL VARIABLES
      integer km
```

```
      dimension STRAIN(3), DDSDDE(3,3)
C
C - READING MATERIAL PROPERTIES FROM ABAQUS CAE
      E11 = props(1)
      E22 = props(2)
      NU12 = props(3)
      G12 = props(4)
      NU21 = (props(2)/props(1))*props(3)
C
C - START ITERATION
      DO 100 km = 1, nblock
C
C - DAMAGE VARIABLES INITIALIZATION
      d1 = 0.0
      d2 = 0.0
      d6 = 0.0
C
C - CHECKING THE PRESENCE OF DAMAGE
      IF (stateOld(km,1) .eq. 1.0) then
        E11 = stateOld(km,5)
        d1 = stateOld(km,12)
        NU12 = stateold(km,7)
      END IF
C
      IF (stateOld(km,2) .eq. 1.0) then
        E22 = stateOld(km,6)
        d2 = stateOld(km,13)
        NU21 = stateOld(km,15)
      END IF
C
      IF (stateOld(km,3) .eq. 1.0) then
        G12 = stateOld(km,8)
        d6 = stateOld(km,14)
      END IF
C
C - FILL JACOBIAN MATRIX (DDSDDE) WITH ZEROS
      DO 20 K1 = 1, 3
        DO 10 K2 = 1, 3
            DDSDDE(K2,K1) = 0.0
10      CONTINUE
20    CONTINUE
C
C - ASSEMBLE THE CONSTITUTIVE TENSOR
      DDSDDE(1,1) = (E11)/(1.0-(NU12*NU21))
      DDSDDE(1,2) = (NU21*E11)/(1.0-(NU12*NU21))
      DDSDDE(2,2) = (E22)/(1.0-(NU12*NU21))
      DDSDDE(2,1) = (NU21*E11)/(1.0-(NU12*NU21))
```

```
      DDSDDE(3,3) = G12
C
C - STRESS PREDICTION
      stressNew(km,1) = stressOld(km,1)
     &                 +DDSDDE(1,1)*(strainInc(km,1))
     &                 +DDSDDE(1,2)*(strainInc(km,2))
     &                 +DDSDDE(1,3)*(strainInc(km,4))
      stressNew(km,2) = stressOld(km,2)
     &                 +DDSDDE(2,1)*(strainInc(km,1))
     &                 +DDSDDE(2,2)*(strainInc(km,2))
     &                 +DDSDDE(2,3)*(strainInc(km,4))
      stressNew(km,3) = stressOld(km,3) + 0.0
      stressNew(km,4) = stressOld(km,4)
     &                 +DDSDDE(3,1)*(strainInc(km,1))
     &                 +DDSDDE(3,2)*(strainInc(km,2))
     &                 +DDSDDE(3,3)*(strainInc(km,4))
C
C - STRAIN CALCULATION
      STRAIN(1) = stateOld(km,9) + strainInc(km,1)
      STRAIN(2) = stateOld(km,10) + strainInc(km,2)
      STRAIN(3) = stateOld(km,11) + strainInc(km,4)
C
C Energy calculation - (!BASE CODE MODIFICATION!)
C (DOES NOT INTERFERE WITH RESULTS)
      stressPower = 0.5*((stressOld(km,1)+stressNew(km,1) )
     &    *strainInc(km,1)
     &    +     ( stressOld(km,2)+stressNew(km,2) )*strainInc(km,2)
     &    +     ( stressOld(km,3)+stressNew(km,3) )*strainInc(km,3)
     &    + 2.0*( stressOld(km,4)+stressNew(km,4) )*strainInc(km,4))

      enerInternNew(km) = enerInternOld(km)
     &                   +stressPower/(1.59e-9)
C
C - EVALUATION OF THE FAILURE MODE INDICES
C -    1. - FIBRE
      IF (stressNew(km,1) .gt. 0.0) THEN
         FF = (stressNew(km,1)/XT)**2.0
      ELSE
         FF = (stressNew(km,1)/XCO)**2.0
      END IF
C
C -    2. - MATRIX
      num1 = (stressNew(km,4)**2.0)/(S12_Y**2)
      num2 = ((stressNew(km,2)-h)**2.0)/(YCO**2)
      FM = sqrt(num1+num2)
C
C - THERMODYNAMIC FORCES
```

```
      IF (stressNew(km,2) .ge. 0.0) then
         TF2 = (stressNew(km,2)**2.0)/(2.0*props(2)*((1-d2)**2))
      ELSE IF (stressNew(km,2) .lt. 0.0) then
         TF2 = 0.0
      END IF
      TF6 = (stressNew(km,4)**2.0)/(2.0*props(4)*((1-d6)**2))
      Y = TF6+b*TF2
C
C - CHECK FAILURE OCURRENCE + PROPERTIES DETERIORATION
C - 1. - DETERIORATE FIBRE PROPERTIES
      IF (FF .ge. 1.0) then
         IF (stressnew(km,1) .gt. 0.0) then
            d1 = 0.99
            E11 = props(1)*(1.0-d1)
            NU12 = props(3)*(1.0-d1)
            stateOld(km,1) = 1.0
         ELSE IF (stressNew(km,1) .lt. 0.0) then
            E11 = ((XC0)/abs(STRAIN(1)))*(1.0-(78.873*STRAIN(1)+1.087))
     &           + (78.873*STRAIN(1)+1.087)*props(1)
            stateOld(km,1) = 1.0
C
         END IF
      END IF
      IF (E11 .lt. 0.01*props(1)) then
          E11 = abs(0.01*props(1))
      END IF
C
      stateNew(km,5) = E11
      stateNew(km,7) = NU12
      stateNew(km,12) = d1
      stateNew(km,1) = 1.0
C
C - 2. - DETERIORATE MATRIX PROPERTIES
C - Condition 1
      IF ((FM .gt. 1.0)) then
         IF ((d6 .lt. 1.0) .and. (sqrt(Y) .ge. (RZY0))
     &       .and.  (sqrt(Y) .lt. (RZY0+RZYC))) then
            d6 = (sqrt(Y)-RZY0)/(RZYC)
            G12 = props(4)*(1-d6)
            stateOld(km,3) = 1.0
         END IF
         IF (d6 .ge. 1.0) then
            d6 = 0.99
         END IF
         IF (d6 .lt. stateOld(km,14)) then
            d6 = stateOld(km,14)
         END IF
```

```
          IF ((stressNew(km,2) .gt. 0.0) .and. (d2 .lt. 1.0)
     &       .and. (sqrt(Y) .ge. (RZY0L))
     &       .and. (sqrt(Y) .lt. (RZY0L+RZYCL))) then
                d2 = (sqrt(Y)-RZY0L)/(RZYCL)
                E22 = props(2)*(1-d2)
                NU21 = ((props(2)/props(1))*props(3))*(1-d2)
                stateOld(km,2) = 1.0
          END IF
          IF (d2 .gt. 1.0) then
             d2 = 0.99
          END IF
          IF (d2 .lt. stateOld(km,13)) then
             d2 = stateOld(km,13)
          END IF
        END IF
C
C - Condition 2
        IF (FM .gt. 1.0) then
           IF (stressNew(km,2) .lt. 0.0) then
              IF ((d6 .lt. 1.0) .and. (sqrt(Y) .ge. RZY0)
     &          .and. (sqrt(Y) .lt. (RZY0+RZYC))) then
                 d6 = (sqrt(Y)-RZY0)/(RZYC)
                 G12 = props(4)*(1-d6)
                 stateOld(km,3) = 1.0
              END IF
              IF (d6 .gt. 1.0) then
                    d6 = 0.99
              END IF
              IF (d6 .lt. stateOld(km,14)) then
                    d6 = stateOld(km,14)
              END IF
              stateOld(km,8) = G12
              stateOld(km,14) = d6
              IF (abs(stressNew(km,2)) .gt. YC0) then
                    E22 = ((YC0)/abs(STRAIN(2)))*(1.0-(4.1763*((STRAIN(2)))
     &                 +0.03182))+(4.1763*((STRAIN(2)))+0.03182)*props(2)
                    stateOld(km,2) = 1.0
              END IF
              stateOld(km,6) = E22
           END IF
        END IF
C
        IF (E22 .lt. 0.001*props(2)) then
              E22 = 0.001*props(2)
        END IF
C
C - STATE VARIABLES UPDATE
```

```
      stateNew(km,6) = E22
      stateNew(km,15) = NU21
      stateNew(km,13) = d2
      stateNew(km,8) = G12
      stateNew(km,14) = d6
      stateNew(km,3) = 1.0
      stateNew(km,2) = 1.0
      stateNew(km,9) = STRAIN(1)
      stateNew(km,10) = STRAIN(2)
      stateNew(km,11) = STRAIN(3)
C
      IF (stateNew(km,2) .lt. 10.0**(-6.0)) then
           stateNew(km,2) = 0.0
      ELSE IF (stateNew(km,3) .lt. 10.0**(-6.0)) then
           stateNew(km,3) = 0.0
      END IF
C
C - CONDITION FOR DELETING ELEMENTS - ((d1 or d2 or d6) >=0.99)
      IF((stateOld(km,12) .ge. 0.99) .or. (stateOld(km,13) .ge. 0.99)
     & .or. (stateOld(km,14) .ge. 0.99)) then
        stateNew(km,17) = 0.0
      END IF

100   CONTINUE
        C
      RETURN
      END
```